ALMA MATER STUDIORUM · UNIVERSITÀ DI BOLOGNA

DOTTORATO DI RICERCA IN
GEOFISICA
Ciclo XXVIII

Settore Concorsuale di afferenza: 04/A4
Settore Scientifico disciplinare: GEO10

Study of the transient deformation of Central and Southern Apennines from GPS observations

Presentata da: Francesca Silverii

Coordinatore Dottorato:
Prof.ssa Nadia Pinardi

Relatore:
Dott. Nicola D'Agostino

Co-relatore:
Prof.ssa Maria Elina Belardinelli

Esame finale anno 2016

Racconta una vecchia ed amara leggenda
che Maia, la figlia d'Atlante, stupenda,
scampata al nemico fuggì dall'oriente
con l'unico figlio ferito e morente.
Raggiunto d'Italia un porto roccioso,
sfruttando le forre e il terreno insidioso,
condusse il ferito, vicino al trapasso,
in alto lassù sopra il monte Gran Sasso.
A nulla giovaron, nell'aspra caverna,
le cure profuse da mano materna:
al giovane figlio volò via la vita
lasciando alla madre una pena infinita.
E proprio quel monte d'Abruzzo nevoso
racchiuse la salma all'estremo riposo.
Il grande dolore di Maia la diva
escluse al suo cuore la gioia istintiva;
non ebbe più pace, non valse l'apporto
dei propri congiunti a darle conforto.
Sommersa dal lutto, sconvolta dal dramma,
non ebbe più pianto, non era più mamma.
Di vivere ancora non ebbe coraggio:
si spense nell'ultima notte di maggio.
Un mesto corteo con fiori per Maia
salì a seppellirla in un'altra giogaia,
rimpetto alla tomba del figlio adorato
strappato alla madre dal barbaro fato.
E quella montagna, al cospetto del mare,
d'allora Maiella si volle chiamare.
"Amaro" ebbe nome la vetta maggiore
per dare risalto al materno dolore.
–Mario Lolli

Contents

Abstract

In the last years, geodetic measurements have shown that temporal variations in total groundwater content induce transient deformations of the crust that are mostly reflected in the vertical component. Here we present new GPS observations showing a noticeable non-tectonic transient deformation in the Apennines (Italy), mostly evident in the horizontal components, that correlate with multi-annual hydrological signals as measured by rainfall, GRACE (Gravity Recovery and Climate Experiment) and discharge of karst springs. The observed transient signal is superimposed on the long-term ∼3 mm/yr NE-SW directed active extension, correlates with the seasonal recharge/discharge cycle of groundwater flow and its multi-annual variations and appears to modulate the intensity of tectonic extensional opening in those regions characterized by large carbonate aquifers. In particular, periods of increasing discharge from karstic spring correlate with an enhanced extensional signal, whereas exhaustion periods correlate with reduced extensional signal.

Vertical observations, being correlated with GRACE data, reflect the hydrological load variation over regional (European) scale. Horizontal deformations, conversely, affect mostly the sites located near the large carbonate massifs of the Apennines and can't be explained as load induced response. We suggest that the horizontal observed deformation is related to the presence of highly fractured shallow crust that deforms according to variable conditions of the hydraulic head within the large carbonate aquifers. We therefore propose two different models that simulates the effect of a medium

permeated with sub-vertical opening fractures.
These new findings could contribute to the understanding of the deformation of the large carbonate aquifers and to an improved management of these important natural resources.
By focusing on the 2009 L'Aquila earthquake, we finally highlight the difficulties that arise for the estimation of interseimic trends and small tectonic signals in areas affected by such significant non-tectonic deformations.

Introduction

In the last decades increasing interest has been focused on the detection of transient deformation signals in geophysical observations. These are usually related to transitory and non-secular strain accumulation in the crust and appear as temporary deviations from steady-state, long-term displacements associated to the plate motions and the interseismic strain accumulation on active faults.

Due to the usually unknown features of transient events (magnitude, duration and spatial coverage), their detection needs accurate and temporally continuous measurements of the surface deformation over large areas. Space geodesy, and, in particular, continuously operating Global Positioning System (GPS) networks, recording station position changes with millimetre-level accuracy, have therefore provided a special tool in this regard.

Several kinds of transient signals have been identified so far, which are characterized by wide magnitude variations and affect various spatial and temporal scales. In particular both transients related to tectonic and non-tectonic sources have been highlighted. Tectonic transients includes several phenomena such as the postseismic deformation, the slow slip or creeping processes and the volcanic deformation. These phenomena are widely studied since they can provide fundamental insights about the main features and hazard estimation of seismic and volcanic areas.

Recently the detection and analysis of transients related to non-tectonic causes have raised strong interest and it is well known nowadays that surface measurements of the Earth's deformation can be affected by hydrological

processes. Geodetic data substantially improve the accuracy and space distribution of the observations with respect to the classical hydrology dataset. The study of hydrologically-related transient deformations has numerous applications in the understanding of the global- and regional-scale water mass redistributions and of the aquifers-system response. Furthermore the detection of this kind of transients in the geophysical observables is fundamental in order to correctly identify and estimate the transient and long-term deformations of tectonic nature (e.g., interseismic strain, postseismic and eventual preseismic deformation).

In this work we have evidenced a non-tectonic multi-annual transient signal in GPS time-series of Central and South-Central Italy. This signal is strongly correlated with hydrological data, shows a well defined spatial pattern and reveals a noticeably high amplitude (up to 1 cm) even in the horizontal components.
The observed transient signal is superimposed on the long-term $\sim$3 mm/yr NE-SW directed active extension, correlates with the seasonal recharge/discharge cycle of groundwater flow and its multi-annual variations and appears to modulate the intensity of tectonic extensional opening in regions characterized by large carbonate aquifers. Central and South-Central Apennines are in fact characterized by the presence of wide carbonate ridges that are able to store a huge quantity of water and therefore represent the main water resources of this area.
The study of such a transient deformation and the understanding of the involved processes is particularly interesting for several reasons. It could help to figure out the ongoing deformation of the Apennines, which are a particularly complex and seismogenic area, and it could contribute to the understanding of the role and the behaviour of the karst systems in conveying large amounts of water. Furthermore this analysis highlights the importance of taking into account the presence of strong non-tectonic (multi-annual) signals when dealing with tectonic-related deformations in the Apennines area. These signals in fact heavily complicate the interseismic rate estimation from

short time-series and could interfere (or obscure) with tectonic signals associated to moderate earthquakes.

The aim of this thesis is to deeply analyse the main features of the highlighted transient deformation and to investigate the processes which could produce it.
A short excursus about tectonic and non-tectonic transient signals and of the importance of their analysis is outlined in the first chapter. In the second one the main features of karst aquifers are described, in particular highlighting the peculiarities that characterize the carbonate aquifers of Central and South-Central Apennines.
In the third chapter we delineate the theoretical background of the three models that we have tested to explain the observed deformation. The first one is the elastic response to surface loads on homogeneous and stratified half-spaces, which is often employed to explain the deformation of the Earth's surface due to hydrological loads. The second one describes the deformation produced by tensile dislocations buried in an elastic half-space. This model will be used to simulate the deformation associated with the opening of hydrofractures in the Earth's crust. The third one is the effective stress theory which provides a relatively simple mean to simulate the deformations of porous aquifers due to water table height variations.
In the fourth chapter we briefly illustrate the basic principles of the GPS technique and, in particular, of high-precision GPS observations.
In chapter 5 we present the examined observables, i.e. GPS data and three different kinds of hydrological observables: the rain-gauge data, the discharge data of some of the main karst springs of the Apennines and the terrestrial water storage observations by GRACE (Gravity Recovery and Climate Experiment) satellite. In the last section we develop a deepened comparison between GPS and hydrological data, focusing on the correlation of both GPS horizontal and vertical components with the different hydrological observables.

In the last chapter by employing the three previous mentioned models, we investigate the processes that could have a role in causing the transient deformation we have highlighted in Central and South-Central Apennines. Then, focusing on the 2009 L'Aquila earthquake event, we reflect on the difficulties related to the estimation of interseimic trend and small tectonic signals in the areas affected by significant non-tectonic deformations.

Chapter 1

Tectonic and non-tectonic transient signals

Transients can be defined as transitory and non-secular strain accumulation in the crust. They therefore differ from long-term displacements due to plate motions and interseismic strain accumulation on active faults, which are constrained as steady-state at the time scale of the instrument observation.

Transient signals are characterized by wide magnitude variations, ranging from spatially coherent surface displacements of several centimetres to only a few millimetres, and can also span over time-intervals varying from year-long signals (e.g. Miyazaki et al., 2003) to short episodes lasting only a few days (e.g. Rogers and Dragert, 2003).

Usually transients associated to a common cause are detected on the basis of their combined temporal and spatial coherency, i.e., they show a measurable temporal evolution and a systematic spatial distribution. This is the basic concept used for the identification of transients by means of different statistic tools (e.g. Ji and Herring, 2013; Riel et al., 2014; Gualandi et al., 2015; Bekaert et al., 2016; Walwer et al., 2016).

In order to identify transient events characterized by unknown amplitude, duration and spatial coverage, accurate and temporally continuous measure-

ments of surface deformation over large areas are needed. In this context, the development of space geodesy, and, in particular, of dense, large-scale and continuously operating GPS networks providing three-dimensional observations, have permitted great improvements in transients detection and analysis. Geodesy based on repeat imagery (e.g., interferometric synthetic aperture radar (InSAR)) furnishes spatially dense observations of surface displacement but it is characterized by poor temporal sampling. However, several developments such as the incoming of long time span InSAR time series, new techniques for the analysis of the temporal evolution of interferogram signals and incoming InSAR missions with shorter repeat times are enabling sufficiently high temporal resolution to capture several transient processes (e.g. Decriem and Árnadóttir, 2012; Tolomei et al., 2015).

Different causes of transient deformation exists, which can be distinguished between tectonic and non-tectonic.

1.0.1 Tectonic transient signals

Tectonic transients comprise several phenomena of tectonic origin that produce temporary deviations from the interseismic deformation of the crust. Some examples are represented in Figure 1.1.
In seismically active regions, transients can be the surface manifestation of postseismic processes that occur after even moderate earthquakes, such as the aseismic slip on the fault plane (afterslip), the viscoelastic relaxation of the coseismic stresses in the lower crust/upper mantle and the poroelastic relaxation, due to coseismic change in pore pressure in the rock hosting the main fault (e.g. Wang et al., 2009; Bie et al., 2014; Cheloni et al., 2014; Silverii et al., 2014). These different postseismic deformation sources are usually hard to be distinguished on the basis of the surface observations. Generally the deformation arising in the first days/months after an earthquake is associated with afterslip. Viscoelastic postseismic deformation is associated to the viscous flow in the lower crust/upper mantle which relaxes the earthquake-

induced stress changes and tends to become important on longer time-scales (years/decades).
Aside from signals due to postsesimic processes, even transient deformations occurring before seismic events have been highlighted in the last years, which have been often related to aseismic slip on the plate interface occurring before the mainshock event (e.g. Ruegg et al., 2001; Bouchon et al., 2011; Ruiz et al., 2014).
In the first years of the 21th century, a new source of transient deformation has been identified in subduction zones such as south-West Japan (Obara, 2002) and Cascadia (Rogers and Dragert, 2003). This phenomenon, defined *episodic tremor and slip*, consists in non-earthquake seismic tremor and slow slip along the plate interface. This process is difficult to be measured directly with traditional seismological instruments and the availability of GPS observations has therefore proved fundamental for its detection (Beroza and Ide, 2011). Slow slip or creeping phenomena have been now widely observed on strike-slip faults too, such as North Anatolian fault (Western Turkey) (e.g. Cakir et al., 2005) and Tibetan faults (e.g. Jolivet et al., 2012).
In volcanically active regions, transients are often related to phases of ground deformation due to underlying magmatic activity, such as growth of dikes and sills or magmatic chamber pressurizations (e.g. Owen et al., 2000; Langbein, 2003; Ji and Herring, 2011; Cannavò et al., 2015).

The study of transient tectonic deformation provides fundamental information on geophysical phenomena, e.g. the estimation of afterslip distribution gives insights on earthquake related stress propagation on a fault; the viscoelastic relaxation helps to constrain the rheology and structure of the lower crust/upper mantle; the examination of preseismic signals provides insights into the seismic gap history, seismic hazard and nucleation process of the main earthquakes; slow earthquakes, by virtue of their locations and their properties, provide new understanding on the behaviour of subduction or strike-slip zones; the observation of volcanic transients furnishes informations about the shape/position of magma reservoirs and helps to estimate

the volcanic hazard.

1.0.2 Non-tectonic transient signals

Non-tectonic transients refer to temporary surface motions that are induced by processes not attributable to tectonic causes. These are mainly ascribable to hydrology, i.e. deformations related to variations in the amount and spatial redistribution of water mass on the Earth surface.
In the last years, increasingly attention has been paid on the capability of GPS, and satellite geodesy in general, to detect transient processes of hydrological, non-tectonic, origin. Accurate observations of the Earth surface by satellite geodesy have revealed, in different geographical areas, ground deformations that can be clearly attributed to hydrological causes. These observations, acting both at annual and inter-annual time-scales, reflect the water mass distribution at global and local scales. This makes space geodesy to provide a new, accurate and spatially distributed tool that complements the classical hydrology dataset. Recently even GPS reflection data (multipath, see section 4.2.4) are used to measure soil moisture, snow depth, sea level and vegetation water content (e.g. Larson et al., 2015; Wan et al., 2015). Essentially, some of the signals that appear in GPS time-series, which were previously discarded or tried to be removed in order to observe, say, tectonic processes, have revealed to be the sources of interesting informations.
GPS measurements of crustal motion have proven useful to study surface loading due to ice, snow, water, or atmospheric mass. In fact, by monitoring the deformation with GPS, it is possible to place constraints on the change in mass or on the Earth's structure, if the mass change is provided in some other way, such as by gravimetric data (e.g. GRACE satellite data) (Chanard et al., 2014). The analysis of hydrologically related transients provides unprecedented insights on climate trends and water cycle variations and can help to understand aquifers-system response (e.g. González and Fernández, 2011; Moreau and Dauteuil, 2013). Furthermore the study of eventual interactions between hydrologically-related deformations and seismicity has

important implications for the understanding of earthquake nucleation and fault rheology (e.g. Bettinelli et al., 2008; Amos et al., 2014; Stabile et al., 2014).
To name a few examples, GPS observations have been used by Amos et al. (2014) and Argus et al. (2014) to analyse the hydrologically-related deformation in California, by Borsa et al. (2014) to investigate the recent drought that is affecting the Western USA and by Chanard et al. (2014) to examine seasonal variations of continental water storage in the Himalayas region. In these works, deformation is explained as the response to surface loading and most of the attention is focused on the vertical component of the deformation (Figure 1.2). The main reasons why horizontal displacements have not received the same level of attention are that loading induced horizontal displacements tend to be much smaller than vertical displacements (see section 3.1) and that large trends are usually present in horizontal components, due primarily to tectonic motion (Wahr et al., 2013). As we will see in chapters 5 and 6, in this work we have highlighted a multi-annual signal in GPS time-series around Central and Southern Apennines which is strongly correlated with the hydrological data and reveals a surprisingly high horizontal deformation.

Beside the numerous and interesting applications of transient observations stated before, another essential motivation for the identification (and modelization) of transient signals is to obtain the best possible estimates of long-term parameters of motion. This is fundamental for the analysis of plate motions and strain-rate distributions. Moreover, the correct estimation of the long-term velocities, in particular the vertical one, is important for terrestrial reference frames realizations. As an example, Liu et al. (2015) suggested that the 1992 Landers and 1999 Hector Mine earthquakes (Eastern California Shear Zone) altered the deformation field in the Mojave Desert, affecting negatively the use of GPS observations (starting mostly after 1992) to estimate the secular deformation field in this region.
Non-tectonic transient signals have to be carefully detected and not be con-

fused with the ones due to tectonic processes, as transient deformation related to seismic or volcanic events. Westerhaus et al. (2008), by analysing transient signals in the time-series of some tiltmeters located at the flanks of Merapi volcano (Indonesia), highlighted that ground water induced soil movements, under unfavourable conditions, may imitate the deformation field of an internal pressure variation.

As we will examine deeply in chapters 5 and 6, transient signals represent crucial aspects in the Apennines area, where only moderate earthquakes with related small (postseismic) transient deformation occur and where we have highlighted the presence of a noticeable multi-annual hydrological related deformation that produces temporary modulations of the interseismic trend. This is particularly important in the context of the study of the recent L'Aquila earthquake, which, being a moderate magnitude earthquake that has been recorded by several kinds of data (e.g., GPS, InSAR and seismological data), can provide very useful informations about the normal faulting seismicity in Central and Southern Italy. However, when dealing with deformation data, particular attention has to be paid in discerning tectonic and non-tectonic signals.

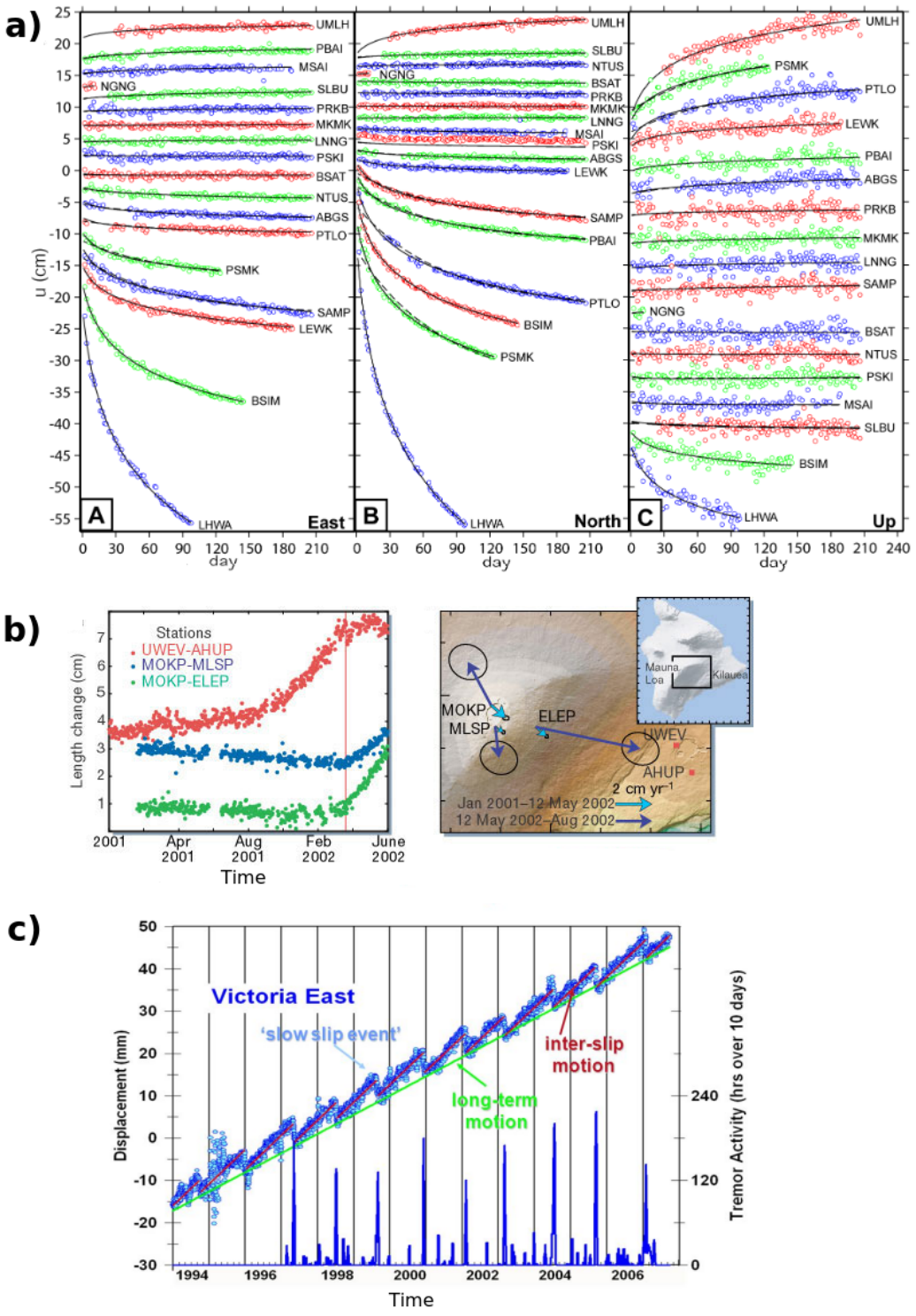

Figure 1.1: (Continued on the following page.)

Figure 1.1: Some examples of different tectonic transient signals. a) Postseismic time-series for 18 analysed stations after the 2005 M_w 8.7 Nias earthquake (Indonesia); solid and dashed lines are best-fit logarithmic and exponential functions, respectively (from Kreemer et al. (2006)). b) Transient deformation attributed to the inflation of the magma reservoir at Mauna Loa (Hawaii) in 2002. Left: changes in line length between GPS stations; right: horizontal-velocity vectors on Mauna Loa before and after the 12 May event (from Miklius and Cervelli (2003)). c) Comparison of slip and tremor activity observed for the Victoria area (Canada). Blue circles show day-by-day changes in the east component of the GPS site ALBH (Victoria) with respect to the GPS site near Penticton, which is assumed to be fixed on the North America plate. The bottom graph shows the total number of hours of tremor activity observed for southern Vancouver Island within a sliding 10-day period (modified from Rogers and Dragert (2003)).

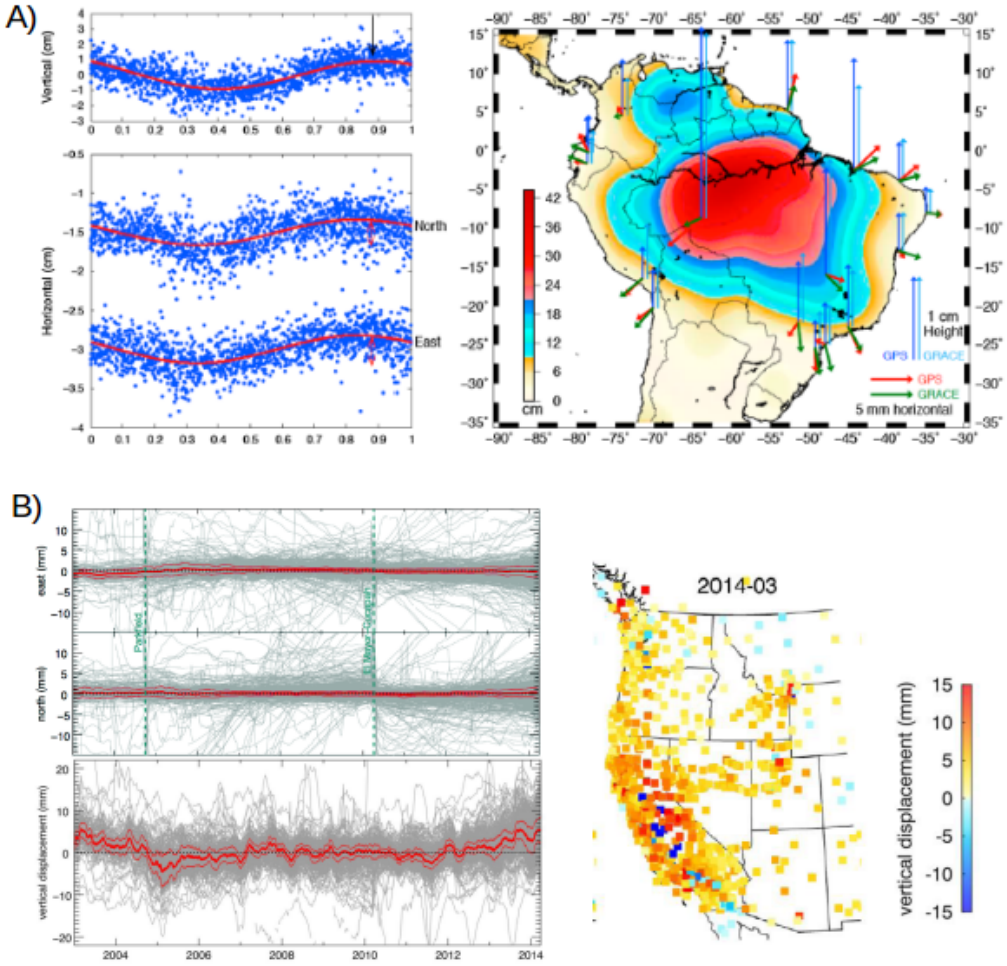

Figure 1.2: Two examples of hydrology-related deformation recorded from GPS. A) Seasonal loading of rain water in the Amazon Basin: GPS time series at one site (left); observed and modelled GPS displacements as due to load response (right) (from Fu et al. (2013)). B) Ongoing drought-induced uplift in the western United States: observed stacked GPS time-series (left), observed vertical displacements (right) (from Borsa et al. (2014)).

Chapter 2

Hydrogeology of the Apennines

2.1 Introduction to karst

Karst aquifers occupy only the 7-12% of the Earth's continental area, but provide water for about one quarter of the global population (Hartmann et al., 2014).
Karst typically develops from carbonate rocks, such as limestone and dolomite rock. Most carbonate rocks form from calcareous deposits that accumulate in marine environments and are derived from calcareous algae or the skeletal remains of marine organisms. The original texture and porosity of carbonate deposits are highly variable because of the wide range of environments in which the deposits form, therefore the primary porosity of the deposits can range from 1% to more than 50%. Several diagenetic processes, such as compaction, cementation, and dolomitization, act on the carbonate deposits to change their porosity and permeability.
The principal post-depositional process that acts on carbonate rocks and causes the formation of secondary porosity is dissolution. Raindrops absorb atmospheric carbon dioxide (CO_2) and vegetation and microbial processes in the soil further increase the CO_2 concentration in the water after the rain has fallen on the land surface and infiltrated in the soil. This acidic water partially dissolves carbonate rocks, initially by enlarging pre-existing openings

such as pores or joints and fractures in the rocks. These small solution openings become larger especially where a vigorous ground-water flow moves the acidic water through the aquifer and the openings sometimes join as hierarchically organized networks. At the land surface, the result of carbonate-rock dissolution is expressed as typical karst topography, characterized by caves, dolines, sinkholes, and other kinds of solution openings, and by the presence of only few surface streams.

Karst aquifers are complex and heterogeneous hydrological systems, however they can be classified into 3 different types (Civita, 1975) depending on the peculiar features and development of their drainage network (Figure 2.1):

- Karst type 1 (young karst): disperse and unhierarchized drains, not very deep dissolution dolines, covered or scarcely uncovered karst, few caves, absence of well developed deep drains, and hydraulic characteristics similar to those of an aquifer with permeability due to fractures and porosity. Presence of a broad phreatic zone.

- Karst type 2 (rather developed karst): partially hierarchic, but still interdependent, drains, frequent surface forms, scarce cover, wide and deep dissolution dolines, spread corrosional forms and caves with large drainage galleries. Presence of quite developed phreatic zone.

- Karst type 3 (holokarst): well hierarchic dominant drains, extremely developed karst landscapes, wide and deep dissolution and/or breakdown dolines, scarce cover, complex karst systems with presence of large horizontal galleries and huge vertical pits. Presence of a poorly developed or absent phreatic zone.

Tipically karst aquifers present two main flow regimes as a function of the extent of aquifer karstification: slow flow (diffuse flow) through karst fissures of small dimensions, generally in the laminar regime and turbulent fast flow (conduit flow) through larger fissures and irregular karst conduits, with dimensions varying from 10 mm to one metre or more (Bonacci, 1993; Fiorillo and Doglioni, 2010). The characteristics and development of the drainage

network influence the discharge of the aquifers and this is reflected in the outflow hydrographs (discharge time-series) of karst springs, (Figure 2.1). When karst features are not developed (karst type 1), flow occurs primarily as diffuse flow and spring hydrographs present high base flow, low time variations and relatively high delay time between precipitation and peak discharge. These karst aquifers therefore retain water for a much longer time than conduit karst systems. The shape of the spring hydrographs produced by these systems is consequently characterised by very few or only one smoothed peak that occurs after a time lag with regard to the rainy season. In case of rather developed karst (karst type 2), aquifers present few springs with a constant base flow but high time variations of their hydrochemistry and/or hydrodynamics. Very developed karst aquifers (karst type 3) show instead springs with scarce base flow but sudden and really high time variations in correspondence of rainfall events (Bonacci, 1993; Cucchi et al., 2004).

Karst systems are conceptually divided into three layers that are, from the top, epikarst, infiltration or vadose zone, and saturated or phreatic zone (Mangin, 1975). The epikarst zone includes both soil and weathered rock and has 5-30 m thickness, the vadose zone is mostly composed of massive rock with penetrative fissures and conduits, and a rather fast vertical water percolation is possible through it, the phreatic zone is formed by water saturated fissures, fractures and conduits and ensures a mostly horizontal water flow to the outlet (Figure 2.2).

2.2 Aquifers of Central-Southern Apennines

2.2.1 Evolution of Central-Southern Apennines

The present work analyses an area that goes from Central to South-Central Italy, approximately between 39.5°N and 43.5°N latitude. This area has been interested by the development of the Apennines chain, which evolved from west to east. Orogenesis in the central-southern Apennines developed since the Middle Miocene through alternating tectonic phases

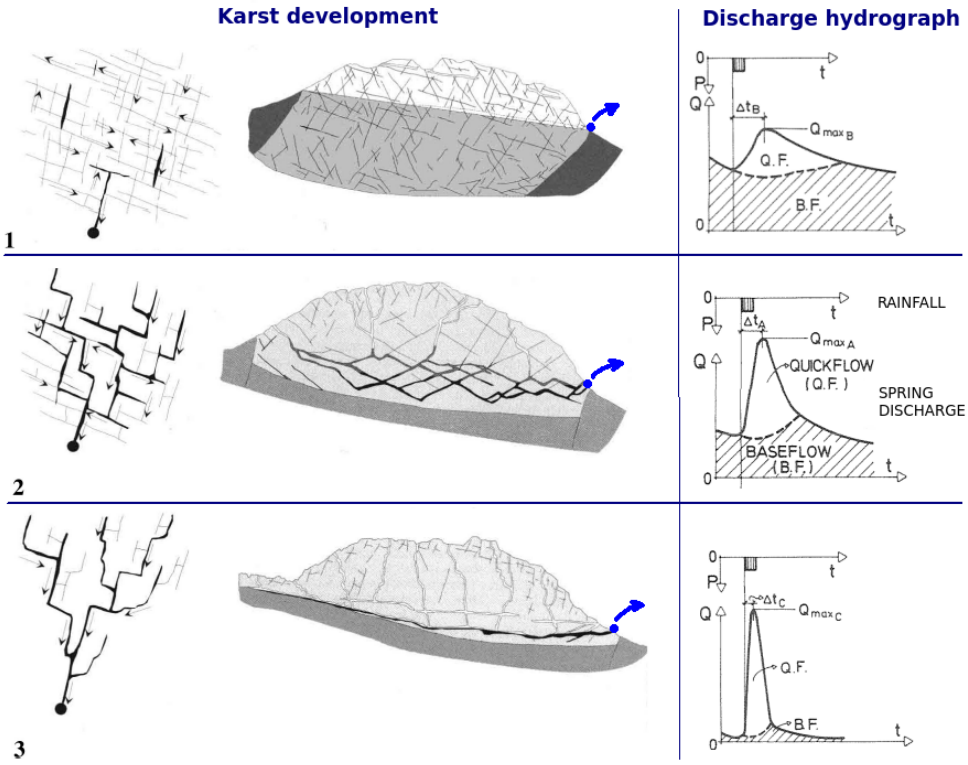

Figure 2.1: Conceptual models of karst aquifers with their relative drainage pattern and shape of spring discharge hydrograph (Q) as a reaction to the same rainfall (P): 1) young karst with a disperse drainage, 2) developed karst with interdependent drains, 3) holokarst with a dominant drain. Modified from Bonacci (1993) and Cucchi et al. (2004).

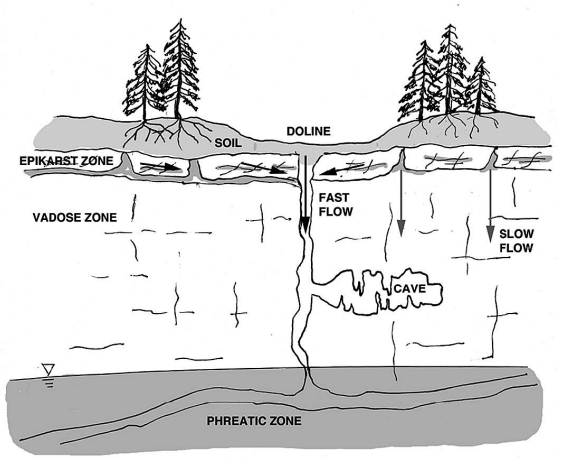

Figure 2.2: Schematic classification of the principal layers of karst aquifers. From Jones (2013)

of stress and strain (Boni, 2000). To the west, the Tyrrhenian margin presents narrow coastal plains filled up by transitional Quaternary deposits and it is juxtaposed to the peri-Tyrrhenian volcanic belt, that developed during the recent extensional tectonic phases. The main domain is the Meso-Cenozoic central-southern carbonate Apennines, which was tectonically deformed, fragmented, and piled up toward ENE in the fold-and thrust belt Apennines structure during the Miocene orogenic phases (Patacca and Scandone, 2007). To the east, the foredeep basin along the front of the thrust belt is characterized by silicoclastic deposits, partially overthrusted toward the Adriatic margin, and by large coastal plains filled up mostly by continental and marine deposits. A phase of main extensional tectonic and erosion started from the Quaternary and is still ongoing (e.g. Chiarabba et al., 2005; D'Agostino, 2014). This enhanced the development of intermontane plains and alluvial valleys among the carbonate ridges (Cavinato et al., 1993; Cavinato and DeCelles, 1999).

The wide carbonate ridges of Central-Southern Apennines act as the main aquifers, which are able to store huge quantities of water. Groundwater is drained by large flow springs with steady regimen at the borders of the aquifers, where carbonate rocks are in contact with low-permeability deposit

outcrop. The spatial distribution of the principal carbonate massifs in Italy is displayed in Figure 2.3

2.2.2 Carbonate aquifers of the Apennines

In the carbonate Apennines groundwater is supplied by wide recharge areas that are highly permeable due to fracturing and epigean and hypogean karst formations, which facilitate and accelerate infiltration towards the phreatic zone. This causes huge water infiltration and mostly negligible overland runoff (Boni, 1986). Carbonate rocks reach thickness of 2500 m and are heavily fractured and faulted (Fiorillo and Guadagno, 2010; Amoruso et al., 2013).

The extensional tectonic movements that are affecting internal Apennines areas since the Quaternary caused the fast deposition of very thick continental depositional sequences in the intermontane plains. This fast sedimentation rate and tectonic activity induces continuous oscillations of the base level of the aquifer (D'Agostino et al., 2001; Petitta, 2009; Petitta et al., 2014), affecting groundwater flow in the surrounding fractured carbonate aquifers and hindering the development of a mature karst network in the discharge areas of the aquifers (Fiorillo et al., 2015b). In the phreatic zone there is therefore prevalence of diffuse flow through fractures and the dense fracture network, superimposed to the only locally developed karst conduits, is able to slow down the groundwater flow and to regularly distribute it over time, as a typical diffuse karst system (Fiorillo et al., 2015b). The basal karst springs of the Apennines range (i.e., the ones fed by the groundwater coming from the phreatic zone at the base of the aquifer) are therefore characterized by a discharge response outstandingly high, almost steady and modulated by seasonal recharge, with no high and sudden discharge peaks in response to meteoric inflow. Water discharge occurs even in dry periods (Fiorillo and Doglioni, 2010). High altitude seasonal and ephemeral springs can generate from perched groundwater flow and tipically show high variability, no yield during dry periods and mean annual discharges generally lower than 0.01

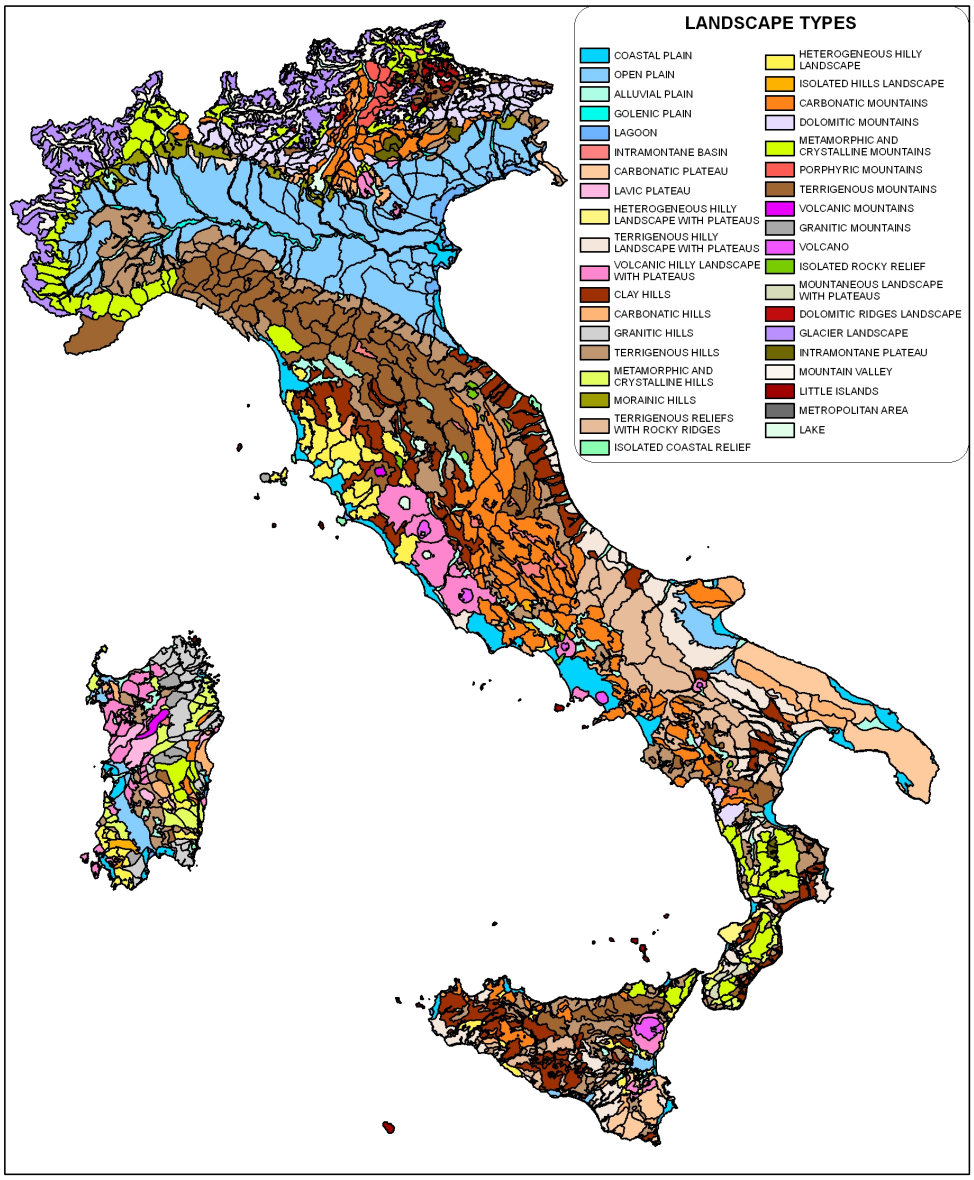

Figure 2.3: Map of the Italian landscape physiographic types and units. From http://www.isprambiente.gov.it

m^3/s (Allocca et al., 2014).
The peculiar hydrogeological context of Apennines aquifers makes them to differ from the other karst aquifers of the Mediterranean area and leads to a double advantage: the karst development in recharge area ensures high-rate infiltration and consequently huge renewable resources, whereas the flow concentrated in the fracture network of the saturated zone feeds basal springs that discharge several m^3/s of water with a regular and predictable discharge regime, unlike many other karst areas (see also section 2.2.3). Carbonate aquifers of the Apennines are characterized by a primary fracture pattern oriented in NW-SE direction (Celico et al., 1994; Del Prete et al., 2007; Pastori et al., 2009), that is perpendicularly to the direction of the tectonic extension that affects Central and Southern Italy (D'Agostino, 2014). In particular, results from anisotropy studies for the Alto Tiberina Fault area, the L'Aquila region and the Val D'Agri basin agree with the hypothesis of the presence of rock volumes pervaded by fluid-saturated microcracks or fractures aligned by the active stress field (Pastori et al., 2009, 2012).

2.2.2.1 Central Apennines

The total area of the carbonate central Apennines (in the regions of Umbria, Marche, Lazio, Abruzzo and Molise, from about 41°N to 43.5°N latitude) is about 15000 km^2. Recharge areas have a large extent, feeding about 80 springs and streambed springs with mean discharges between 1 and 18 m^3/s (Boni, 1986, 2000) (Figures 2.4, A.1 and A.2a). Altitude ranges from sea level to a maximum of about 2900 m.
Geological conditions are quite diverse over the area. After the Paleozoic, more than 1000 m of evaporitic, dolomitic and calcareous sediments were initially deposited on a metamorphic basement. This original large basin split into two sedimentological environments during the Early Jurassic (Boni, 2000; Cosentino et al., 2010): 1) a subsiding carbonate shelf, composed of a thick and rigid sequence of limestone and dolomite without terrigenous intercalations (shallow water limestones), developed in the south-eastern sector

(carbonate platform domain), 2) a typical carbonate-series basin filled with biomicrite and associated marl and chert (deeper-water carbonates) in the north-west (pelagic basin domain). A large transitional belt lies between them (Figure 2.4).

In the carbonate-platform domain several (up to seven) distinct hydrogeological structures have been recognized (Boni, 2000). This domain is characterized by:

- area of about 9000 km^2
- karst aquifers supplying a mean discharge of about 230 m^3/s from around 140 springs
- mean annual rainfall from 950 to 1500 mm
- mean annual effective infiltration from 750 to 1000 mm

The transitional belt is characterized by:

- effective infiltration from 600 to 900 mm
- mean annual evapotranspiration from 400 to 600 mm

In the carbonate-platform domain, because of the lack of impervious intercalations and the extensive fracture network, infiltration is abundant and distributed evenly over the region (60÷70% of total precipitation) and overland runoff is negligible. The karst network is extensive and deep infiltration feeds large basal aquifers that extend to the bottom of all hydrogeological structures.

In the pelagic-basin domain three main aquifers are identified separated by impervious complexes. This domain is characterized by an extensive network of perennial rivers, acting as base levels with respect to the main karst aquifers. Rivers and streams fed by groundwater show a regular discharge regime. The main features of this domain are:

- area of about 5000 km^2
- 80 major springs
- mean discharge of 75 m^3/s
- mean annual effective infiltration is 500 mm (≈50% of total precipitation).

Unlike Umbria and Lazio, a precise subdivision of the ranges in the

Abruzzo region is not easy (Boni, 1975). A large hydrogeological unit can be identified, which extends from the Peschiera springs (18 m^3/s), south-eastward to the Velino group and continues (including the Fucino and the sector of the Marsica to the south-west of the Sangro) up to Capovolturno springs (6 m^3/s), located at the south of Monti della Meta massif (Figures 2.4 and A.2a) (Boni, 1975). The extreme northeast sector of the Abruzzi Apennines, at the margin of the carbonate shelf, shows marked stratigraphic irregularity and the homogeneity of hydrogeological behaviour is lost (Boni, 1975).

2.2.2.2 Southern Apennines

In Southern Apennines (Campania region and part of Basilicata region) the regional hydrogeological setting is essentially characterised by carbonate karst aquifers formed by limestone, dolomitic limestone and a dolomitic series of carbonate platform facies, as in the carbonate-platform domain of Central Apennines. Aquifers are confined by aquitards or aquicludes composed of flysch and basinal series (Figure 2.5 and A.2b) (Celico et al., 2000; Allocca et al., 2007).
Given their proximity to volcanic centers (Figure 2.5), the carbonate aquifers of this area have been covered by variable thickness of pyroclastic deposits (De Vita et al., 2006) erupted during the Quaternary, whose presence influences the epikarst development (Celico et al., 2010).
The groundwater recharge of karst aquifers occurs chiefly by autogenic recharge due to diffuse-direct net infiltration through the epikarst and it feeds basal springs with mean annual discharges varying from 0.1 to 5 m^3/s. The total discharge of carbonate aquifers amount to about 70 m^3/s (Allocca et al., 2014).

2.2.3 Climate and spring discharge

In Central-Southern Apennines the climate is of the mountain variety of the Mediterranean type, with dry summers and rainy autumn-winters.

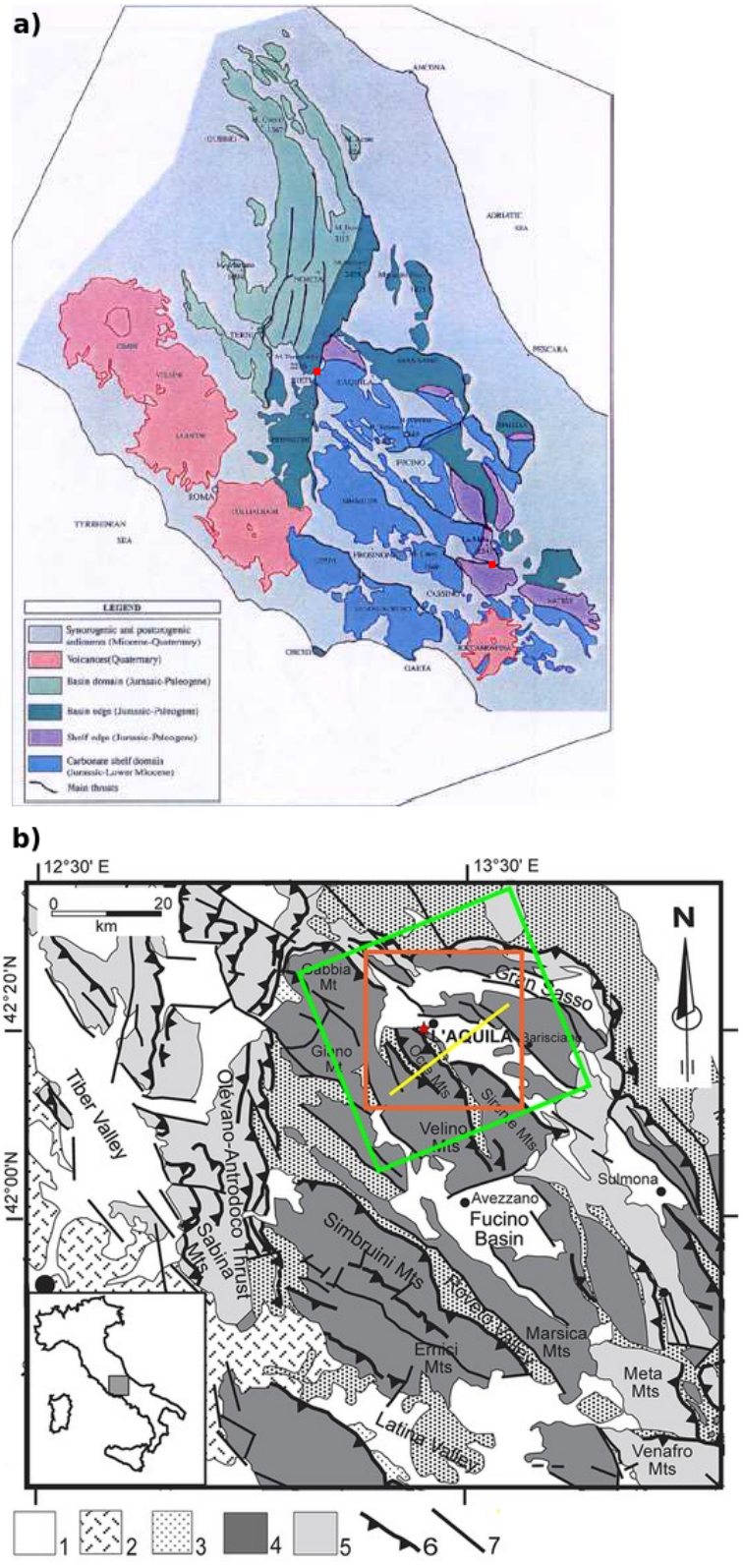

Figure 2.4: (Continued on the following page.)

Figure 2.4: Simplified geological map of Central Italy. a) Carbonate platform domain in the southeastern sector (blue), carbonate basin domain in the northwest (green) and transition domain between the two (slate grey). Red squares indicate respectively the position of Peschiera springs (to the north) and Capovolturno springs (to the south). Modified from Boni (2000).
b) Key to the legend: 1) marine and continental clastic deposits (Pliocene-Quaternary); 2) volcanic deposits (Pleistocene); 3) syn-orogenic, hemipelagic, and turbiditic sequences; 4) carbonate platform deposits; 5) slope and pelagic deposits; 6) main thrust; 7) main normal and/or strike-slip fault. The red star indicates the epicentral location of the 2009 Mw 6.3 earthquake. Modified from Albano et al. (2015).

On the eastern slopes the climate is more continental than on the western, with its winters being dominated by cold north-east winds. The air temperature and the spatial distribution of the precipitation are influenced by the topography, indeed the Apennines chain works as a barrier against the humid masses coming from the Thyrrenian Sea, causing the highest precipitation (about 2000 mm/y) on the top of the morphological divide (Roe, 2005; Houze, 2012) and the lowest ones eastward of the Apennines ridge (700-900 mm/y). The mean annual temperature ranges from 16°C at sea level to and 3.2°C at 2200 m (Boni, 2000).
The climatic characteristics of the Apennines and their temporal variability strongly control the recharge of karst aquifers, that occurs prevalently during autumn and winter. Generally during spring and mainly summer, due to high rate of evapotranspiration, recharge is null.
Thanks to their peculiar characteristics (see section 2.2.2), karst aquifers act as large natural reservoirs of rainfall that release water throughout the hydrological year through large basal springs. Spring discharge reflect both the seasonal recharge cycle and long-term climate change because of a multi-annual "memory" effect due to the reservoir storage (Fiorillo and Guadagno, 2010, 2012). Prolonged periods of poor rainfall can reduce the response of the spring discharge (Fiorillo, 2009).
In most of the basal springs, single rain event has no direct influence on

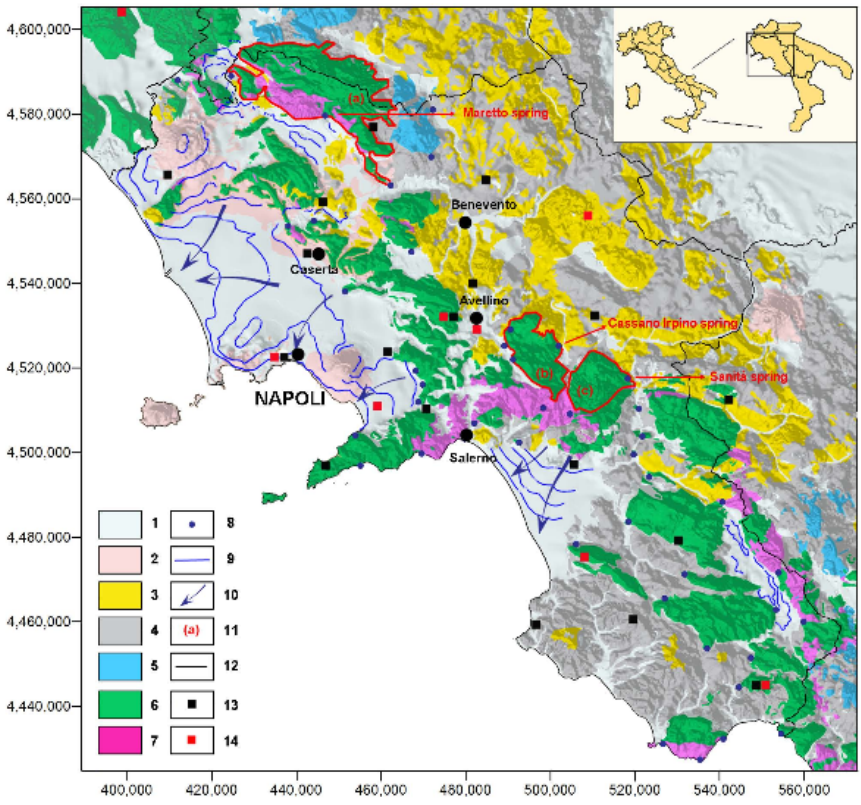

Figure 2.5: Hydrogeological map of Southern Apennines (Campania region). Legend: (1) alluvial and epiclastic units (Quaternary); (2) volcanic units (Pliocene-Quaternary); (3) late orogenic molasses and terrigenous units (Upper Miocene-Pliocene); (4) pre-orogenic and syn-orogenic terrigenous units of inner and thrust-top basins series (Cretaceous-Upper Miocene); (5) siliceous-marly units of outer basin series (Trias-Paleogene); (6) limestone and dolomitic limestone units of carbonate platform series (Jurassic-Paleogene); (7) dolomitic units of carbonate platform series (Trias-Jurassic); (8) main basal springs of carbonate karst aquifers; (9) groundwater head contour lines in alluvial and volcanic aquifers; (10) main preferential drainage axes of groundwater flow in alluvial aquifers; (11) identification of some the carbonate karst aquifers: a) Matese Mount; b) Terminio Mount; c) Cervialto Mount; (12) regional boundary; (13) rain gauge stations; (14) air temperature monitoring stations. From De Vita et al. (2012)

the spring discharge, which is generally characterised by one smoothed peak during the spring season reflecting the antecedent recharge occurred during the autumn-winter period. This is mostly due to the absence or scarcity of quick flow, because of a poor development or connection of the karst conduits (Figure 2.1) (Fiorillo, 2009). In Figure 2.6 some examples of spring hydrographs from different karst aquifers of the Mediterranean region are presented. It should be noted the difference between discharge of well developed karst areas (Figure 2.6a,b), where spring hydrograph show high-flow events following important precipitation, and of Apennines karst areas (Figure 2.6c), that show a smooth shape with no sudden peaks after high rain events. Discharge time-series from others karst spring of the Apennines are shown in chapter 5 (section 5.2.2).

According to diffusive models of water in unconfined porous aquifers (Manga, 1996, 1997, 1999), the time lag between groundwater recharge and the time of peak discharge at the spring describes the time required for variations in the height of the water table due to the recharged water to propagate along the aquifer and reach the spring. This time has not to be confused with the mean residence time of groundwater, that is estimated from hydrochemistry and isotope analysis and ranges from ten to over 40 years for the main springs of the Apennines (Boni, 2000).

A different model assumes that once the percolating water reaches the saturated zone, the pressure pulse is forced through phreatic conduits and almost instantaneously influences the spring discharge (Ford and Williams, 2007). Thus, the time lag between recharge and discharge could be related to the duration of percolation through the vadose zone of the aquifer (Fiorillo and Doglioni, 2010).

Another factor that influence the time lag between recharge and discharge is the time shift between snowfalls and snow melting. Several recharge areas, in fact, lie above 1000 m a.s.l., therefore precipitation frequently occurs as snow during winter and melts during spring, inducing a delay in the onset of infiltration. In addition, for some aquifers, the presence of a cover made

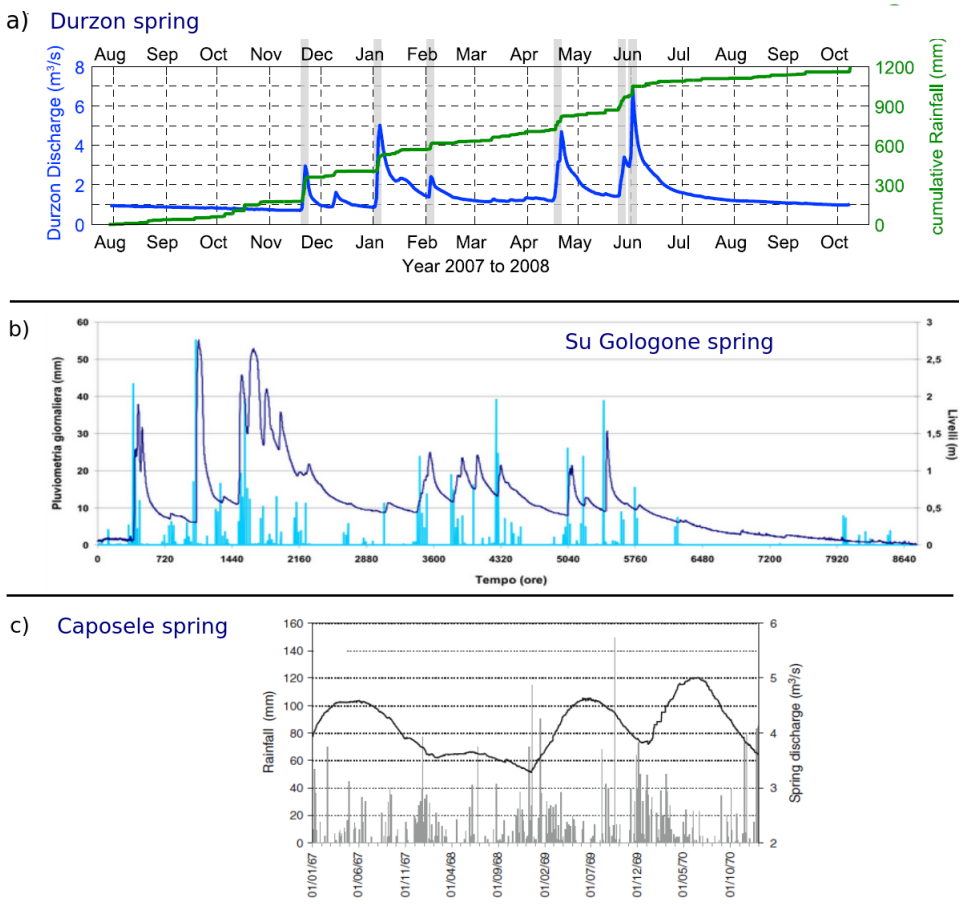

Figure 2.6: Spring discharge time-series and related rainfall time series from some karst areas of Mediterranean region: a) Durzon spring (Larzac, France) (Jacob et al., 2010), b) Su Gologone spring (Sardegna, Italy) (from http://gruppogrottenuorese.it/), c) Caposele spring (Campania, Italy) (Fiorillo and Doglioni, 2010)

of pyroclastic deposits can reduce the rapid infiltration into the karst system (Fiorillo and Doglioni, 2010). The overall area of the spring also appears to control the time lag of the spring hydrograph (Fiorillo et al., 2015b).

The zonal atmospheric circulation over the northern Atlantic Ocean dominates the interannual climate variability in Europe (Valty et al., 2015). In the Mediterranean area, and therefore in the study area, the effect of the North Atlantic Oscillation (NAO) on the interannual and long-term trend of precipitation and air temperature has been demonstrated (e.g. Brandimarte,

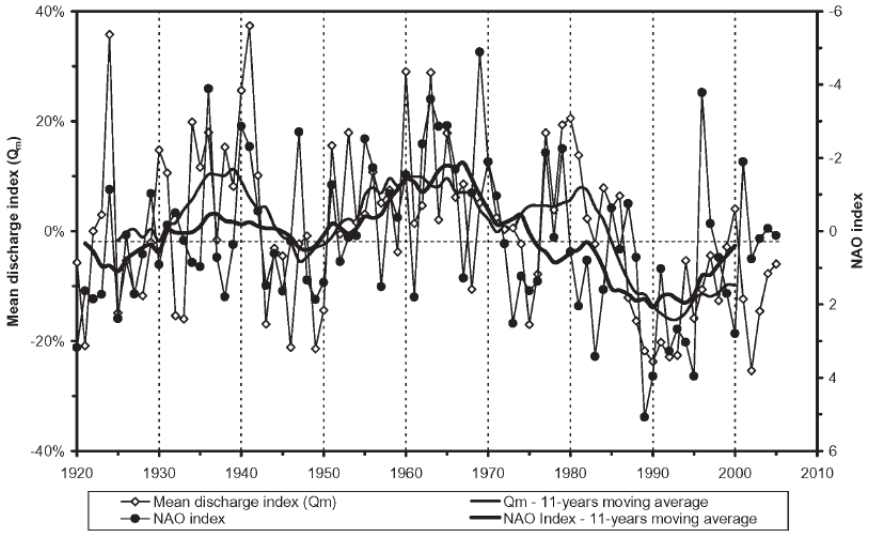

Figure 2.7: Comparison between the NAO index and the mean annual discharge index (Qm) of the spring Sanità in Caposele (Campania region) (1920-2005). From De Vita and Fabbrocino (2007).

2011; Valty et al., 2015). NAO is a weather phenomenon in the North Atlantic Ocean that consists in fluctuations in the difference of atmospheric pressure at sea level between the Subpolar (Icelandic) low and the Subtropical (Azores) high. The oscillation of the NAO affects the areas of origin of the humid masses that controls the regime of precipitation causing periods with values higher than the average and dry periods with deficient rainfalls. In the Southern Apennines significant correlations have been highlighted between the NAO index and hydrological time series, such as spring discharge (Figure 2.7), demonstrating the strong influence of the NAO on the hydrological cycle of the karst aquifers (De Vita et al., 2012).

Álvarez-GarcÍa et al. (2012) pointed out a quasi-quadrennial variability in European precipitation, possibly connected with the impact of El Niño-Southern Oscillation (ENSO), NAO and other climatic processes confined to the Atlantic and Mediterranean areas.

Chapter 3

Theoretical framework of the employed models

In this chapter we outline the theoretical background of the models that we have employed in chapter 5 to explain the observed deformation. Firstly the theory behind the elastic response to surface loads on homogeneous and stratified half-spaces is described. This model is usually used when dealing with hydrological loads which deform the Earth's surface. Secondly we illustrate the theory of the deformation due to a tensile dislocation buried in an elastic half-space, which provide a means to simulate the deformation associated with the opening of hydrofractures in the Earth's crust. Lastly we delineate the principles of the effective stress theory which represent a relatively simple way to deal with porous materials at pseudostatic hydraulic conditions.

3.1 Earth deformation by surface loads

Here we refer to the problem of finding the deformation produced in a solid elastic half-space by a normal force applied at the plane boundary. This problem, known as the classical problem of Boussinesq, was first solved by Boussinesq in the late nineteenth century (Boussinesq, 1885) and has been

resolved again in the following years using different mathematical techniques (e.g. Lamb, 1902; Mindlin, 1936). Starting from the solutions of this simplest configuration, the solutions for more realistic Earth models , i.e. spherical, radially stratified, gravitating earth models have been computed (Farrell, 1972). These are of primary interest in many geophysical field dealing with the Earth's deformation due to surface load variations such as tides in the solid earth (Agnew, 1996, 1997), atmosphere pressure changes (Kainuth and Vetter, 2006) and hydrological loads (i.e. ice, snow, continental water storage) (e.g. Blewitt et al., 2001; Grapenthin et al., 2006; Fu et al., 2012).
Here the solution for the simplest case of surface pressure on a non-gravitating, homogeneous, elastic half-space is presented firstly in order to highlight the principal features of the displacements due to surface loads. A quick overview on the derivation of the solutions for more complex models is then given. An extended description of the calculation involved can be found in Farrell (1972) and references therein.

3.1.1 Boussinesq problem

We first consider an unitary point load applied at the surface of an elastic half-space. Considering an elastic homogeneous nongravitating medium, the static displacement vector $\boldsymbol{u}$ satisfies the equilibrium equation in absence of body forces

$$\mu\nabla^2\boldsymbol{u} + (\lambda+\mu)\nabla(\nabla\cdot\boldsymbol{u}) = 0 \tag{3.1}$$

where λ and μ are Lamé parameters. Because of the axial symmetry of the problem, it is useful to use cylindrical coordinates (r, θ, z), where the point load is applied in the origin at $z = 0$ and the half-space occupies the volume $z \leq 0$ (Figure 3.1) and the components of the displacement vector are $u(r, z)$ (along z) and $v(r, z)$ (along r).

A way to resolve the Boussinesq problem uses the Hankel (or Fourier-Bessel) transforms of order 0 and 1 on the r variable by transforming the equilibrium equation and introducing the stress-strain relations. This gives

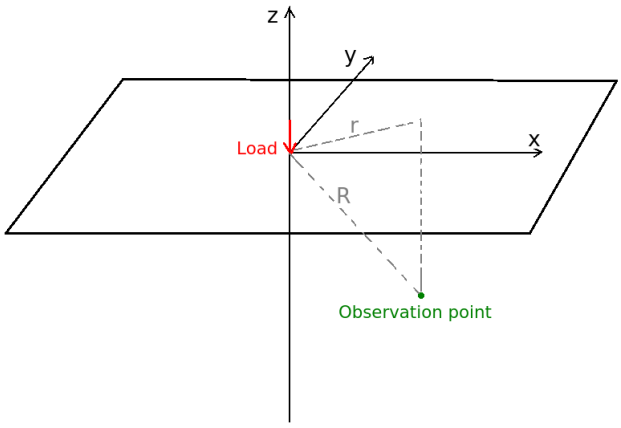

Figure 3.1: Reference system used in Boussinesq problem.

rise to a differential matrix equation in the transformed displacements and stresses U, V, T_{zz}, T_{rz}. Letting τ_{zz} be the stress arising from a unit force acting uniformly over a disk of radius α, the boundary condition at the surface are $\tau_{zz} = -\frac{1}{\pi\alpha^2}$ for $r < \alpha$, $\tau_{zz} = 0$ for $r > \alpha$ and $\tau_{rz} = 0$. The boundary condition for τ_{zz} gives rise to a "disk factor" in the Hankel transformed boundary conditions, that, in the case of a point load ($\alpha \to 0$), can be imposed to be unity. The standard solutions for the displacements caused by a unit point force pressing vertically on the surface of an elastic half-space finally are

$$\begin{aligned} u(r,z) &= -\frac{1}{4\pi\mu R}\left(\frac{\lambda+2\mu}{\lambda+\mu} + \frac{z^2}{R^2}\right) \\ v(r,z) &= -\frac{1}{4\pi\mu r}\left(1 + \frac{z}{R} + \frac{(\lambda+\mu)r^2 z}{\mu R^3}\right) \end{aligned} \tag{3.2}$$

where $R^2 = r^2 + z^2$.

Figures 3.2 and 3.3 illustrate the trend of radial (v) and vertical (u) displacement given by the equations 3.2 with $\lambda = \mu \Rightarrow$ Poisson's ratio $\nu = 0.25$, that can be assumed as an average value for the continental crust (e.g. Zamdt and Ammond, 1995). The vertical displacement is always negative (subsidence) for every value of depth and distance from the load source and its value decays with the distance from the load source. The radial displacement is negative (directed toward the load source) at the surface and at low depths

and becomes positive at higher depths, with lower amplitude. The depth at which the radial displacement changes sign ($v(z^*) = 0$) increases with the distance from the load. In particular, it has a trend described by a best fit straight line $z^* \approx -0.4r + 10^{-4}$.
The vertical displacement is larger than the radial displacement at every depth and distance from the load source (Figure 3.4). This is true both for equal and different values of the elastic parameters λ and μ. At the surface $\frac{u(z=0)}{v(z=0)} = \frac{\lambda}{\mu} + 2$, therefore the minimum value of the vertical-to-horizontal ratio is 2, when $\lambda \ll \mu$. In order to show the depth dependence of vertical over radial displacement ratio for different values of the elastic parameters (λ, μ and therefore ν), we have varied them over several magnitude orders: when $\lambda = \mu$ ($\nu = 0.25$), the ratio is at least 3 (at the surface), when $\lambda \ll \mu$ ($\nu \to 0$) the ratio is at least 2 (at the surface) and when $\lambda \gg \mu$ ($\nu \to 0.5$) the ratio is much higher at the surface and at least ≈3 (at a certain depth). This analysis has simply the aim to show that the vertical displacements due to surface loading are always higher (at least of a factor of 2) then the horizontal ones, even for extreme values of the elastic parameters.

For the case of a unit force acting uniformly across a disk of radius α, the same technique of point load can be used by putting the disk factor back in the transformed solutions. In general, in order to deal with distributed loads, the point load solutions have to be integrated over load areas.

3.1.2 Layered half-space

When the elastic parameters λ and μ vary with depth, as in the case of realistic Earth models, the displacements due to a surface load can't in general be determined analytically and the Green's functions are found by numerical methods. In this case, the governing partial differential equations could be resolved by the finite-difference or finite-element techniques, obviating the Hankel transforms. These techniques permit to model almost any spatial variation in material properties. Nevertheless, the Hankel transform approach used for the half-space represents a proper way to deal with plane-

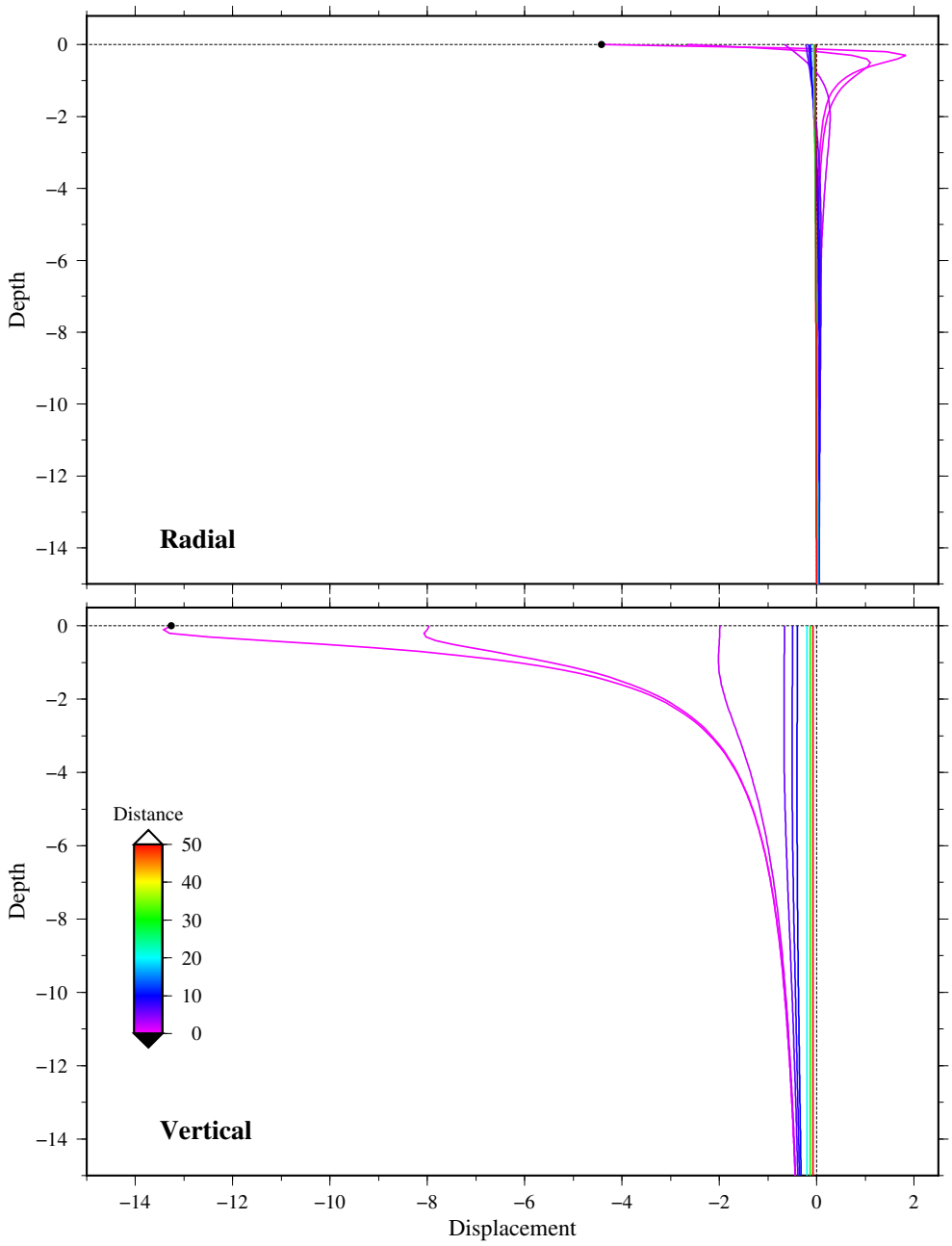

Figure 3.2: Depth dependence of radial (top) and vertical (bottom) displacement due to an unitary point load imposed at the origin. Each colored line corresponds to increasing values of the distance from the load source. The displacements have been calculated imposing Lamé parameters values of $\lambda = \mu = 3$ GPa in equation 3.2. The results have been then multiplied by a factor of 10^{11} to deal with non infinitesimal numbers.

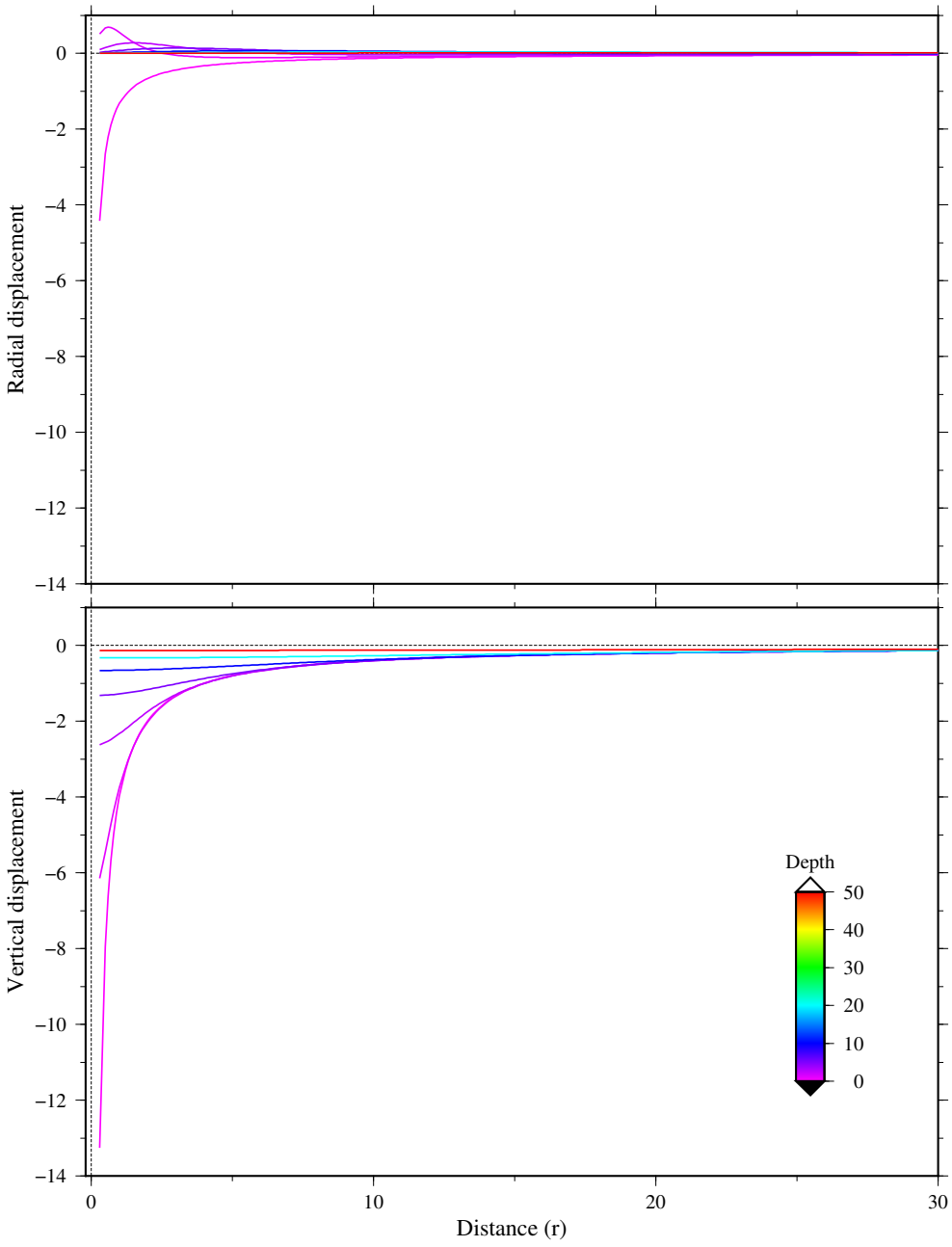

Figure 3.3: Radial (top) and vertical (bottom) displacement due to an unitary point load imposed at the origin at different depths (color coded). The displacements have been calculated imposing Lamé parameters values of $\lambda = \mu = 3$ GPa in equation 3.2. The results have been then multiplied by a factor of 10^{11} to deal with non infinitesimal numbers.

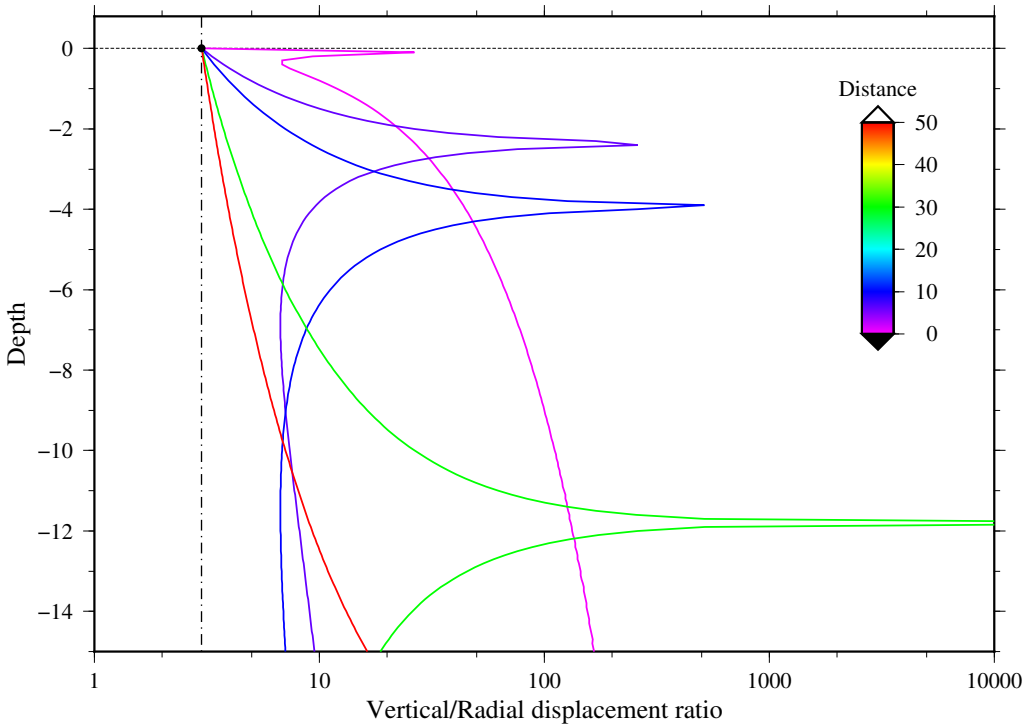

Figure 3.4: Depth dependence of the ratio between vertical and radial displacement magnitude at different distances from the load source (color coded). The dash-dot vertical line highlight a value ratio $\frac{vertical\ displacement}{radial\ displacement} = 3$. Notice the logarithmic scale on the x-axis.

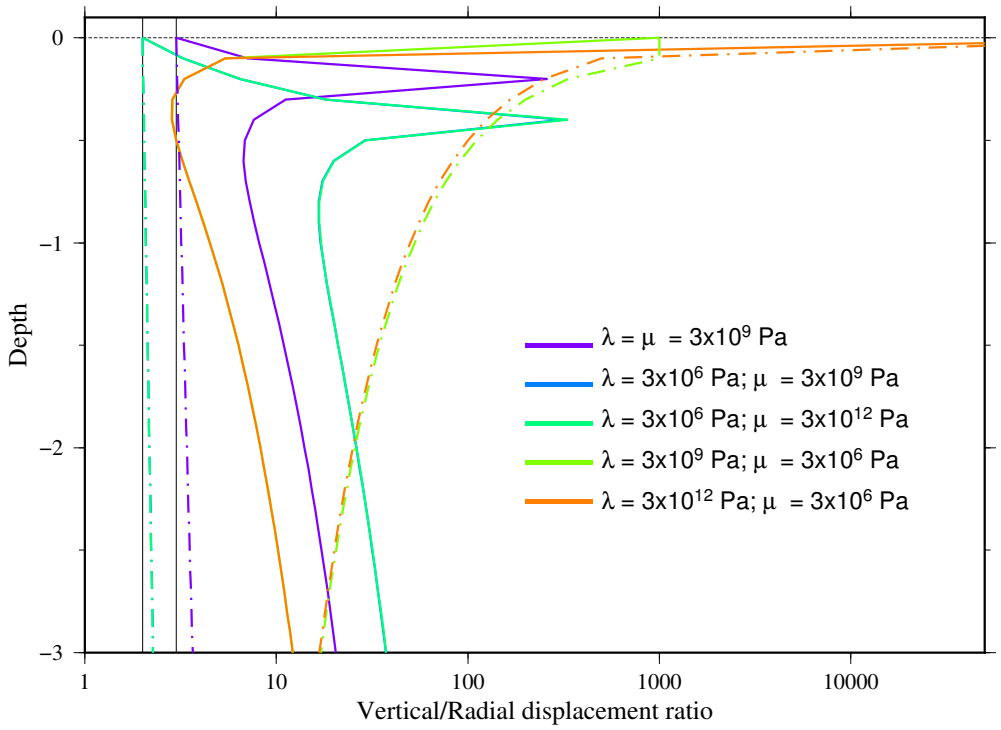

Figure 3.5: Depth dependence of the ratio between vertical and radial displacement magnitude for different values of elastic parameters (color coded) at two fixed distance r from the source: near the point load ($r = 0.5$, continue lines) and far from it ($r = 50$; dash-dot lines). The vertical black lines mark values of $\frac{vertical\ displacement}{radial\ displacement} = 3$ and $\frac{vertical\ displacement}{radial\ displacement} = 2$. Notice the logarithmic scale on the x-axis.

layered models. In this case the starting point is again to transform the equilibrium equation and reduce it to a matrix equation in the transformed displacements and stresses (U, V, T_{zz}, T_{rz}). To solve this equation, firstly the medium beneath some starting depth z_0 is assumed to be a uniform half-space and starting solutions at z_0 are found considering $\lambda = \lambda(z_0)$ and $\mu = \mu(z_0)$. Then these starting solutions can be propagated to the surface by a series of matrix multiplications, in each layer the propagator or layer matrix being formed from the four homogeneous solutions for U, V, T_{zz}, T_{rz}. Alternatively, the matrix differential equation can be numerically integrated from z_0 to the surface. As for the uniform half-space, the transformed solution are controlled by the surface boundary conditions. Finally, the displacement Green's functions are obtained by calculating numerically the Hankel inversion integrals.

3.1.3 Gravitational effects

To consider the gravitational effects, the equation of motion in a homogeneous self gravitating medium has to be considered, that is much more complicated than the purely elastic equation 3.1. Some approximations can be assumed, however, due to the fact that, for conventional values of elastic parameters and densities, the elastic forces dominate the gravitational ones. In order to found the gravitational potential perturbation ϕ in Boussinesq problem, therefore, the elastic-gravitational coupling can be neglected and the Poisson equation

$$\nabla^2 \phi = -4\pi \mathcal{G} \rho \nabla \cdot \mathbf{s} \tag{3.3}$$

has to be solved, where ρ is the Earth's mean density and $\mathcal{G}$ is Newton's gravitational constant and $\mathbf{s}$ components are given by 3.2.

3.1.4 Spherical, self-gravitating elastic Earth

In order to deal with spherical earth, usually a spherical coordinate system is used and $\mathbf{s}$ and ϕ are expanded in spherical harmonics. ϕ represents the perturbation of the ambient gravitational potential ϕ_1 plus the potential of any externally applied gravitational force field ϕ_2. Being the surface load axially symmetric, the solution doesn't depend on longitude and only the Legendre order $m = 0$ occurs in the expansions:

$$\begin{aligned} \mathbf{s} &= \sum_{n=0}^{\infty} \left(U_n(r) P_n(\cos\theta)\mathbf{e}_r + V_n(r) \frac{\partial P_n(cos\theta)}{\partial \theta} \mathbf{e}_\theta \right) \\ \phi &= \sum_{n=0}^{\infty} \Phi_n(r) P_n(\cos\theta) \end{aligned} \tag{3.4}$$

where $U_n(r)$ is associated to vertical displacements and $V_n(r)$ to horizontal ones.

Analogously to the half-space case, by transforming the equations of motions, the Possion equation for the gravitational potential and by introducing the stress-strain relations leads to a matrix equation in $U_n, V_n, T_{rr,n}, T_{r\theta,n}, \Phi_n, Q_n$, where the last is the transform of a variable related to the potential gradient. The boundary conditions have to be imposed by expressing them as Legendre series expansion. In particular, the expansion of a unit mass distributed uniformly across a disk of radius α is (Farrell, 1972)

$$\begin{aligned} \gamma &= \sum_{n=0}^{\infty} \Gamma_n P_n(\cos\theta) \\ with \quad \Gamma_n &= \frac{P_{n-1}(\cos\alpha) - P_{n+1}(\cos\alpha)}{4\pi a^2(1-\cos\alpha)} = \\ &= \frac{2n+1}{4\pi a^2} \left[-\frac{1+\cos\alpha}{n(n+1)\sin\alpha} \frac{\partial P_n(\cos\alpha)}{\partial \alpha} \right] \quad n > 0 \\ \Gamma_0 &= \frac{1}{4\pi a^2} \end{aligned} \tag{3.5}$$

where a is the Earth's radius. The first quantity in Γ_n is the Legendre expansion of the δ function in spherical coordinates, whereas the bracketed

part is again a disk factor associated with the finite sized distribution and can be assumed equal to one in the limit of a point load (as for the half-space case).
The perturbation in the gravitational potential at the Earth's surface is

$$\Phi_{2,n} = \frac{4\pi\mathcal{G}a}{2n+1}\Gamma_n \overset{\text{point mass load}}{=} \frac{ag}{m_e} \tag{3.6}$$

where g is the acceleration of gravity and m_e is the mass of the earth. This leads to the transformed boundary conditions

$$\begin{aligned} T_{rr,n}(a) &= -g\Gamma_n \\ T_{r\theta,n}(a) &= 0 \\ Q_n(a) &= -4\pi\mathcal{G}\Gamma_n \end{aligned} \tag{3.7}$$

Usually the static deformation of an elastic sphere is expressed in terms of the dimensionless Love numbers h_n, l_n, k_n, each of which is a function of the two variables n and r. When, as in this case, displacements U_n, V_n and $\Phi_{1,n}$ arise from an axially symmetric force field with transformed potential $\Phi_{2,n}$, the Love numbers are defined by

$$\begin{bmatrix} U_n(r) \\ V_n(r) \\ \Phi_{1,n}(r) \end{bmatrix} = \Phi_{2,n}(r) \begin{bmatrix} \frac{h_n(r)}{g} \\ \frac{l_n(r)}{g} \\ k_n(r) \end{bmatrix} \tag{3.8}$$

From equations 3.6 and 3.8, the surface vertical u and horizontal v displacements at distance θ from the point mass load are

$$\begin{aligned} u(\theta) &= \frac{a}{m_e}\sum_{n=0}^{\infty} h_n P_n(\cos\theta) \\ v(\theta) &= \frac{a}{m_e}\sum_{n=1}^{\infty} l_n \frac{\partial P_n(cos\theta)}{\partial\theta} \end{aligned} \tag{3.9}$$

In summary, the Green's function approach is based on load Love numbers theory, in which the Earth's deformation response is a function of the

spherical harmonic components of the incremental gravitational potential created by the surface load. For a layered earth, Love numbers, and therefore the Green's functions in equation 3.9, have to be calculated numerically and their values depend on the considered earth model. Several computed Green's functions have been published in the last years, related to different earth models, such as Gutenberg-Bullen A model (in Farrell (1972)), PREM model (in Guo et al. (2004); Wang et al. (2012)), iasp91 and ak135 models (in Wang et al. (2012)). As an example, Figure 3.6 (Wahr et al., 2013) represents both the vertical (positive upward) and the horizontal (positive away from the load area) surface displacements, due to the removal from the Earth's surface of a uniform disc of mass, with radius 20 km and with mass-per-area equivalent to that of 1 m of water thickness. Results are computed for Earth model PREM (Dziewonski and Anderson, 1981) and show that for a localized load on a realistically stratified, spherical, elastic Earth, the ratio of the vertical displacement to the horizontal displacement at the surface is between 2.0 and 3.0, depending on how far away the load is. The vertical-to-horizontal ratio can be much larger than that for the more usual case where the load is spread over a wide region since, given, for example, positive loads, the vertical displacements always add constructively, while the horizontal displacements can add destructively depending on the spatial distribution of the load(Wahr et al., 2013). The values of this ratio for the Gutenberg-Bullen A structural model are smaller than those given here for PREM, but only by 5-10% (Wahr et al., 2013).

3.2 Earth deformation due to tensile dislocations

Tensile dislocation models have several important geophysical applications. Field observations of sills, dikes and hydrofractures have in fact shown that these structures can be modelled as planar intrusions characterized by an opening that is orders of magnitude smaller than the length or the height

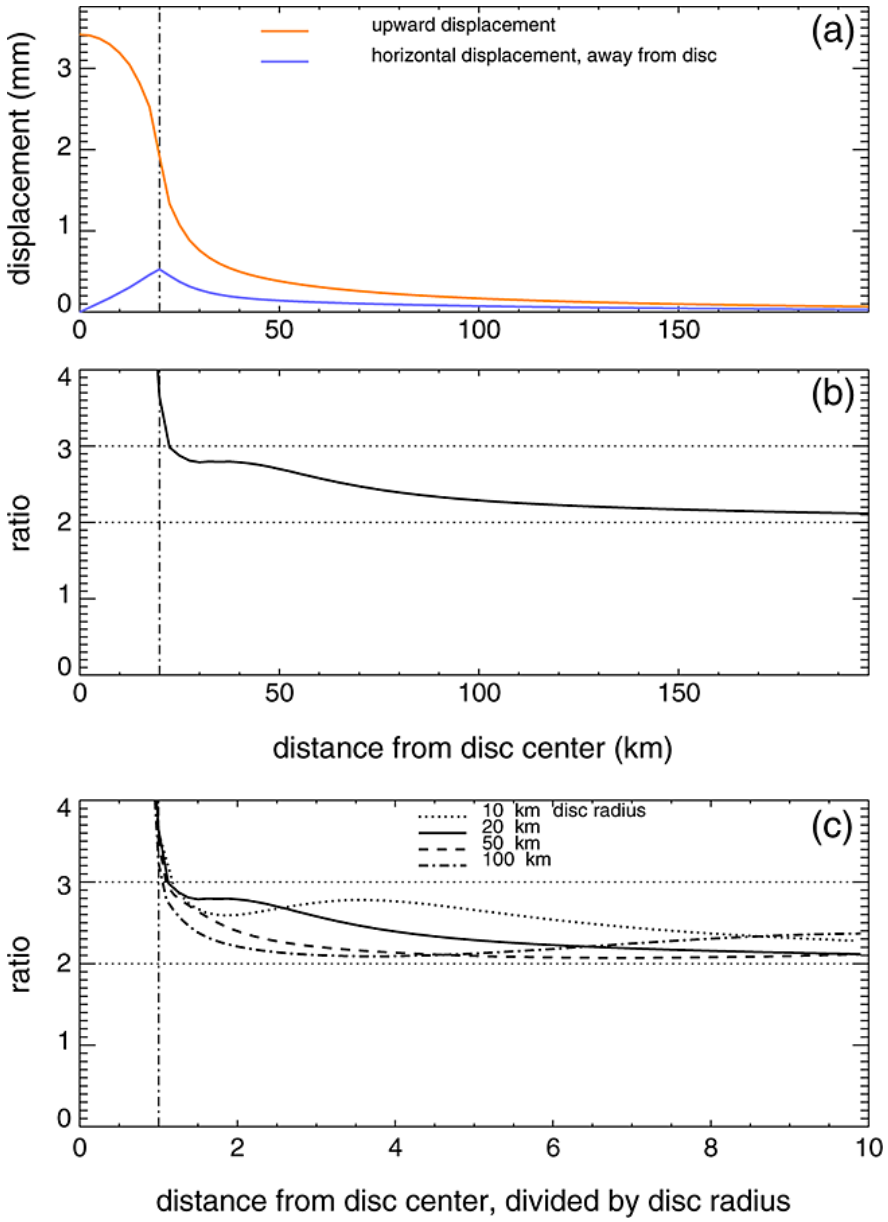

Figure 3.6: (a) Vertical and horizontal crustal displacements caused at the surface by removing a uniform disc load of radius 20 km and 1 m equivalent water thickness as a function of the distance to the center of the disc. The vertical dot-dashed line marks the edge of the disc. (b) Vertical to horizontal displacements ratio. (c) Vertical to horizontal ratio for discs of various radii (distances on the x axis are normalized by the radius of the disc). From Wahr et al. (2013).

of the fissure (Davis, 1983). Tensile dislocations are used in volcanology to describe the deformation due to tabular intrusions such as dikes or sills (e.g. Owen et al., 2000; Montgomery-Brown et al., 2011), i.e. elongated approximately planar fractures filled with magmatic fluids whose formation and propagation is due to some combination of regional extension and fluid pressure (Pollard and Holzhausen, 1979). Other than volcanology, tensile dislocations model are in general applied to study fluid-driven cracks. Evans and Wyatt (1984) highlighted a relation between changes in the water-head inside a borehole and ground surface deformation in the surrounding region. Since subsurface hydraulically conductive fractures respond to changing fluid pressure, they suggested a tensile crack model to explain the observation. Several works that studied deformation of karst regions by means of tiltmeters, strainmeters and GPS have explained the observed deformation by means of opening tensile fractures (Evans and Wyatt, 1984; Longuevergne et al., 2009; Jacob et al., 2010; Devoti et al., 2015).

Fractures in the Earth crust

Natural fractures can remain locked open, highly conductive and possess apertures of several millimetres even down to considerable depth (Dyke, 1995). Sausse (2002) showed that the contact area of natural fractures could be smaller than 40-60% for normal stress smaller than 35 MPa, i.e. at a depth of about 1500 m. On the basis of the average tensile strength of solid rocks (around 3 MPa), and of the the density values of the uppermost part of the crust (2100–2500 kg/m^3) all extension fractures existing at depths greater than about 1 km have to be formed by fluid pressure, that is, they must be hydrofractures (Gudmundsson, 2011).
In order to open a (pre-existing) tensile hydrofracture, the variation of hydrostatic stress (water overpressure inside the fracture) has to be higher than the normal stress acting on the fracture walls (e.g. Jolly and Sanderson, 1997). In the near surface of the Earth's crust (4-5 km), stresses are usually caused by gravity (overburden pressure), deformation, and temperature gradients and

are affected by several factors such as rock property contrasts, topography, stress relaxation, rock strength, and pore fluids (Savage et al, 1992).
The simplest stress configuration is the one that arises from the assumption that the crust is a laterally constrained, isotropic and homogeneous elastic half-space under its own weight (lithostatic stress, see section 3.3.2). In this case the principal components of stress are respectively perpendicular (vertical stress) and parallel (horizontal stresses) to the half-space surface. The value of the horizontal stress σ_h, that is the stress component that acts normally to the sub-vertical tensile fractures, is reduced by a factor of $\frac{\nu}{1-\nu} \overset{\nu=0.25}{=} 1/3$ (ν Pisson's ratio) with respect to the vertical stress $\sigma_v = \rho g z$ (ρ is rock density, g is gravity acceleration, z is depth, see equation 3.35). This state of stress is often assumed as a reference stress configuration to which perturbations caused by the other factors mentioned above are added. The presence of a tectonic horizontal extensional stress, such as the one characterizing the Apennines (section 2.2.1), mitigates the horizontal compression due to the lithostatic pressure (Savage et al, 1992). Furthermore, the inclusion of rock mass anisotropy, which can be caused by stratification, foliation, schistosity, and jointing, broadens the range for predicted horizontal stresses in rock masses (Savage et al, 1992). Topographic relief can cause stresses of sufficient magnitude to break rock, creating fracture sets having a spatial distribution and orientation governed by landforms shape and the regional state of stress (Miller and Dunne, 1996).

3.2.1 Displacement discontinuity model vs crack model

Fundamentally two methods exist to model the displacements, strain and stresses induced by fractures/faults, namely the displacement discontinuity model and the crack model. In the first case, the displacement discontinuity Δu, or slip/opening, is prescribed as a boundary condition. Such models don't explain why the displacement discontinuity occurs and its constant value leads to non-physical stress singularities at the fracture/fault tip, however rather simple analytical expressions exist to compute induced deforma-

tion and stresses (Okada, 1985, 1992). In the second case, the stress drop $\Delta\sigma$ on the dislocation surface associated with the fracture slip/opening is specified, rather than the amount of slip/opening (e.g. Bonafede and Danesi, 1997). Even the simplest crack problem involves mixed boundary condition: the stress drop is specified inside the crack, whereas outside the crack no displacement discontinuity is imposed. The stress change outside the crack and the displacement discontinuity have to be solved for. This second technique is more realistic since usually stress drop can be estimated, rather than displacement discontinuity, and it leads to more realistic crack shapes with a variable amount of opening. The main disadvantage is that it can be difficult to find closed form expressions to the mixed boundary value problem and the calculation can be computationally hard, especially for three dimensional cases.

In general, the main features of the displacement field produced by a fracture can be computed by using a dislocation model (by considering the constant value of the dislocation as a mean of the variable slip/opening of a crack) if we are not interested in the displacement field very near to the dislocation. Davis (1983) demonstrated that a dipping rectangular tensile dislocation buried in an elastic half-space furnish a computationally efficient method to model deformation related to a planar tension crack. Differences in the predicted deformation are small and are only apparent near the fracture and both models satisfy the free-surface boundary condition. Bonafede and Danesi (1997) showed that with analytical constant-dislocation models surface displacements compare reasonably well with crack-model solutions if the upper tip is not too shallow (ratio between dislocation centre depth and dislocation half-width > 1.5).

As an example, Figures 3.7 and 3.8 show the comparison between slip and surface displacements computed from displacement discontinuity model (uniform dislocation) and two kinds of (screw) crack model in a two-dimensional half-space (Segall, 2010). For the dislocation the slip is constant (s) for $0 < z < a_d$, where a_d is the dislocation depth. In the first crack model a

Model	*Slip* s(z)	*Surface displacement* u(x)
Uniform dislocation	$s(z) = \begin{cases} s & z \le a_d \\ 0 & z > a_d \end{cases}$	$u(x) = \frac{s}{\pi} \tan^{-1}\left(\frac{a_d}{x}\right)$
Constant-stress drop crack	$s(z) = s\sqrt{1-\left(\frac{z}{a_c}\right)^2}$	$u(x) = \frac{s}{2}\left[\mathrm{sgn}(x)\sqrt{1+\left(\frac{x}{a_c}\right)^2} - \left(\frac{x}{a_c}\right)\right]$
Tapered crack	$s(z) = s\left[1-\left(\frac{z}{a_s}\right)^2\right]^{3/2}$	$u(x) = -\frac{3}{4}s\left\{\left(\frac{x}{a_s}\right) + \frac{2}{3}\left(\frac{x}{a_s}\right)^3 - \frac{2}{3}\mathrm{sgn}(x)\left[1+\left(\frac{x}{a_s}\right)^2\right]^{3/2}\right\}$

Figure 3.7: Normalized slip distributions and corresponding surface displacement fields for displacement discontinuity model and two kinds of crack models. From Segall (2010).

constant stress drop $\Delta\sigma = \sigma_0$ is imposed and the maximum slip is $s_{max} = s(z=0) = \frac{2\sigma_0 a_c}{\mu}$, where a_c is crack depth, in the second one a tapered stress drop distribution is imposed $\Delta\sigma(z) = -c_2\left(2\left(\frac{z}{a}\right)^2 - 1\right)$ with $0 < z < a_s$ and the maximum slip is $s_{max} = s(z=0) = \frac{4c_2 a_s}{3\mu}$, where c_2 is a term of the expansion of the stress drop on the crack surface in terms of Chebyshev polynomials. In order to compare the displacements for the various sources, the slip distributions have been normalized so that they have the same slip at surface ($s(z=0)$). The depths at which the slip vanishes (a_d, a_c, a_s) have been chosen such that the integrals of the slip distribution with depth are the same. Requiring the maximum slip for the tapered crack to be equal to that for the uniform stress drop crack leads to $c_2 = \frac{3}{2}\sigma_0\frac{a_c}{a_s}$. The results indicate that, even if the the slip distributions are quite different (Figure 3.8A), the surface displacement patterns are similar (Figure 3.8B). The difference in displacement between the constant stress drop crack and the uniform dislocation is lower 12 mm per meter of maximum slip, whereas for the tapered crack and the uniform dislocation, the maximum difference is about 20 mm per meter of maximum slip (Figure 3.8C).

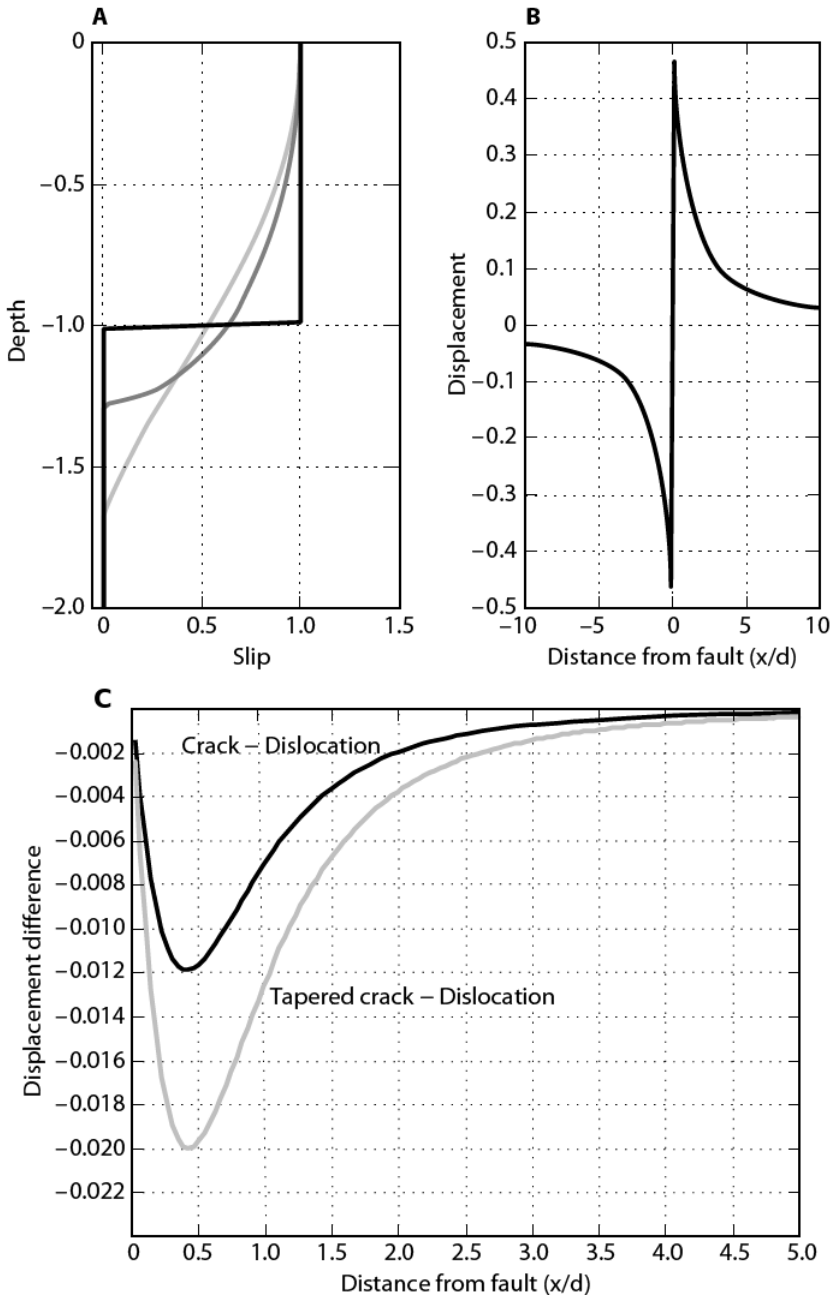

Figure 3.8: A) Slip distributions associated with uniform-slip dislocation, a constant stress drop crack and and a tapered crack. B) Surface displacement distributions associated with the slip distributions in A. C) Differences between the slip distributions of crack models in B respect to to the slip distributions of the uniform slip dislocation model. The slip values on the vertical axes are normalized respect to the maximum slip value. From Segall (2010).

3.2.2 Tensile dislocation from displacement discontinuity model

Here we address the explanation of the main steps that lead to the formulas for the displacement field on the free surface of an elastic half-space due to the opening on a buried rectangular tensile dislocation surface. One way of derivation is based on the Volterra's equation and the reciprocal theorem. Let's consider a dislocation $\Delta\mathbf{u}(\xi)$ in a body distributed on a dislocation surface Σ and the stress $\sigma^i_{jk}(\xi, \mathbf{x})$ at ξ due to a unit body force acting in the i direction and localized at $\mathbf{x}$. The resulting displacement field $\mathbf{u}(\mathbf{x})$ in $\mathbf{x}$ is given by the *Volterra's formula*

$$u_i(\mathbf{x}) = \int_\Sigma \Delta u_j(\xi)\sigma^i_{jk}(\xi, \mathbf{x})n_k \, d\Sigma(\xi) \tag{3.10}$$

where n_k represents the k-th component of the unitary vector perpendicular to Σ. Volterra's formula can be rewritten in a different form by expressing the stress $\sigma^i_{jk}(\xi, \mathbf{x})$ in terms of the *elastostatic Green's tensor*.
The Green's tensor $G_{ki}(\mathbf{x}, \xi)$ is the displacement at $\mathbf{x}$ in the k direction, due to a concentrated unit force at ξ acting in the i direction. By integrating, it is thus possible to compute the displacement due to an arbitrary distributed force starting from the Green's tensor.
By means of *Hooke's law*, the stress associated with the displacement G_{ki} can be expressed as $\sigma_{jk} = C_{jkpq}\varepsilon_{pq}$, where C_{jkpq} is the elasticity tensor and ε_{pq} is the strain tensor.
Volterra's formula 3.10 can be then written as

$$u_i(\mathbf{x}) = \int_\Sigma C_{jkpq}\Delta u_j(\xi)\frac{\partial G_{pi}(\xi, \mathbf{x})}{\partial \xi_q}n_k \, d\Sigma(\xi). \tag{3.11}$$

We can now use the Green's tensor *source-receiver reciprocity*

$$G_{ki}(\xi, \mathbf{x}) = G_{ik}(\mathbf{x}, \xi) \tag{3.12}$$

that means that the k^{th} component of displacement at ξ due to a force at $\mathbf{x}$ in the i direction is exactly equal to the i^{th} component of displacement at $\mathbf{x}$

due to a force at ξ in the k direction.
Now equation 3.11 can be rewritten as

$$u_i(\mathbf{x}) = \int_\Sigma C_{jkpq} \Delta u_j(\xi) \frac{\partial G_{ip}(\mathbf{x}, \xi)}{\partial \xi_q} n_k \, d\Sigma(\xi) \tag{3.13}$$

For an isotropic elastic medium

$$C_{jkpq} = \lambda \delta_{jk} \delta_{pq} + \mu(\delta_{jp}\delta_{kq} + \delta_{jq}\delta_{kp}) \tag{3.14}$$

where μ and λ are the Lamé constants, and Volterra's equation becomes

$$u_i(\mathbf{x}) = \int_\Sigma \Delta u_j(\xi) \left[\mu \left(\frac{\partial G_{ij}}{\partial \xi_k} + \frac{\partial G_{ik}}{\partial \xi_j} \right) + \lambda \delta_{jk} \frac{\partial G_{im}}{\partial \xi_m} \right] n_k \, d\Sigma(\xi) \tag{3.15}$$

To use the Volterra's equation in order to infer an expression for the dislocation displacement field $u_i(\mathbf{x})$, now the explicit expressions of Green's function should be known.

Full-space and half-space Green's functions

The elastostatic Green's function in a three-dimensional full-space can be found by resolving the *equilibrium equations* for an unlimited isotropic elastic medium

$$(\lambda + \mu)\nabla(\nabla \cdot \mathbf{u}) + \mu \nabla^2 \mathbf{u} + \mathbf{f} = 0 \tag{3.16}$$

It can be shown that Green's tensor that satisfies this equations is

$$G_{jk}(\mathbf{x}, \xi) = \frac{1}{16\pi\mu(1-\nu)} \left[(3 - 4\nu)\frac{\delta_{jk}}{R} + \frac{r_j r_k}{R^3} \right] \tag{3.17}$$

where

$$R = |\mathbf{r}| = |\mathbf{x} - \xi| = \sqrt{(x_1 - \xi_1)^2 + (x_2 - \xi_2)^2 + (x_3 - \xi_3)^2} \tag{3.18}$$

is the distance between the source position and the observation position.

To calculate the Green's functions for an half-space bounded by a free surface (null shear and normal tractions) the *method of images* can be used. This method consists in adding a (fictitious) source with opposite sign and

equidistant from the putative free surface in order to annul the shear tractions on the plane boundary. In general the result is obtained by starting with the solution for an infinite body (equation 3.17) and guessing the nuclei of strain to add outside the semi-infinite body so as to annul the tractions on the plane boundary.
Expressions of half space Green's functions (Mindlin, 1936) can be found in Segall (2010) (equations 3.93 and 3.94) where the coordinate system is such that the positive x_3 axis points upwards, thus $x_3 < 0$ points within the earth. The source is located at $\xi_1 = \xi_2 = 0, \xi_3$, the image source is located at $\xi_1 = \xi_2 = 0, -\xi_3$ and the distance r_1 from the source and r_2 from the image source are given by

$$\begin{aligned} r_1 &= \sqrt{x_1^2 + x_2^2 + (x_3 - \xi_3)^2} \\ r_2 &= \sqrt{x_1^2 + x_2^2 + (x_3 + \xi_3)^2}. \end{aligned} \tag{3.19}$$

Point source and finite rectangular source

Volterra's formula 3.15 can be used to derive the displacements due to an arbitrary dislocation in a three-dimensional half-space. The dislocation surface geometry is defined in Figure 3.9. Elementary dislocations $\Delta u_1 = U_1, \Delta u_2 = U_2, \Delta u_3 = U_3$ refer to strike-slip, dip-slip and tensile components of an arbitrary dislocation.

Given the geometry defined above, Volterra's formula 3.15 in the case of tensile sources ($U_1 = U_2 = 0$) becomes

$$\begin{aligned} u_i(\mathbf{x}) = U_3 \Delta\Sigma \Bigg[& \lambda \frac{\partial G_i^n}{\partial \xi_n} + 2\mu \left(\frac{\partial G_i^2}{\partial \xi_2} \sin^2 \delta + \frac{\partial G_i^3}{\partial \xi_3} \cos^2 \delta \right) \\ & - \mu \left(\frac{\partial G_i^2}{\partial \xi_3} - \frac{\partial G_i^3}{\partial \xi_2} \right) \sin 2\delta \Bigg] \end{aligned} \tag{3.20}$$

where U_i is slip, $\Delta\Sigma$ if the dislocation surface area increment, δ is the dip angle and the product $U\Delta\Sigma$ represents the source strength.
By introducing the formulas for the half-space Green's functions G_{ij} into the preceding expressions and by resolving for a source located at $\xi_1 = \xi_2 =$

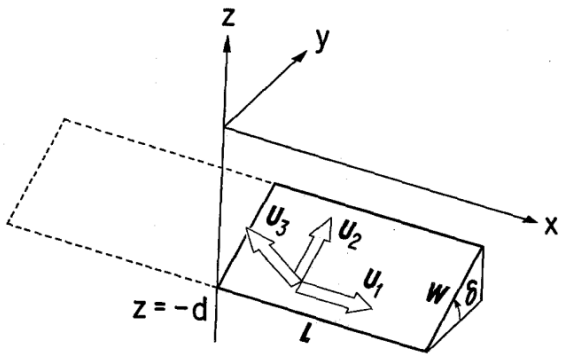

Figure 3.9: Definition of geometric parameters for a finite dislocation. Each displacement vector represents the movement of hanging-wall side block relative to foot-wall side block. From Okada (1985).

$0, \xi_3 = -d$ the following expressions for the displacement at an observation point located on the earth's surface $(x_1, x_2, x_3 = 0)$ are found for a tensile dislocation

$$\begin{aligned} u_1 &= \frac{U_3 \Delta\Sigma}{2\pi}\left(\frac{3x_1 q^2}{r^5} - I_3^0 \sin^2\delta\right) \\ u_2 &= \frac{U_3 \Delta\Sigma}{2\pi}\left(\frac{3x_2 q^2}{r^5} - I_1^0 \sin^2\delta\right) \\ u_3 &= \frac{U_3 \Delta\Sigma}{2\pi}\left(\frac{3dq^2}{r^5} - I_5^0 \sin^2\delta\right) \end{aligned} \tag{3.21}$$

where

$$\begin{aligned} I_1^0 &= (1-2\nu)x_2\left[\frac{1}{r(r+d)^2} - x_1^2\frac{3r+d}{r^3(r+d)^3}\right] \\ I_2^0 &= (1-2\nu)x_1\left[\frac{1}{r(r+d)^2} - x_2^2\frac{3r+d}{r^3(r+d)^3}\right] \\ I_3^0 &= (1-2\nu)\left(\frac{x_1}{r^3}\right) - I_2^0 \\ I_5^0 &= (1-2\nu)\left[\frac{1}{r(r+d)} - x_1^2\frac{2r+d}{r^3(r+d)^2}\right] \end{aligned} \tag{3.22}$$

and

$$\begin{aligned} q &= x_2 \sin\delta + d\cos\delta \\ r^2 &= x_1^2 + x_2^2 + d^2 = x_1^2 + p^2 + q^2 \end{aligned} \tag{3.23}$$

The solution for a finite source can be obtained by integrating the point source solution over the actual source surface, according to Volterra's formula 3.15. For general three-dimensional fault geometries this integration is hard solvable in analytic way, however, for the particular case of a finite rectangular fault with length L and width W and spatially uniform slip, the displacement field can be calculated in closed form. Following Okada (1985), point sources can be distributed on the fault by substituting $x \to x - \xi', y \to y - \eta' \cos\delta, d \to d - \eta' \sin\delta$ in the equations obtained in the previous section and by performing the integration

$$\int_0^L d\xi' \int_0^W d\eta'. \tag{3.24}$$

It is convenient to change variables from ξ', η' to ξ, η by

$$\begin{aligned} x - \xi' &= \xi \\ p - \eta' &= \eta \end{aligned} \tag{3.25}$$

where $p = y\cos\delta + d\sin\delta$ as before. The above integration then becomes

$$\int_x^{x-L} d\xi \int_p^{p-W} d\eta. \tag{3.26}$$

The final results are listed below into compact forms using the notation $\|$ to represent the substitution

$$f(\xi,\eta)\| = f(x,p) - f(x,p-W) - f(x-L,p) + f(x-L,p-W). \tag{3.27}$$

For tensile dislocation

$$\begin{aligned} u_1 &= \frac{U_3}{2\pi}\left[\frac{q^2}{R(R+\eta)} - I_3 \sin^2\delta\right] \| \\ u_2 &= \frac{U_3}{2\pi}\left[-\frac{\tilde{d}q}{R(R+\xi)} - \sin\delta\left(\frac{\xi q}{R(R+\eta)} - \tan^{-1}\frac{\xi\eta}{qR}\right) - I_1\sin^2\delta\right] \| \\ u_3 &= \frac{U_3}{2\pi}\left[\frac{\tilde{y}q}{R(R+\xi)} + \cos\delta\left(\frac{\xi q}{R(R+\eta)} - \tan^{-1}\frac{\xi\eta}{qR}\right) - I_5\sin^2\delta\right] \| \end{aligned} \tag{3.28}$$

where

$$
\begin{aligned}
I_1 &= \frac{\mu}{\lambda+\mu}\left[\frac{-\xi}{(R+\tilde{d})\cos\delta}\right] - \frac{\sin\delta}{\cos\delta}I_5 \\
I_3 &= \frac{\mu}{\lambda+\mu}\left[\frac{\tilde{y}}{(R+\tilde{d})\cos\delta} - \ln(R+\eta)\right] + \frac{\sin\delta}{\cos\delta}I_4 \\
I_4 &= \frac{\mu}{\lambda+\mu}\frac{1}{\cos\delta}\left[\ln(R+\tilde{d}) - \sin\delta\ln(R+\eta)\right] \\
I_5 &= \frac{\mu}{\lambda+\mu}\frac{2}{\cos\delta}\tan^{-1}\left[\frac{\eta(X+q\cos\delta)+X(R+X)\sin\delta}{\xi(R+X)\cos\delta}\right]
\end{aligned}
\tag{3.29}
$$

and p, r are the same as defined in equation 3.23, and

$$
\begin{aligned}
\tilde{y} &= \eta\cos\delta + q\sin\delta \\
\tilde{d} &= \eta\sin\delta - q\cos\delta \\
R^2 &= \xi^2+\eta^2+q^2 = \xi^2+\tilde{y}^2+\tilde{d}^2 \\
X^2 &= \xi^2+q^2
\end{aligned}
\tag{3.30}
$$

When the source surface is vertical, dip $\delta = \frac{\pi}{2} \rightarrow \cos\delta = 0$, terms I_1, I_3, I_4, I_5 are replaced by simpler expression which don't contain singularities (Okada, 1985).

The displacements in equation 3.28 are restricted to the free surface. The procedure for computing the displacements within the half-space (approximating the Earth) is analogous and expressions for $\mathbf{u}(x_1, x_2, x_3)$ are given by Okada (1992).

It should be noticed the elastic parameters appear only in form of the ratio $\frac{\mu}{\lambda+\mu} = 2\nu$, therefore displacements depend only on the value of Poisson's ratio, that can assumed equal to 0.25 for the continental crust (e.g. Zamdt and Ammond, 1995).

The principal features of surface displacement due to a tensile dislocation are represented in Figures 3.10, 3.11 and 3.12. Figure 3.10 shows the pattern of the vertical and horizontal deformation induced by a finite vertical rectangular dislocation surface that has a length equal to four times the depth of its top edge. Maximum displacements lie in two lobes at the flank of the dislocation surface and the vertical maxima are located at a lower distance

than the horizontal maxima. Strong gradient in the vertical and horizontal displacements and a fanning of the horizontal displacement characterize the end of the dislocation. Steeply dipping extensional fractures show small horizontal inward motion along strike, near the fault ends.
For sub-vertical dislocation surface (dip $\approx 90°$) the displacement is symmetrical with respect to the dislocation surface, the horizontal displacement is higher than vertical one and it decays at a lower rate going far from the dislocation surface (Figure 3.11).
Figure 3.12 shows the displacement variation due to the increasing of the dislocation surface width, while the top of the source and the amount of opening are kept constant. Only a small change affects the profiles near the source surface, but farther out deformation increases with the dislocation surface width. Nevertheless, since the profiles are similar, with real data and associated uncertainties it is difficult to distinguish an increase in source width from an increase in the amount of opening (Lisowski, 2007).

Some considerations on fractures and fractured media

Dealing with the opening of hydrofractures constituting a fractured medium, like carbonate rocks, is difficult because of the numerous, and generally unknown, involved parameters, such as the fractures number, their dimension (varying widely between 10^{-6} and 10^{2} m), position, orientation and amount of opening. Realistically estimating the contribute of each fracture is practically impossible and usually equivalent models are used that simulate the behaviour of the fractured medium as a whole (e.g. Sitharam et al., 2001; Jade and Sitharam, 2003).
At a certain distance, the horizontal displacement caused by a group of small tensile fractures embedded in a region is roughly equivalent to the one caused by a single big dislocation located inside the region. A simple conceptual model of this is presented in Figure 3.13, where the displacement fields for a single tensile fracture and for a fractured region are represented. The single fracture has a length of 30 km, a width of 1.2 km and an opening of 1

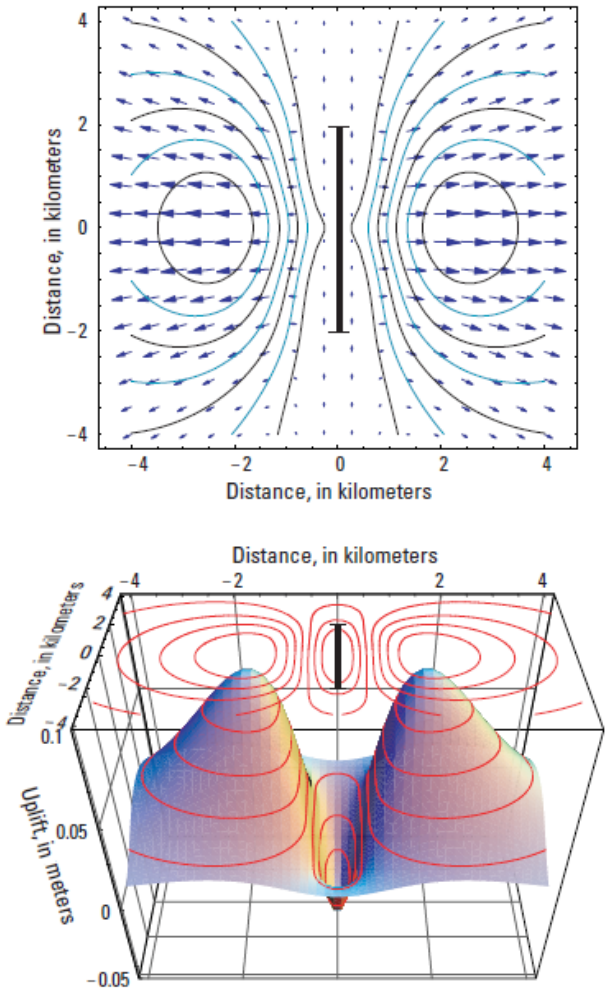

Figure 3.10: Horizontal (contoured horizontal vector displacements, top) and vertical (contoured 3-D displacement surface, bottom) for a vertical rectangular opening dislocation with length L = 4 km, width W = 2 km, top edge at 1 km depth, and opening b = 1 m. The solid black line indicate the surface projection of the dislocation. From Lisowski (2007).

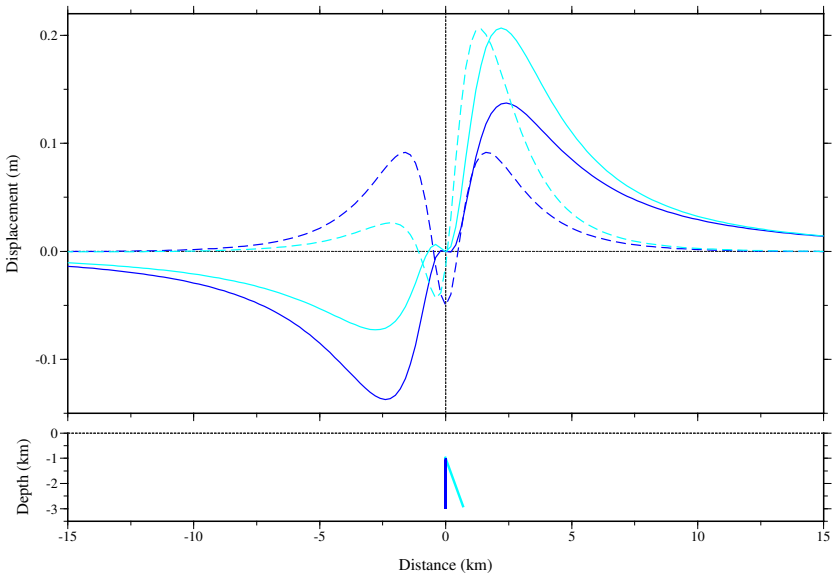

Figure 3.11: Profiles of horizontal (bold lines) and vertical (dashed lines) surface displacements across the center of an opening dislocation (same parameters of Figure 3.10) for two values of dip angle: 90° (blue) and 70° (cyan).

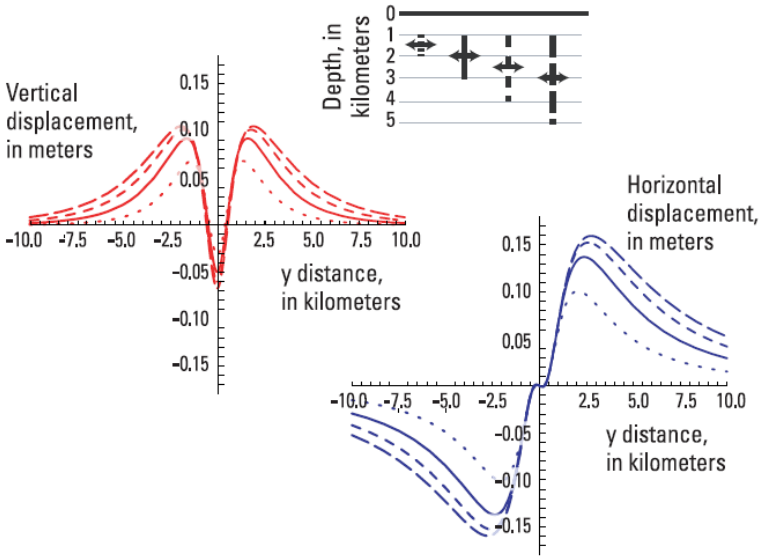

Figure 3.12: Profiles of surface displacements across the center of a vertical opening dislocation with fixed length L = 4 km, top edge at 1 km and opening b = 1 m and varying width W = 1; 2; 3; 4 km. From Lisowski (2007).

cm. The fractures composing the fractured region have a uniformly random length between 5 and 500 m and a width of 50 m, they occupy a depth of 1.6 km and have a spacing of 700 m horizontally and 10 m vertically. All fractures are vertical, oriented along a strike of 0° and are buried at a depth of 100 m. Despite inside the fractured region the displacement field is noticeably different, depending on the sum of the contribution of every fracture, outside the two models display a very similar behaviour. For sake of simplicity, in this example the single contributions of the fractures are linearly summed without taking into account the interactions between the fractures. These interactions can be accounted for by means of the *boundary element method* and more sophisticated models confirm this equivalence (Maccaferri, 2010).
Using a single big fracture in place of a fractured medium is of course a strong simplification that can't provide unambiguous information about the fractured medium (also because of the trade-off between width and opening of the tensile dislocation), but can help to understand if the opening of fractures is a reasonable mechanism to explain the first order of the observed deformation (see section 6.2.1).

In Figure 3.13 all fractures are assumed to have the same orientation (strike angle equal to 0°). In a real medium, however, even when fractures show a preferential orientation, their strike angles are not exactly all the same. Figure 3.14 shows the effect of introducing some variability of the strike angle of the fractures, by assigning a value with a random Gaussian distribution with mean = 0° and standard deviation = 30°. The main effect of the variable strike distribution is to spread the displacement pattern, especially at the tips of the fractured region, where a single fracture provide an inward pattern (Figures 3.10 and 3.13). This effect is accentuated if a wider random Gaussian distribution is considered, i.e. standard deviation > 30°, providing an increasing isotropic pattern, that is lower lateral displacement and higher outward displacement at the tips (Figure 3.15) .

A last observation can be made about the shape of the fractured medium.

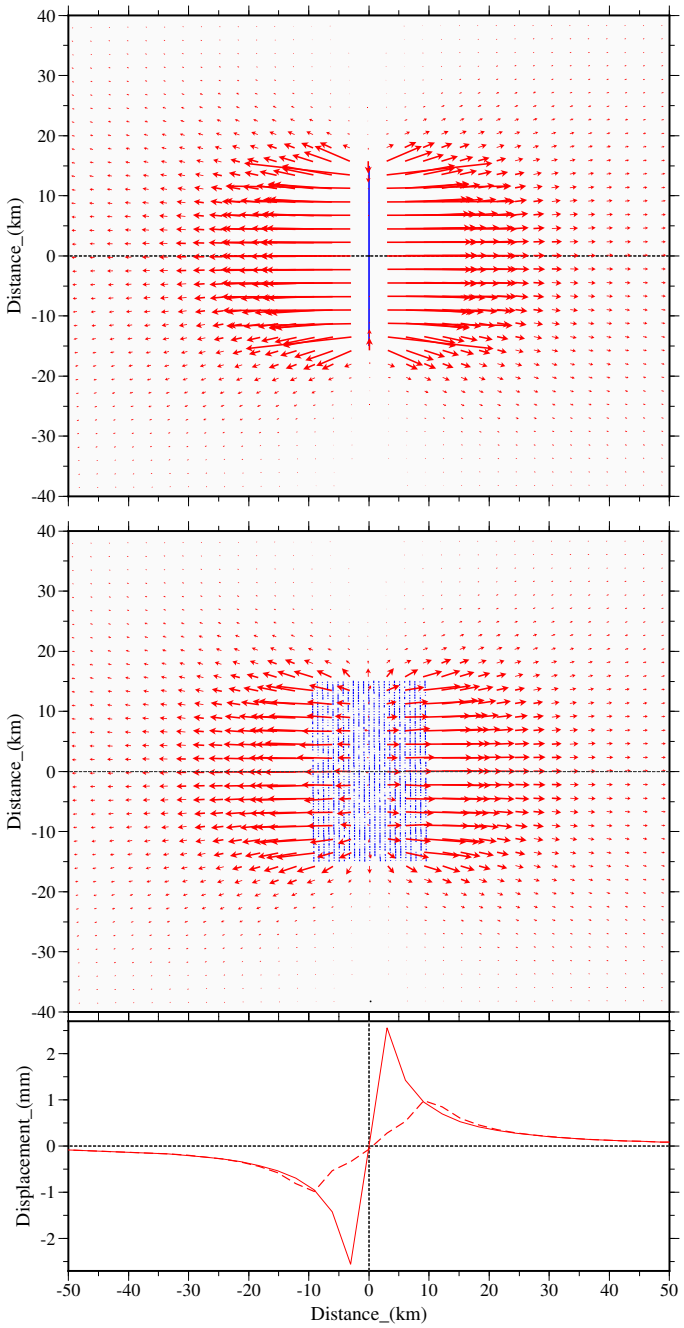

Figure 3.13: Comparison between the horizontal displacement (red arrows) caused by a group of small tensile fractures embedded in a region (centre) and the one caused by a single big dislocation located inside the region (top). The blue lines indicate the projection of the fractures. Bottom: Displacement profile along the dashed gray lines for the single fracture model (bold line) and the multiple fractures model (dashed line).

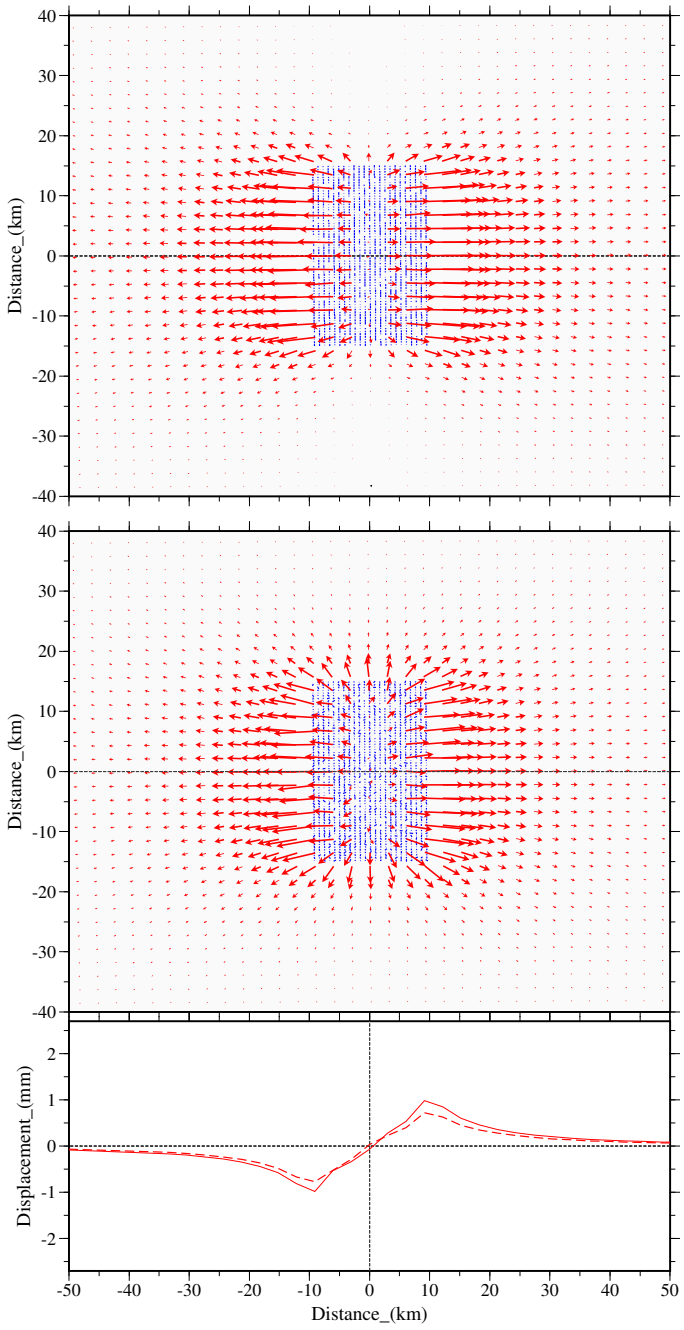

Figure 3.14: Comparison between the horizontal displacement (red arrows) caused by a group of small tensile fractures embedded in a region all having the same orientation (strike = 0°) (top) and the one caused by small tensile fractures with a Gaussian random distribution of strike value ($0° \pm 30°$) (centre). The blue lines indicate the projection of the fractures. Bottom: Displacement profile along the dashed gray lines for the aligned fractures model (bold line) and the randomly oriented fractures model (dashed line).

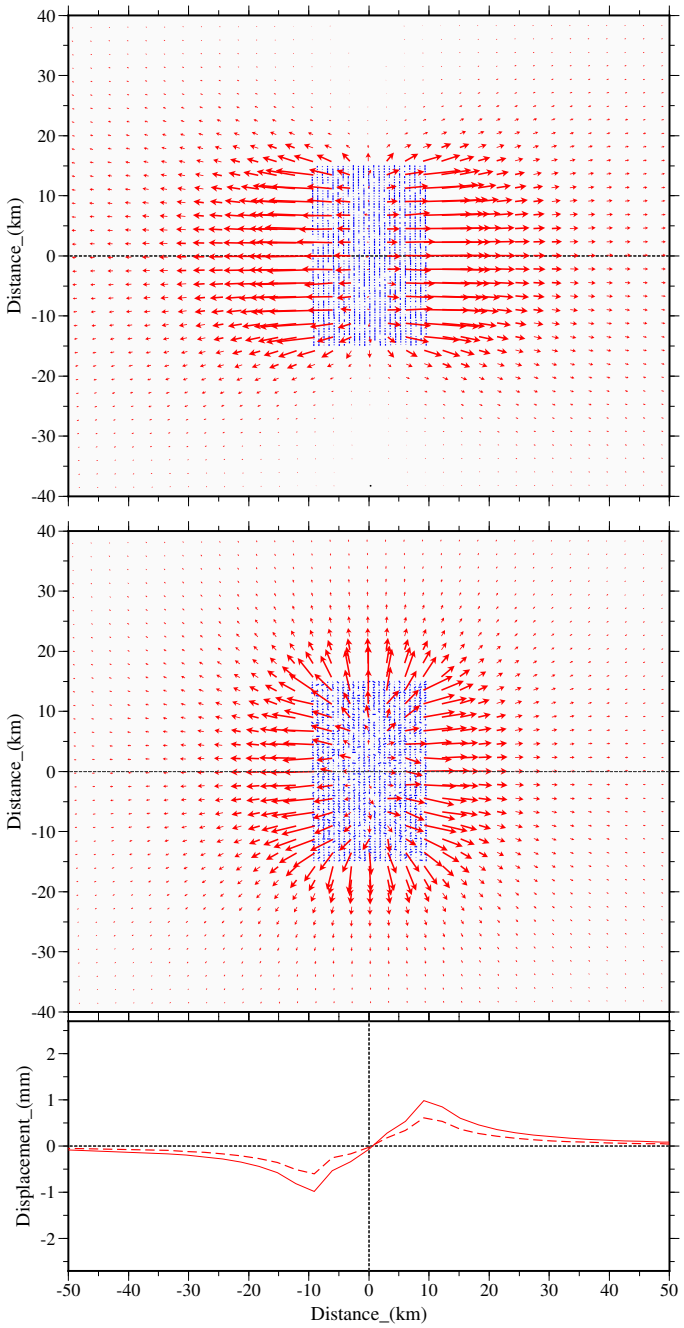

Figure 3.15: Comparison between the horizontal displacement (red arrows) caused by a group of small tensile fractures embedded in a region all having the same orientation (strike = 0°) (top) and the one caused by small tensile fractures with a Gaussian random distribution of strike value ($0° \pm 60°$) (centre). The blue lines indicate the projection of the fractures. Bottom: Displacement profile along the dashed gray lines for the aligned fractures model (bold line) and the randomly oriented fractures model (dashed line).

Let's consider a simple approximately elliptic fractured region and analyse three different situations: 1) fractures with the same strike, 2) fractures with a Gaussian random distribution of strike values, 3) fractures with strikes that roughly mimic the shape of the fractured area. The first two examples are analogous to the ones previously analysed and show similar features (Figure 3.16), that is a more isotropic deformation in the case of random distributed strike values. The third example has the aim to model a condition in which the fractures direction is influenced by the shape of the region and roughly follow the orientation of the perimeter of the area (Figure 3.17). This last example represents an intermediate case: laterally with respect to the largest axis of the fractured region the displacement resembles the fixed strike case (Figure 3.17(bottom)), whereas near the tips of the largest axis it resembles to the random strike case. The main difference compared to the random strike example (Figure 3.17(bottom)) concerns the displacements inside the fractured region, that show a north-south pattern trending toward the middle of the fracture area.

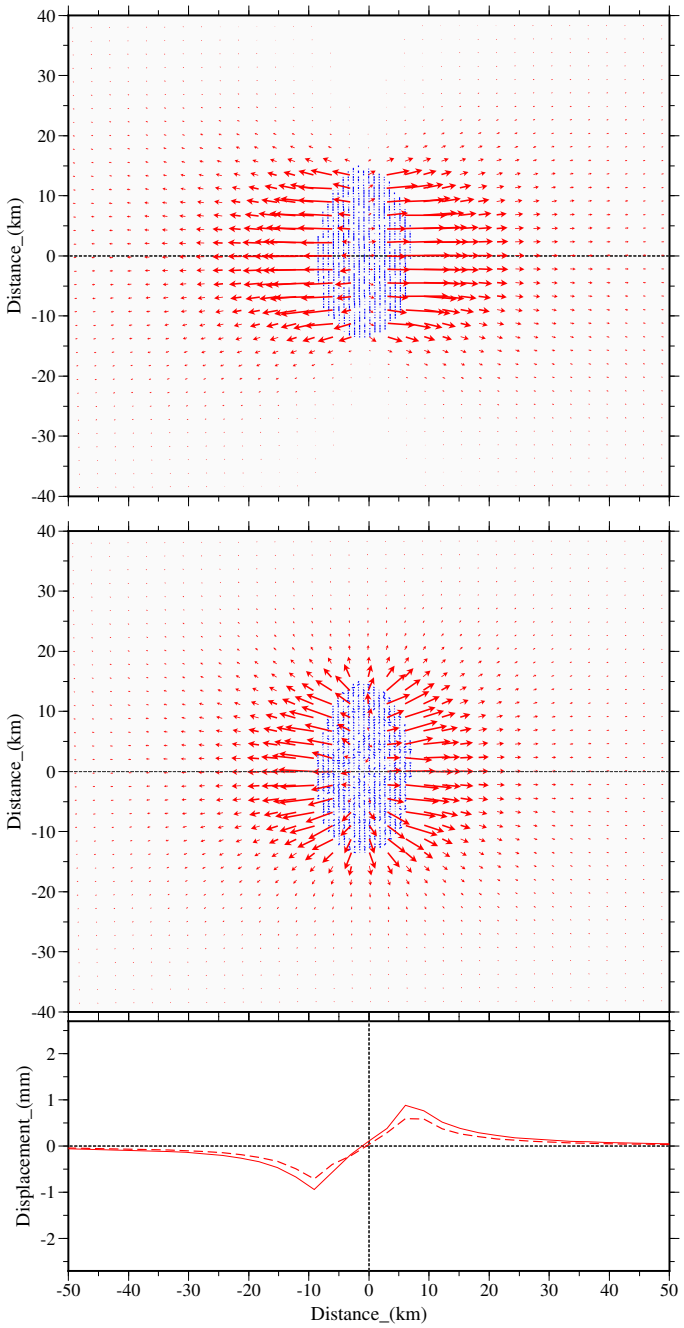

Figure 3.16: Comparison between the horizontal displacement (red arrows) caused by a group of small tensile fractures embedded in a region all having the same orientation (strike = 0°) (top) and the one caused by small tensile fractures with a Gaussian random distribution of strike value (0° ± 40°) (centre). The blue lines indicate the projection of the fractures. Bottom: Displacement profile along the dashed gray lines for the aligned fractures model (bold line) and the randomly oriented fractures model (dashed line).

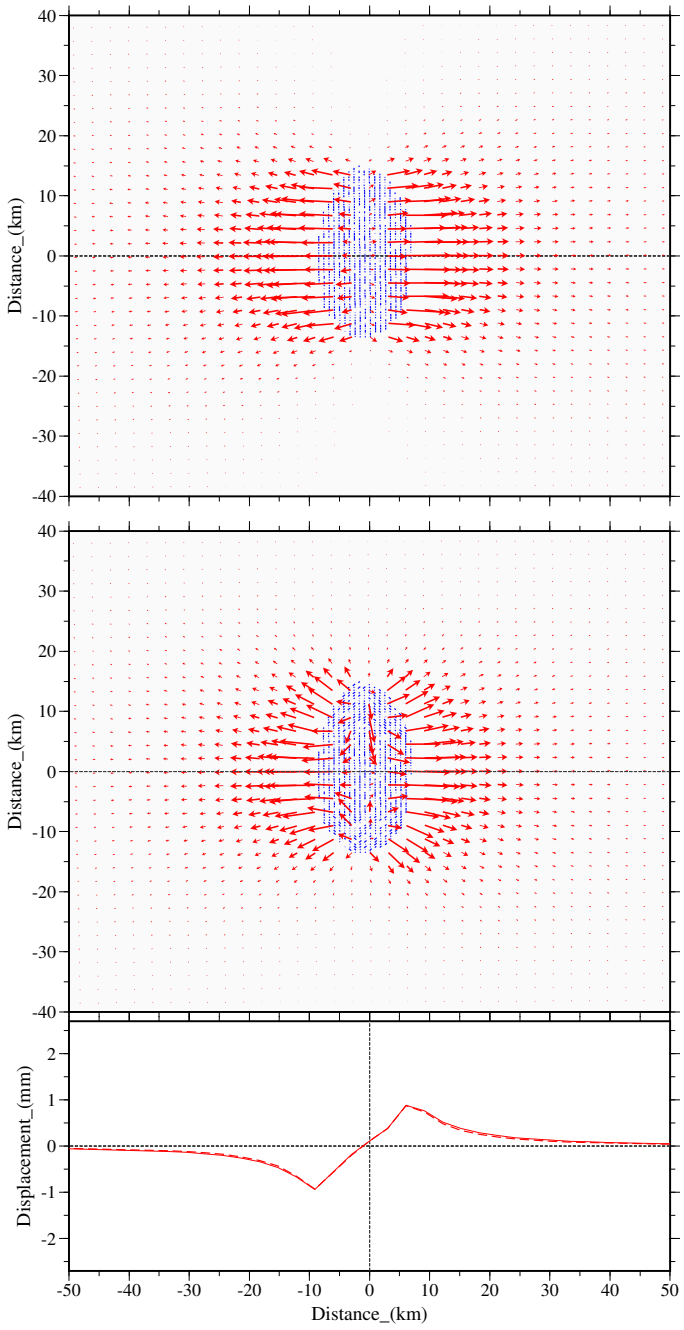

Figure 3.17: Comparison between the horizontal displacement (red arrows) caused by a group of small tensile fractures embedded in a region all having the same orientation (strike = 0°) (top) and the one caused by small tensile fractures with a distribution of strike value that mimics the shape of the fractured area (centre). The blue lines indicate the projection of the fractures. Bottom: Displacement profile along the dashed gray lines for the aligned fractures model (bold line) and the oriented fractures model (dashed line).

3.3 The effective stress principle

In this section we introduce the main concepts of the effective stress principle. This theory is usually used to study the deformations related to stress variations in porous materials. In general, well developed karst aquifers are not properly assimilable to porous materials such as soils, since they are permeated with large conduits and galleries where most of the water flows rapidly. However, as described in chapter 2, carbonate aquifers of the Apennines are characterized, especially in the phreatic zone, by a dense fracture network and scarcely developed conduits. This makes them assimilable, at least at a first order, to porous aquifers.

3.3.1 The Terzaghi effective stress principle

Porous media, such as soils, are multiphase materials composed by heterogeneous mixtures of a porous skeleton of solid mineral particles of different sizes and shapes and fluids, generally water and/or air filling the pore space. The mechanical behaviour of porous media due to variations of the external conditions depends on the interaction among the different phases. In fact, the behaviour of every single particle is related to the surrounding particles and the interstitial fluid, but the analysis of all these interactions at grain-scale is infeasible for practical applications. A different approach is therefore used, that considers the global behaviour of the medium and that assimilates a fluid saturated soil to two superimposed continuous medium, one solid and the other fluid, that occupy the same space volume. This strategy permits to extend to soils the concepts of *stress* and *strain* defined for continuous media. Naturally in this case a law has to exist to rule the interactions between solid and fluid phases occupying the same volume. An empiric principle that rules the solid-fluid interaction has been enunciated by Terzaghi (1936). It is known as *the effective stress principle* and states:
The stress in any point of a section through a mass of soil can be computed from the total principal stresses σ_1, σ_2 and σ_3 which act at this point. If

the voids of the soil are filled with water under a stress p the total principal stresses consist of two parts. One part p acts in the water and in the solid in every direction with equal intensity. It is called the neutral stress (or the pore pressure).
The balance $\sigma'_1 = \sigma_1 - p$, $\sigma'_2 = \sigma_2 - p$ *and* $\sigma'_3 = \sigma_3 - p$ *represents an excess over the neutral stress p and it has its seat exclusively in the solid phase of the soil. This fraction of the total principal stress will be called the effective principal stress.*
All measurable effects of a change of stress, such compression, distortion and a change of shearing resistance, are exclusively due to changes in the effective stresses.

The analysis of the mechanical behaviour of saturated porous materials (soils) can be therefore developed by considering two superimposed continuous medium and by defining in every point the total stress σ_{ij}, the pore pressure p and the effective stress $\sigma'_{ij} = \sigma_{ij} - p\delta_{ij}$. The latter can't be measured directly, but can be estimated only by knowing the total stress and the pore pressure.
This principle, for example, explains why changes in water level below ground (water table changes) result in changes in effective stresses below the water table and deformation of the medium, whereas changes in water level above ground (e.g. in lakes, rivers) do not cause changes in effective stresses in the ground below and consequently no ground deformation results.
Please note that in all section 3.3 normal tensile stresses are negative, while compressive stresses are positive.

Terzaghi's principle is an empiric principle based on experimental observations, however an approximate physic interpretation of effective stress concept can be provided by considering an element of saturated material and a surface (area A_t) that crosses it without sectioning the grains (Figure 3.18) (Facciorusso et al., 2006). Being A_c the contact area between the grains, the total vertical force F_t^v acting on the surface will be the sum of all the vertical components of the forces transmitted by the grains at the contact areas and

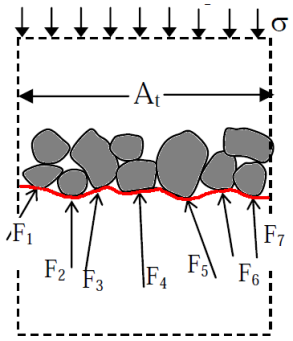

Figure 3.18: Scheme used to explain the meaning of effective stress. The red line indicate the crossing surface over which stresses are calculated. Modified from Facciorusso et al. (2006).

the pore pressure acting at the contact between the water and the surface A_t

$$F_t^v = \sum_i F_i^v + p(A_t - A_c) \tag{3.31}$$

By dividing the two members for A_t and defining $\sigma = \frac{F_t^v}{A_t}$ (total vertical mean stress on the surface A_t)

$$\sigma = \frac{\sum_i F_i^v}{A_t} + p\left(1 - \frac{A_c}{A_t}\right) \tag{3.32}$$

By defining the effective stress as $\sigma' = \frac{\sum_i F_i^v}{A_t}$ and assuming that $\frac{A_c}{A_t} \ll 1$ (true in several cases), we have

$$\sigma = \sigma' + p \tag{3.33}$$

The effective stress therefore represents a mean stress (over the surface A_t, not A_c) due to all the intergranular forces.

3.3.2 Geostatic stresses

Stresses within soils are due to the weight of the soil itself and to external factors. Perturbations of the stress conditions, e.g. loads applied at

the surface or variations of the water table level, provoke the deformation of the medium. Once the variation of the stress conditions are estimated, the induced deformation of the medium can be calculated by means of the constitutive equations.
Usually soils cannot be assumed to be linear elastic media and the induced deformations depends, other than on the stress variations, on the initial state of stress and on the stress-deformation history.

The stress due to the weight of the soil is called *geostatic (or lithostatic) stress*. Usually the geostatic stress represents the initial state of stress of a soil.
The pattern of geostatic stresses within soils can be complicated and it depends on several factors: geometry of the medium, water table condition, material characteristics, stress history. However, when the ground surface is horizontal, the nature of the medium varies slightly in the horizontal direction (e.g. sedimentary soils) and the water level is horizontal and in hydrostatic equilibrium, the evaluation of the stress stress state due to the overburden is very simple. In this case horizontal and vertical planes within the soil are principal planes of stress and there are no shear stresses upon vertical and horizontal planes (Figure 3.19). The state of stress can be therefore defined by a vertical stress $\sigma_v = \sigma_z$ and an horizontal stress $\sigma_h = \sigma_x = \sigma_y$. The equilibrium equations give

$$\begin{aligned} \frac{\partial \sigma_h}{\partial x} &= \frac{\partial \sigma_h}{\partial y} = 0 \\ \frac{\partial \sigma_v}{\partial z} &= \rho(z) g \end{aligned} \tag{3.34}$$

3.3.2.1 Vertical stresses

From the equilibrium equation 3.34 the total vertical stress is

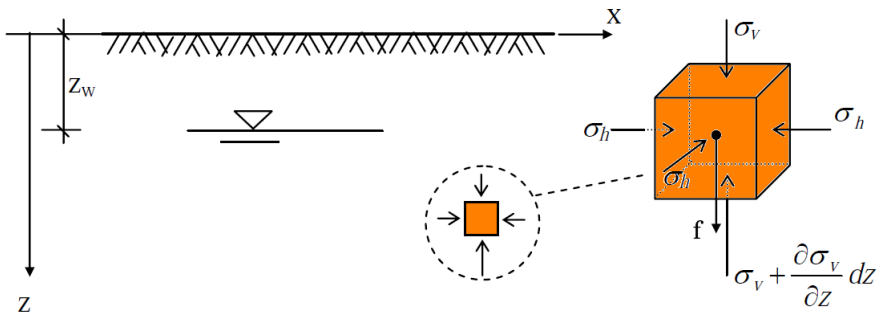

Figure 3.19: Geostatic stress in a horizontal soil. The state of stress is represented for a zoomed element of the medium. The triangle indicates the water table depth (z_w). Modified from Facciorusso et al. (2006).

$$\begin{aligned} \sigma_v &= \int_0^z \rho(z) g dz && \text{depth-varying density} \\ \sigma_v &= \rho g z && \text{homogeneus medium} \\ \sigma_v &= \sum_i \rho_i g \Delta z_i && \text{stratified medium} \end{aligned} \tag{3.35}$$

Regarding pore pressure **u**, when water is in quiet its pressure is the hydrostatic one (in most cases in fact, empty spaces in soils are interconnected and water-saturated below the water table depth z_w). The hydrostatic pressure is equal in every direction and is equal to

$$\begin{aligned} p &= 0 && z < z_w \\ p &= \rho_w g (z - z_w) && z \geq z_w \end{aligned} \tag{3.36}$$

where ρ_w is the water density.

The effective vertical stress is therefore given by the difference between the total stress and the hydrostatic pressure

$$\begin{aligned} \sigma'_v &= \sum_i \rho_i g \Delta z_i && z < z_w \\ \sigma'_v &= \sum_i \rho_i g \Delta z_i - \rho_w g (z - z_w) && z \geq z_w \end{aligned} \tag{3.37}$$

Further insights are given in section 3.3.2.3.

3.3.2.2 Horizontal stresses

The estimation of horizontal stresses in soil media is uncertain since the equilibrium equations simply give $\sigma_h = const$, without furnishing any specific information. Indications about the horizontal stress values are therefore deduced by experimental observations.
Experimental observations show that, analogously to vertical stresses, the effective horizontal stress value depend on the medium geometry, the water table, the soil characteristics and the stress history.
Horizontal stresses are usually related to vertical stresses by means of the *coefficient of lateral stress* (or *lateral stress ratio*)

$$K = \frac{\sigma'_h}{\sigma'_v} \tag{3.38}$$

Even when stresses are geostatic, the value of K can vary widely depending on whether the ground has been stretched or compressed in the horizontal direction. When there has been no lateral strain within the soil (horizontal strain prevented by a particular soil geometry and symmetry), the coefficient K is defined *coefficient of lateral stress at rest* and is indicated as K_0. In case of a linear elastic isotropic medium, the K_0 coefficient is proportional to the Poisson's ratio ν according to the following relation

$$K_0 = \frac{\nu}{1-\nu} \tag{3.39}$$

Therefore $0 < K_0 < 1$ for the typical range of values for the Poisson's ratio $0 < \nu < 0.5$. In natural soils K_0 can vary over a wide range and both values higher and lower to 1 have been observed, depending on the state of consolidation of the soil ($K_0 < 1$ for normally consolidated soils, $K_0 > 1$ for heavily overconsolidated soils) (Lambe and Whitman, 1969) (Figure 3.20).

In conclusion, by knowing the values of the lithostatic vertical effective stress σ'_v in a point inside a soil and of K_0, the lithostatic horizontal effective

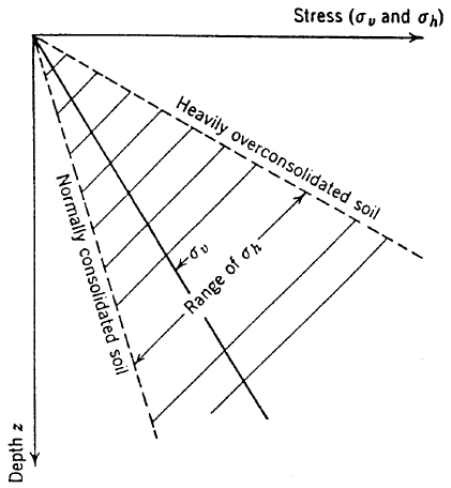

Figure 3.20: Horizontal and vertical geostatic stresses in soils. From Lambe and Whitman (1969).

stress σ'_h can be estimated from $\sigma'_h = K_0\sigma'_v$. Te total lithostatic horizontal stress σ_h then is $\sigma_h = \sigma'_h + p$.

3.3.2.3 Effective stress and varying water table level

The density of porous materials is defined according to the degree of saturation S and porosity n. The porosity is defined as the ratio of the volume of voids to the total volume of the material, the degree of saturation is defined as the ratio of the volume of water to the volume of voids. When $S = 0$ (dry material) the density is defined *drained (dry) density* ρ_d; if also $n = 0$, ρ_d coincides with the density of the solid portion (:non porous materials). In general, when $S, n \neq 0$ the density is defined *undrained (natural) density* ρ_s and

$$\rho_s = \rho_d + nS\rho_w \tag{3.40}$$

where ρ_w is the fluid (water) density.

Let's consider an homogeneous porous medium with an horizontal ground surface. The medium is saturated (S=1) below the water table, which is initially at depth z_{w1} ((a) in Figure 3.21) and than arises at a depth z_{w2} ((b)

in Figure 3.21). We assume the density of the material being ρ_d over the water table (for simplicity we don't consider the effect of capillarity) and ρ_s below the water table.
The vertical stresses in the initial state are ((a) in Figure 3.21):
total stresses

$$\begin{aligned} \sigma_{v1} &= \rho_d g z && z < z_{w1} \\ \sigma_{v1} &= \rho_s g(z - z_{w1}) + \rho_d g z_{w1} && z \geq z_{w1} \end{aligned} \tag{3.41}$$

pore pressure

$$\begin{aligned} p_1 &= 0 && z < z_{w1} \\ p_1 &= \rho_w g(z - z_{w1}) && z \geq z_{w1} \end{aligned} \tag{3.42}$$

effective stresses (from $\sigma_{v1} - u$)

$$\begin{aligned} \sigma'_{v1} &= \rho_d g z && z < z_{w1} \\ \sigma_{v1} &= \rho_s g(z - z_{w1}) + \rho_d g z_{w1} - \rho_w g(z - z_{w1}) = \\ &= \rho' g(z - z_{w1}) + \rho_d g z_{w1} && z \geq z_{w1} \end{aligned} \tag{3.43}$$

where $\rho' = \rho_s - \rho_w$

The vertical stresses in the modified state ((b) in Figure 3.21) are analogous to the previous ones, by replacing the depth value z_{w1} with z_{w2}. Note that the two considered state are static equilibrium states and we're not looking at the water diffusion that occurs between them.
The stress variations between the modified and initial state are therefore:
total stresses

$$\begin{aligned} \Delta\sigma_v &= \sigma_{v2} - \sigma_{v1} = 0 && z < z_{w2} \\ \Delta\sigma_v &= \sigma_{v2} - \sigma_{v1} = (\rho_s - \rho_d) g(z - z_{w2}) && z_{w2} \leq z < z_{w1} \\ \Delta\sigma_v &= \sigma_{v2} - \sigma_{v1} = (\rho_s - \rho_d) g(z_{w1} - z_{w2}) && z \geq z_{w1} \end{aligned} \tag{3.44}$$

pore pressure

$$\begin{aligned} \Delta p &= p_2 - p_1 = 0 && z < z_{w2} \\ \Delta p &= p_2 - p_1 = \rho_w g(z - z_{w2}) && z_{w2} \leq z < z_{w1} \\ \Delta p &= p_2 - p_1 = \rho_w g(z_{w1} - z_{w2}) && z \geq z_{w1} \end{aligned} \tag{3.45}$$

effective stresses

$$\begin{aligned} \Delta\sigma'_v &= \sigma'_{v2} - \sigma'_{v1} = 0 && z < z_{w2} \\ \Delta\sigma'_v &= \sigma'_{v2} - \sigma'_{v1} = -(\rho_d - \rho')g(z - z_{w2}) && z_{w2} \leq z < z_{w1} \\ \Delta\sigma'_v &= \sigma'_{v2} - \sigma'_{v1} = (\rho_d - \rho')g(z_{w2} - z_{w1}) && z \geq z_{w1} \end{aligned} \tag{3.46}$$

Being $z_{w1} > z_{w2}$ and $\rho_s > \rho_d > \rho'$, the total stress and pore pressures increase below the water table , in particular the variation is constant below $z = z_{w1}$. The effective stress consequently decreases below the water table ($\Delta\sigma'_v < 0$ for $z > z_{w2}$).

The vertical deformations and displacements due to this increase of the water table level can be computed analytically starting from the constitutive equations for elastic media, where the stress is now the effective stress, that intrinsically contains the effect of the pore pressure. In fact, starting from the constitutive equations for poroelastic media and considering completely saturated materials

$$\begin{aligned} \sigma_{ij} &= -2\mu e_{ij} - (K - \frac{2\mu}{3})e_{kk}\delta_{ij} + \alpha p\delta_{ij} \\ \rightarrow \sigma_{ij} - \alpha p\delta_{ij} &\overset{\alpha=1}{=} \sigma'_{ij} = -2\mu e_{ij} - (K - \frac{2\mu}{3})e_{kk}\delta_{ij} \end{aligned} \tag{3.47}$$

where e_{ij} is the strain tensor, δ_{ij} is the Kronecker delta, μ is the shear modulus, K is the drained bulk modulus and α is the Biot coefficient, that is equal to 1 for saturated materials.
In the analysed case, assuming to be in a uniaxial deformation configuration with $e_x = e_y = 0$ and $e_z = e_v = \frac{\partial u}{\partial z} \neq 0$ (no lateral deformation), the relation between the effective stress variation and the consequent strain variation is

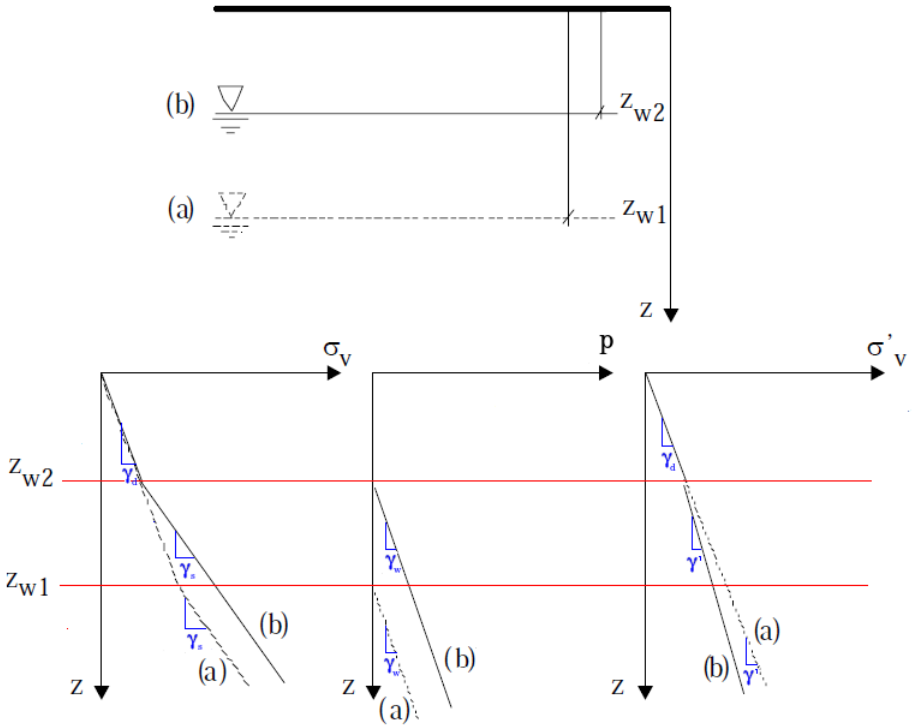

Figure 3.21: Geometrical framework and depth dependence of the stresses involved in the increase of the water table height described in section 3.3.2.3. Modified from Facciorusso et al. (2006).

$$\Delta\sigma'_v = -(K + \frac{4\mu}{3})\Delta e_v \tag{3.48}$$

Being in this case $\Delta\sigma'_v < 0$ (:tensile stress), $\Delta e_v > 0$, that imply uplift. In fact, considering a region between $z = 0$ (surface) and $z = H$ (bottom), by substituting values of $\Delta\sigma'_v$ from equations 3.46 into 3.48 and integrating by imposing the boundary condition $u = 0$ at the bottom, the vertical displacement u are (Figure 3.22):

$$\begin{aligned}
u &= -A\left[\frac{z_{w2}^2}{2} - \frac{z_{w1}^2}{2} + H(z_{w1} - z_{w2})\right] && 0 < z < z_{w2} \\
u &= -A\left[-\frac{z^2}{2} + zz_{w2} - \frac{z_{w1}^2}{2} + H(z_{w1} - z_{w2})\right] && z_{w2} \le z < z_{w1} \\
u &= -A\left[-(z_{w1} - z_{w2})z + H(z_{w1} - z_{w2})\right] && z_{w1} \le z \le H \qquad (3.49)
\end{aligned}$$

(3.50)

where $A = \frac{(\rho_d - \rho')g}{K + \frac{4\mu}{3}} > 0$. The vertical displacement is therefore constant above z_{w2}, is negative (upward displacements) and depends quadratically from the depth z between z_{w2} and z_{w1}, whereas is negative and depends linearly from the depth for $z > z_{w1}$.

Numerical methods for complex configurations

For simple configurations as the one shown above (horizontal geometry and uniaxial deformation) analytical solutions for the displacements induced by stress variations can be found. However, in case of more complex configurations, as the ones including topography, non-horizontal water table geometry and anisotropy, numerical methods have to be employed to solve the differential equations that relate stress variations and the associated displacement.

One technique usually used to calculate numerical solutions of sets of differential equations, given initial values and/or boundary values, is the *finite difference method* (e.g. Desai and Christian, 1977). In this method, every

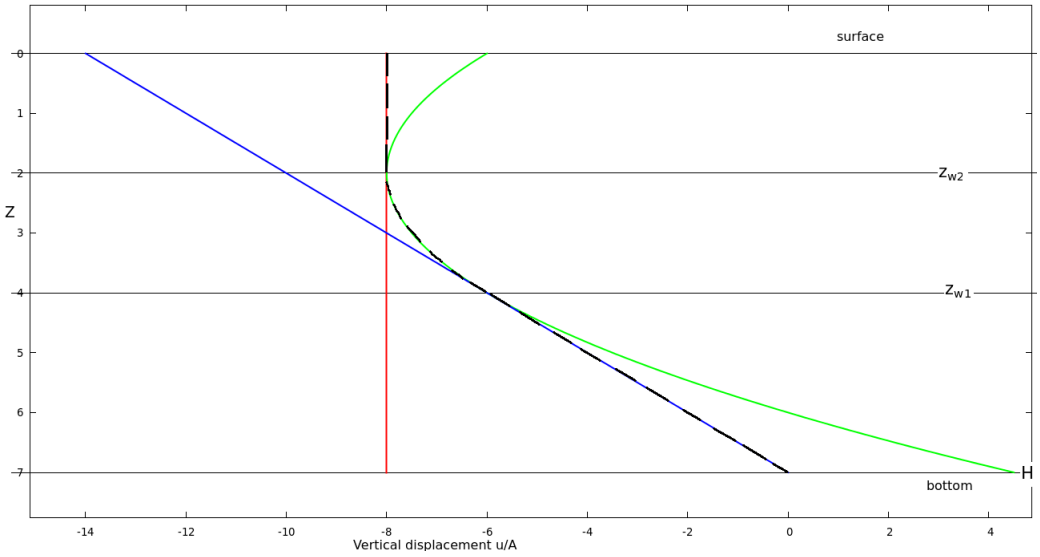

Figure 3.22: Depth dependence of the vertical displacement, up to a factor $A = \frac{(\rho_d - \rho')g}{K + \frac{4\mu}{3}} > 0$, with $z_{w2} = 2$, $z_{w1} = 4$ and $H = 7$. The three coloured lines represent the three functions (constant-red, quadratic-green, linear-blue) from which u is defined in the three depth intervals (black dashed line).

derivative in the set of governing equations is replaced directly by an algebraic expression written in terms of the field variables (e.g., stress or displacement) at discrete points in space, whereas these variables are undefined within elements.

Chapter 4

The GPS technique

4.1 Introduction

The Global Positioning System (GPS) is a space geodesy technique, part of the space-based global navigation satellite system (GNSS), that provides three-dimensional location and time information in all weather conditions anywhere on or near the Earth. Initially conceived for military purposes, it has been made gradually available for public use in after 1995. It is maintained by the United States government and is freely accessible by anyone with a GPS receiver.

The use of GPS and of others space geodesy techniques in geophysics is well-established nowadays thanks to the numerous advantages provided by these techniques with respect to the terrestrial surveying, such as true three-dimensional positioning, toleration of a broader range of weather conditions, higher precision and accuracy of the observations and easier data reproducibility. The high precision of space geodesy, its global surveying and its continuous acquisition of data using permanent stations have permitted in the last decades to study Earth processes over distance scales ranging ten orders of magnitude from 10^0 to 10^{10}m and over time-scales ranging ten orders of magnitude from 10^{-1} to 10^9s (Blewitt, 2015).

In comparison with other space geodetic techniques, like satellite laser rang-

ing (SLR) and very long baseline interferometry (VLBI), GPS provides a series of advantages, such as its easy and economical access to hardware and software, ease of deployment of field equipment, all weather capability, temporally continue and global geographical coverage and dramatic improvements in techniques for high-precision GPS geodesy. GPS allows for continuous acquisition of data using permanent stations with communications to a data processing centre, enabling continuous monitoring of geophysical processes. Earth surface motion is fundamentally determined as a time series of positions relative to a global reference frame. Furthermore GPS provides three-dimensional displacement data (North, East and Up components).
The disadvantage of GPS is that it is subjected to both the systematic errors associated with orbit dynamics and atmospheric moisture. Furthermore, the omnidirectional antennas of GPS lead to multipath errors. Thus geodetic GPS has an essential role in improved sampling of the Earth surface positioning in time and space, but ultimately depends on SLR and VLBI to put such measurements into a reference frame provided with long-term stability. Indeed the WGS-84 and various reference frames based on SLR, VLBI, or a combination of SLR and VLBI, are the most commonly used in high precision geophysical applications of GPS (Abusali et al., 1995). Another disadvantage is that with GPS only spatially discrete measurements are operable, therefore quite dense GPS network are required. In this sense Interferometric synthetic aperture radar (InSAR) could be of help since it provides one-dimensional but continuous measurements in space.

4.2 Basic principles

4.2.1 Pseudoranges

GPS positioning is based on the principle of *trilateration*, which consists in determining locations by measuring distances (ranges) between points of known positions. Trilateration requires at least three ranges to three known points. In the case of GPS, known points are the positions of the satellites in

view and the measured ranges are the distances between the GPS satellites and a user's receiver. The positioning is realized in practice by continuously tracking the satellite microwave signal along with its transmission time so that it can be compared with a clock in the receiver and the transit time interval can be estimated. The range estimated by GPS receivers by multiplying the difference in time between the receiver's local clock and satellite's clock by the speed of light is not, however, the true value of the distance because of a synchronization error between the two clocks (satellite's clock are very precise and monitored atomic clock, while receiver's clock are much cheaper instruments, typically quartz oscillators). The so estimated distances are therefore called *pseudoranges* and are defined as:

$$\text{Pseudorange} = (\text{receiver time} - \text{satellite time}) \times \text{speed of light} \qquad (4.1)$$

The clock time is sent by the satellites to the user's receiver through an encoded microwave signal (see section 4.2.3). The receiver generates an identical replica code, and then performs a cross-correlation with the incoming signal to compute the time shift required to align the codes. The pseudorange measurement estimated starting from this time shift is biased by the error in the receiver's clock. However, this bias at any given time is the same for all observed satellites, thus it can be estimated as one extra parameter in the positioning solution. In order to determine the user position four unknown have to be solved for: the three point coordinates contained in the true range and the clock error, consequently at least four satellites have to be tracked simultaneously. In order to look at at least 4 satellites from every point on Earth at every time, a constellation of at least 24 satellites in 6 different orbits at 20.200 km high is required. In addition, there is typically an active spare satellite in each orbital plane, bringing the total number of satellites closer to 30.

It should be noted that there are also much smaller errors in the atomic clocks on satellites, but GPS satellites handle them by communicating to the receiver the error in its clock through the transmission of an additional

code. This error is routinely monitored and updated by the US Department of Defense.

4.2.2 GPS System Design

The GPS system is organized in three distinct segments.

1. *Space Segment*: constellation of about 30 GPS satellites that transmit signals to the users. The emitted signals include both the ones that enable a user's receiver to measure the pseudorange to each satellite in view, and the ones that communicate to the receiver several informations as the current satellite position, the current error in the satellite clock, and other useful informations to compute the receiver's position.

2. *Control Segment* (in the US Department of Defense): organization that consists of five monitor stations, a master control station (Colorado Springs, California) and some ground control stations located around the world. It has the aim of monitoring the Space Segment and uploading of information used to predict the GPS satellite orbits and clock errors into the near future, which the Space Segment can then transmit down to the user. Monitor stations, equipped with accurate atomic clocks, receive all the time signals from GPS satellites and send data to the master control station which calculate orbits and clock parameters of the satellites. This information is sent to the ground control stations, that transmit correction information back to individual satellites.

3. The *User Segment*: user's GPS hardware (receivers and antennas) and GPS data-processing software for many different applications.

4.2.3 Satellite signal structure

Signals are transmitted and received by the satellite using microwaves. The GPS satellites send two main kind of signals:

- Carrier signals/sinusoids : L_1 (frequency 1.575 GHz) and L_2 (frequency 1.228 GHz), that are ultra-high frequency signals (passing through

clouds) (Figure 4.1A).

- Codes: binary signals P/Y (Precise-Y code affected by antispoofing by US army up to 2000), and C/A (Coarse Acquisition) codes. The C/A-code repeats every 1023 bits and is placed on the L_1 carrier only, the P/Y-code is repeated once a week and is placed on both carrier signals.

The two carriers are modulated by codes (sequences of +1 or -1) to provide satellite clock readings to the receiver and to transmit some information, such as the orbital parameters. This is the so-called *biphase modulation* that is performed by a 180° shift in the carrier phase whenever a change in the code state occurs (figure 4.1B).

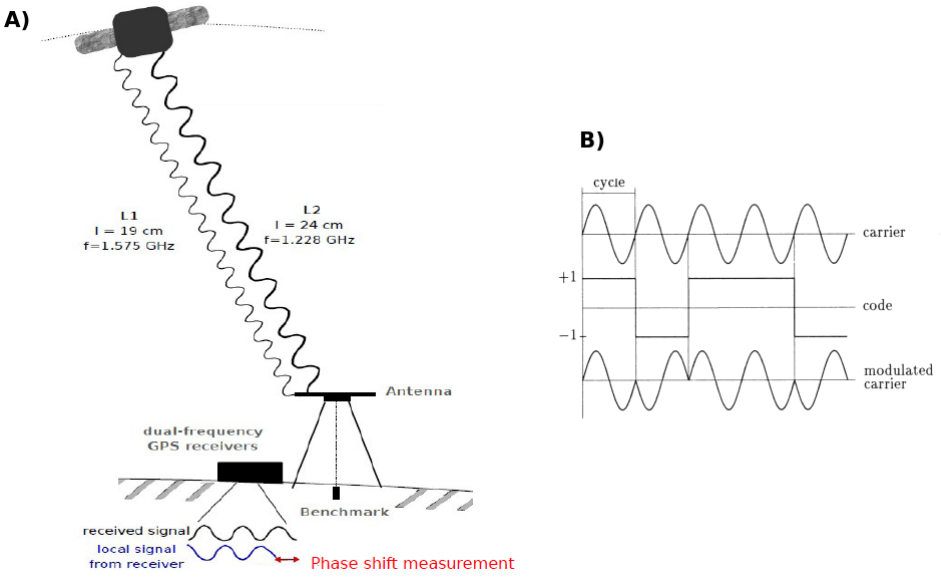

Figure 4.1: A) Schematic representation of the carrier signal transmission between GPS satellites and receivers. B) Process of biphase modulation of the carrier wave. Modified from Hofmann et al. (1993).

The carrier signal is finally encoded with the *Navigation Message*, which can be read by the user's GPS receiver. The Navigation Message includes information about the satellite health status, the satellite clock, various correction data and orbit parameters (often called *Broadcast Ephemeris*), from which the receiver can compute satellite coordinates as Cartesian coordinates

(X, Y, Z) in a geocentric system.
The codes signals are unambiguous since their repeating time is high and every satellite has its own code, but they are limited to a precision of tens of meter (for C/A) or cm (for P/Y if no antispoofing is applied). The C/A code is the basis for civilian GPS use in which no further processing or correction is applied.

4.2.4 High-Precision GPS

Through the determination of pseudoranges to at least four satellites, GPS can readily provide users with a relatively low-cost equipment a positioning accuracy of meters and a timing accuracy of 0.1μs. Nevertheless geodetic GPS positioning with an accuracy of a few millimetres requires several significant improvements, most of which can be applied only during data-processing, not in real-time.
First of all, for high-precision GPS purposes, the carrier phases are used in order to estimate pseudoranges, since they could potentially offer millimetre accuracy (fraction of their wavelength). The phase of the signal received at a given time t is given by

$$\Phi_S(t) = ft - \frac{fd}{v} \tag{4.2}$$

where f is the signal frequency, d is the satellite-receiver distance and v is the wave (light) velocity. In the receiver an identical signal is produced and, at the time t, its phase is $\Phi_R(t) = ft$. The phase-difference $\Delta\Phi_{SR} = \Phi_R(t) - \Phi_S(t) = \frac{fd}{v}$ theoretically provide the unknown pseudorange d. In practice, since $d \gg \lambda$ (where λ is the carrier wavelength), the carrier signals are ambiguous and an unknown number of cycles N (*ambiguity*) arises

$$d = (\Delta\Phi_{SR} + N)\frac{v}{f} \tag{4.3}$$

The receiver calculates the satellite-receiver phase shift $\Delta\Phi_{SR}$, but it is unable to determine directly the exact ambiguity N. Furthermore, all along the satellite-station path, the signal is influenced by the inhomogeneous medium

it traverse. A more complete expression for the pseudorange d can be written as

$$d = (\Delta\Phi_{SR} - \Phi_{clock} - \Phi_{iono} - \Phi_{tropo} - \Phi_{noise} + N)\frac{v}{f} \tag{4.4}$$

Furthermore, an accurate knowledge of the GPS satellite positions and satellite clock offsets is required. For standard GPS positioning, this ephemeris information is broadcast by the GPS satellites in the Navigation Message, but it is not sufficiently accurate for scientific applications. For this purpose, several civilian networks, usually referred as *Service Segment*, were born in order to provide the User Segment with data and services, such as high-accuracy data on satellite orbits and clocks. Using such reprocessed orbits (for instance from International GNSS Service) improves greatly the position calculation (Beutler et al., 1999). Figure 4.2 schematically represents the main error sources of GPS measurements and indicates the techniques used to mitigate them.

The term Φ_{clock} refers to the clock drifts of both the satellite and receiver oscillators. The satellites atomic clock has small drift of 10^{-9} s/day that is regularly detected and corrected by the control segment. The receiver clock is a commercial low-quality clock with an average drift of $10^{-6} \div 10^{-5}$ s/day. In order to correct for the receiver clock drift a technique called *simple difference* is used that consists in a simple combination of measurements between one receiver and two satellites. As regards the satellite clock drift, two different methods are currently used. *Double difference* technique combining all the phase measurements from 2 satellites and 2 receivers, provides high precision data, but leads to the calculation of the baseline between the two receivers rather than to the position calculation. Therefore, this technique implies to process all the stations of the network together, which is quite time consuming. An alternative to the double difference is to use the simple difference phase measurements together with the global parameters (precise ephemerides, clock errors of GPS satellites and earth rotation parameters) estimated precisely by the JPL (Jet Propulsion Laboratory), or other processing centres, on the basis of a global GPS observation network. This

method, called Precise Point Positioning (PPP) gives an absolute position for each station independently (Zumberge et al., 1997).

The term Φ_{iono} is the delay that the signal undergoes while it crosses the ionosphere, which is a diffracting medium affecting the wave velocity as depending on its frequency and on the electrons density of the ionosphere. The ionospheric delay impact is removed by combining both L_1 and L_2 phase measurements (*LC combination technique*).

Φ_{tropo} refers to the tropospheric delay which is due to the fact that the troposphere is a refractive medium, which influences the GPS signals propagation by inducing an excess propagation path length. Two kinds of delay are identified: the dry delay due to the troposphere width and the satellite location, and the wet delay due to the water vapour content. The dry tropospheric path delay depends mainly on the pressure and therefore it varies quite slowly in time. It is corrected by calculating the *zenithal dry delay* as a function of the width of the troposphere above the station, which is estimated by using some hydrostatic mapping functions of the troposphere (e.g. Simmons at al., 2007; Lagler et al., 2013) and correcting from the elevation angle of the satellite. The wet tropospheric path delay depends on the water vapour distribution and changes much faster in both space and time. It is usually inverted every 2 hours or even more in the processing together with some horizontal gradients. Bad estimates of Φ_{tropo} will produce large errors mainly on the vertical position, since errors on the horizontal position will be averaged in some way if measurements are conducted on an entire day or more due to the satellite trajectory.

Φ_{noise} embraces a series of noise sources, such as the multipath effect and the phase-center drift. The first one is due to the reflection of the signal before it reaches the receiver, which causes a wrong distance estimation. This noise can mitigated by the choice of the site location (far from possible reflectors) and by long measurements that, thanks to the satellite motion in the sky, produce an averaged position close to the real antenna position. The second one is due to the fact that the antenna phase-center position depends

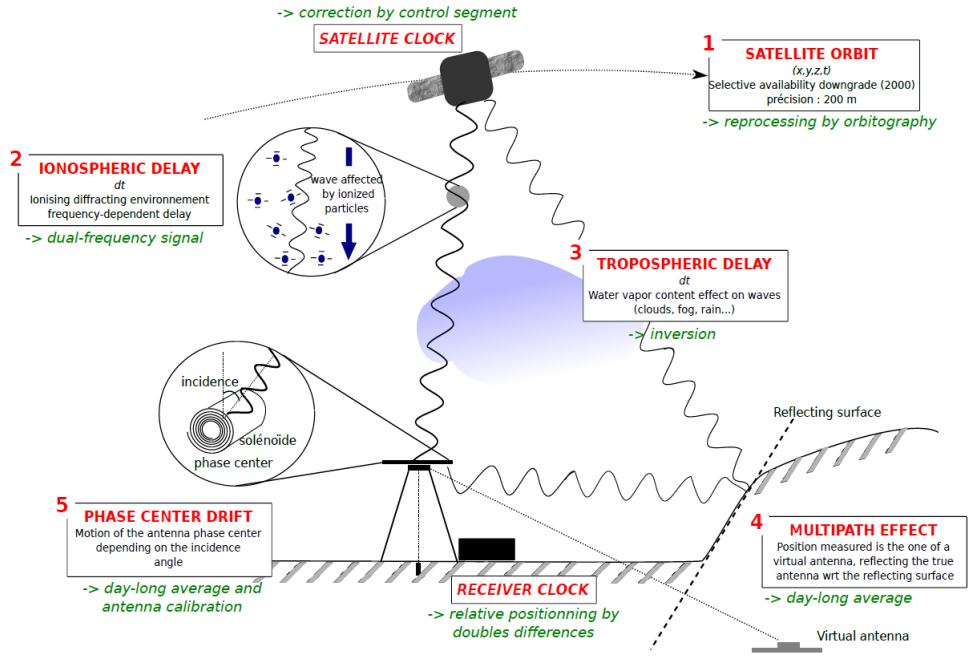

Figure 4.2: Schematic representation of the main sources of errors in GPS technique and of the methods used to mitigate them. Courtesy of M. Métois.

on the incidence angle of the signal relative to the coil that transform the GPS signal into electric signal. Again this can be mitigated through time averages and post-processing.

Finally the resolution of the ambiguity N is essential to achieve the highest possible precision for geodetic applications. The basic idea to estimate the ambiguity value is based on combining all the available phase and code observations to get a set of equations from which a least-square algorithm can be applied to estimate both the distance and the ambiguity value. Since the 1980s, GPS data processing algorithms, which estimate positions and other parameters, have frequently resolved ambiguities by fixing double-differenced phase bias ambiguities to integer values and using linear combinations of GPS carrier phase bias estimates from pairs of transmitters and pairs of receivers in order to cancel receiver and transmitter hardware delays.

In the case of PPP with a single receiver, estimates of biases from at least

one other station with the same satellites in view are needed. A successful method now in common use is known as the *wide-lane and phase bias* (WLPB) method (Bertiger et al., 2010). It estimates biases for the IGS network during the GPS orbit estimation procedure. These phase bias estimates are then made available to the single-receiver user along with the GPS orbit and clock parameters making the user able to perform ambiguity resolution through PPP with a single receiver.

In summary GPS for geophysical purposes requires:
- GPS receivers capable of acquiring dual-frequency carrier phase data;
- satellite orbit and clock information, which is available from the IGS;
- simultaneous observations to a minimum of five satellites;
- specialized post-processing software (not on the receiver itself).

Geodetic data processing software are a result of intensive geodetic research, mainly by various universities and government institutions around the world. These are highly specialized stochastic multi-parameter estimation software able to model the carrier phase data, the satellite-station geometry, Earth's atmosphere, solid-Earth tides, Earth rotation, antenna effects and relativistic effects. They are also capable of detecting and correcting cycle slips and of resolving the integer ambiguity in the initial phase measurements. In order to do that, such software embody leading-edge models of the solid Earth, atmosphere, and satellite dynamics. They also contain data processing algorithms (signal processing and stochastic parameter estimation). There are three ultra-high-precision software packages widely used by researchers all over the world:

- BERNESE software, by Astronomical Institute,University of Bern, Switzerland (Rotarcher et al., 1990);
- GAMIT-GLOBK software, by MIT, USA (King and Bock, 2005);
- GIPSY-OASIS II software, by JPL, California Institute of Technology, USA (Webb and Zumberge, 1993).

Chapter 5

Analysis of the transient deformation of the Apennines: observations

In the previous chapters the geographical and hydro-geological contexts have been delineated, the theory about the deformation related to surface loading, tensile dislocations and effective stress variations have been presented and the basic principles of the GPS technique have been outlined.
In this and in the following chapter we present the analysis of a hydrologically-related multi-annual transient deformation in the Apennines that we have highlighted from GPS time-series.
Here we introduce the GPS data we dealt with and three different kinds of observables that provide information about hydrological phenomena: the rain-gauge data, the discharge data of some of the main karst springs and the terrestrial water storage observations by GRACE satellite. We then develop a deepened comparison between GPS data and hydrological observables that let us to propose the hydrologically-related cause of our observations.

5.1 GPS data and analysis

In this work we used the daily observations from permanent GPS stations in Central and South-Central Apennines, most of which belong to the Rete Integrata Nazionale GPS (RING) network (`http://ring.gm.ingv.it` and Avallone et al. (2010)). The locations of RING sites and additional stations can be found in Figure A.3.

GPS data were reduced using the Jet Propulsion Laboratory (JPL) GIPSY-OASIS II software (ver. 6.2) in a Precise Point Positioning mode applied to ionospheric-free carrier phase and pseudorange data (Zumberge et al., 1997) and using JPL's final fiducial-free GPS orbit products. We correct second order ionospheric effects using the *jplg* ionospheric model retrieved from `ftp://cddis.gsfc.nasa.gov/gps/products/ionex`. We applied the GPT2 tropospheric mapping function (Lagler et al., 2013) and estimated tropospheric wet zenith delay and horizontal gradients as stochastic random-walk parameters every 5 min (Bar-Sever et al., 1998) in order to model tropospheric refractivity. We have computed the ocean loading from the FES2004 tidal model coefficients provided by the Ocean Tide Loading Provider (`http://holt.oso.chalmers.se/loading` and Scherneck (1991)) and applied it as a station motion model. Ambiguity resolution is performed using the wide lane and phase bias (WLPB) method (Bertiger et al., 2010). Finally, station coordinates obtained in the loose frame of JPL fiducial-free GPS orbits are transformed into the IGS08 reference frame (Rebischung et al., 2012) using daily 7-parameter transformations provided by JPL. In order to analyse and interpret station velocities relative to the Eurasia plate and to reduce the common mode signal, we have specifically developed a terrestrial reference frame suitable for crustal deformation studies in and around that plate following the approach of Blewitt et al. (2013). This frame is defined by 6 Cartesian coordinates and velocities of each of 174 stations selected by specific quality criteria. Our Eurasian frame is aligned in origin and scale with IGS08 (Rebischung et al., 2012). GPS velocities are obtained by fitting a linear trend plus annual and semi-annuals terms and site specific offsets to

position time-series, assuming a white+flicker noise stochastic model. This frame is implemented to have no-net rotation with respect to the stable interior of the Eurasian plate, realized by a 69-station core subset.
The uncertainties associated with the so-processed GPS data are ~ 1 mm for the horizontal components and $\sim 2 \div 4$ mm for the vertical component.

In order to emphasize the long-term, secular $\sim$3 mm/yr NE-SW directed active extension across the Apennines (D'Agostino, 2014), crustal velocities in Figure 5.1 are shown in a Tyrrhenian reference frame, obtained by minimizing horizontal velocities of some selected stations on the Tyrrhenian coast. Sites possibly affected by ongoing volcanic deformations near Naples (Vesuvio and Campi Flegrei) have been excluded.
Time-series of vertical and horizontal components are shown in Figure 5.2, progressively ordered from the Tyrrhenian (bottom) to the Adriatic (top) coasts. Horizontal components are represented as projections in directions respectively perpendicular and parallel to the long-axis of the Apennines. Instrumental jumps and the offset related to the 2009 L'Aquila earthquake have been previously removed. These time-series show that, from the Central to South-Central Italy, the interseismic $\sim$3 mm/yr extensional opening in the axial part of the Apennines (D'Agostino, 2014) is modulated by annual and multi-annual signals that modify the stationarity of the tectonic signal. This modulation can be particularly appreciated in the perpendicularly projected horizontal component (N65E direction in Central Italy, N45E direction in South-Central Italy, Figure 5.2d-e) and appears to affect mostly the sites located along the Apennines and to progressively vanish towards the coasts. In Figures 5.2b, 5.2c and 5.2e, both the annual and multi-annual perpendicularly projected horizontal signals display episodes of specular enhanced or reduced outward motion relatively to an axis of symmetry running approximately along the crest of the Apennines. In Figure 5.2b this symmetry axis runs between sites TERI and ROPI, in Figure 5.2c between sites VAGA and CERA and in Figure 5.2e between sites CDRU and SAL1. Time-series in Figure 5.2d, in contrast, don't show a clear multi-annual signal, as we will

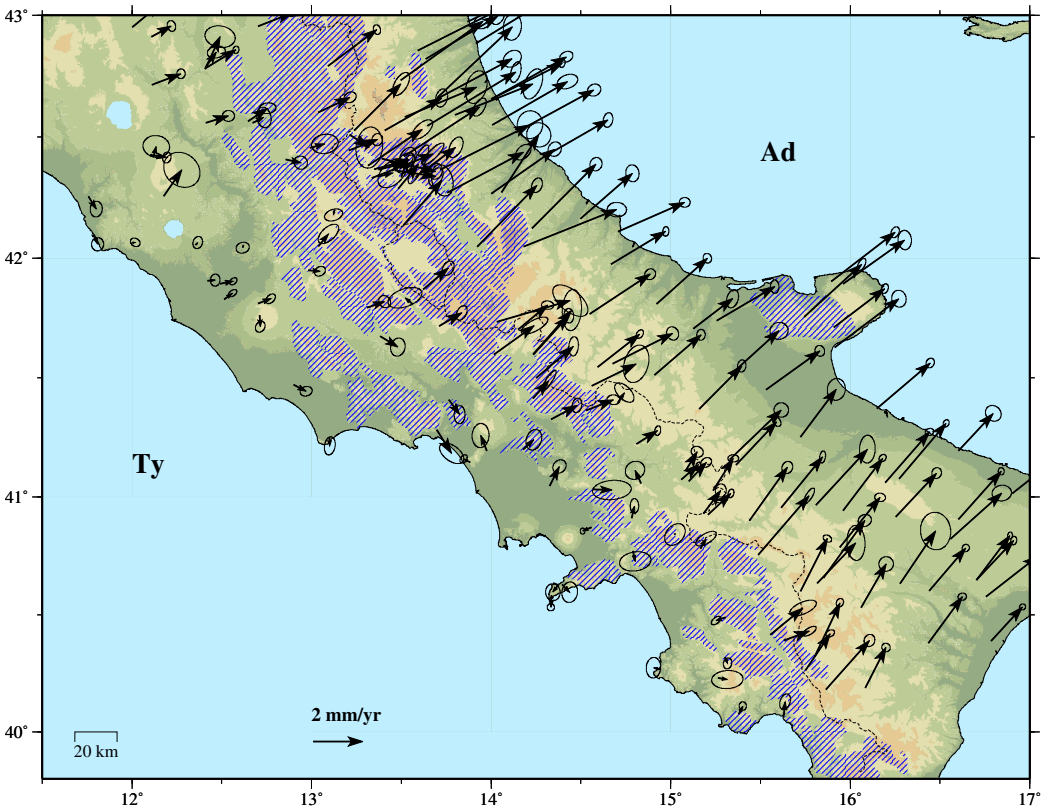

Figure 5.1: General framework of the study area. Black vectors represent GPS horizontal interseismic velocities in a Tyrrhenian reference frame. The black dashed line indicates the drainage divide and the blue striped areas outline the main carbonate massifs.

discuss later.

In Figure 5.2 we have highlighted two multi-annual episodes (each 2.5 year long) of inward (T1, 2006.4-2008.9) and outward (T2, 2008.95-2011.45) motion of the stations in the axial part of the Apennines. We have estimated the deviations from the long-term trend (∼2005-2015) in these two time intervals by firstly fitting time-series with a linear trend and annual and semi-annual periodicities for each interval, assuming a white+flicker noise (CATS software by Williams (2008)). Then we have subtracted the long term trend from the fitting trends in order to obtain the deviations from it (e.g. Figure 5.3). Since T2 encloses the L'Aquila earthquake epoch and

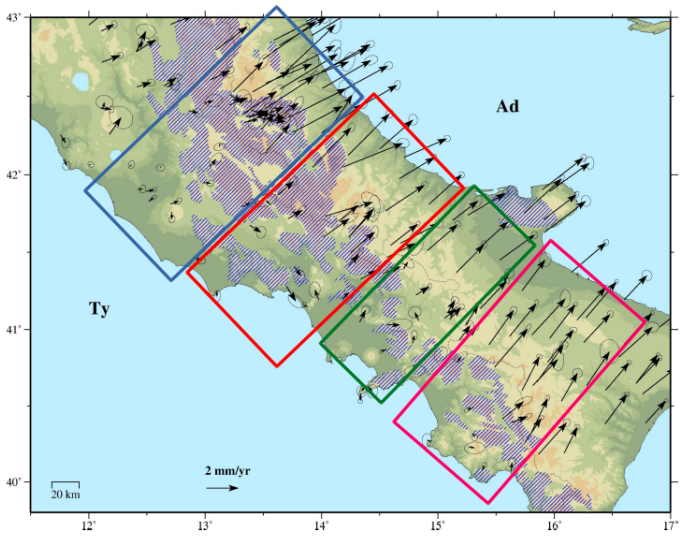
Ad
Ty
2 mm/yr
20 km
43°
42°
41°
40°
12°
13°
14°
15°
16°
17°

(a)

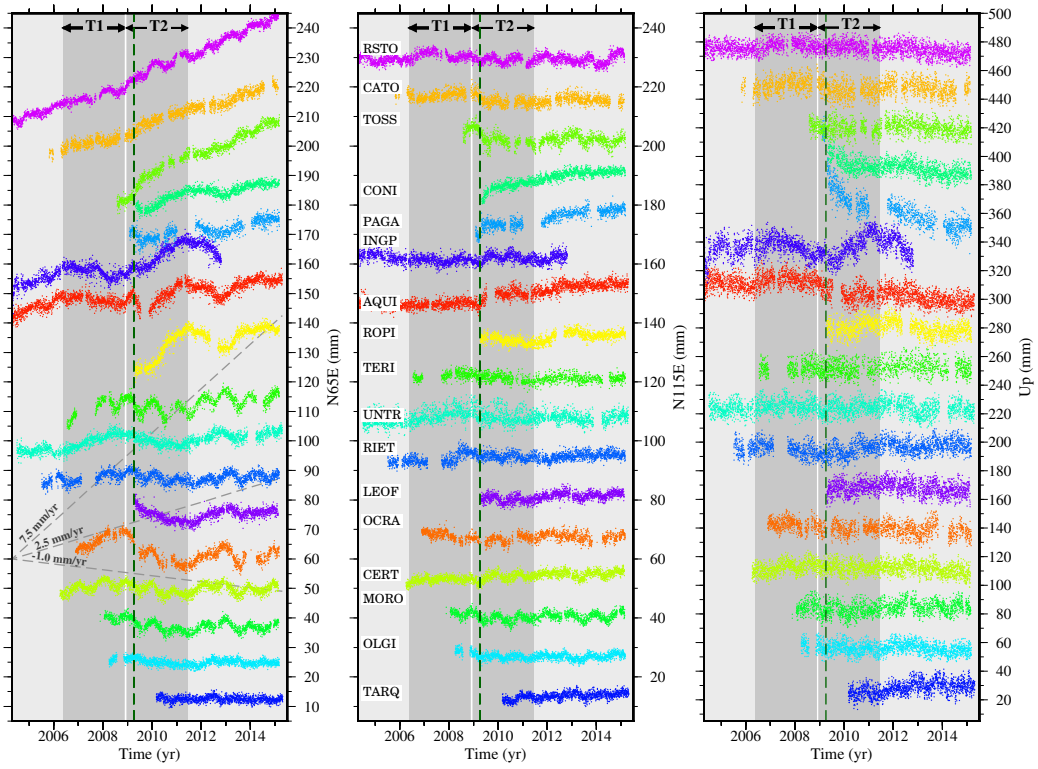
T1
T2
RSTO
CATO
TOSS
CONI
PAGA
INGP
AQUI
ROPI
TERI
UNTR
RIET
LEOF
OCRA
CERT
MORO
OLGI
TARQ
7.5 mm/yr
2.5 mm/yr
-1.0 mm/yr
N65E (mm)
N115E (mm)
Up (mm)
Time (yr)
2006
2008
2010
2012
2014

(b)

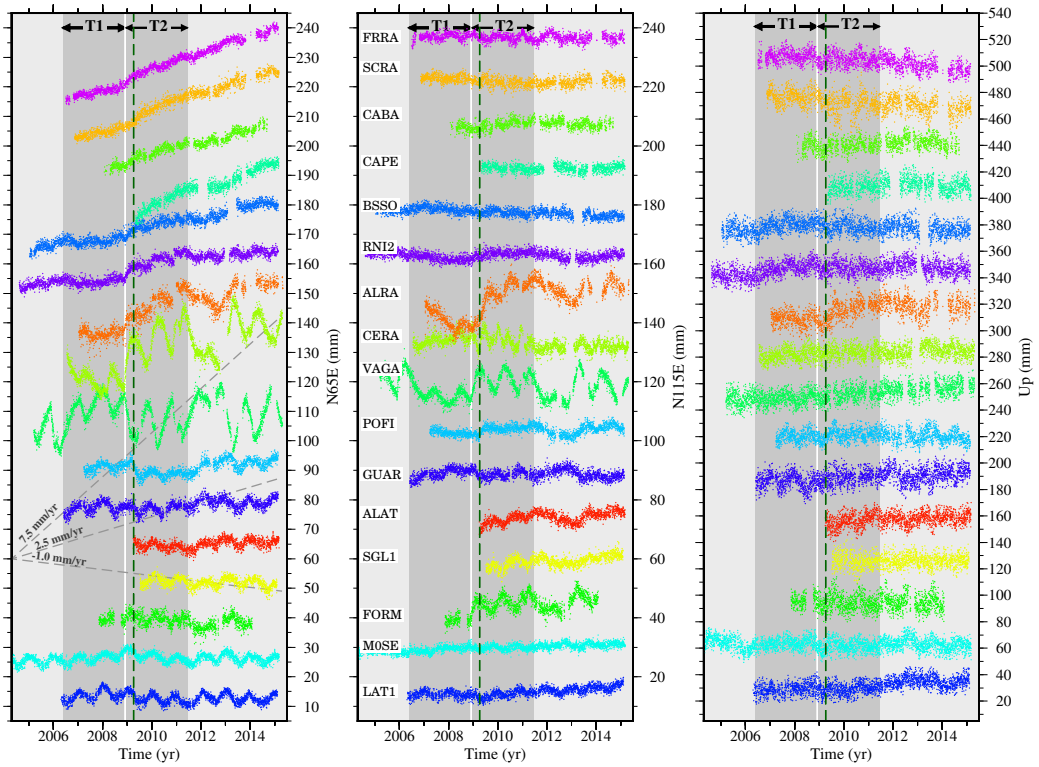
T1
T2
FRRA
SCRA
CABA
CAPE
BSSO
RNI2
ALRA
CERA
VAGA
POFI
GUAR
ALAT
SGL1
FORM
M0SE
LAT1
7.5 mm/yr
2.5 mm/yr
-1.0 mm/yr
N65E (mm)
N115E (mm)
Up (mm)
Time (yr)

(c)

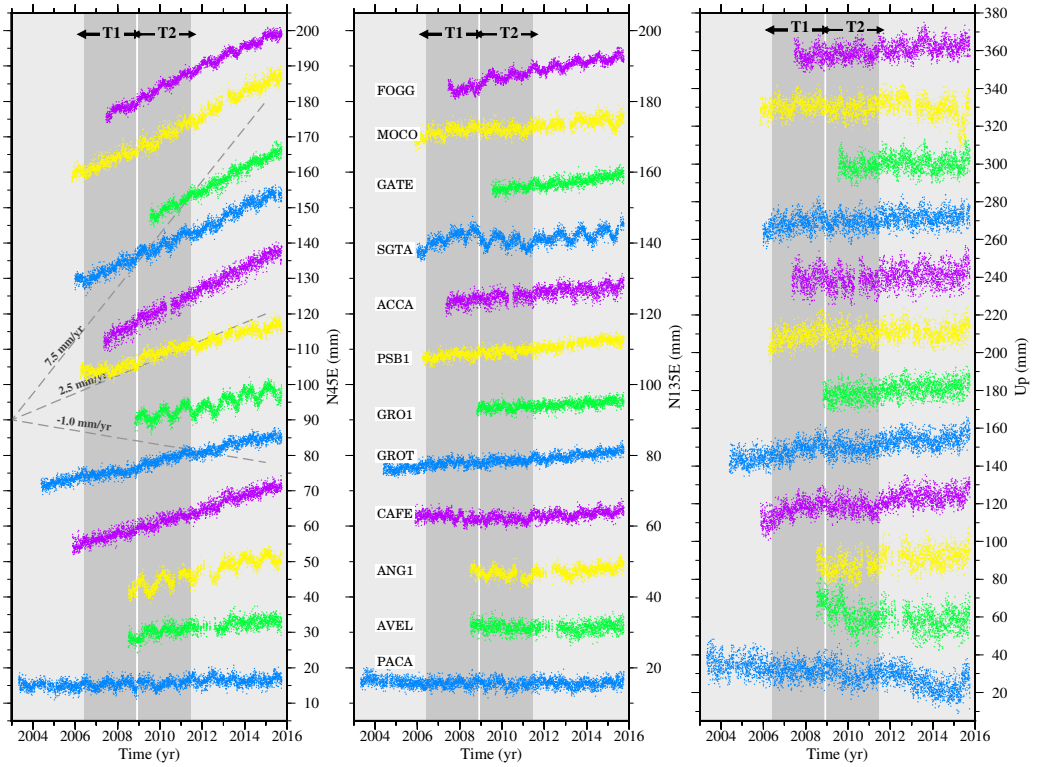
T1
T2
FOGG
MOCO
GATE
SGTA
ACCA
PSB1
GRO1
GROT
CAFE
ANG1
AVEL
PACA
7.5 mm/yr
2.5 mm/yr
-1.0 mm/yr
N45E (mm)
N135E (mm)
Up (mm)
Time (yr)

(d)

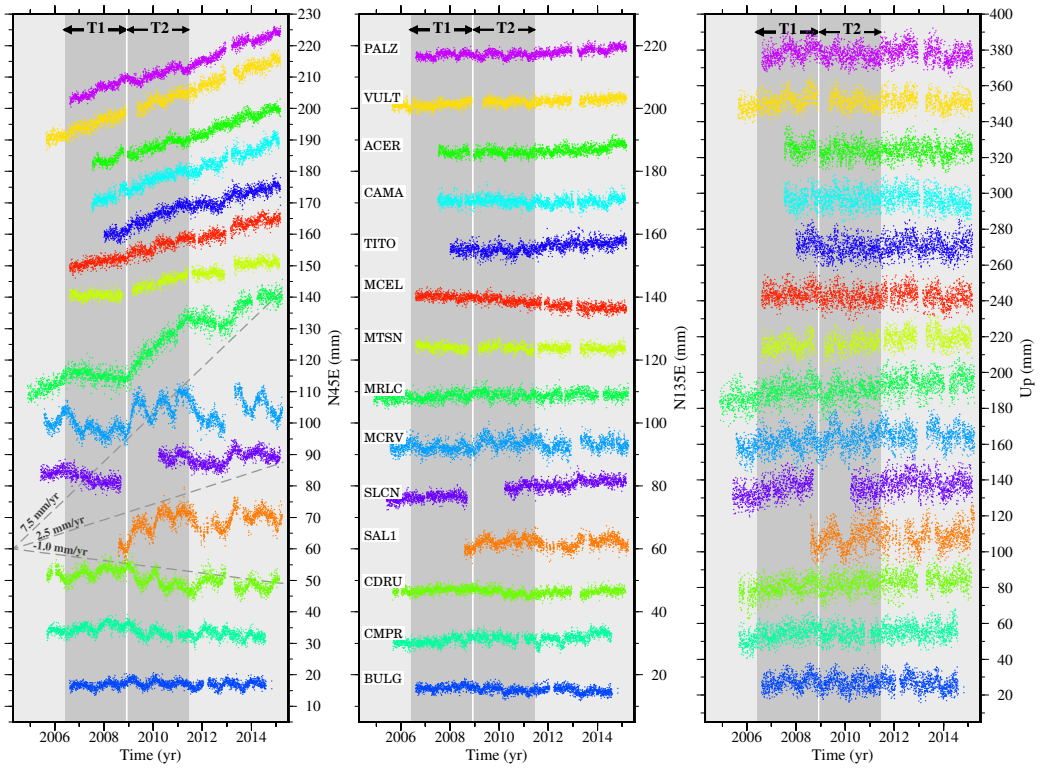

(e)

Figure 5.2: Observed (coloured dots) time-series at some GPS stations in the boxes outlined in the map in (a). Time-series in (b), (c), (d) and (e) refer respectively to sites in the blue, red, green and pink boxes. GPS sites are ordered from Tyrrhenian coast (bottom) toward Adriatic coast (top). Left: horizontal component projected along a direction perpendicular to the long-axis of the Apennines; centre: horizontal component projected along a direction parallel to the long-axis of the Apennines; right: vertical component. T1 and T2 are the two time intervals (evidenced by two vertical grey bars in each panel) during which velocities represented in Figure 5.4 are calculated. The green vertical dashed lines in (b) and (c) depict the 2009 L'Aquila earthquake epoch. Notice that these time-series are shown in a Tyrrhenian reference frame and the long-term trend have not been removed.

the following afterslip transient signal, the estimation of the deviation from the long-term trend for the GPS sites of Central Italy has been performed excluding a period of about four months after the earthquake, after which most of the afterslip signal should have extinguished (Cheloni et al., 2014; Gualandi et al., 2014).

The spatial distribution of the deviations from the long-term trend (Figure 5.4) clearly show shortening/extensional (T1/T2) episodes in the axial part of the Apennines. Stations affected by significant deviations from the long-term trend are not homogeneously distributed, but are preferentially located close to the limestone mountain ridges hosting large karstic aquifers (Allocca et al., 2007, 2014). Central Italy seems to be characterized by a closing/opening pattern around the main carbonate massifs, which displays an approximately radial pattern at the Northern and the Southern edges of the massif (Figure 5.4). For this reason the time-series of some sites in this area still show a significant multi-annual signal in the horizontal projection parallel to the Apennines (N115E direction), e.g. ALAT, ALRA, CERA, UNTR, VAGA (Figure 5.2b and 5.2c). In Southern Italy a clear closing/opening pattern is evident, mainly with respect to a NW-SE trend, near the main carbonate massifs, that acquire a more linear NW-SE trend in this area (Figure 5.2e). Finally stations far from calcareous lithologies (as the stations included in the green box in Figure 5.2a) do not display a clear evidence of such transient deformation in the horizontal components (Figure 5.2d).

In Figures 5.4a and b, the ellipse errors are not displayed for clarity. The mean uncertainty of the estimated rates is ≈ 0.5 mm/yr, therefore most of the rate values in the two time intervals results to be higher than the associated uncertainty (Figure 5.4c).

Figure 5.5 represents the East and North components and the related uncertainties of T1 (Figure 5.5a) and T2 (Figure 5.5b) rates along three transversal cross-sections of the Apennines. The rates along profiles A and C show remarkable opposite trends at the two sides of the main carbonate massifs with a decreasing magnitude toward the coasts, whereas a clear pattern is

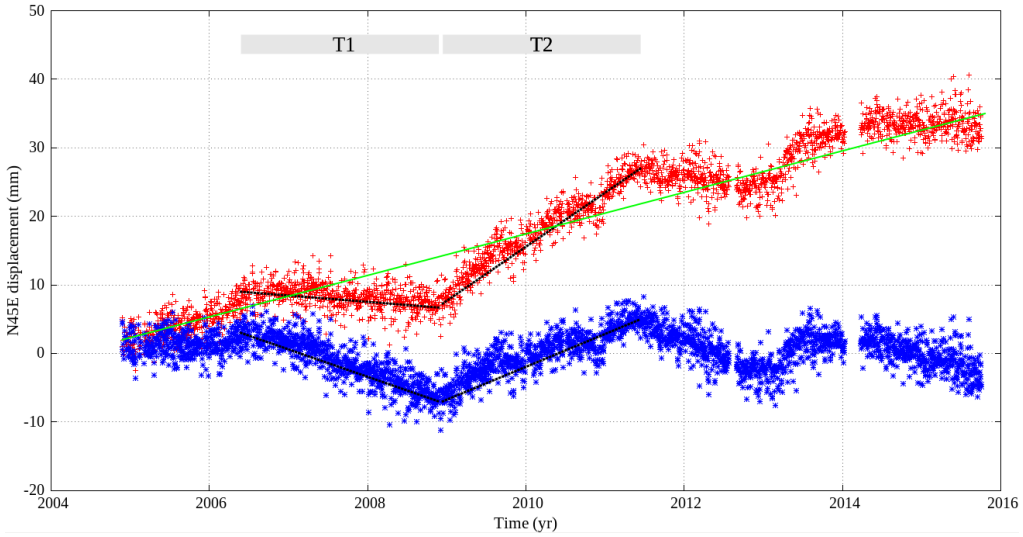

Figure 5.3: Example of the estimation of the deviations from the long-term trend in the two intervals T1 and T2. The red and blue points represent the time-series at MRLC site (see Figure 5.2e) respectively before and after removing the long-term trend (indicated as a green straight line). The black dashed lines outline the trends in the two selected intervals.

not highlighted along the profile B.

The simple spatial correlation we have highlighted with the surface lithology points to hydrological effects associated to varying water storage in the large karstic aquifers and rule out any contribution from processing artefacts. As a test, we have successfully checked that analogue multi-annual signal with comparable amplitude can be highlighted in time-series processed by other research groups with different software and methods (e.g. Gualandi et al. (2015) and Nevada Geodetic Laboratory products (`http://geodesy.unr.edu/NGLStationPages/GlobalStationList`)).

Vertical GPS time-series are characterized by a lower signal-to-noise ratio (see section 4.2.4) that obscures anomalous vertical multi-annual signals at most individual stations (Figure 5.2). More accurate results are obtained by stacking the daily values of detrended vertical time series for a large number of stations in the study area. The results (Figure 5.6) confirm the presence of a coherent annual seasonal signal (peak of uplift in summer and of subsidence

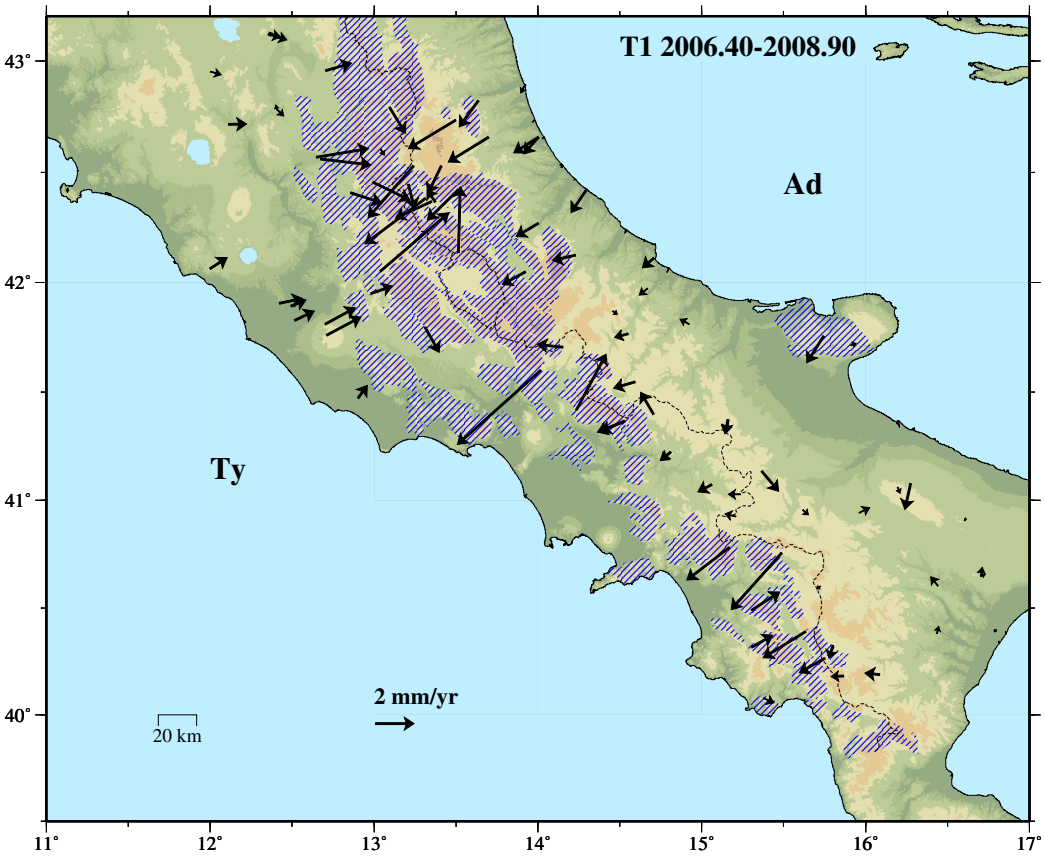

(a)

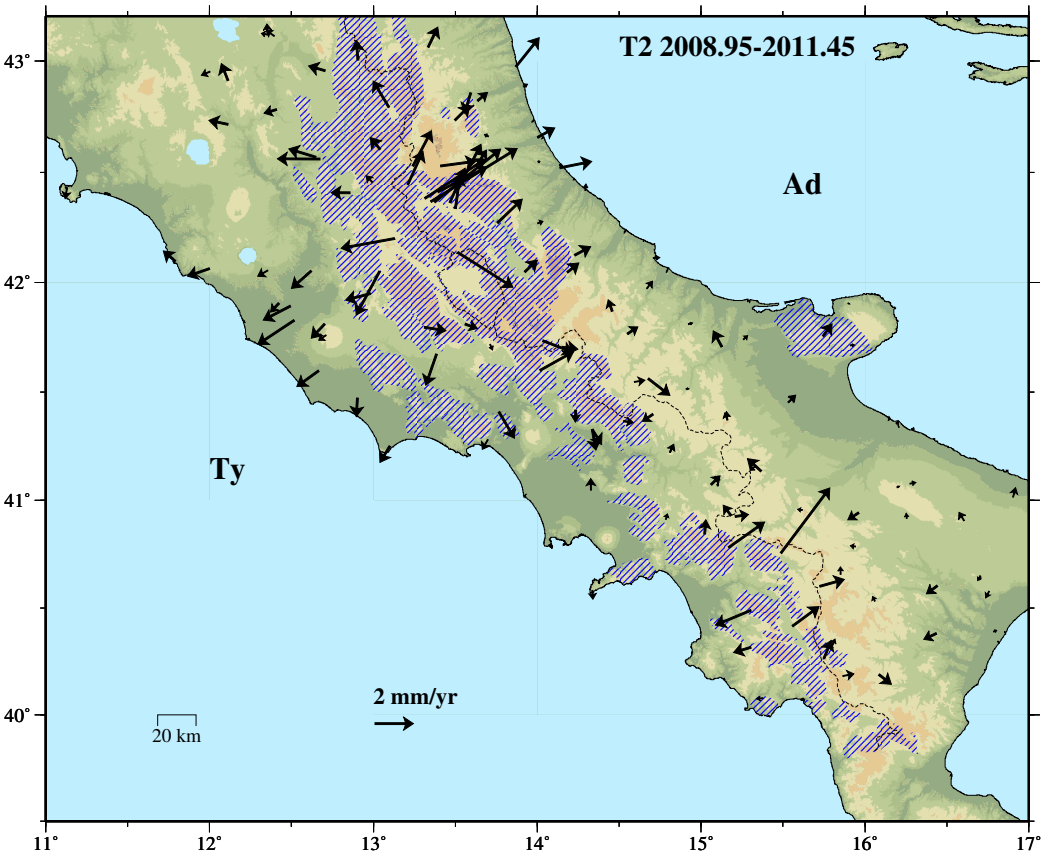

(b)

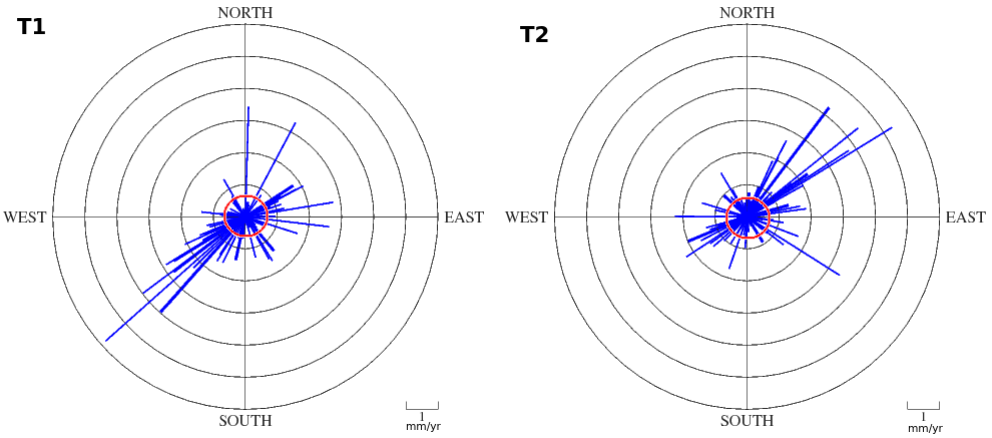

(c)

Figure 5.4: GPS velocities calculated as deviation from the long-term trend in T1 (a) and T2 (b) time intervals (see Figures 5.2 and 5.3). Rates are plotted only at sites that have at least 2 years of data in the selected time intervals. The black dashed line indicates the drainage divide and the blue striped areas outline the main carbonate aquifers. c) Rose diagram representation of the T1 and T2 rates, the red circles depicts a value of 0.5 mm/yr, that is approximately the average value of the estimated rates uncertainties.

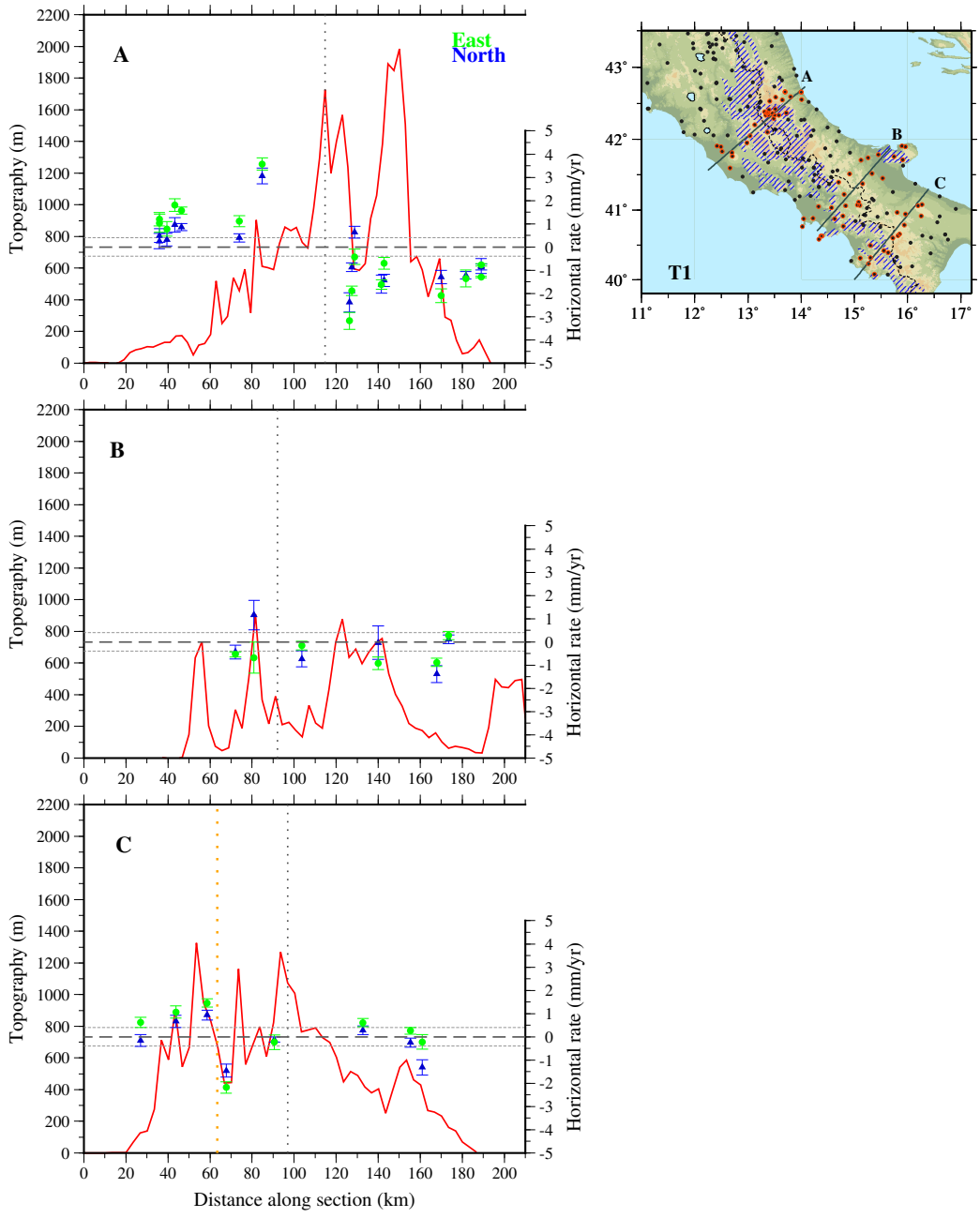
A
B
C
East
North
Topography (m)
Horizontal rate (mm/yr)
Distance along section (km)
T1

(a)

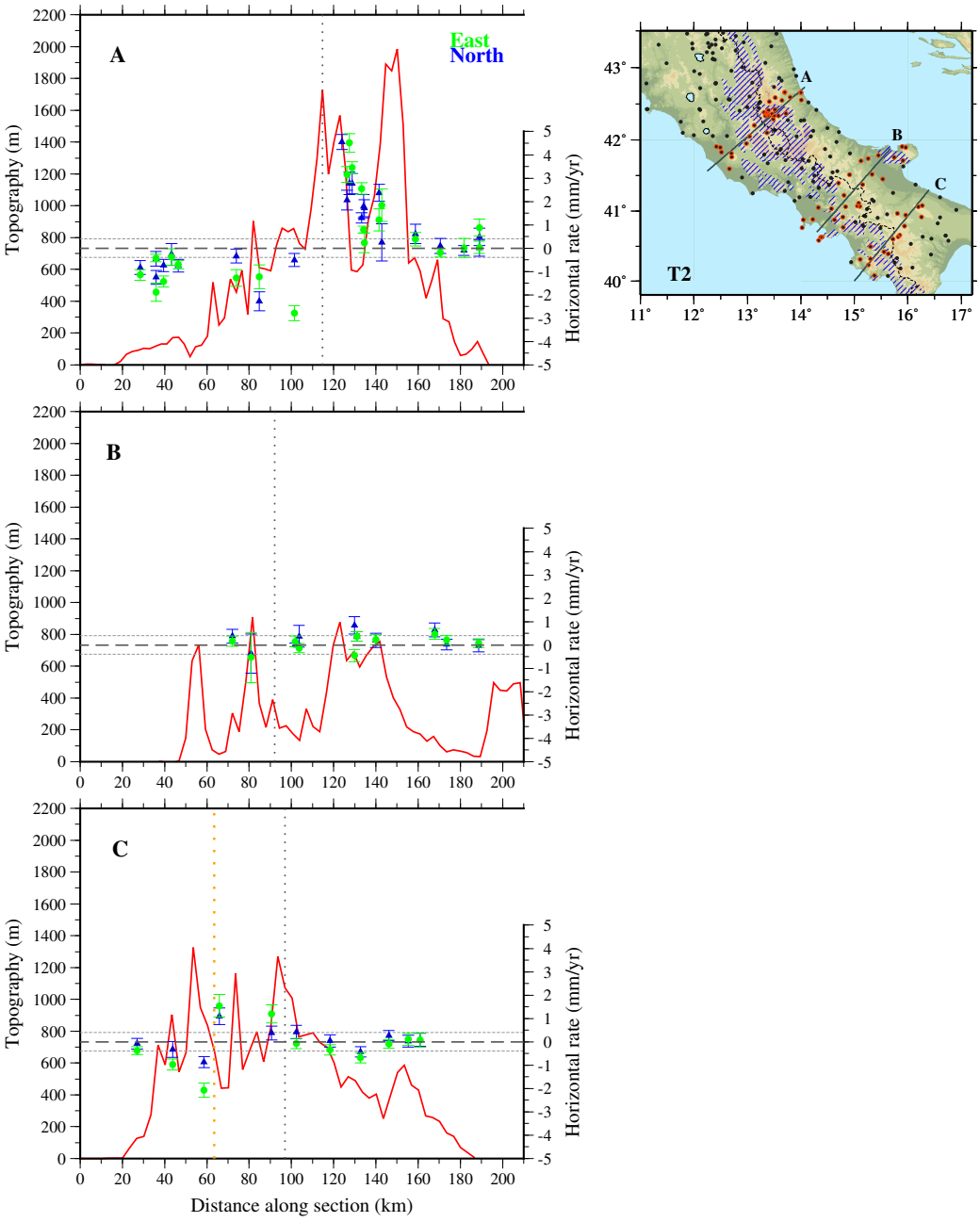

(b)

Figure 5.5: (Continued on the following page.)

Figure 5.5: Cross-section representations of the estimated East (green) and North (blue) component of the rates in T1 (a) and T2 (b) time intervals. Three cross-sections are depicted (gray segments in the inset) and the rates of stations in a range of 20-30 km (red open circles in the inset) are displayed in the plots. The horizontal dotted lines in the plots represent the mean uncertainty value ±0.5 mm/yr. The black vertical dotted lines indicate the positions of the drainage divide along the sections, that is where the transition between the two opposite horizontal trends occurs along section A, the orange dotted line indicates where the transition between the two opposite horizontal trends occurs along section C. The cross-section of the topography is plotted as a red line.

in winter), but also highlight, in both Central and South-Central areas, two peaks of upward motion in 2007 and 2012, clearly visible applying a low-pass 2.5-years Gaussian filter to the daily vertical stack. Notice that this vertical pattern is consistent everywhere, conversely to the horizontal signal that changes from one side of the Apennines to the other.
The maximum amplitude of the horizontal deformation at the sites near the carbonate massifs is about 1 cm (Figure 5.2b, 5.2c, 5.2e) and is therefore comparable to the maximum amplitude of the vertical displacement (Figure 5.6).

5.2 Hydrological data

5.2.1 Rainfall data

Annual precipitation in the study area ranges between 1000 and 2000 mm (at the highest elevations) and rainfall typically reaches a maximum during November and a minimum in July (Allocca et al., 2014) (see section 2.2.3). We have analysed rainfall time-series recorded at rain-gauges covering almost all the studied area. Here we show daily time-series of rainfall data from four rain-gauges that, for their record completeness and their position, can be assumed as indicative of the precipitation trend in the last decade in Central and South-Central Apennines. Two of them, Leonessa and Campoli Ap-

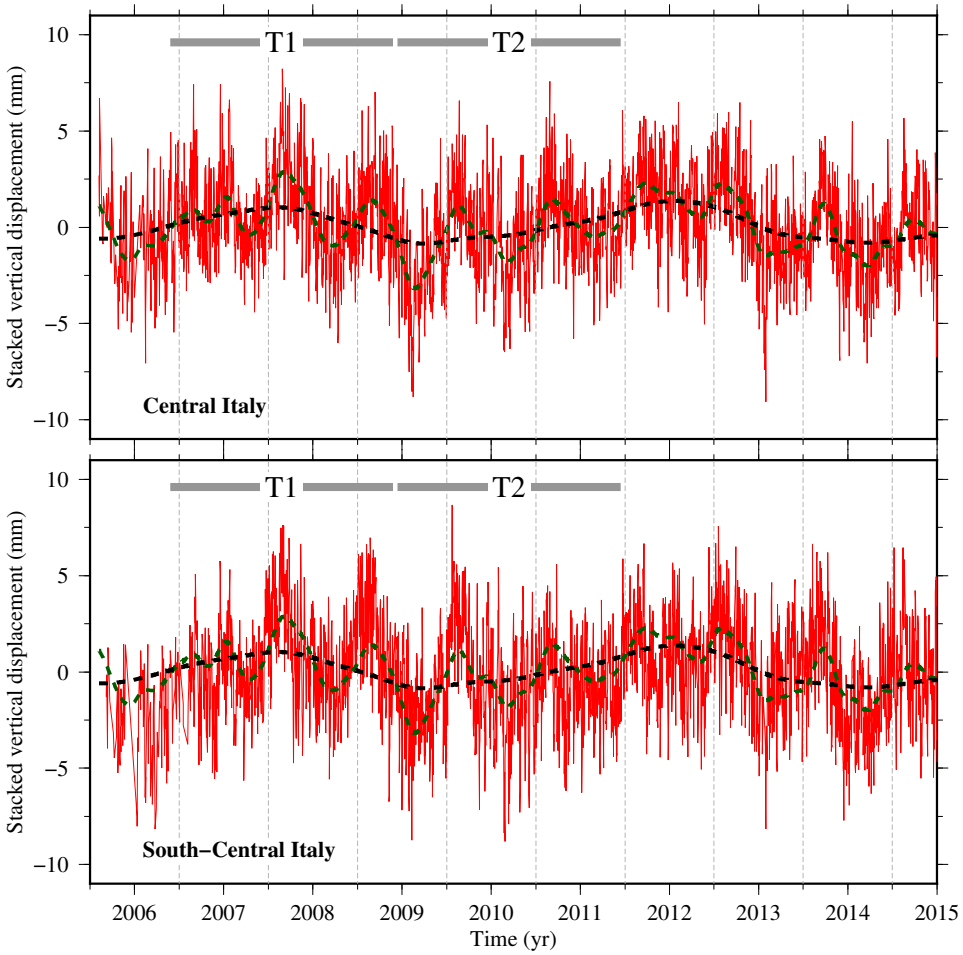

Figure 5.6: Vertical daily time-series obtained by stacking data from multiple stations (red line) for selected GPS sites in Central and South-Central Italy. The dashed lines represent a Gaussian filter to the stacked data with a width of, respectively, 6-months (dark green) and a 2.5-years (black). T1 and T2 time intervals, used as reference for the horizontal displacements, are also indicated.

Table 5.1: Characteristics of rain-gauge stations.

Name	Lon	Lat	Elevation (m a.s.l.)	Mean monthly rainfall (mm)	St. dev. (mm)
Leonessa	12.96	42.57	945	112	84
Campoli A.	13.68	41.74	679	109	75
Gioi Cilento	15.226	40.291	691	119	94
Senerchia	15.206	40.739	578	145	117

pennino, are located in Central Apennines and are managed by Ufficio Idrografico of Regione Lazio (`http://www.idrografico.roma.it/`). The others, Gioi Cilento and Senerchia, are located in Southern Apennines and are managed by Protezione Civile Regione Campania (`http://centrofunzionale.regione.campania.it/index.php/rete-di-monitoraggio`) (data updated until December 2014). The position of the rain gauge stations are shown in Figure 5.7 and their coordinates and main features are listed in Table 5.1. Rain-gauges time series are shown in Figure 5.8 as monthly discrete values and cumulative daily values. Detrended daily cumulative series (Roeloffs, 2001) are also shown in order to accentuate deviations relative to the long term (∼2003-2015) average trend. Precipitations are generally concentrated in November-February and show significant inter-seasonal variability and a visible multi-annual trend with significant reduction in drought years 2007-2008 and 2012. The previously defined T1 and T2 intervals correspond to periods of anomalously low (T1) or high (T2) precipitations.

5.2.2 Karst spring discharge

Daily discharge time-series of large karst springs in the Apennines give further evidence of interannual hydrological variability (Fiorillo et al., 2015b). Here the main features and discharge data of some of the main basal karst springs (see section 2.2.2 for the definition) of Central and South-Central Apennines are presented (Figures 5.7, 5.9 and A.2 and Table 5.2).

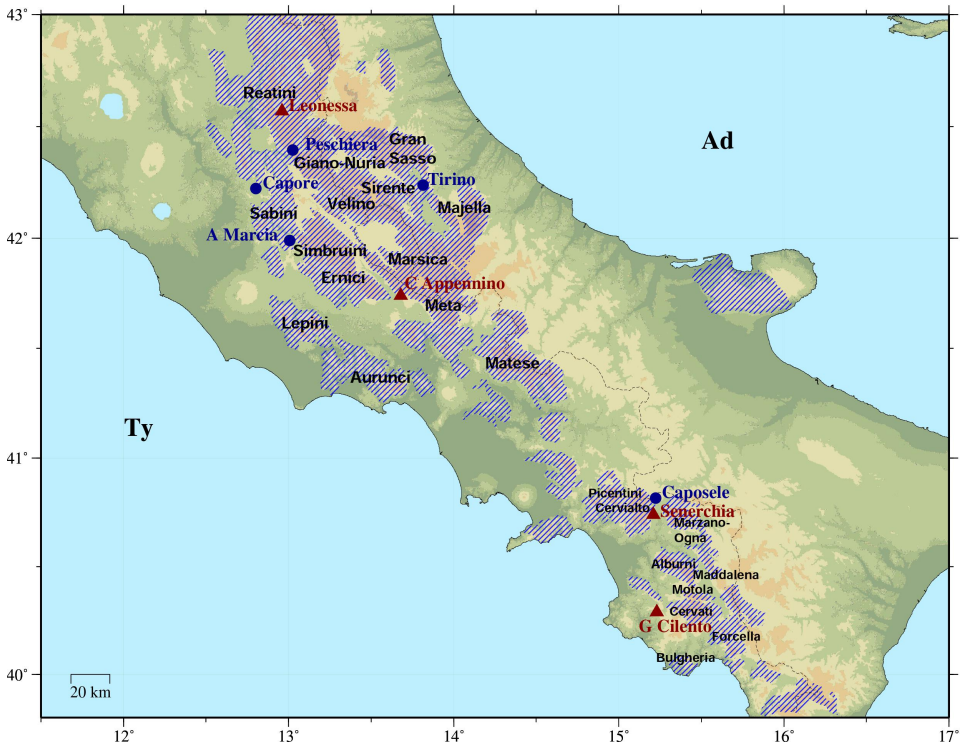

Figure 5.7: Position and name of rain-gauges (red triangles) and springs (blue circles) considered in this section. Blue striped areas show the position of the main carbonate massifs. The names of the main carbonate massifs are also indicated.

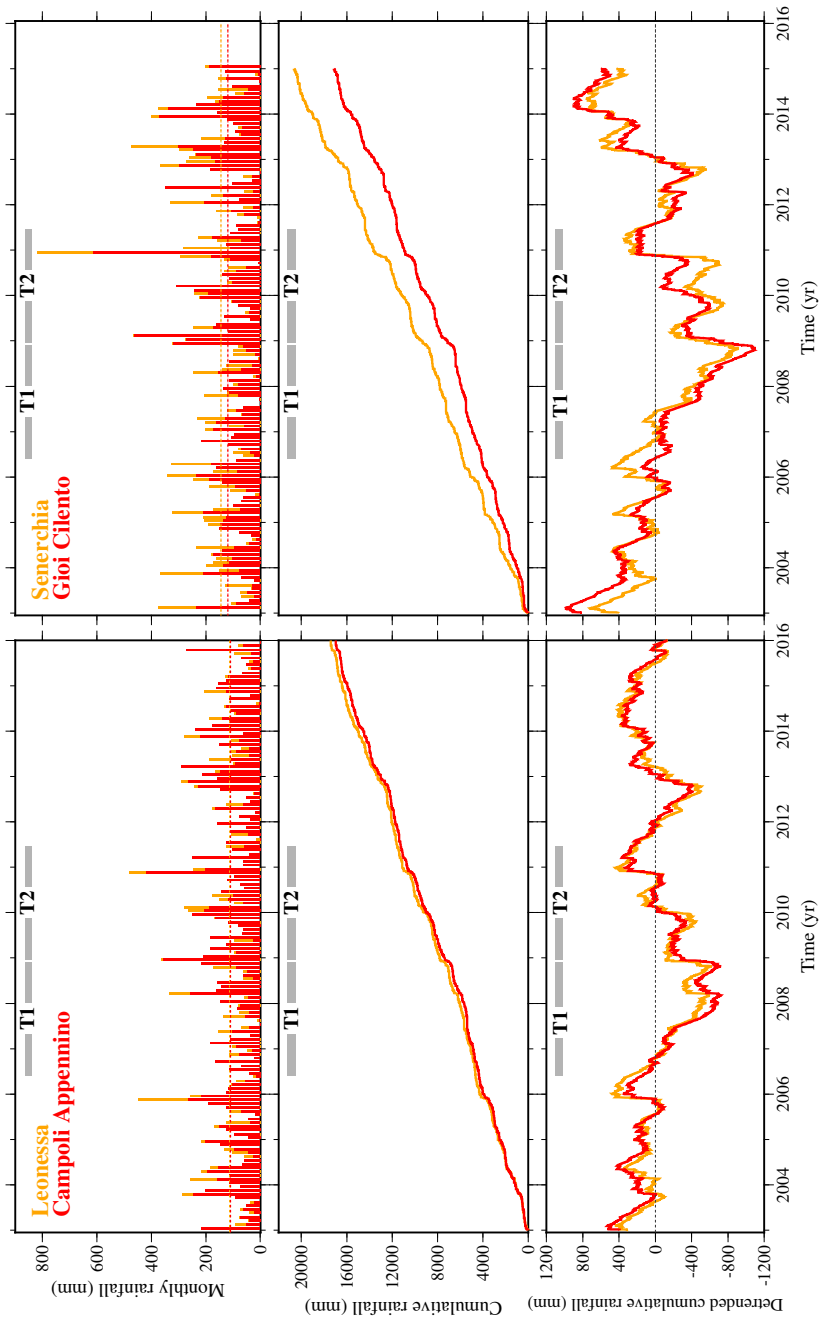

Figure 5.8: Rainfall data at the four selected rain-gauges in Central (left) and South-Central (right) Apennines (Figure 5.7) shown as cumulative monthly values (top), daily cumulative (centre) and daily de-trended cumulative (bottom) time-series. The orange/red horizontal dashed lines (top) depict the mean monthly cumulative values indicated in Table 5.1.

Table 5.2: Main features of the analysed karst springs.

Name	Acqua Marcia	Capore	Caposele	Peschiera	Tirino
Mean discharge (m^3/s)	5	4.7	4	18	6
Elevation (m a.s.l)	322-329	246	417	410	310-340
Catchment	Simbruini	Sabini	Picentini	Giano-Nuria Velino	Gran Sasso
Catchment area (km^2)	250	280	103	1000	700
Data series time interval	Jan 2007 -Dec 2014	Jan 2009 - Dec 2014	Jan 2005 -Sep 2015	Jan 2007 -Dec 2014	Jan 2000 -Dec 2010

Tirino springs

Tirino river springs are located at the south-eastern boundary of Gran Sasso aquifer and are fed by the main groundwater flow directed to this part of the aquifer (Amoruso et al., 2013; Fiorillo et al., 2015b). Discharge data (Servizio Idrografico e Mareografico Regione Abruzzo, `http://www.regione.abruzzo.it/xIdrografico/`) refer to a gauging station (Bussi Madonnina, Abruzzo) along the Tirino river, where waters coming from the main springs are collected. Since runoff contribution is very negligible in the Tirino catchment, the Tirino river is totally fed by the groundwater flow and the river flow corresponds to the spring discharge of the higher part of the Tirino valley (Amoruso et al., 2013; Fiorillo et al., 2015b). The gauging station on the Tirino river can be therefore used as representative of the main drainage of the Gran Sasso aquifer into the Tirino valley (Amoruso et al., 2013; Fiorillo et al., 2015b). The mean long-term discharge of the Tirino river calculated at the Bussi gauging station is about $6 m^3/s$ (Figure 5.9 and Table 5.2), and it shows scarce seasonal changes, but noticeable discharge variations on longer ($\sim$ 4 yr) periods (Boni et al., 2002). The drainage from the highway tunnels

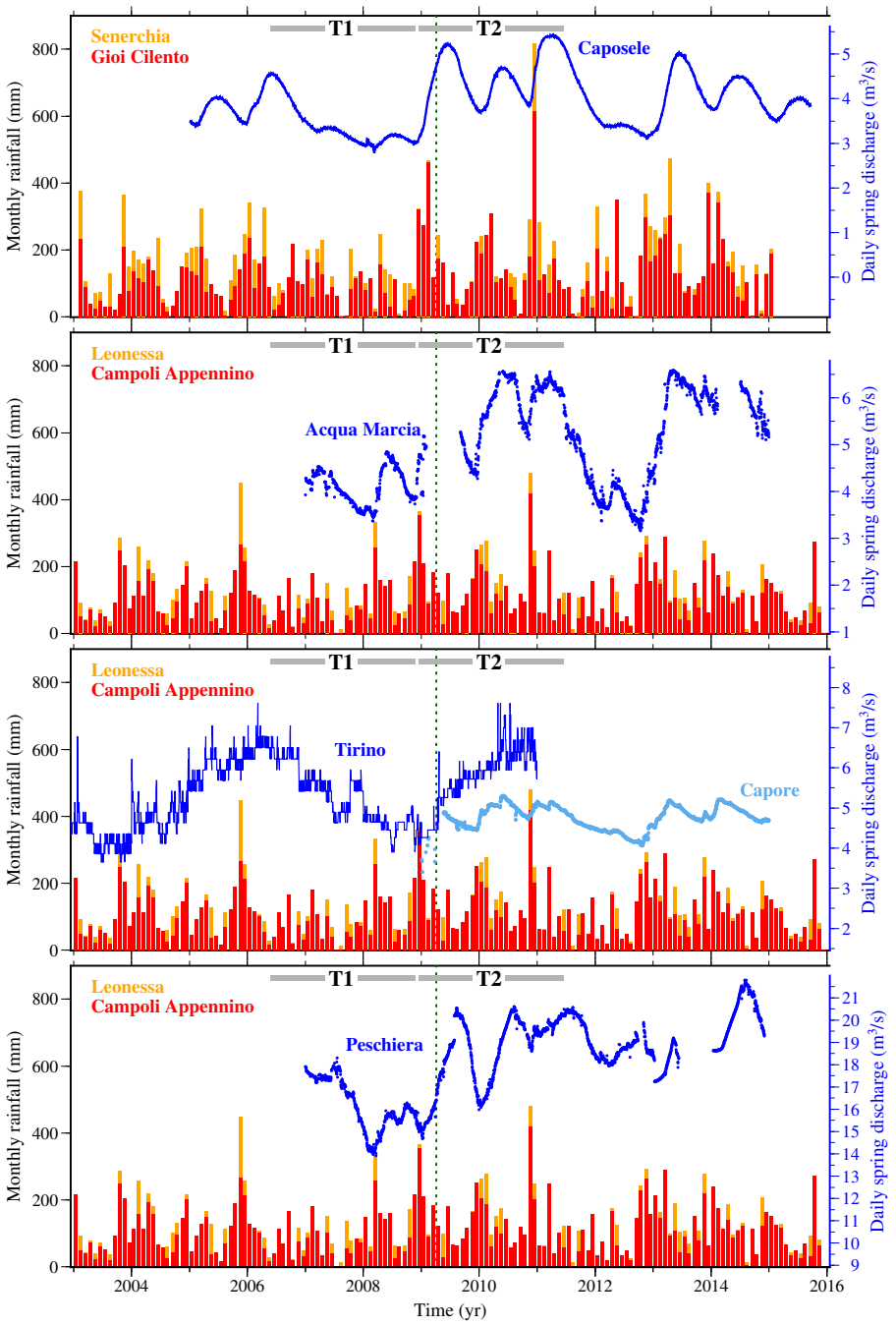

Figure 5.9: Discharge time-series of some of the main karst springs of Central and South-Central Apennines (blue/lightblue lines). Cumulative monthly rainfall recorded at rain-gauges in the two areas is also shown (red/orange bars). The green vertical dashed line indicate 2009 L'Aquila earthquake epoch.

in the 1980s affected the discharge of all Gran Sasso springs, including the Tirino ones. More recently, on April 6th 2009, L'Aquila earthquake caused a discharge increase along the boundary of the aquifer (Amoruso et al., 2011; Adinolfi Falcone et al., 2012; Galassi et al., 2014).

Peschiera springs

The Peschiera springs are situated in the Velino river valley at the northern boundary of the S. Vittorino Plain, in the province of Rieti (Lazio). They are fed by the regional recharge area of the Giano-Nuria-Velino Mts. aquifer (Petitta, 2009). With a mean discharge of about 18 m^3/s (Figure 5.9 and Table 5.2), they form the largest group of springs in the Central Apennines (Petitta, 2009; Civita and Fiorucci, 2010). Water is collected and diverted by ACEA S.p.a. to supply Rome, much of its hinterland and most of northern-middle Lazio. Discharge data are provided by ACEA S.p.a.. The Velino river valley is situated on an important tectonic line (Olevano-Antrodoco-Posta) which separates the two different geological domains of the Latium-Abruzzi carbonate Apennines and the Umbria-Marche-Sabina domain (Parotto and Pratulon, 1975; Civita and Fiorucci, 2010) (see section 2.2.2 and Figures 2.4 and A.2a).

Acqua Marcia springs

Acqua Marcia springs are composed by a number of springs located between 322 and 329 m a.s.l. at the northern end of the carbonate Simbruini Mts. aquifer (Figure 5.7). The recharge area occupies the north-western part of the hydrostructure for 250 km^2 (Fiorillo et al., 2015b). Discharge data, provided by ACEA S.p.a, show a mean discharge of about 5 m^3/s (Figure 5.9 and Table 5.2).

Le Capore springs

The Le Capore spring along the Farfa stream, near Frasso Sabino (Lazio), delivers about 5 m^3/s of water (Figure 5.9 and Table 5.2), that are totally tapped to supply Rome and the nearby area. Its recharge zone extends from the western to the southern Sabini Mts. (Figure 5.7) (Martarelli et al., 2008). Discharge data are provided by ACEA S.p.a..

Caposele springs

One of the largest karstic spring of Southern Italy is located near Caposele (Sorgente Sanità). This spring is located along the north-eastern boundary of the Picentini Mountains and is primarily fed by the Cervialto massif (Figure 5.7) (Celico and Civita, 1976) with a mean-annual discharge of about 4 m^3/s (Figure 5.9 and Table 5.2). Caposele can be considered the only spring draining the Cervialto mountain, since other springs have a considerably lower discharge (Fiorillo et al., 2015a). For this reason the spring discharge can be assumed as a robust regional indicator for the state of recharge of the large karstic aquifers in Southern Italy. Daily discharge for the Caposele spring are provided by the Aqueduct Company of Puglia (Acquedotto Pugliese S.p.A.) for the period from January 2005 till October 2015.

Main features of the springs hydrographs

The time-series of the karst springs discharge (also called hydrographs) depicted in Figure 5.9 show similar features. All the springs have high baseflow, providing water even in dry seasons, and periods of low and high flow are common to all the springs. The maximum discharge usually occurs some months after a period of heavy precipitation. Hydrographs are relatively smooth and not affected by single events of rainfall, responding to the precipitation cumulated during several months. These latter characteristics are particularly visible for Caposele and Acqua Marcia hydrographs and can be ascribed mainly to the prevalence of diffuse flow through fractures in the

discharge zone of the aquifer and to others factors, as described in section 2.2.3. Peschiera springs discharge data are quite noisy, but even in this case no sudden response to precipitation events and time lag between wet periods and spring discharge can be noticed. Capore springs show a slightly different behaviour, with a quicker response to rainfall which overlap the base flow component (see section 2.1). This could be ascribed to an higher contribution of the fast component of the flow on the discharge, as suggested for the similar case of the Torano spring (Mt. Matese, Northern Campania) by Fiorillo and Doglioni (2010). In general, variations among discharge of the different springs can be attributed to diversities in the local geological-hydrogeological asset, as the fracture and karstification degree, the amount of distribution of liquid and solid precipitation, which is a function of the ground elevation of spring catchments and the orographic conditions, and the size of the spring catchment area (Fiorillo et al., 2015b).
Spring discharge time series present a marked variation of annual signals corresponding to years of heavy and light rains, as remarked for rainfall time-series in the previous section. In particular the periods 2007-2008 (T1 period) and 2012 are characterized by limited precipitation and limited aquifers recharge which translate into the absence of the characteristic increase of discharge otherwise observed during years with more abundant precipitations. Aquifer recharge and abundant precipitation with delayed discharge increases characterize the following years (e.g. T2 period). These pluriannual variations common to all the springs are attributable to the climate influence at a larger scale than the aquifer ones (see section 2.2.3).

5.2.3 GRACE data (Gravity Recovery and Climate Experiment)

The Gravity Recovery and Climate Experiment (GRACE), launched in March 2002, provides monthly measurements of the Earth's gravity field (Tapley et al, 2004).
Taking into account the atmospheric circulation, changes in the gravity field

over the continent are mainly attributed (Wahr et al., 1998) to variations in terrestrial water storage (TWS), which is a vertically integrated measure of water storage including groundwater, soil moisture, surface water, snow water, and vegetation water. Other mass change sources in the study area, such as glacial isostatic adjustment (GIA) and ice loss, are probably not significant or of much lower magnitude (e.g. Peltier, 2004). GRACE gravity data can be therefore used to infer temporal variations in TWS and to estimate the response of the solid Earth to such a loading.

Monthly measurements of the Earth's gravity field are usually translated into mass in units of equivalent water height (EWH). In this work, estimates of EWH have been obtained from the land monthly mass grids (GRCTellus Land, Swenson (2012)) calculated from the RL05 spherical harmonic solution and available at `http://grace.jpl.nasa.gov`, supported by the NASA MEaSUREs Program. We calculated solutions from the three different processing centres of the official GRACE Science Data System: JPL (Jet Propulsion Laboratory; RL05.DSTvSCS1411 solution), GFZ (GeoforschungsZentrum Potsdam; RL05.DSTvSCS1409 solution) and CRS (Center for Space Research at University of Texas, Austin; RL05.DSTvSCS1409 solution).

We extracted and averaged values from the monthly mass grids for the two areas of interest for the present study, considering grid locations within 400 km from the point 15.6°E 40.5°N for the South-Central Italy and from the point 13.5°E 42°N for the Central Italy. Data covariance between nearby grid points (Swenson and Wahr, 2006) have been taken into account to estimate TWS uncertainties using de-correlation lengths of 300 and 100 km for measurement and leakage errors respectively, following Landerer and Swenson (2012). To suppress errors at short spatial wavelengths (Wahr et al., 1998) a Gaussian smoothing function with a 300km half-width is applied to GRCTellus Land (Swenson, 2012).

The solutions from the three data centres are represented in Figure 5.10 from April 2002 to April 2015 as anomalies with respect to the 2004-2010 average. The three time-series are in very good agreement between $\sim$ 2004 and 2011,

whereas they are more scattered in the remaining time. This is probably due to the presence of an high number of data gaps before the year 2003 and after 2011, when active 'battery management' of GRACE satellites started (Jean et al., 2015). In order to improve the solution, we generated a combined solution (grey dashed line in Figure 5.10) by calculating the arithmetic mean of the three time-series (Sakumura et al., 2014; Jean et al., 2015). The differences between results of Central and South-Central Italy are small and lie inside the data uncertainties ($\approx 25 \div 30$ mm).

The $\sim$300 km resolution of the GRACE solution does not allows to spatially define the source of mass variability at the scale of the study area and, likely, the contribution from adjacent offshore regions, leaking into our results, significantly influences the estimates of EWH. The 300 km scale is in fact large enough for the GRACE mass solution to be an average of the rapidly changing TWS in the Apennines and the more stable mass anomalies in the nearby areas, such as the Balkans (Wahr et al., 1998). However we have analysed these data since they provide useful informations about the temporal variability of the TWS and about the influence of long wavelength changes of the TWS on the observed GPS signal (see sections 5.3 and 6.1). In fact, as introduced in section 2.2.3, European climate is likely influenced by large-scale climatic phenomena, such as North Atlantic Oscillation (NAO), which affect the hydrological cycle of the karst aquifers (De Vita et al., 2012). GRACE TWS time-series (Figure 5.10) show that higher annual TWS values generally occur in December-February and, interestingly, the drought years highlighted in rainfall and spring discharge time-series (i.e. 2007-2008 and 2012) present smaller TWS peaks in winter months than in average. T1 and T2 intervals correspond to TWS values respectively significantly below and above the long term average and, consistently with rainfall and spring discharge data, indicate a significant multi-annual variation of surface water and groundwater storage (see also Figure 5.13).

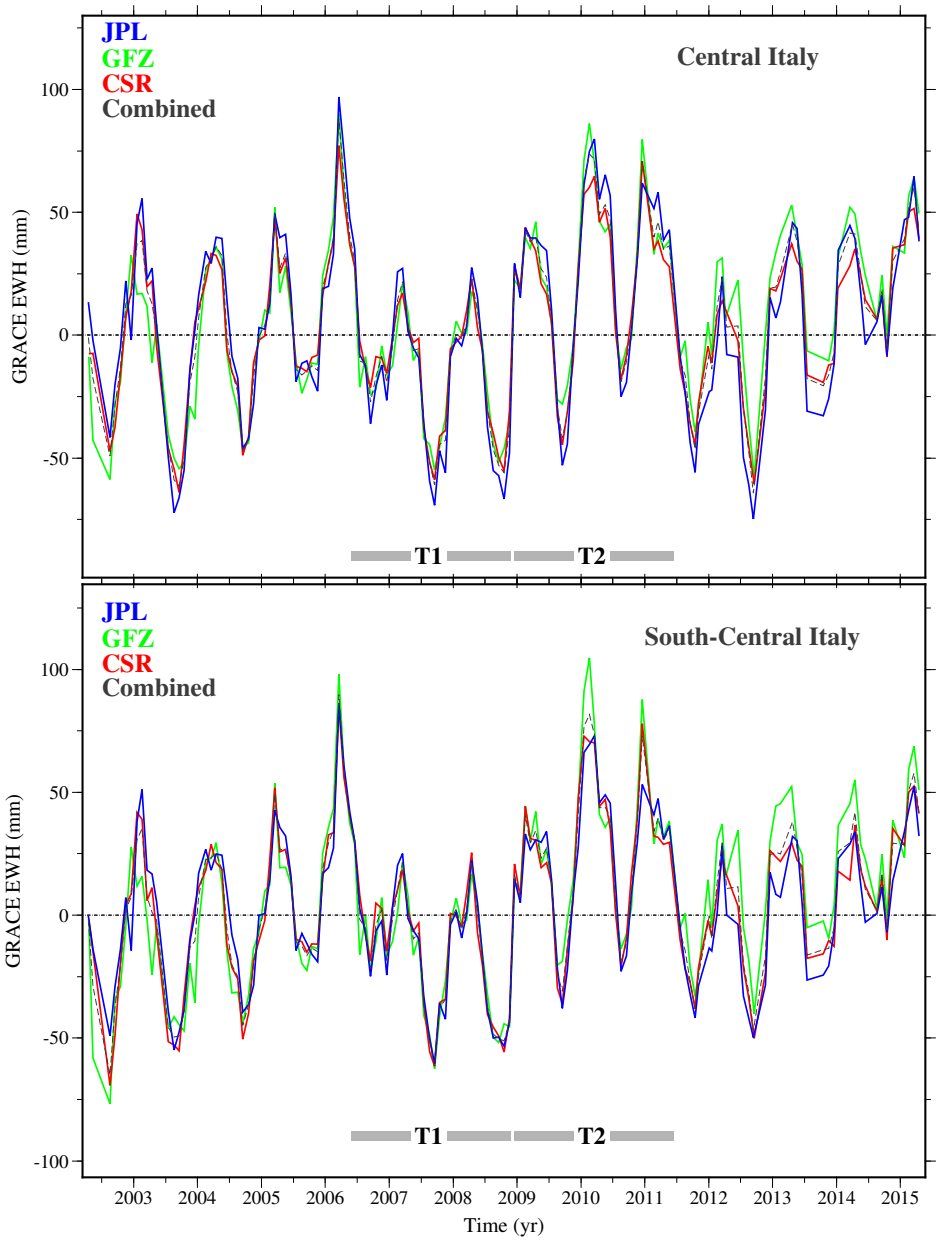

Figure 5.10: GRACE equivalent water height time-series as fluctuations with respect to the long term average. Solutions from three institutes are represented (JPL, GFZ and CSR) together with the combined averaged solution (grey dashed line).

5.3 Comparison between GPS and hydrological observations

Previous analysis have shown that hydrological (rainfall, spring discharge and GRACE TWS) time-series are characterized by significant variability of the seasonal signals and departures from linear trends. A characteristic time shift of several months can be depicted between rainfall, and therefore water storage (GRACE), that show positive peaks in autumn-winter, and discharge of several main springs, that shows positive peaks in spring (Figures 5.9 and 5.11).

The temporal patterns of the hydrological time-series appear to be strictly correlated with the observed GPS horizontal and vertical displacements. This can be stressed in Figure 5.11 where horizontal GPS time-series are compared to rainfall, spring discharge and equivalent water height GRACE data. In particular we observe a strong correlation between GPS horizontal time series at stations close to karstic aquifers and discharge from the main springs. High correlation (correlation values of about 0.8, see Appendix B) is observed not only at a local scale, e.g. between Acqua Marcia spring and OCRA station (Figure 5.11b, inter-distance of $\sim$ 8 km) or between Caposele spring and MCRV station (Figure 5.11c, inter-distance of $\sim$ 6 km), but also between spring discharge and displacements at GPS sites located tens of kilometres away, e.g. between Acqua Marcia spring and CERA site (Figure 5.11b) or between Caposele spring and SAL1 site (Figure 5.11c).

Sites located in the near field of L'Aquila earthquake area (e.g. AQUI, INGP, ROPI, PAGA, CONI, CATO and TOSS in Figures 5.2b and 5.11a) show a trend analogous to the sites not affected by the earthquake (such as ALRA, BSSO, RNI2 in Figure 5.2c or sites in South-Central Apennines MCRV, CDRU, SAL1, CMPR in Figures 5.2e and 5.11c), with similar periods of positive and negative deviation from the long term trend, except during the months following the mainshock, when they are strongly affected by the afterslip signal (e.g. Cheloni et al., 2014; Gualandi et al., 2014). The latter

has caused a transient displacement in the SW direction in the sites located on the hanging wall of the fault (Figure A.4), such as AQUI, INGP, ROPI, PAGA and CONI, which, in the first months after the mainshock, exhibit an anomalous trend with respect to other GPS sites located in the "Adriatic side", such as ALRA, CATO, CERA, RNI2, MCRV, MRLC and TOSS.

In order to clarify the relationship between the observed horizontal deformation and spring discharge, we chose to focus first on a simpler tectonic area located in South-Central Apennines where no relatively large earthquakes have occurred since 1990 (Basilicata - Potentino earthquake M_w 5.8). There, we calculated the dilatational strain (Figure 5.12) in a polygon defined by stations CDRU, CMPR, SAL1 and SLCN, that are located between 36 and 58 km from the Caposele spring (Figure A.3b). By comparing the detrended strain and the Caposele spring discharge time-series a similar trend is highlighted, that suggests a regional character of the multi-annual discharge observed at the Caposele spring. In particular, negative precipitation trends and aquifer exhaustion are associated with reduced or negative dilatational strain (i.e. compression) and upward motion (T1), whereas episodes of increasing rainfall (aquifer recharge) are associated to enhanced dilatation and downward motion (T2).

Vertical displacements appear to be well correlated with GRACE TWS data, showing subsidence in high water storage periods (autumn-winter), and uplift in summer. In order to compare vertical GPS displacements and monthly GRACE TWS data, we have computed monthly averages of the daily vertical GPS stacked position centred on the date of GRACE acquisitions. The uncertainty has been estimated from the standard deviation of the monthly average (Figure 5.13). We have observed that the two sets of measurements present a remarkable inverse correlation (-0.4 $\div$ -0.7, see Appendix B), especially in the 2005-2011 time window, both in Central and South-Central areas (notice reverse scale for GRACE data in Figure 5.13), with a limited time lag (GPS vertical stack anticipates GRACE of 0 $\div$ 1

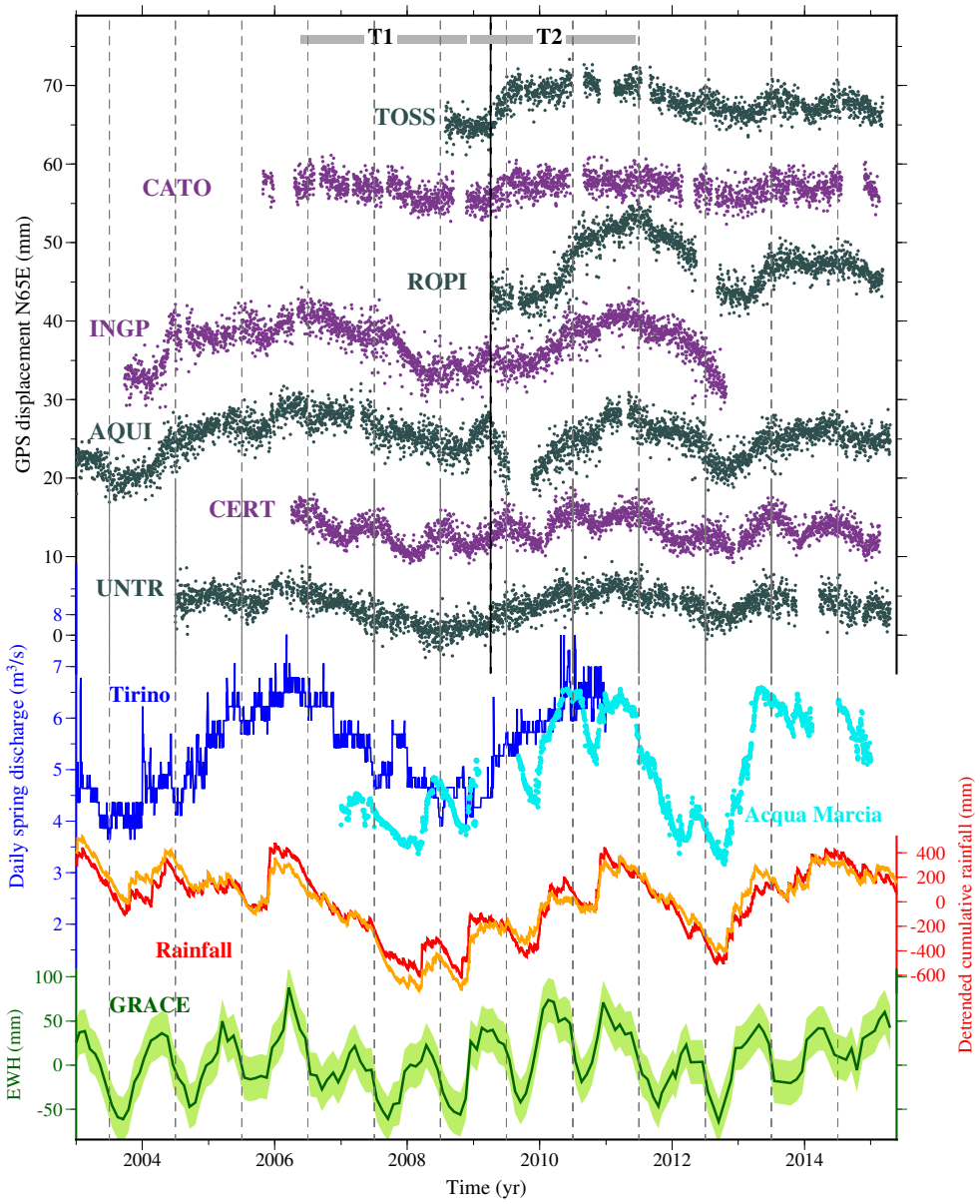
T1
T2
TOSS
CATO
ROPI
INGP
AQUI
CERT
UNTR
GPS displacement N65E (mm)
Tirino
Acqua Marcia
Daily spring discharge (m³/s)
Rainfall
Detrended cumulative rainfall (mm)
GRACE
EWH (mm)
Time (yr)

(a)

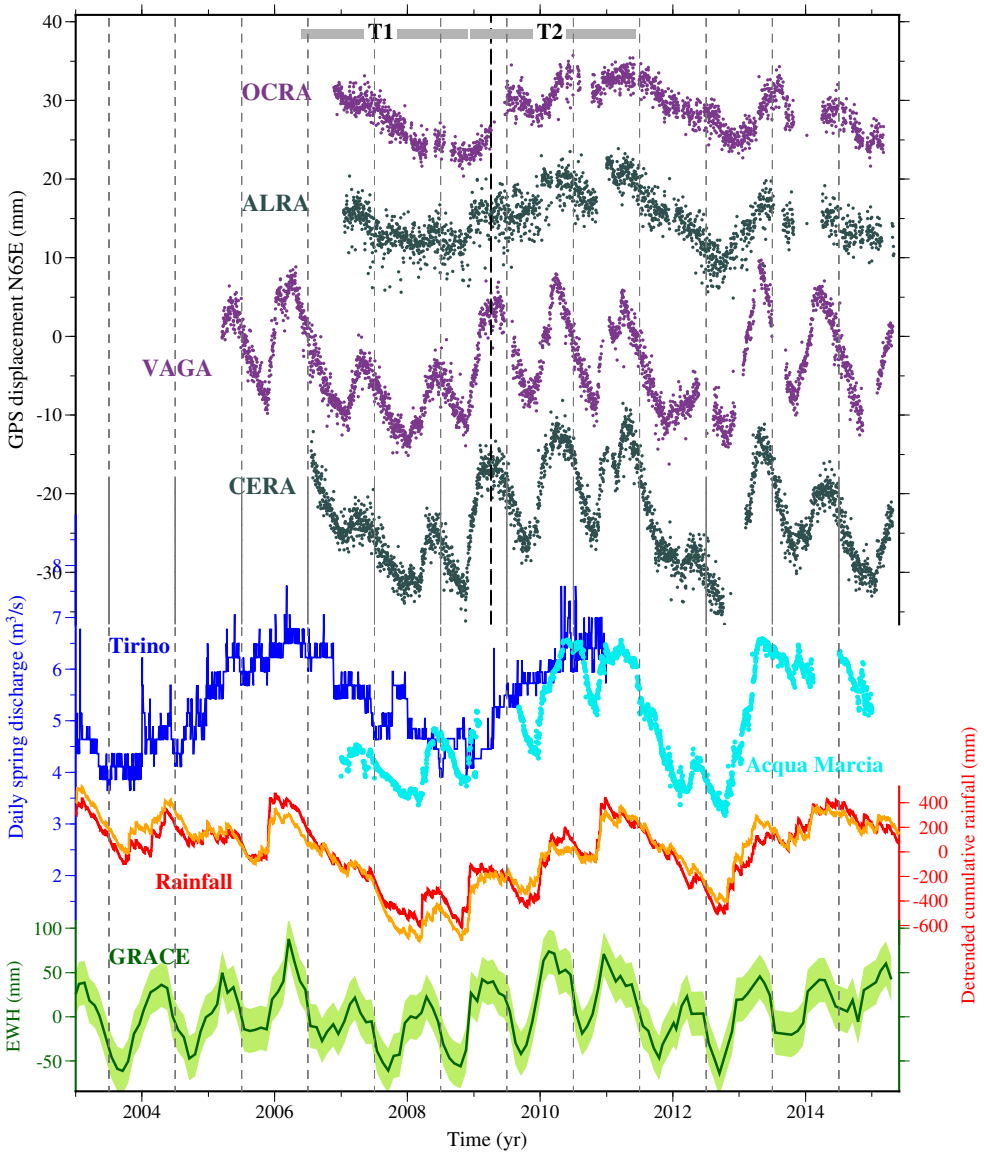
T1
T2
OCRA
ALRA
VAGA
CERA
GPS displacement N65E (mm)
Tirino
Acqua Marcia
Daily spring discharge (m³/s)
Rainfall
Detrended cumulative rainfall (mm)
GRACE
EWH (mm)
Time (yr)
2004
2006
2008
2010
2012
2014

(b)

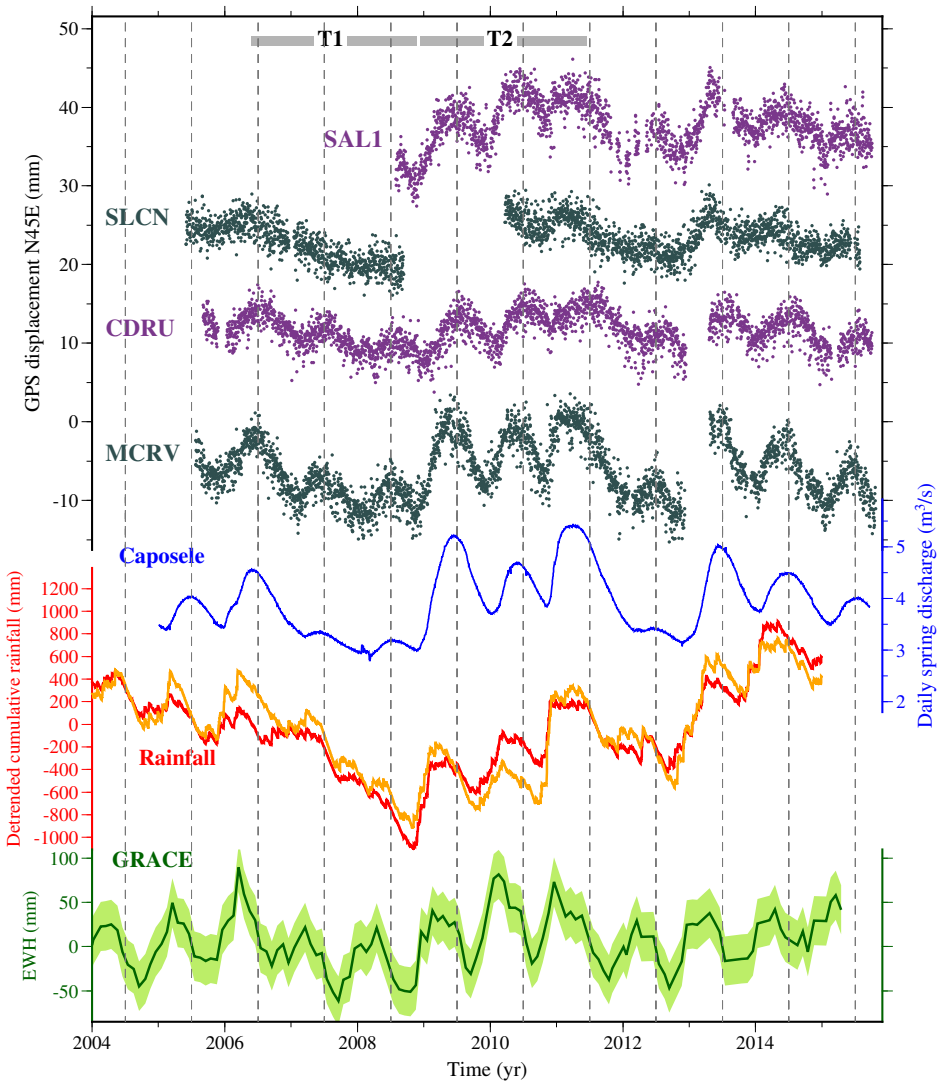

(c)

Figure 5.11: (Continued on the following page.)

Figure 5.11: Comparison between the GPS time-series and rainfall, spring discharge and equivalent water height GRACE data. GPS time-series (purple and slate-grey dots) represent the detrended horizontal component along the direction perpendicular to the Apennines (N65E and N45E) at some sites in the blue (a), red (b) and pink (c) box in Figure 5.2a (cfr Figure 5.2b,c and e). Note that the vertical axes for UNTR and CERT in (a), OCRA and VAGA in (b) and CDRU in (c) is inverted for clarity. Daily precipitation data at Leonessa, Campoli Appennino (respectively orange and red line in (a) and (b)), Senerchia and Montesano Terme (respectively orange and red line in (c)) rain-gauges are represented as de-trended cumulative rainfall (see Figure 5.8). The cyan and blue lines show daily discharge data of Acqua Marcia, Tirino and Caposele springs. Monthly data of equivalent water height from GRACE satellite represent averages over the areas under examination (green line ± uncertainty). The black vertical line in (a) and (b) depicts L'Aquila earthquake epoch.

month, see Appendix B). The worse correlation in the last ∼4 years is probably related to the decreasing GRACE data quality after 2011 (Jean et al., 2015), as we discussed in section 5.2.3.
It must be noticed that the GRACE measurements and the GPS vertical stack data (calculated from stations with long time series distributed on a spatial scale much wider than the karst aquifers) are likely to be due to a larger spatial scale process with respect to the horizontal signal. The latter in fact has been observed close to karst aquifers and quickly decays with distance from the karst massifs (Figure 5.2). The vertical component thus likely reflects the regional response of the crust to variation of TWS at least at the scale of GRACE resolution (300 km).

Additional insights about the relation between observed GPS displacements and hydrological data are provided by cross-correlation analysis. The latter show that high cross correlations between horizontal displacements and spring discharge are associated to lag times of ± 2 months (Figure B.1), possibly indicating minor temporal variability of the ground deformation associated to spring discharge. Further details about the cross-correlation analysis are given in Appendix B.

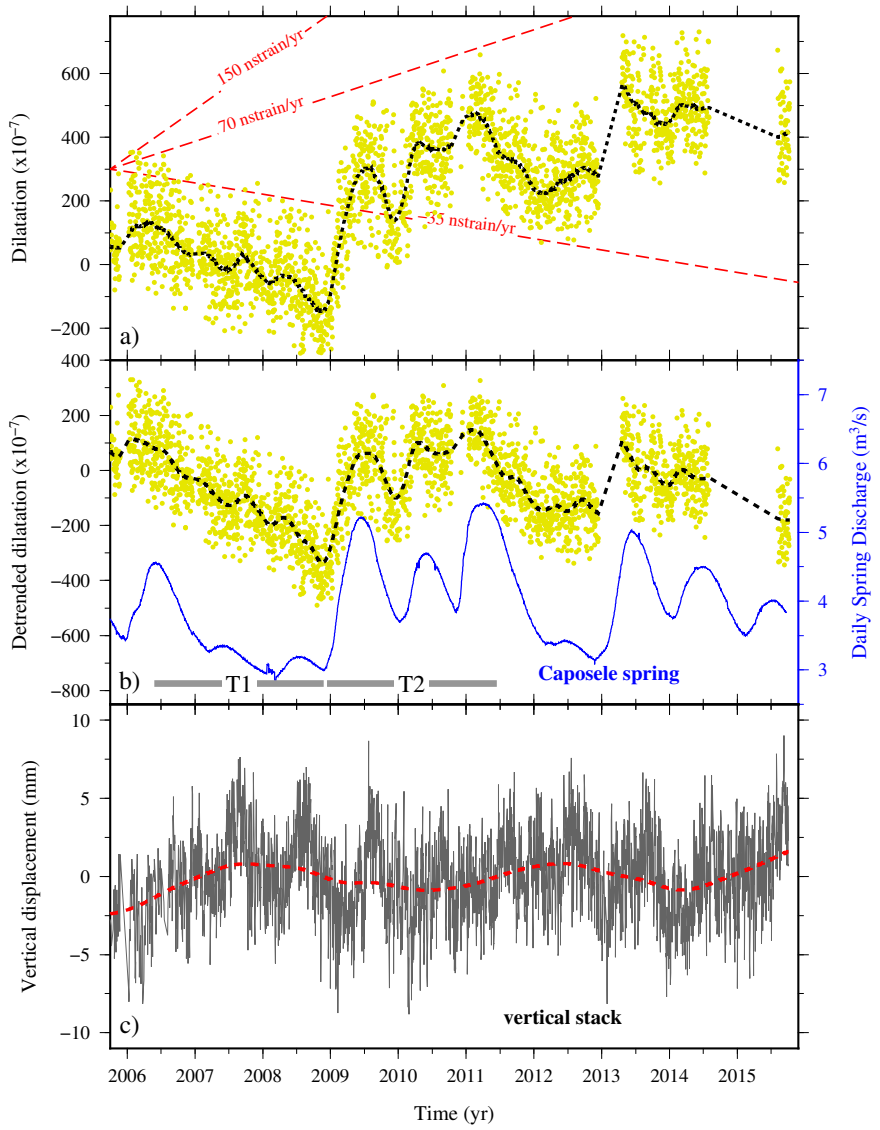

Figure 5.12: Dilatation time-series. a) Daily dilatation time-series calculated in the polygon represented in Figure A.3b (yellow dots) and its 6-month Gaussian filter (black dashed line). b) Detrended dilatation time-series and daily discharge data of the Caposele spring (blue line). c) Vertical daily time-series obtained by stacking data from multiple stations (gray line) and its 2.5-years Gaussian filter (red dashed line).

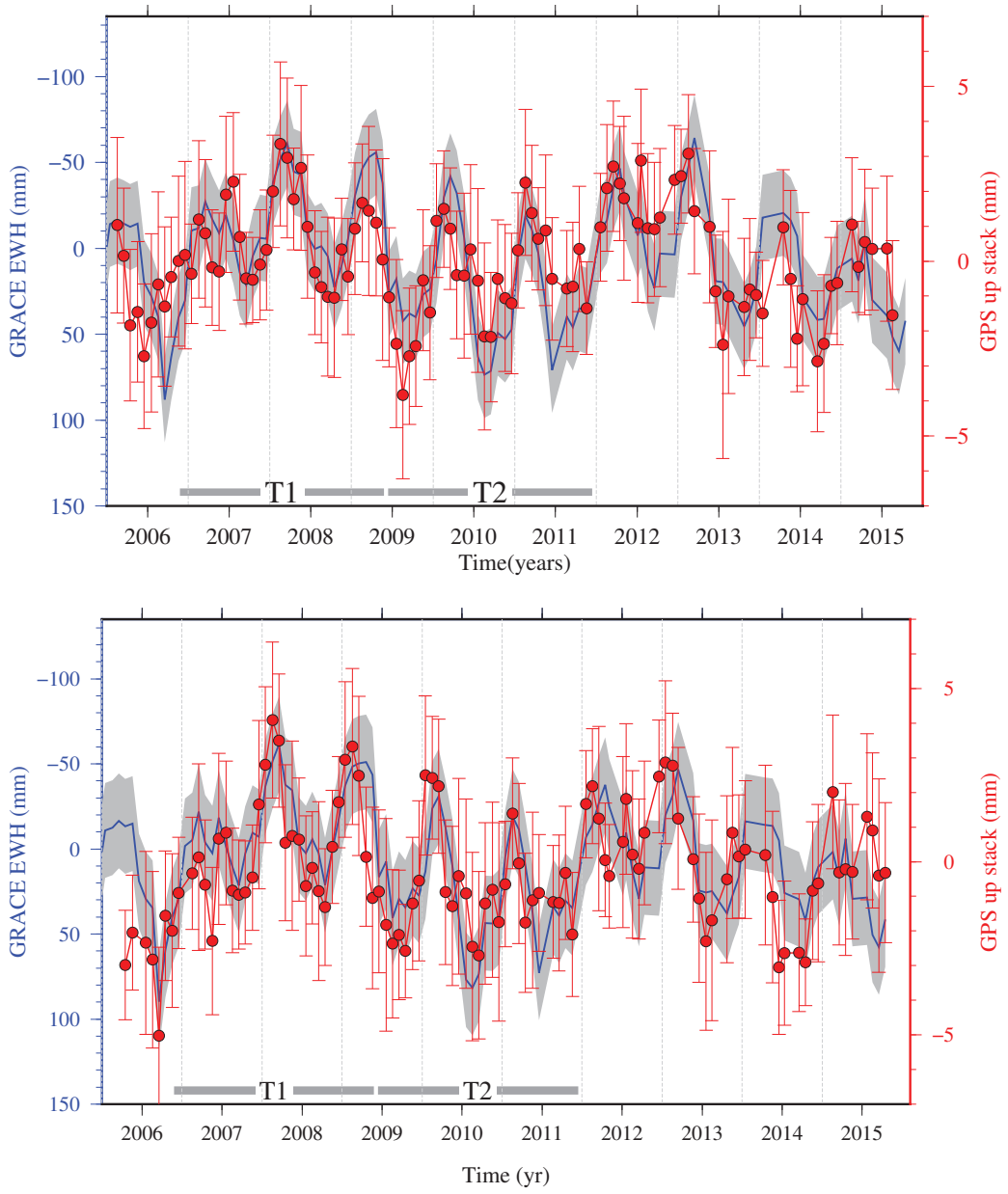

Figure 5.13: Comparison between monthly equivalent water height GRACE data (blue line ± uncertainty) and stacked vertical GPS displacements sampled at the same epochs (red circles ± uncertainty). Top: Central Italy; bottom: South-Central Italy. Notice that the vertical axis is inverted for the GRACE plot. The GPS sites we used to compute the stacked time-series are: for Central Italy, ALRA, AQUI, BARS, BLRA, CAOC, CAPE, CATO, CERA, CERT, CONI, GUAR, INFN, INGR, LEOF, LNSS, M0SE, MORO, MTTO, OCRA, OLGI, OVRA, RENO, RIET, ROMA, ROPI, RSTO, SCRA, SMRA, TERI, TOSS, UNTR, VAGA; for South-Central Italy, ACER, AV04, BULG, CAMA, CAS1, CDRU, CMPR, MCRV, MRLC, PALZ, SLCN, TITO, SAL1, VULT

In conclusion, a deep examination of the yearly and multi-annual peaks and phases for the different observables (horizontal and vertical GPS, rainfall, spring discharge and GRACE TWS variations) reveals a different behaviour and phase for horizontal and vertical deformations: 1) peaks in outward horizontal GPS displacements with respect to the Apennines axis and dilatation strain (Figures 5.11 and 5.12) occur in late spring-summer and are closely correlated with discharge of the main karst springs; 2) vertical GPS motion appears to be inversely correlated and approximately in phase with TWS variations recorded by GRACE with peak values (negative GPS, postive TWS) displacements occurring in late fall-winter months (Figure 5.13).

Chapter 6

Analysis of the transient deformation of the Apennines: models

In this section we firstly investigate the processes that could have a role in causing the transient deformation we have highlighted in Central and South-Central Apennines. The latter embraces a wide area and involves different phenomena and local specificities, therefore a completely realistic modelization would be extremely difficult, if achievable. Our purpose is to bring out the processes that could explain the main characteristics of the observed signal that show common features in the whole studied area. We employ three different models (described in chapter 3), i.e. surface loading over an elastic layered Earth, tensile dislocations within an elastic half-space and effective stress variations due to water table increase inside an aquifer.
Finally we examine a further possible source of transient deformation in Central Apennines, i.e. viscoelastic postseismic deformation of L'Aquila 2009 earthquake, focusing on the difficulty of detecting small tectonic signals from moderate earthquakes in areas affected by significant non-tectonic deformations.

6.1 Elastic response to hydrological loading

Several previous works have related the geodetic observations of hydrological-related deformations to the response to surface loading over an elastic medium (e.g. Amos et al., 2014; Borsa et al., 2014; Chanard et al., 2014) (see chapter 1). We firstly test if this process could be able to explain both the horizontal and vertical deformation observed in the Apennines.

6.1.1 Localized load model

In our case, the observed spatial pattern of horizontal deformation (Figure 5.4) suggests that the area of load accumulation should correspond to carbonate aquifers, that are able to store huge quantities of water (Fiorillo et al., 2015b).
In order to test the loading model, we have therefore assigned a time-varying load to an area that roughly corresponds to Central and South-Central carbonate massifs of the Apennines (Figure 6.1). A spatially uniform time-dependent load has been imposed by scaling its magnitude to the monthly GRACE equivalent water height time-series, taken as a proxy for the temporal variation of the water storage. We have fixed a maximum water load variation of $\pm$1000 mm, which is higher than realistic monthly cumulative values of rainfall in these areas (Figure 5.8). We are therefore looking at an upper bound model. We have computed the surface displacements induced by loading by using the Matlab script by Chanard et al. (2014) (`http://www.tectonics.caltech.edu/resources`) which considers a layered non-rotating spherical Earth model (Farrell, 1972; Guo et al., 2004) based on the Preliminary Reference Earth Model (Dziewonski and Anderson, 1981) and a continental crust based on the CRUST 5.1 model (Mooney et al., 1998).

In Figure 6.2 the comparison between the observed and modelled time-series is represented for some stations near the carbonate massifs, respectively

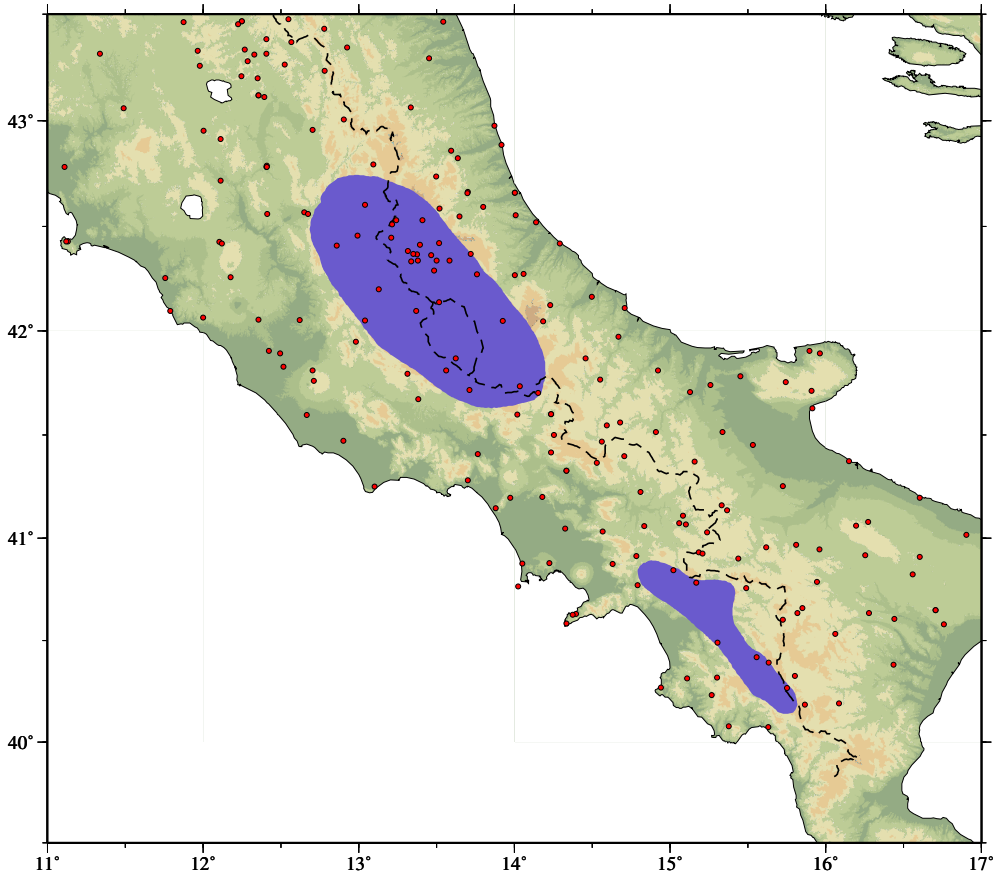

Figure 6.1: Areas where load is imposed for the surface simulation of the elastic response to localized hydrological loading. Red circles indicate the position of GPS stations.

in Central (Figure 6.2a) and South-Central Italy (Figure 6.2b) and far from carbonate massifs (Figure 6.2c). As expected (see section 3.1), the modelled time series clearly show a vertical deformation considerably higher than the horizontal one, with vertical to horizontal displacement ratio varying between about 15 at the sites located inside the load areas (e.g. AQUI, LEOF), to about 2 at the sites far from the load areas (e.g. ROMA, MATE). Though the modelled vertical deformation is comparable to the observed one, the horizontal deformation provided as a response to load variation is lower than the observed one, especially at sites located near carbonate massifs, where the observed displacements are more than one order of magnitude higher than the modelled ones.
Furthermore, surface loading predicts uplift and outward horizontal deformation when load is removed, that is in drought periods (e.g. T1 interval), and subsidence and inward horizontal motion when load is applied, that is in high rainfall periods (e.g. T2 interval). The modelled horizontal deformation therefore shows an opposite versus compared to the observed one (Figure 6.3). Although the horizontal deformation predicted by surface loading reverses sign at a certain depth (Figures 3.2 and 3.3), this depth raises with the distance from the load together with an increasing vertical to horizontal displacement ratio (Figures 3.4 and 3.5). We can consequently conclude that, since we are dealing with observations at the surface and with horizontal displacements comparable to the vertical ones, in our case neither the direction nor the magnitude of the horizontal deformation can be explained as the elastic response to a surface loading.

As regards the vertical deformation, its behaviour (uplift in summer, subsidence in winter) and its correlation with GRACE data (Figure 5.13) indicate that it could be explained as the response to surface loading. The load model we tested, however, gives a signal amplitude comparable to the observed one only in the sites located inside the load distribution area (compare Figures 6.2a and 6.2b with Figure 6.2c), whereas the amplitude of the observed signal doesn't show an evident spatial pattern and appears to be more

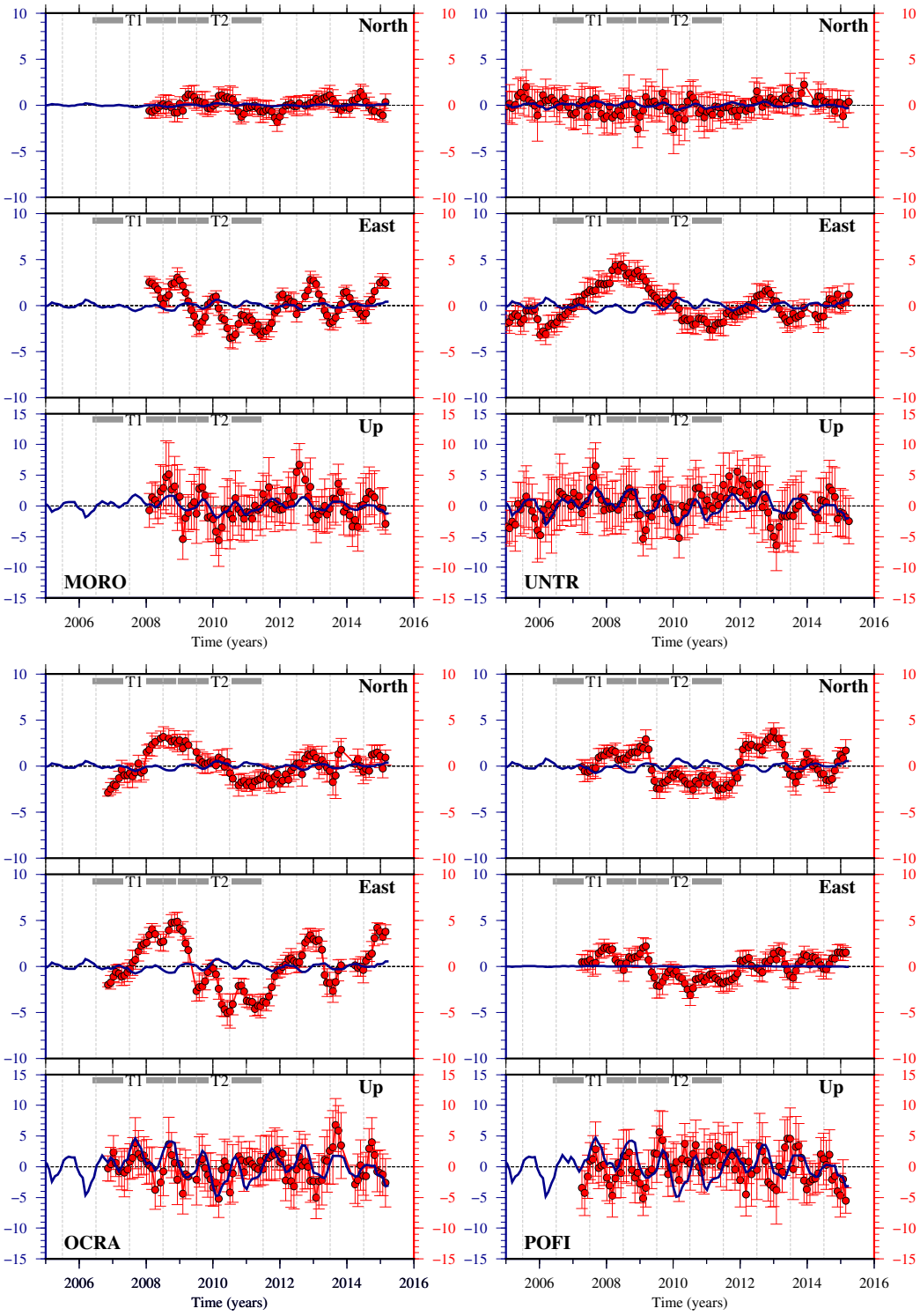

(a) Central Italy - Sites near carbonate massifs

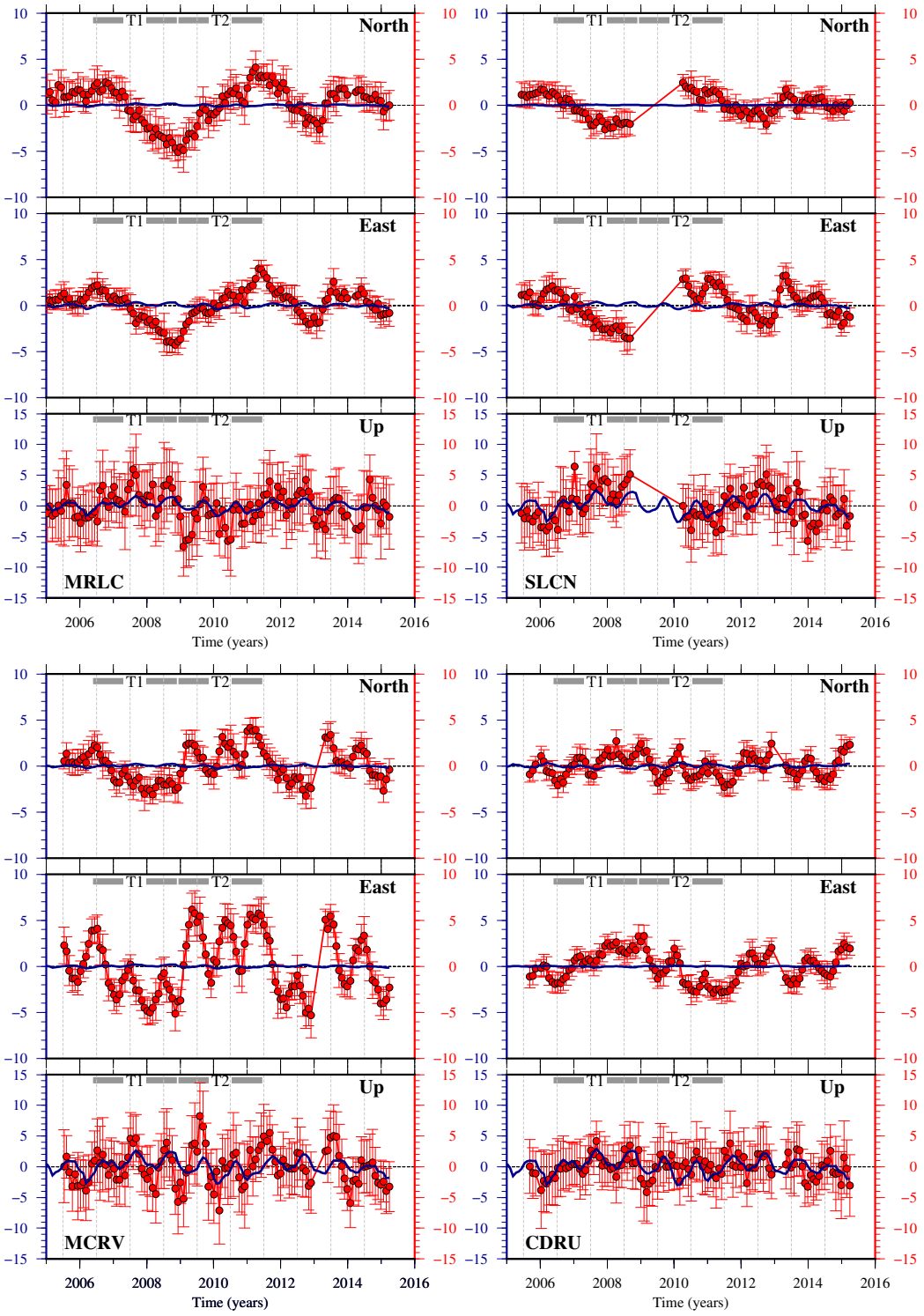

(b) South-Central Italy - Sites near carbonate massifs

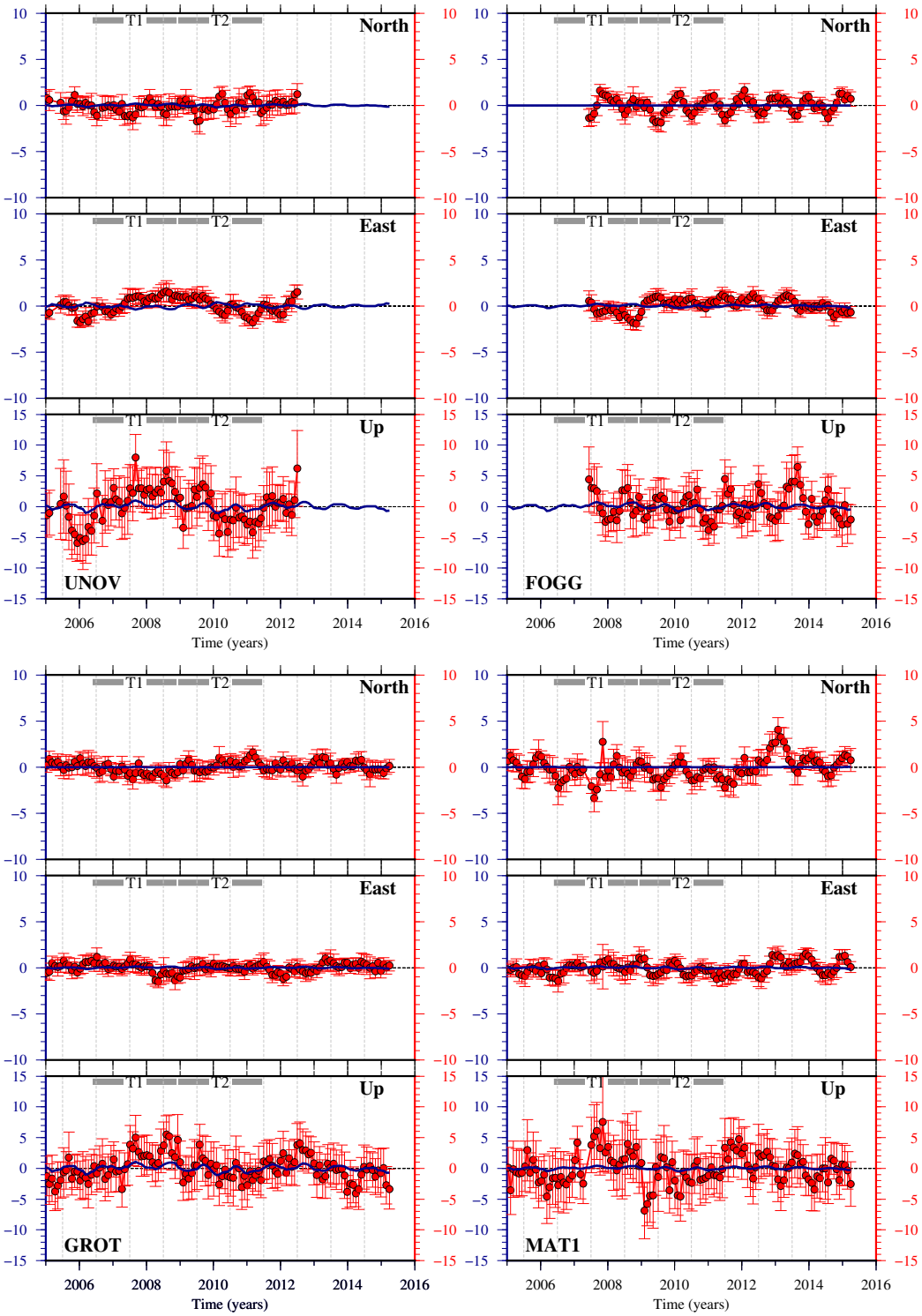

(c) Sites far from carbonate massifs

Figure 6.2: Comparison between monthly modelled time-series (blue line, model in Figure 6.1) and observed GPS time-series sampled at the same epochs (red circles ± uncertainty).

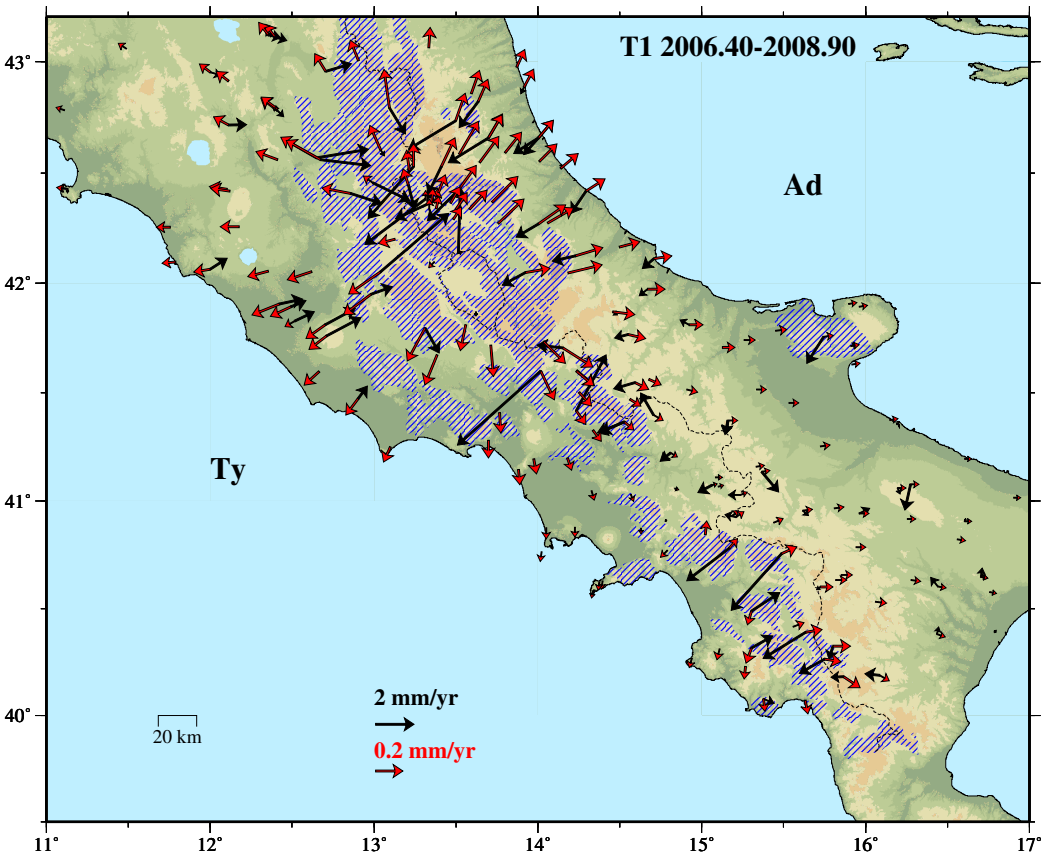
T1 2006.40-2008.90
Ad
Ty
2 mm/yr
0.2 mm/yr
20 km
43°
42°
41°
40°
11°
12°
13°
14°
15°
16°
17°

(a)

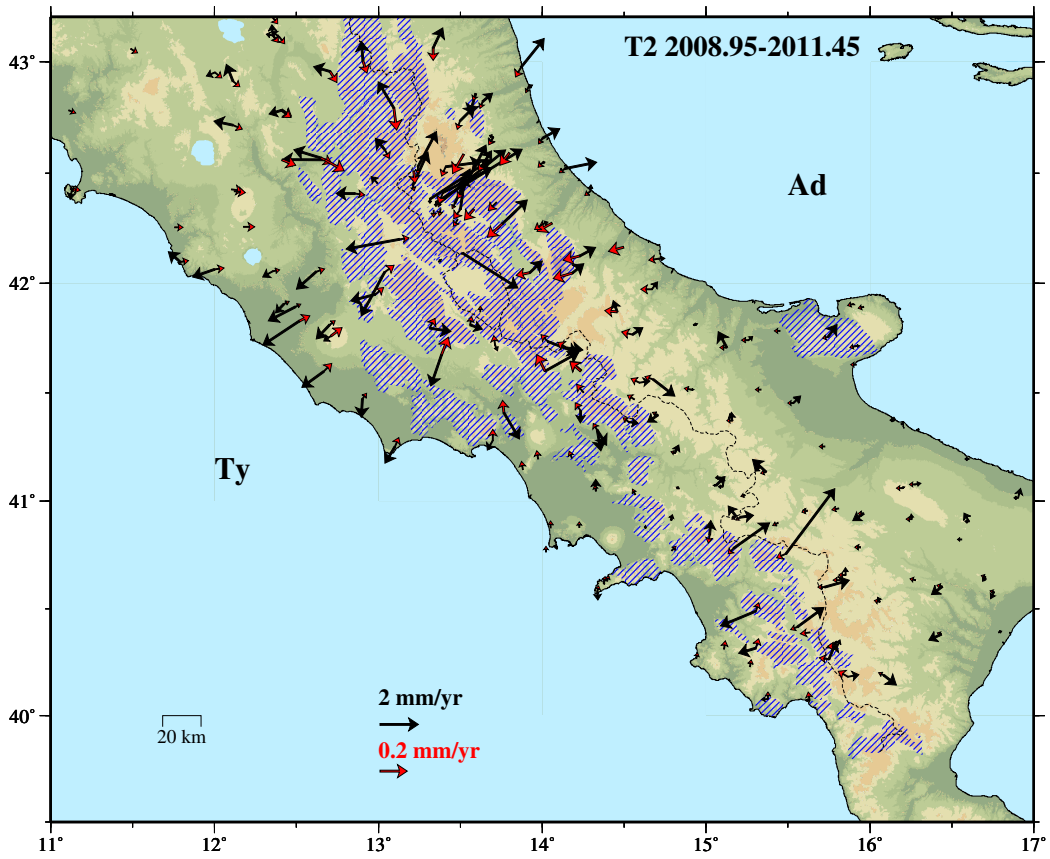

(b)

Figure 6.3: Horizontal rates in the T1 and T2 time intervals computed from the observed time-series (black arrows, same as Figure 5.4) and modelled time-series (red arrows) as a response to load variation at the surface (the load geometry is that of Figure 6.1). Notice that the observed and modelled arrows are plotted with different scales.

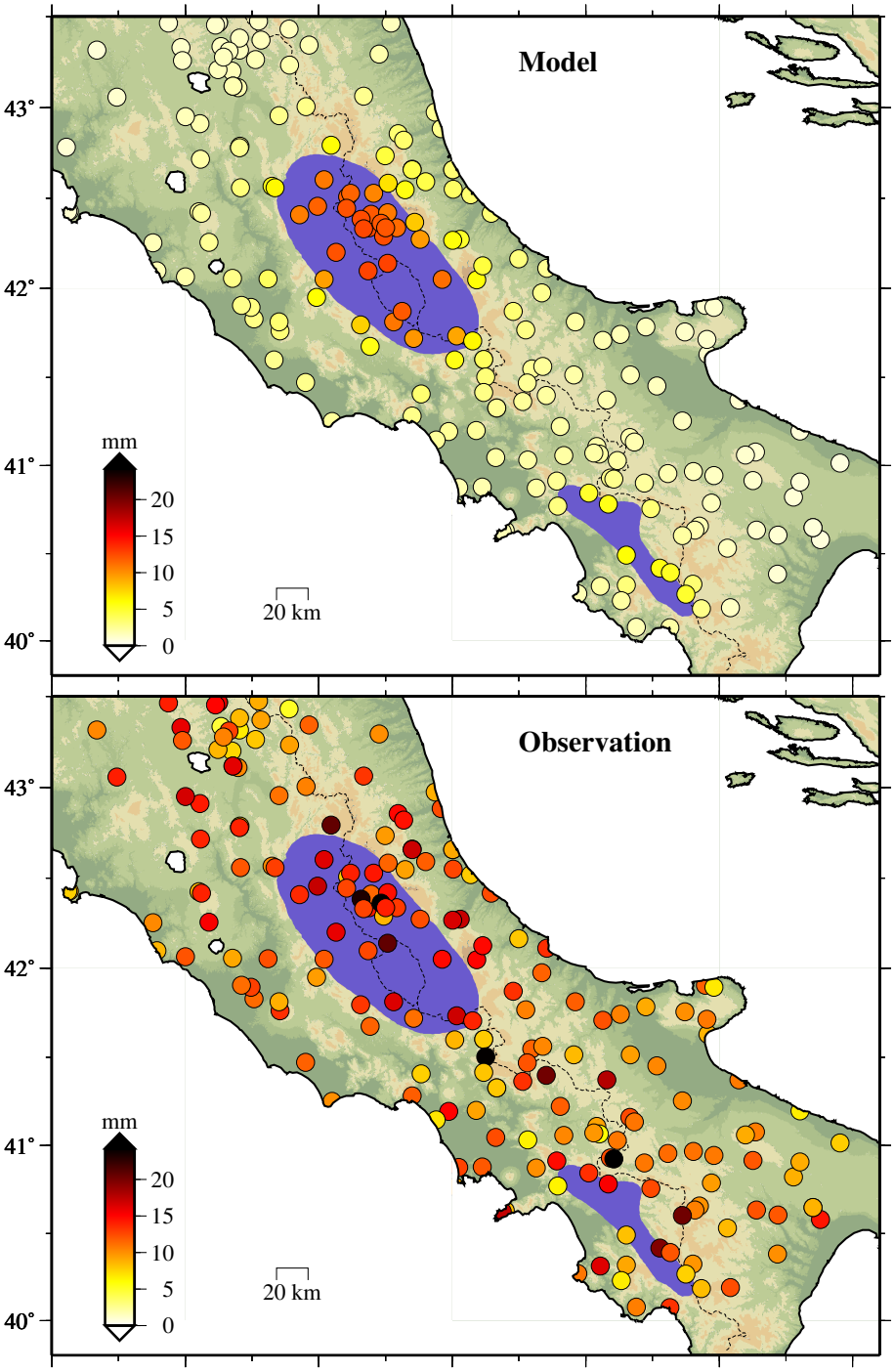

Figure 6.4: Comparison between the observed and modelled (load response model) maximum amplitude of the vertical displacement . The lightblue regions depict the areas where load has been imposed.

uniformly distributed (Figure 6.4). As anticipated in section 5.3, this suggests that the observed vertical deformation is related to a longer wavelength load distribution than the one considered in Figure 6.3, which is suitable to be recorded by GRACE satellites. This load distribution will of course produce also an horizontal deformation, that however we expect to be much smaller than the vertical one (horizontal deformation is much lower for distributed loads (Wahr et al., 2013)) and to be masked by local processes, especially near carbonate massifs.

6.1.2 Wide load model

In order to verify if the observed vertical displacements could be mainly caused by a wide load signal, we have calculated the surface deformation induced by the equivalent water height distribution variations over Europe recorded by GRACE satellite. In particular, we have considered increasing surface of the load area around Italy and we have evaluated the consequent deformation. The best agreement is achieved by considering load distributions within a range of $\approx 1000 \div 2000$ km.
The results are shown in Figure 6.5 for the same GPS sites of Figure 6.2. This second "wide load" model provide a visible improvement of the fit with the vertical displacement time-series, especially at sites far from carbonate massifs (see also amplitude maps in Figure 6.6). Furthermore this model relies on real terrestrial water storage values, whereas in the previous one we imposed exaggerated values of water load.
As expected, even in this case the horizontal modelled displacements are too small (of more than one order of magnitude) and can't explain the observed ones, especially at sites near carbonate aquifers.

It should be noticed that, although we observe consistent GRACE and vertical GPS time-series, their agreement is inevitably limited by the fact that GPS deformations give local information, that may explain a large part of the small-scale variations observed inside the Apennines belt, whereas GRACE

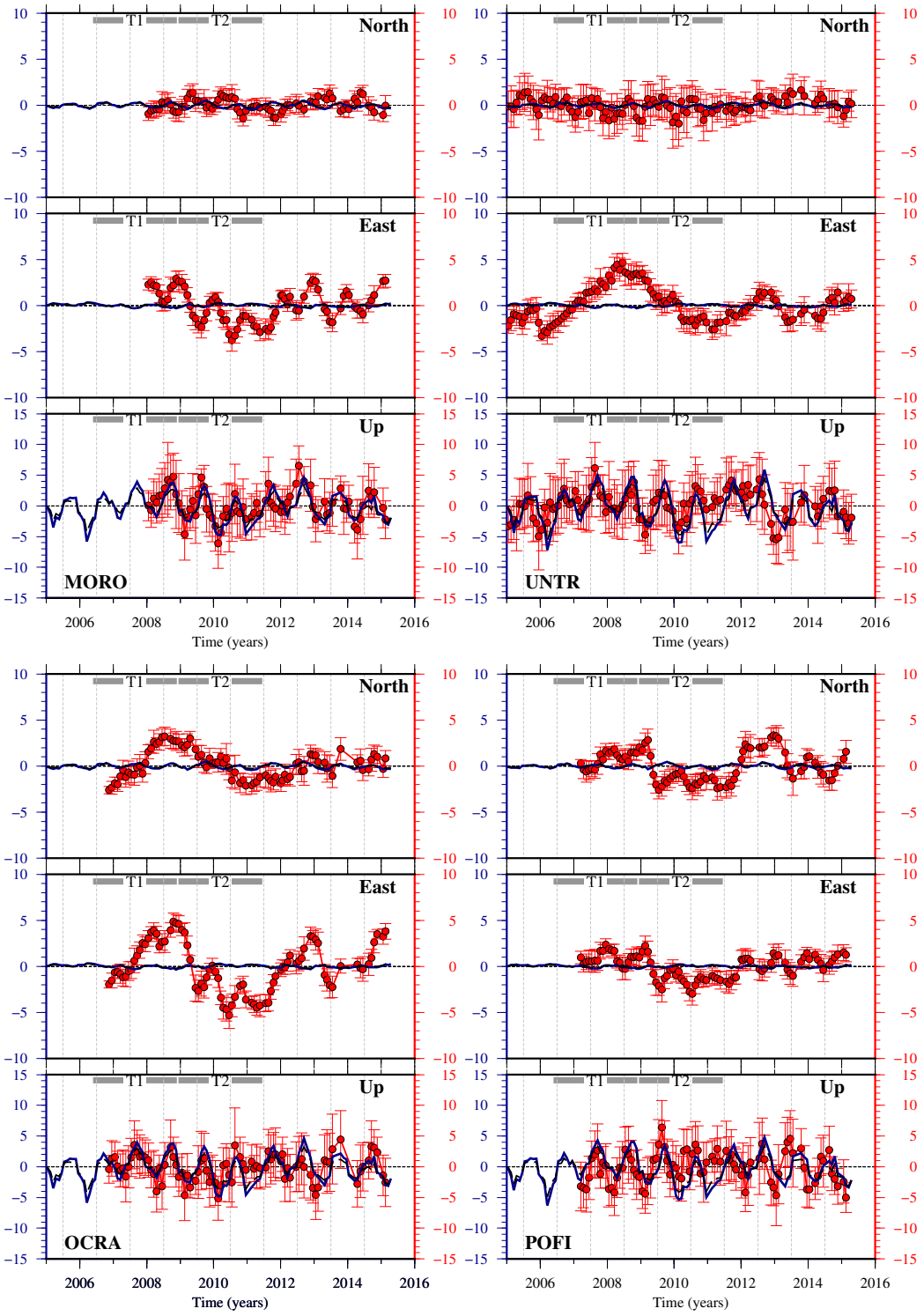

(a) Central Italy - Sites near carbonate massifs

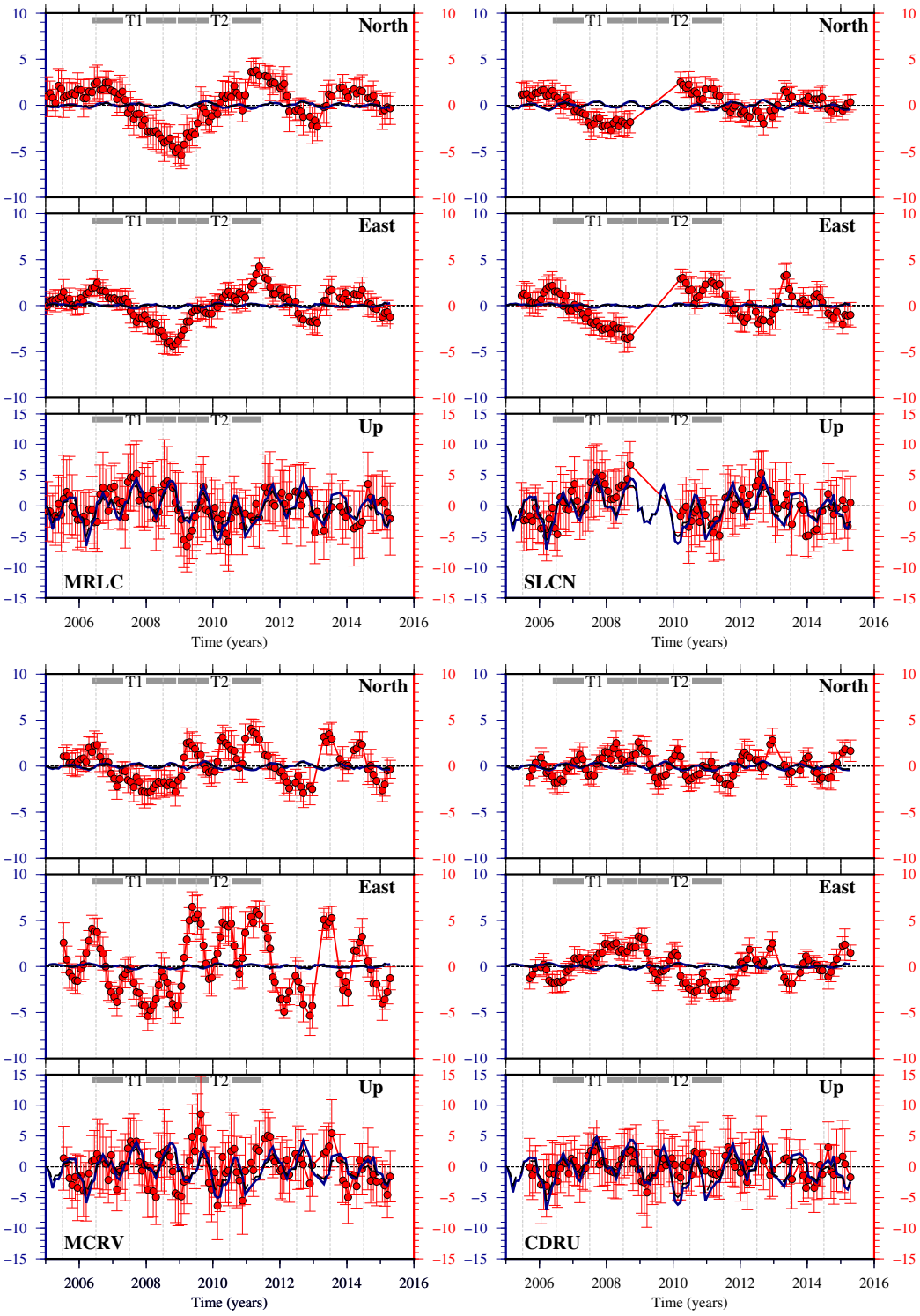

(b) South-Central Italy- Sites near carbonate massifs

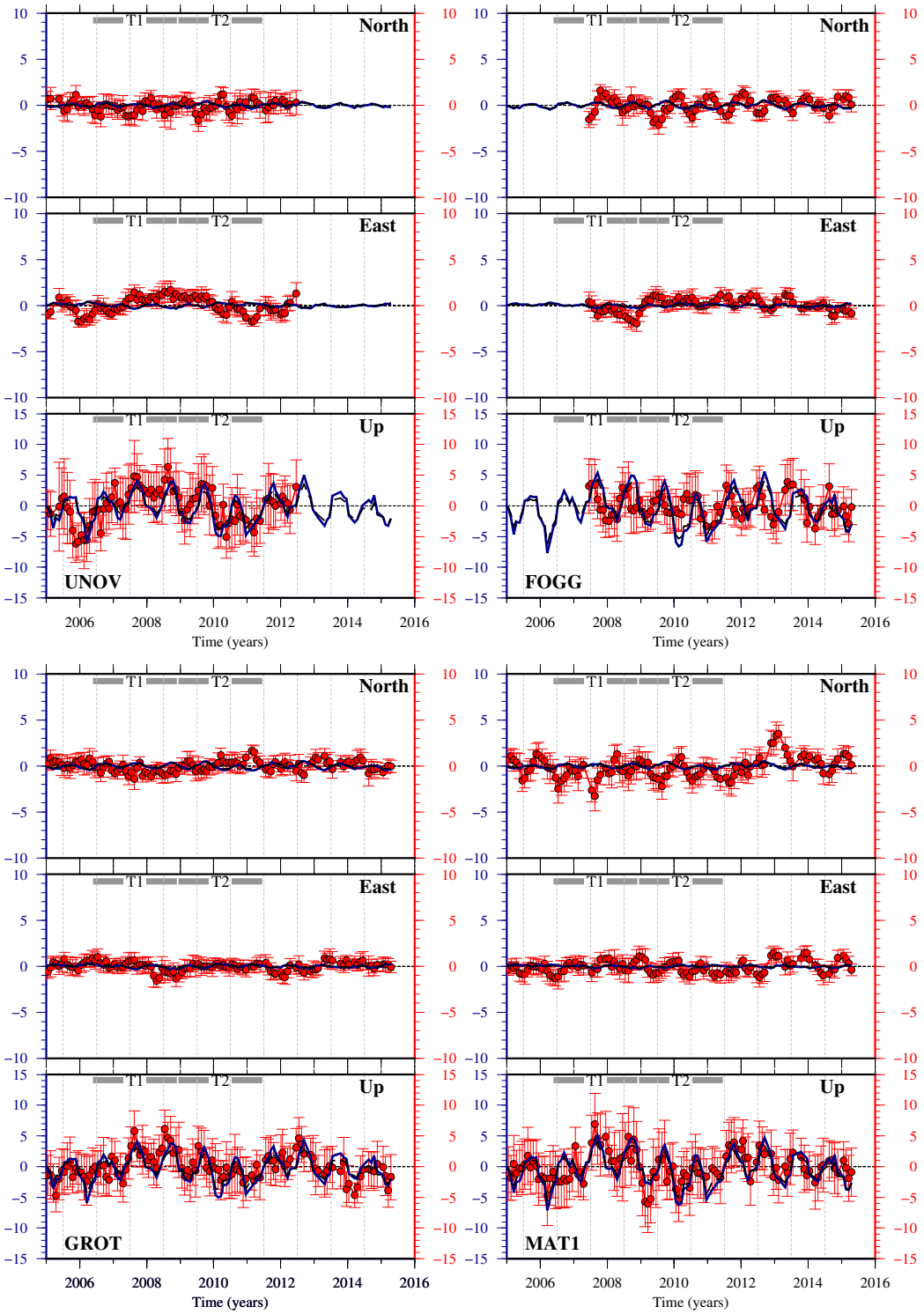

(c) Sites far from carbonate massifs

Figure 6.5: Comparison between monthly modelled time-series induced by the "wide load" model and the observed GPS time-series sampled at the same epochs (red circles ± uncertainty). The blue and black dashed lines respectively indicate results obtained with a 2000 km and 1000 km load range.

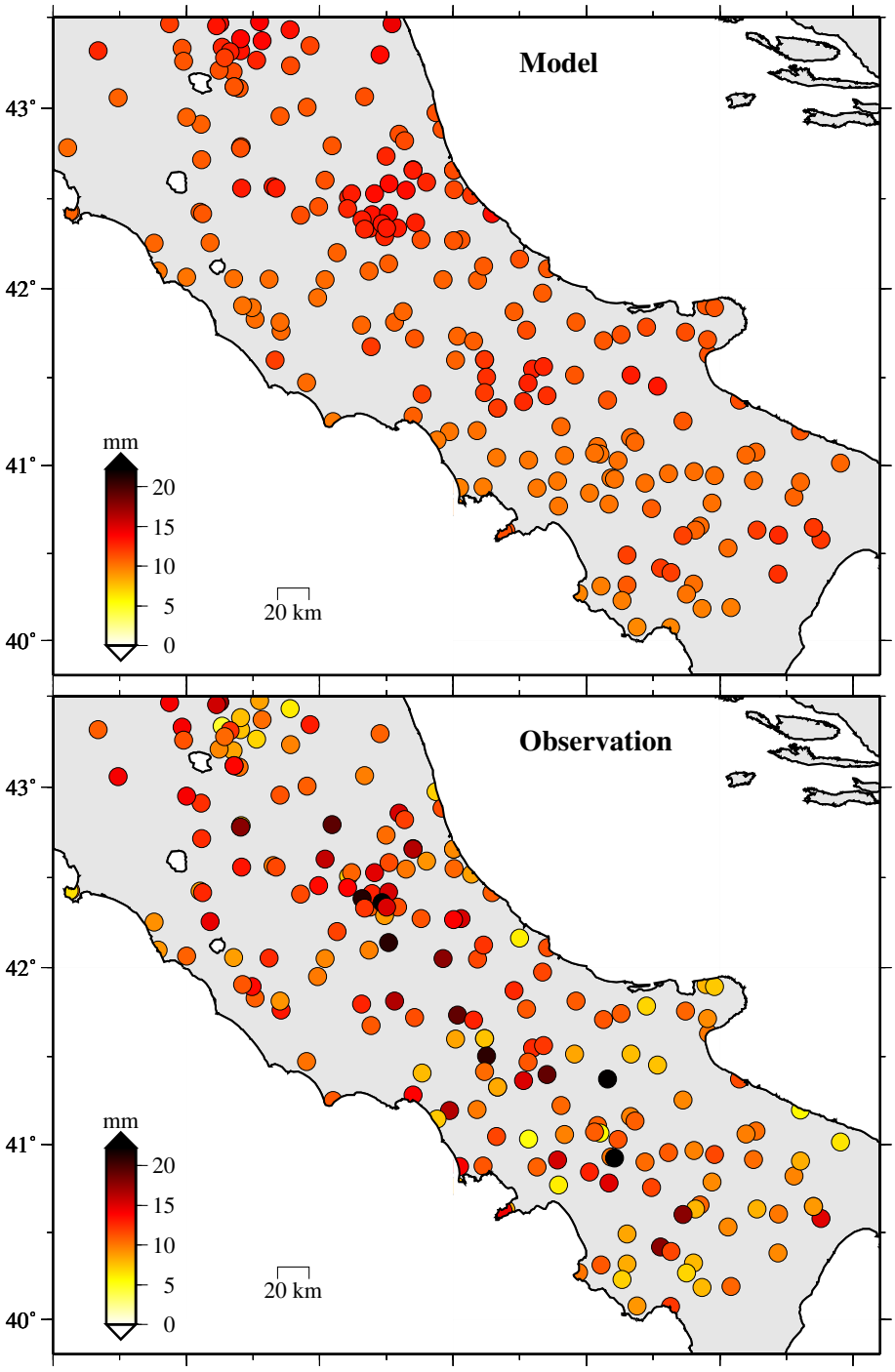

Figure 6.6: Comparison between the observed and modelled ("wide load" model with 2000 km radius) maximum amplitude of the vertical displacement.

data are resolved at a spatial scale of 400 km. For this reason results from both techniques should be interpreted carefully, without excluding the possibility for GPS data to contain hydro-geological signals of local origin. On the other hand, the high degree of correlation between GPS and GRACE data and the order of magnitude agreement with modelled vertical displacement suggest that the regional-scale (within a radius of about 1000÷2000 km) hydrological loading signals are well captured by vertical GPS data.

6.2 Response of an anisotropically-fractured crust to variations of hydrostatic pressure

The comparison of the observed GPS deformation with hydrological observables (section 5.3) suggests that vertical deformation reacts almost simultaneously to rainfall loading, whereas horizontal deformation is delayed and better correlated with spring discharge. In light of these observations and of the results about the elastic load model analysed in the previous section, we suggest that two different mechanisms could be involved in the observed deformation. Vertical displacements are consistent with the elastic response to surface loading affecting the whole studied area, whereas the peculiar trend and magnitude of the horizontal deformation here considered are specifically related to the presence of highly fractured carbonate aquifers.

The pattern and the magnitude of the observations analysed in this study suggest that the main process responsible for the deformation related to carbonate aquifers should be able to produce an anisotropic deformation with a significant magnitude in the horizontal direction.
Simple models of water circulation in unconfined karst aquifers relate the variations of the spring discharge to the elevation of the water table (Manga, 1996, 1997, 1999; Fiorillo, 2011; Amoruso et al., 2013), with high water tables increasing the hydrostatic pressure ($\Delta P = \rho_w g \Delta h$) in the basal, saturated part of the aquifer (see Figure 8 in Fiorillo (2013)). Aquifers hold in carbonate rocks can experience seasonal fluctuations of the water table

height of considerable magnitude, reaching tens of meters (e.g. LeGrand and Stringfield, 1971; Miller, 2008). Following this hypothesis, horizontal ground deformation could be mostly sensitive to water infilling interconnected voids and fractures in the phreatic zone.
Carbonate aquifers of the Apennines can store a considerable quantity of water (Fiorillo et al., 2015b) and are characterized by a primary fracture pattern oriented in NW-SE direction (Celico et al., 1994; Billi et al., 2007; Del Prete et al., 2007; Pastori et al., 2009). This fracture orientation is parallel to the direction of the Apennines range and perpendicular to the orientation of the interseismic maximum horizontal stress (D'Agostino, 2014) and to the main direction of the observed transient horizontal deformation (Figure 5.4). The latter can be therefore ascribed to the bulk deformation of the rock due to the variation in opening of fractures in carbonate aquifers.
Several works that studied the deformation of karst regions using tiltmeters and strainmeters have explained the observed data by means of opening tensile fractures (Evans and Wyatt, 1984; Longuevergne et al., 2009; Jacob et al., 2010; Devoti et al., 2015). These authors, however, dealt with local data and small wavelength deformations and they related them mostly to hydrologically active fractures/conduits located in the nearby of the instruments, in the epikarst or the vadose zone of the aquifer (depth $\sim 10^2$ m). Devoti et al. (2015) have analysed some GPS measurements at Cansiglio Plateau karst region (Northern Italy), over an area of 12x5 km^2, that show that the plateau expands and rebounds radially suddenly after rain by an amount up to a few centimetres with only small vertical deformation. The authors linked these observations with subsurface hydrological processes in the karstic vadose zone.

In this study we observe a regional deformation, over an area of ~ 1000 km^2 and an horizontal signal that is delayed compared to rainfall and is mostly in phase with the spring discharge. These features suggest that the horizontal deformation is due to deep-rooted processes which occur in the phreatic zone of the aquifer and are related to the fluctuation of the water

table level. The deformation occurs once the water has percolated through the vadose zone and has reached the saturated phreatic zone of the aquifer, inducing hydrostatic pressure variations in it and causing the opening of fractures and spring discharge (Figure 6.7).
According to this conceptual model, we ascribe the first order of the observed horizontal signal to the rock deformation related to the variation of fractures dilatation in carbonate aquifers. Sub-vertical planar fractures are likely deformation sources since such fracture geometries are commonly seen underground in karst aquifers (Longuevergne et al., 2009; Jacob et al., 2010). The observed displacements may thus be the result of the sum of individual effects of several distinct sources that form the complex karst network of fractures, whose detailed features (fracture density, position, length, width, orientation, opening) are hard to be known. Consequently, to try to model this mechanism, less complex "equivalent" model has to be used.
Here two different simple models are proposed to reproduce the first order features of the observed horizontal deformation. The first simulates the effect of a medium permeated with sub-vertical opening fractures through a big tensile dislocation located approximately in the middle of the fractured aquifer (section 3.2.2). In the second we calculate the displacements due to the variation of the water table height inside a porous aquifer by using the effective stress principle (section 3.3). In this case, both planar and non-planar geometries and isotropic and anisotropic material properties have been examined.

6.2.1 Tensile dislocation model

South-Central Italy

We focus on the South-Central area (the region surrounded by the pink box in Figure 5.2a), where the horizontal signal is maximum at CDRU, MCRV, MRLC, SAL1 and SLCN, decreases at CMPR, BULG, MCEL, MTSN, SIRI and TITO and vanishes at higher distances from the carbonate aquifers,

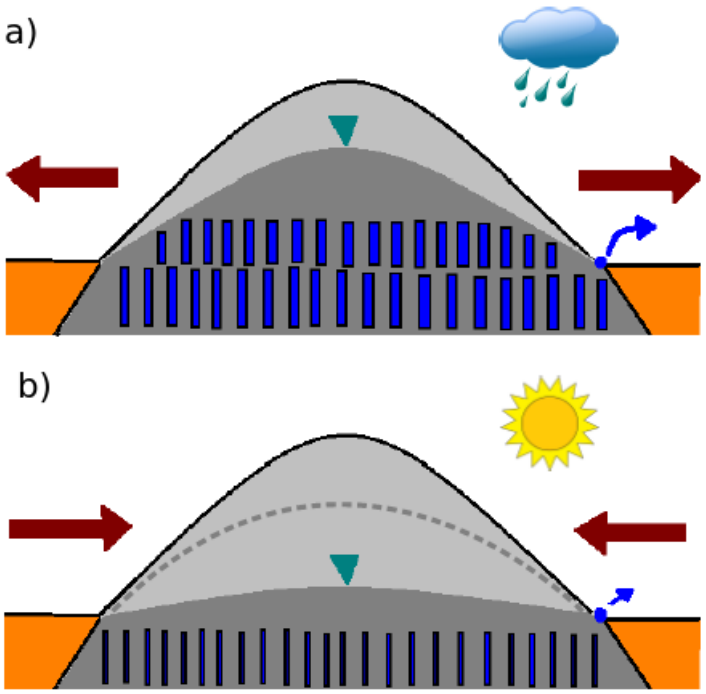

Figure 6.7: Simple conceptual model that illustrate the mechanism hypothesised to explain the observed horizontal deformation. In rainy periods, such as T2 time interval, the water infiltrates into the aquifer increasing the water table height (green triangle). The water pressure in the water filled fractures (blu rectangles) consequently increases making them to open and causing the dilatation of the whole massif. The reverse happens in dry periods (b), such as T1 time interval. The spring (blue dot) is located at the contact between the aquifer and impermeable materials and the higher (a) and lower (b) spring (blue dot) discharges are represented as a blue arrows with different lengths.

showing a symmetric behaviour whose axis can be traced in the NW-SE direction between CDRU and SAL1 (Figures 5.2e, 5.4 and 6.8). This pattern suggests that the deformation is mainly centred around the large carbonate formations of Mounts Picentini, Mount Marzano-Ogna, Mounts Alburni and Mount Cervati (Figures 5.7 and A.2). These represent the main aquifers of this area (Allocca et al., 2007) which are capable to store large quantities of groundwater, releasing it mainly toward springs along the border of the aquifers, at the contact with less permeable materials (sections 2.1 and 2.2.2.2).

As we have shown in section 3.2.2, the displacement caused at a certain distance by a group of small tensile fractures embedded in a region is roughly equivalent to the one caused by a single big dislocation located inside the fractured region (Figure 3.13) (Maccaferri, 2010). Since in the South-Central area most of the observations (GPS stations) lie at the boundaries of the carbonate massifs (Figure A.3) and we aim to reproduce only the first order features of the studied signal, we use big tensile dislocations located roughly at the center of the massifs to simulate the effect of the whole fractured region. In particular, we model the effects of three vertical tensile dislocations (Okada, 1985) buried in an homogeneous elastic half-space with a Poisson's ratio of 0.25. Here we neglect the Earth surface curvature for a first order estimate of near field effects and the exact topographic trend, but we consider the half-space surface as representing an average reference elevation above the sea level (Lisowski, 2007). This simplified model represents a very crude approximation of the complex karstic fractures system, nevertheless it could provide some interesting insights about the processes responsible of the main features of the observed signal.
The positions and lengths of the dislocations (Figure 6.8) are imposed in order to fit the observed GPS displacements and roughly corresponds to carbonate aquifers of Mounts Cervialto and Polveracchio-Raione (near MCRV site), Mounts Marzano-Ogna (near MRLC), and Mounts Alburni, Motola and Cervati (near CDRU, CMPR, SAL1, SLCN, MTSN, MCEL). All the

three dislocations have a strike angle of 140°, that is consistent with the orientation of the primary fracture pattern of this area (Figure A.5) (Celico et al., 1994; Del Prete et al., 2007; Pastori et al., 2009). We have fixed the depth of the top edge of the dislocations at 100 m, since small variations of this parameter only affects the deformation in the very near field.
The opening of water filled fracture in the phreatic zone is due to the variation of hydrostatic pressure, that is in turn related to the variation of the height of the water table. By assuming water table variations proportional to spring discharge, we have imposed a spatially-uniform time-dependent opening of the dislocations by scaling it to the discharge of Caposele spring, taken as a proxy for the regional elevation of the groundwater table within the carbonate aquifers (see section 5.2.2). In this way the dislocation opening varies between 0, in correspondence of the minimum value of spring discharge in the considered time-interval (2005-2015), and a maximum value, in correspondence of the maximum value of spring discharge. We have conducted a grid-search by varying the width of the dislocations between 0.1 and 8 km and the maximum value of the dislocation opening between 0.1 and 20 cm. A well known trade-off exists between the tensile dislocations width and opening (Lisowski, 2007) making difficult to distinguish variations of these parameters from real observations (see section 3.2.2). The observed data do not permit to uniquely estimate these parameters and the root mean square deviation between the horizontal modelled and observed time-series (Figure 6.9) shows a clear trade-off between width and opening of the dislocations.

The results obtained from a couple of values of width-maximum opening (1.5 km; 6 cm) that fall in the minimum RMS area (Figures 6.8, 6.9 and 6.10) shows that our simple modelization permits to satisfyingly reproduce the observed deformation at the first order. The agreement is particularly good at MCRV, located near Caposele spring, but also at farther sites such as CDRU, CMPR, MCRV, MTSN, SAL1 and SLCN. The worse agreement occurs at MRLC, which shows reduced seasonal variations and an enhanced delay compared with the Caposele spring discharge. The modelled vertical

component is almost null at every site (Figure 6.10), since the vertical deformation related to a tensile dislocation decays quickly with the distance from the dislocation (see section 3.2.2, in particular Figure 3.10).
One of the main causes of disagreement between modelled and observed time-series is due to the time shift between the Caposele spring discharge and GPS time-series that we highlighted before by means of cross-correlation analysis (Figure B.1). These time-shifts are probably related to local effects that influence the time-lag between rainfall and spring discharge in different areas, such as morphological and hydrogeological setting of the aquifer, i.e. the aquifer geometrical features, the distance between the recharge area and the spring, the thickness of the unsaturated zone, the degree of karstification of the epikarst, the unsaturated zone and the saturated zone, the snow accumulation and melting and the cover by pyroclastic deposits (Fiorillo and Doglioni, 2010). A role in causing time-lags could be played also by the eventual presence of low permeability barriers, such as faults, that compartmentalize the aquifers (e.g. Celico et al., 2006).
Some interesting information could be inferred from the comparison of the Caposele spring discharge and the horizontal displacement at MCRV, that refer to the same aquifer (i.e. Cervialto massif). MCRV is located between the principal endorheic area of the Cervialto massif (Piano Laceno (Fiorillo et al., 2015b)) and the Caposele spring (Figure A.3b) and displacement at this site results to be highly correlated (0.89) and slightly anticipated (about 20 days) compared with spring discharge. Assuming a diffusion process inside an unconfined aquifer (Manga, 1996, 1997), this negative time lag could be related to the propagation of the variation of the height of the water table from the principal recharge area of the aquifer to the spring.

Central Italy

In Central Italy the presence of the recent L'Aquila earthquake and the spatial distribution, shape, number and dimension of the different carbonate massifs make the simulation of the observed horizontal deformation harder.

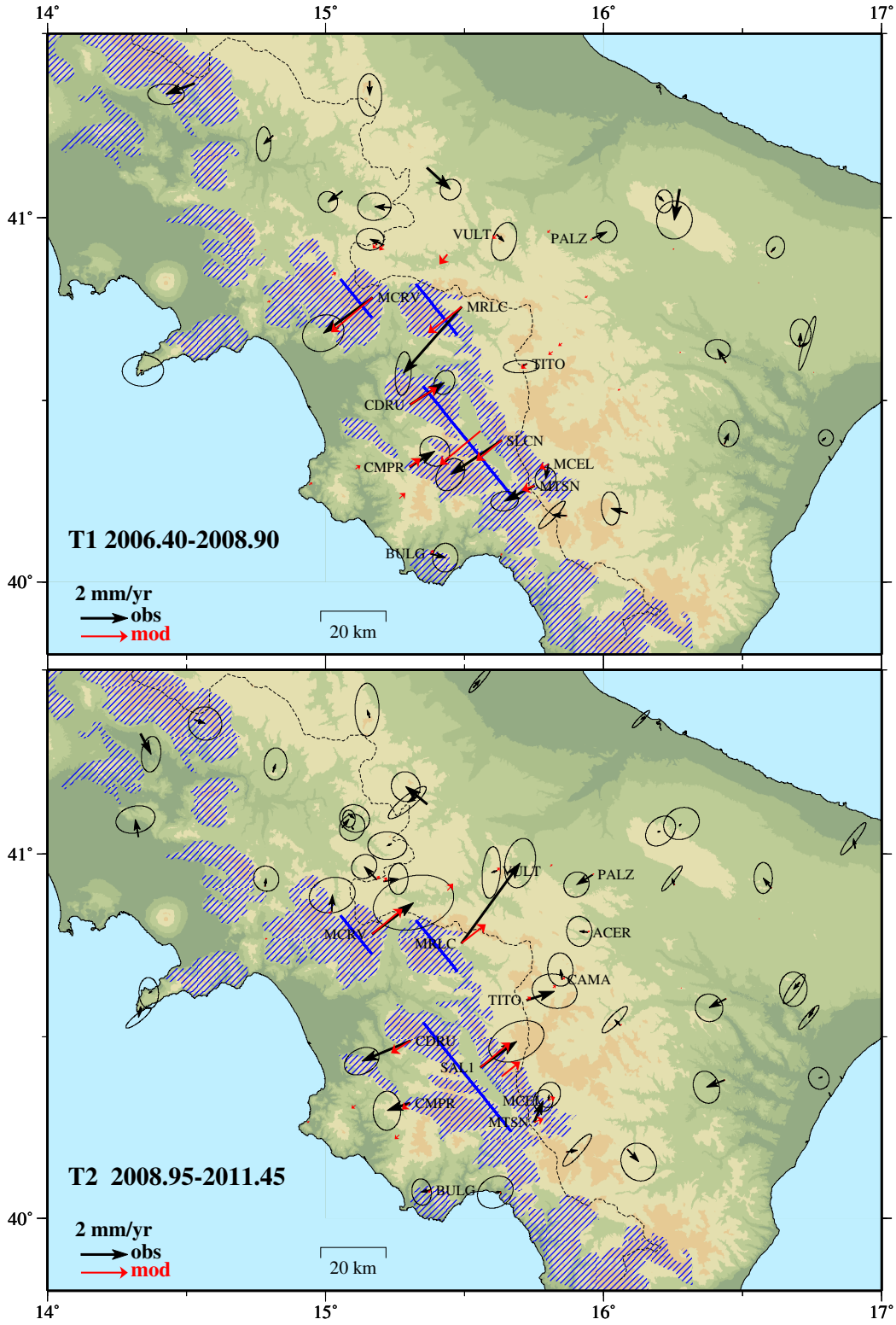

Figure 6.8: Observed (black) and modelled (red) GPS velocities calculated as deviation from the long-term trend in a period of decreasing precipitation and karstic aquifer exhaustion (T1, top) and in a period of increasing precipitation and aquifer recharge (T2, bottom; cfr. Figure 6.10). The thick blue lines indicate the position of the vertical tensile dislocation surfaces used in the model.

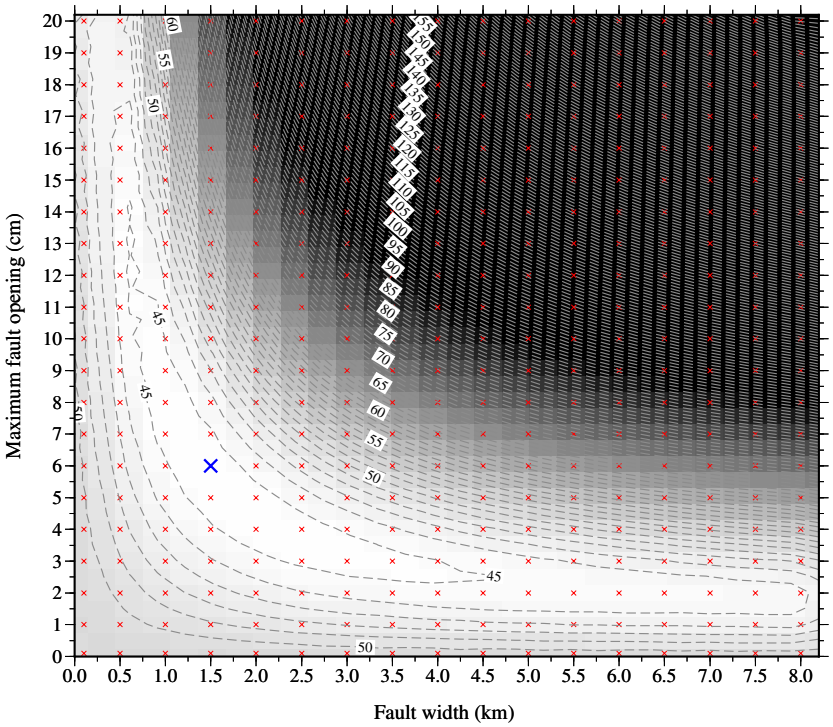

Figure 6.9: RMS deviation (color coded) between the horizontal observed and modelled time-series for different values of the width and the maximum opening of the tensile dislocations. Red crosses indicate model realizations, the grey dashed contours are interpolated between those points and plotted at 1 mm intervals. The RMS value is indicated as labels inside the boxes. The blue cross indicate the best-fit model that has been discussed in the text. The color scale is saturated at 90 mm.

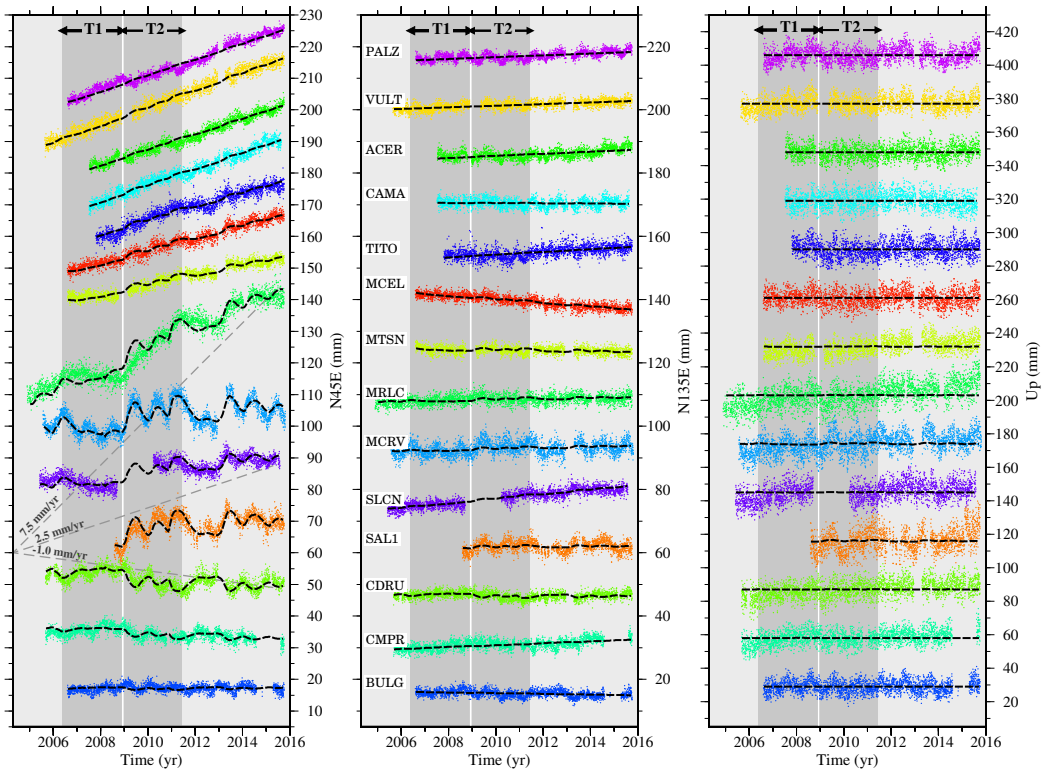

Figure 6.10: Observed (coloured dots) and modelled (black dashed line) time-series at the sites indicated in Figure 6.8. GPS sites are ordered from the Tyrrhenian coast (bottom) toward the Adriatic coast (top). Left: horizontal component is shown as projected along a direction perpendicular to the long-axis of the Apennines (N45E); centre: the horizontal component is shown as projected along a direction parallel to the long-axis of the Apennines (N135E); right: vertical component. T1 and T2 refer to the two time intervals in which velocities represented in Figure 6.8 are calculated.

The latter shows a spatial pattern that can hardly be reproduced through a small number of big tensile fractures, as we did for the South-Central area. The most evident difference is the quasi-radial pattern that the observed deformation assumes at the northern and southern sides of this region (Figure 6.11). Several factors can be hypothesized to influence this trend. (i) A prevalent role seems to be played by the large hydrogeological unit which extends from the Peschiera springs, south-eastward to the Velino group and continues to the Marsica Mounts and up to the Capovolturno springs, located at the south of the Monti della Meta massif (Figure 6.11, see also Figures 2.4, 5.5, and A.2a and section 2.2.2.1). (ii) The largest observed horizontal rates appear to surround the carbonate massifs of the south-eastern sector (roughly Lazio and Abruzzo), whereas the massifs of the north-western sector (roughly Umbria and Marche) appear to contribute to a lesser extent. This could be due to the difference of carbonate rocks structure of these areas (carbonate platform and carbonate basin domains), possibly reflecting the higher infiltration capability and thickness of the platform domain (Boni, 1986, 2000) (see section 2.2.2.1 and Figure 2.4). (iii) The horizontal deformation seems to be influenced by the orientation of the outer carbonate massifs (Figure 6.11). If the main fracture directions followed the strike variability of the fractured massif and of the main tectonic faults (Figures 2.4 and A.1), this could have a role in explaining the direction assumed by the observed pattern of horizontal deformation (Figure 3.17).

6.2.2 Effective stress model

In this section we simulate the effects of the changes in water table height inside a highly fractured aquifer, such as the carbonate aquifers of Central and South-Central Apennines. For this purpose we performed a 2-D plain-strain stress-displacement numerical model using the finite difference code FLAC2D 7.0 (ITASCA, 2011).

This approach follows the idea that a pervasively fractured water saturated medium can be described as an (anisotropic) porous medium which deforms

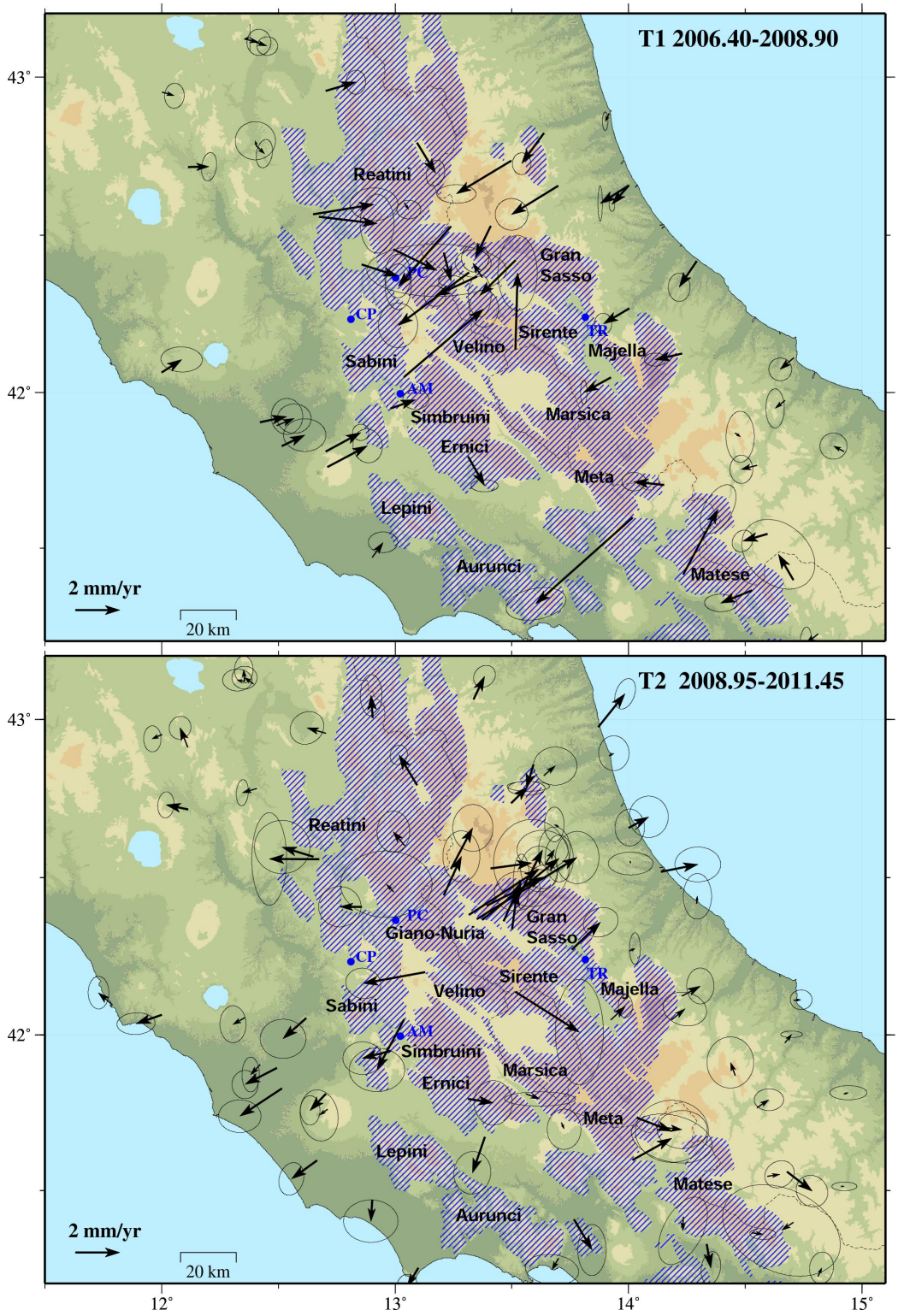

Figure 6.11: Observed (black) GPS velocities calculated as deviation from the long-term trend in a period of decreasing precipitation and karstic aquifer exhaustion (T1, top) and in a period of increasing precipitation and aquifer recharge (T2, bottom). Also the names of the analysed springs (Peschiera (PC), Acqua Marcia (AM), Tirino (TR), Capore (CP)) and of the main carbonate massifs are indicated.

because of the variations of the pore pressure. According to this approach the deformation of the medium is directly induced by realistic variations of the pore pressure and of the elastic constants (isotropic and anisotropic). In the previous model (section 6.2.1), on the contrary, the deformation induced by hydrostatic pressure variations was simulated through the "ad hoc" opening of the tensile dislocations. By means of the model presented here we try, despite the limitations due to the model simplicity and the preliminary results, a more realistic modelization of the observed phenomenon.

Model

The model configuration aims to represent a very simplified aquifer geometry, including topography, with dimensions representing reasonable average values of the carbonate aquifers of the Apennines. Figure 6.12 shows the implemented model geometry. Note that, given the vertical axial symmetry of the model, we have considered only half of the horizontal domain in order to reduce the computing time. The horizontal extent of the domain is 40 km. The topography has been simulated through a Gaussian function with a width (standard deviation sd) equal to 20 and 30 km and reaching a maximum altitude of 1.5 km above the sea level. The water table follows the same Gaussian geometry of the topography: it is horizontal in the valley (at depth 0 m) and reaches a maximum height which has been calculated by using two end-member values of the hydraulic gradient $J = 5 \div 20‰$commonly found in carbonatic and dolomitic aquifers (Boni, 1986; Amoruso et al., 2014).
The lower boundary is set at a depth of 2.5 km, according the average thickness of the carbonate aquifers (Boni, 1986; Fiorillo and Guadagno, 2010; Amoruso et al., 2013).
The grid dimension, about 100 m x 40 m, have an aspect ratio lower than the maximum values ($\sim 5 \div 10$) typically required in order to have reliable numerical results.

At lateral boundaries only vertical displacements have been allowed to reproduce geostatic conditions (section 3.3.2), whereas the horizontal displace-

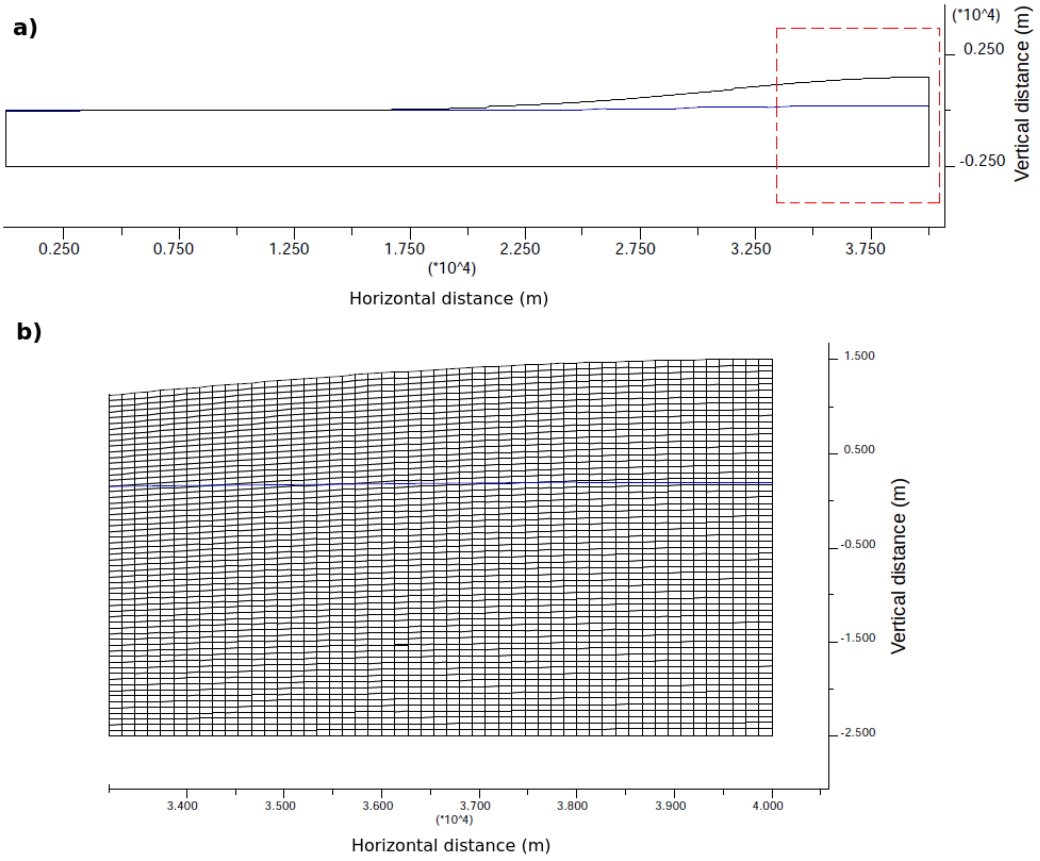

Figure 6.12: Model geometry. a) Whole domain representation, the blue line indicate the water table height at the initial state. b) Zoomed representation of the domain, with the mesh geometry, in the area surrounded by the red dashed rectangle in a).

ments have been fixed. At the bottom, where the aquifer is in contact with less permeable rocks, where no effective stress variation occurs in response to the water table height change, fixed horizontal and vertical displacements have been imposed.

For the numerical modelling, the fractured rock mass has been considered as a continuum elastic equivalent medium (Sitharam et al., 2001). We have tried several model configurations whose features are listed in table 6.1. The value of the natural density $\rho_s = 2600$ kg/m^3 is the same imposed by Amoruso et al. (2014) in the study of the deformation of the Gran Sasso (Central Apennines) aquifer. The value of the dry density ρ_d has been calculated through equation 3.40 by considering a totally saturated medium (saturation $S = 1$) with porosity $n = 10\%$ (from Amoruso et al. (2014)).
Both isotropic and anisotropic Young's modulus have been implemented by using an elastic, transversely isotropic model. Crust anisotropy can be caused by preferentially aligned joints or microcracks (e.g. Amadei, 1996; Pastori et al., 2009). In the case under examination, anisotropy is imposed in order to simulate an highly fractured medium where fractures show a main sub-vertical orientation (compare to the model in section 6.2.1). In this case, we have considered an anisotropic medium where the Young's modulus in the horizontal direction (perpendicular to the plane of transverse isotropy) E_h is reduced (by a factor of 5) compared to the value of the Young's modulus in the vertical direction E_v. Data on the elastic moduli of intact anisotropic rocks show in most cases a ratio between the in-plane and out-of-plane Young's moduli between 1 and 4, however, anisotropic rock masses whose anisotropy is due to a set (or sets) of fractures may exhibit much greater elastic anisotropy ratios (Amadei, 1996).

In the isotropic case the shear modulus G is equal to 20 GPa (corresponding to the fixed values of the Young's modulus and Poisson's ratio). In the transversely isotropic case the cross-shear modulus between the plane of isotropy and the perpendicular plane has been estimated through the empirical equation by Lekhnitskii (1981)

$$G = \frac{E_h E_v}{E_h + E_v(1 + 2\nu)} \tag{6.1}$$

The effect of pore pressure variation in the medium has been simulated following an uncoupled approach. The change in pore pressure is simulated by imposing a variation of the water table height. Then the total stresses are automatically updated according to the fact that the total stress acting in a medium region is the sum of the matrix stress (caused by the forces exerted by the grains of soil or rock matrix) and the fluid pressure, acting in the void spaces (see section 3.3). The model therefore considers two pseudostatic hydraulic conditions, without taking into account the water diffusion and the hydrodinamic pressure (see section 3.3.2.3).

Results

In this section we aim to examine the displacements related to a maximum amplitude variation of the water table between dry periods (e.g., 2007-2008) and wet periods (e.g., 2010-2011). To simulate this variation we have imposed a water table increase reaching a maximum of 50 m at the summit (horizontal distance = 40 km) (e.g. LeGrand and Stringfield, 1971; Miller, 2008).

The results for the displacement at the surface are shown in Figure 6.13 for the eight different models listed in Table 6.1. As expected (see the example in section 3.3.2.3), the vertical displacements experience uplift and reaches a maximum value at the topographic summit. The vertical displacements don't show considerable variations between the examined isotropic models and the highest change (~ 0.8 cm) is related to the variation of the hydraulic gradient J. In all the examined anisotropic models the amount of uplift is noticeably reduced (of $1 \div 2$ cm) compared to the isotropic models.

Horizontal displacements show interesting results indicating an outward motion of the surface reaching maximum amplitudes at the topography sides, where the slope of the topography (and of the water table) is maximum. The produced maximum displacement magnitudes vary between ~ 0.7 cm

Table 6.1: List of the parameters employed for the effective stress model*

Model id	ρ_s (kg/m^3)	ρ_d (kg/m^3)	n (%)	E_v (GPa)	E_h (GPa)	ν	G (GPa)	J (‰)	sd (km)
1 (iso)	2600	2500	10	50	50	0.22	20	5	30
2 (aniso)				50	10		6.1	5	30
3 (iso)				50	50		20	20	30
4 (aniso)				50	10		6.1	20	30
5 (iso)				50	50		20	5	20
6 (aniso)				50	10		6.1	5	20
7 (iso)				50	50		20	20	20
8 (aniso)				50	10		6.1	20	20

* ρ_s = natural density; ρ_d = dry density; n = porosity; E_v = Young's modulus in vertical direction;
E_h = Young's modulus in horizontal direction; ν = Poisson's ratio; G = shear modulus;
J = hydraulic gradient; sd = width of the Gaussian topography/water table;
iso = isotropic model; aniso = anisotropic model.

(mod1) to ~ 2 cm (mod8). High variations ($\sim 0.5 \div 1$ cm) of the horizontal motion are related to the anisotropy. Steeper topography (and hence steeper water table) tend to cause higher and more localized deformation. As for vertical displacements, higher values of J produce higher deformations.
The oscillations shown by the displacements results are due to the mesh discretization.

In order to understand the influence of the topography on the produced displacements, we have replied the models mod1 and mod2 by imposing a flat topography (mod1* and mod2* in Figure 6.14). Even if it is unrealistic to have a non-flat water table with flat topography, this test shows that the signal magnitude is mostly related to the water table geometry.

Despite its simplicity and limitations related to the consideration of pseudostatic, non-coupled conditions and to the imposition of boundary conditions, this model, by using reasonable values of the involved parameters, of the domain geometry and of the water table variation, produces an horizontal deformation whose behaviour agree with the observed one and whose amplitude is comparable (and even higher, with the end-member value $J = 20‰$) to the observed one, characterized by a maximum amplitude displacement of ~ 1 cm. In particular, the model reproduces to the first-order the observed horizontal displacements for realistic variations of the water table within the karstic reservoir and anisotropic variations of the elastic moduli.
The vertical displacement produced by this model doesn't reproduce, as expected, the observed one, that show a time-shifted subsidence (see section 5.3). We have already proposed an explanation for the observed vertical deformation involving the surface loading (see section 6.1.2) and the preliminary model described here doesn't take into account the deformation effect related to the water load. Furthermore the uplift effect is noticeably reduced in the anisotropic models.
Further analysis, especially on the anisotropic assumption and on the parameters values, would be useful to better constrain the model features and the involved processes.

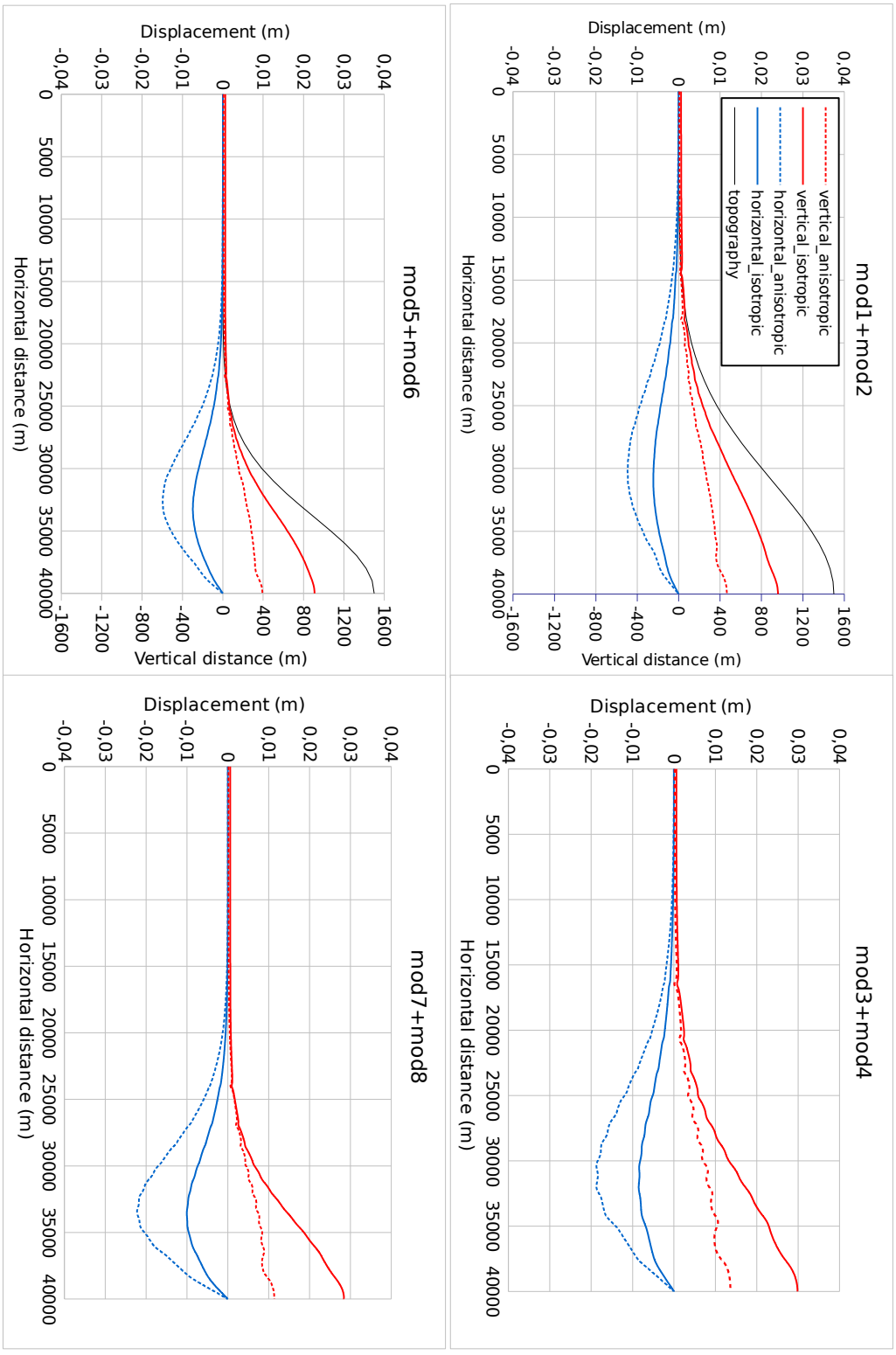

Figure 6.13: Horizontal (blue) and vertical (red) displacements at the surface due to an increase of the water table height. The results for the eight models listed in Table 6.1 are represented.

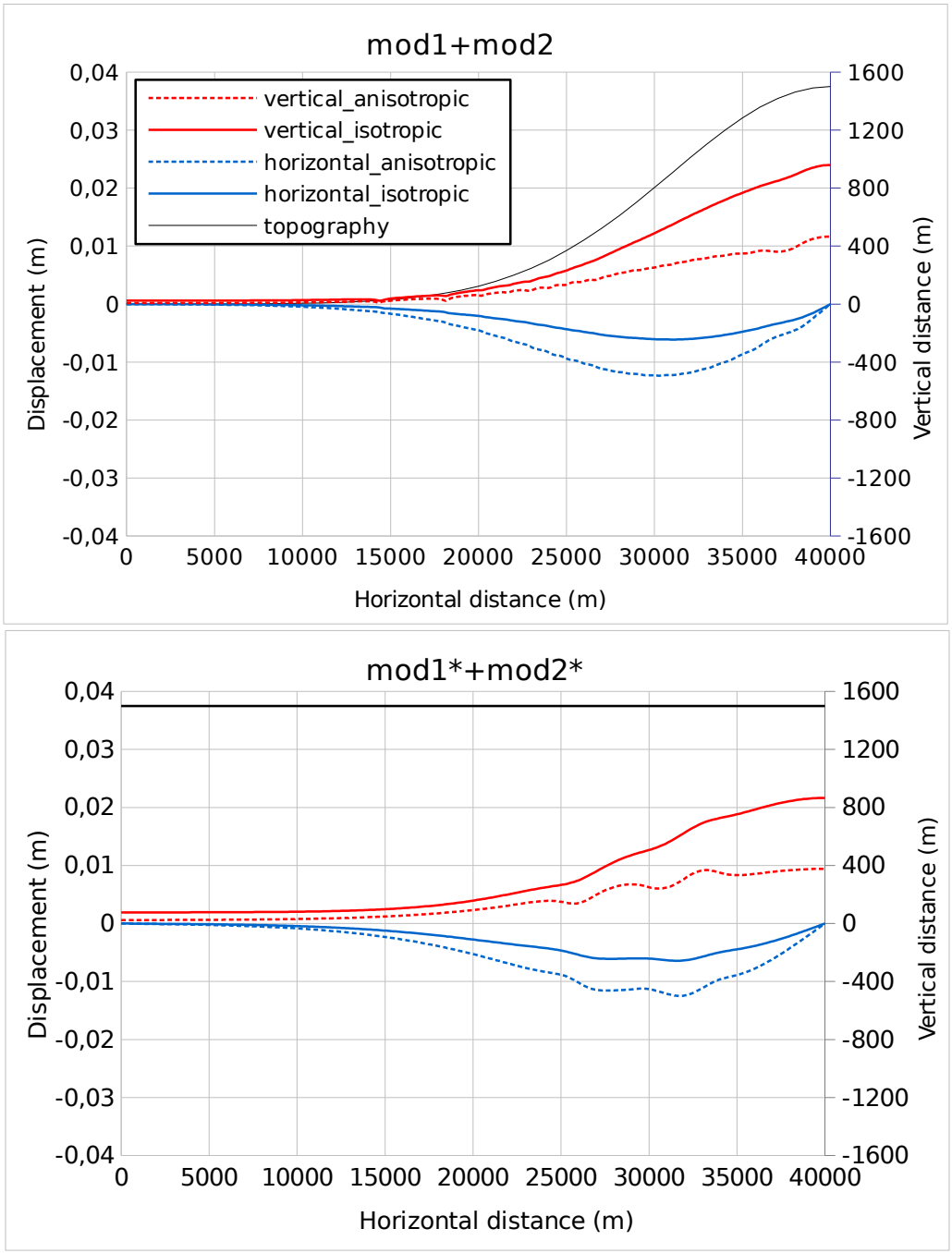

Figure 6.14: Horizontal (blue) and vertical (red) surface displacements. Results for the models 1 and 2 with Gaussian (mod1+mod2, as in Figure 6.13) and flat (mod1*+mod2*) surface topography are represented.

In order to reproduce both the vertical and horizontal observed displacements, a compound model simulating both the effects of surface loading applied over a wide area and of water table variation inside aquifers would be required.

6.3 Analysis of possible transient deformations related to L'Aquila earthquake

As mentioned in the previous paragraphs, the analysis of transient signals in GPS time-series of Central Italy is complicated by the presence of the M_W 6.3 L'Aquila earthquake occurred in April 2009. Seismic events, in fact, besides coseismic offsets, can produce transient postseismic signals in GPS time-series (chapter 1). Furthermore, in the last years increasingly attention has been focused in detecting eventual transient signals preceding the main earthquakes.

After L'Aquila earthquake, a visible postseismic deformation lasting few months has been highlighted by GPS and InSAR observations over an area extending >30 km from the epicentre (e.g. at sites AQUI, INGP, CONI, ROPI, TOSS, CATO, PAGA in Figures 5.2b and 5.11a). This deformation has been satisfyingly explained through afterslip on the main fault (Paganica fault) and on a near fault where several aftershocks occurred (Campotosto fault) (Figure A.4) (e.g. Cheloni et al., 2014; Gualandi et al., 2014).

A few attempts to infer transient signals before L'Aquila earthquake have been made. On the basis of GPS and InSAR data, different deformation processes that occurred a few weeks and a few years before the earthquake have been proposed (Atzori et al., 2013; Borghi et al., 2016).

Since in Italy just a small number of instrumentally recorded moderate earthquakes happened, the L'Aquila earthquake could represent a precious mean to provide important information about the earthquake cycle and the structure and rheology of the lithosphere in this area. In particular, a few attempts to constrain the lower crust/upper mantle viscosity and the thickness of the

elastic crust have been done by using the postseismic deformation after the main earthquakes of the last decades: the 1980 Irpinia earthquake and the 1997 Umbria-Marche earthquake (Riva et al., 2000; Aoudia et al., 2003; Dalla Via et al., 2003).
The multi-annual, hydrologically related, transient deformation that we have highlighted in this work, however, unveils a strong, non tectonic, source of deformation characterizing the carbonate Apennines which can make tectonic-related signals from moderate earthquakes difficult to be detected. Furthermore it is necessary to pay careful attention in order to not to confuse the signals associated with tectonic and non-tectonic sources. The trade-off between tectonic and non-tectonic transients is analysed in the next paragraph (section 6.3.1) focusing on the case of a possible viscoelastic postseismic deformation after L'Aquila earthquake.

6.3.1 Viscoelastic postseismic deformation

In order to verify the extent to which a possible long-term postseismic deformation after the L'Aquila earthquake could be detected by GPS time-series, here we show some simple models of postseismic viscoelastic deformation. These have been produced by using the PSGRN/PSCMP code by Wang et al. (2006), which calculates the viscoelastic postseismic deformation related to a given coseismic slip distribution and Earth structure model. We use a simple Earth model consisting of an elastic layer over a Maxwell viscoelastic half-space with two free parameters, i.e. the thickness of the elastic layer (H) and the viscosity of the half-space (η) (Figure 6.15). We have tested three different coseismic slip models, however, since no meaningful differences arise between them, here we present only the results for the coseismic slip distribution by Cirella et al. (2012).
Figure 6.16 show the cumulative displacement pattern expected 5 years after the earthquakes for two Earth models with $\eta = 10^{18}$ Pas and, respectively, $H = 15$ km (i.e. fault depth) and $H = 30$ km (i.e. approximately the depth of the Moho discontinuity in this area (Di Stefano et al., 2011)). $\eta = 10^{18}$

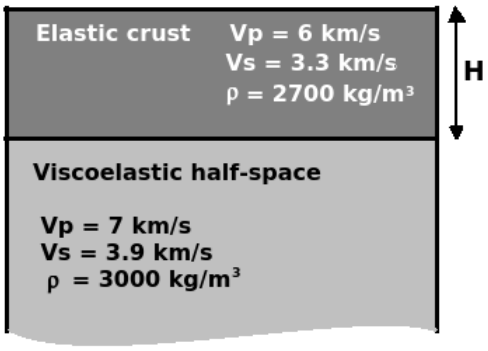

Figure 6.15: Schematic representation of the Earth model and related parameters used to estimate the posteismic viscoelastic relaxation.

Pas can be considered a lower bound for the typical viscosity values of the continental lower crust/upper mantle (e.g. Dalla Via et al., 2003; Wang et al., 2009; Bie et al., 2014), therefore the estimated postseismic deformation represents an upper bound of the expected displacement magnitude. Some main features of the predicted postseismic deformation can be highlighted: spreading horizontal deformation, making the sites on the foot-wall moving toward East and the ones on the hanging-wall toward West; uplift in the hanging-wall area, that is in the opposite direction of the vertical displacement associated with coseismic and afterslip on a normal fault (Figure A.4); deformations with lower magnitude and larger wavelength in the case of a higher thickness (H). The larger wavelength is evidenced in Figure 6.16 by the visible different direction of the horizontal displacement at the sides of the fault, but mainly by the wider area of uplift around the fault.

Firstly, we simply compare the magnitude of the observed multi-annual signal with the one of the modelled viscoelastic deformation. For this purpose, besides the coseismic and instrumental offsets, we remove a long-term (interseismic) trend from the observed time-series by considering the whole available data interval (before and after the earthquake). This comparison is shown in Figure 6.17 for several sites in the near (Figure 6.17a) and far (Figure 6.17b) field of L'Aquila earthquake. Even if the time-series presented in Figure 6.17 can't be directly compared since the seasonal signal and the after-

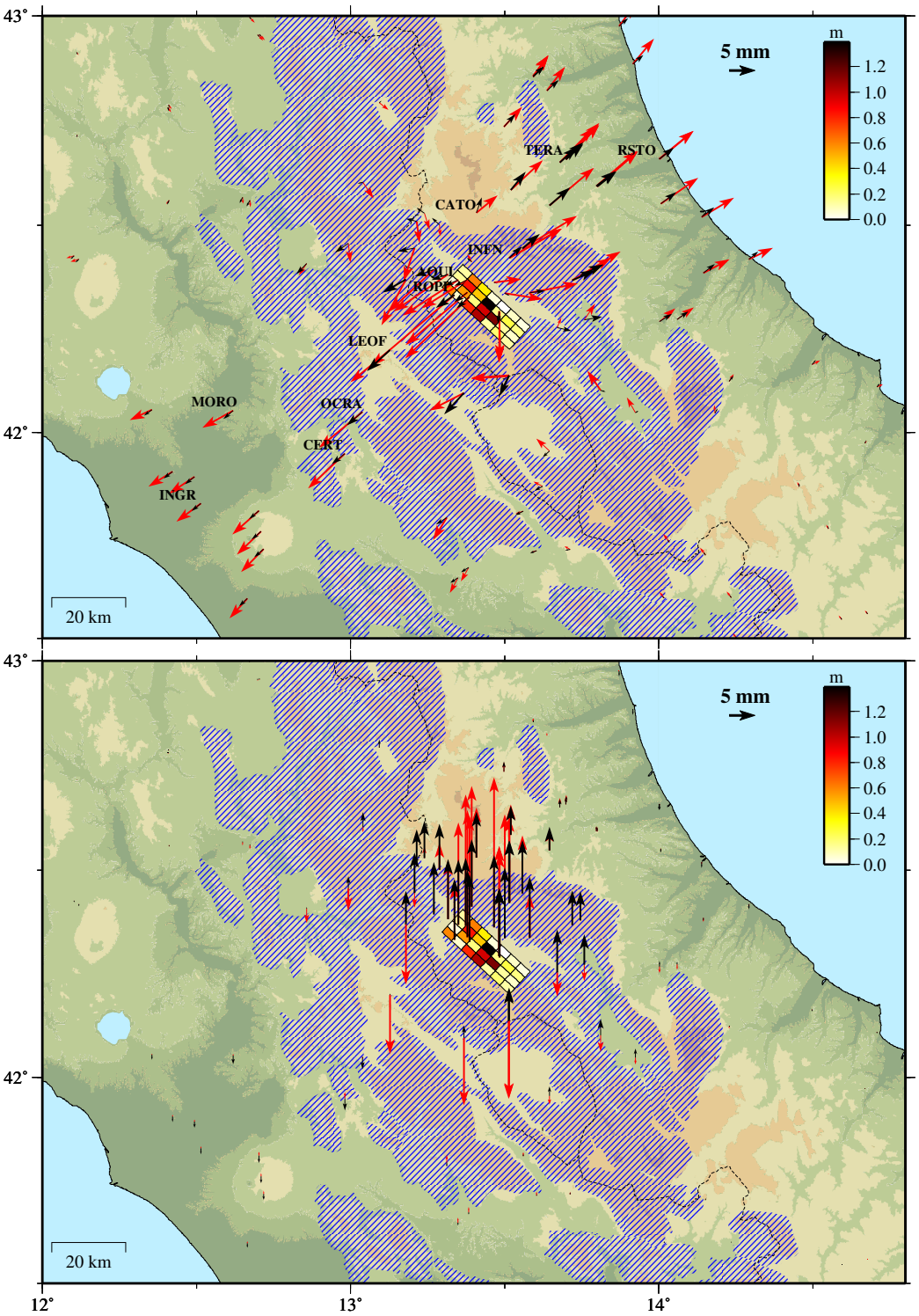

Figure 6.16: (Continued on the following page.)

Figure 6.16: Modelled horizontal (top) and vertical (bottom) cumulative displacements 5 years after the mainshock for a model with viscosity $\eta = 10^{18}$ Pas and two extreme values of the thickness of the elastic layer: $H = 15$ km (red arrows) and $H = 30$ km (black arrows). The rectangle represents the coseismic slip model (color coded, from Cirella et al. (2012)) we used as input for the estimation of the viscoelastic postseismic deformation.

slip haven't been removed from the observed data, their juxtaposition gives an idea of the relative magnitude between the hydrologically related multi-annual signal and the amplitude of an eventual viscoelastic deformation. In particular, at several sites, the amplitude of the multi-annual oscillations is comparable, or even higher, to the expected viscoelastic deformation.
Even if these processes act over different time-scales ($\sim$ 4 years "periodicity" for the hydrological signal, Maxwell relaxation time $\tau_M = \frac{\eta}{\mu}$ for the viscoelastic deformation) this comparison gives an idea of the difficulty that could arise in detecting such tectonic deformation when the time-series are affected by strong non-tectonic transients.

A further, even more dramatic, problem is related to the shortness of the time-series duration. Generally, when postseismic processes have to be analysed from GPS time-series, the interseismic trend is estimated by using only the data interval before the earthquake, taking into account also seasonal oscillations and jumps, if any. This is done because postseismic signals could cause temporary deviations from the secular deformation field (e.g. Liu et al., 2015). The so calculated interseismic trend is therefore removed from the whole time-series so that what remains in the postseismic time-series is, in principle, related only to postseismic processes.
Usually time-series of at least 2.5 years are considered long enough to estimate interseismic rates in a quiescent region (where earthquakes do not occur since enough time) (Blewitt and Lavallée , 2002). In Central Italy lots of GPS sites have been installed after 2006.8, and aren't therefore long enough to estimate a preseismic trend. Just few GPS stations date back to before 2005, however several sites have been installed between 2005 and 2006.8 (Figure A.6). The

latter are therefore, in principle, suitable to estimate a distribution of pre-earthquake, interseismic rates that could be then interpolated in order to assign a long term trend to sites with shorter time-series. In this work, however, we have highlighted that a strong multi-annual signal affects GPS time-series causing visible deviations from the interseismic trend (Figure 5.2). This heavily complicates the interseismic rate estimation from short time-series, since a multi-annual signal of about 4 years makes the 2.5 yr interval no more adequate.
This situation is furthermore made more complex by the fact that the period of about 2.5 yr before the mainshock (i.e. T1 time interval) is characterized by a strong hydrologically related trend (e.g., Figure 5.11). As shown in Figure 6.18, the principal effect of detrending at sites with short (about 2.5 yr) preseisimc time-series and high multi-annual deformation is to produce a strong accentuation of the postseismic trend. This is mainly due to the fact that the multi-annual signal has a symmetric horizontal pattern with respect to the drainage divide that resembles (same direction with opposite versus in T1 and same direction and versus in T2) the horizontal pattern of the viscoelastic deformation, apart from the very near field on the hanging-wall of the fault (compare Figures 6.11 and 6.16(top)). This (accidental?) agreement causes the post-seismic trend to be strongly accentuated making viscoelatic models with (unrealistically) low viscosity (compare the dashed blue lines, $H = 15$ km, $\eta = 10^{18}$ Pas, and the dotted blue lines, $H = 15$ km, $\eta = 5\text{x}10^{17}$ Pas, in Figure 6.18) or low thickness H (compare the dashed blue lines, $H = 15$ km, $\eta = 10^{18}$ Pas, and the bold blue lines, $H = 30$ km, $\eta = 10^{18}$ Pas, in Figure 6.18) to be favoured.

As a proof of the artificial nature of this effect we can see that we re-obtain it if an analogous detrend (i.e. considering only short "preseismic" data) is applied to time-series of South-Central Apennines (Figure A.7a). These show strong multi-annual variations, with the same "periodicity" of the Central Apennines (section 5.3), but are clearly not affected by L'Aquila earthquake.

Unfortunately only a few sites in Central Apennines have pre-earthquake data long enough to mediate over at least two "cycles" of the multi-annual hydrological signal. In Figure A.7b the preseismic trend is removed for 4 time-series beginning between 2000 and 2002. In this case, some trend variation can be seen after the mainshock. This could be referred to viscoelastic deformation in a couple of sites in the far field (INGR and RSTO) whereas AQUI, located in the very near filed, doesn't show a good agreement. Several factors, however, could influence this trend variation, such as errors in the removal of coseismic and instrumental offsets and the afterslip.
On the basis of the already highlighted strong influence that water filled rocks play on the GPS time-series and the impact of L'Aquila earthquake on the nearby aquifers (Amoruso et al., 2011; Adinolfi Falcone et al., 2012; Galassi et al., 2014), some contribution from postesismic poroelastic deformation in the sites near Paganica fault cannot be excluded.

6.3.2 Comments about the tectonic and non-tectonic transients trade-off

The previous analysis evidences the importance of keeping in mind the presence of strong non-tectonic multi-annual signals when dealing with tectonic-related deformations in the Apennines area. The postseismic viscoelastic deformation affects time-series mainly as a (gentle) trend variation after the earthquake, especially for low values of viscosity/high values of thickness H (Figure 6.18), therefore its detection, and the consequent estimation of the rheological parameters of the Earth, heavily depend on a correct estimation of the interseismic trend. In the case of Central and South-Central Italy, strong limitations are related to the short length of the preseismic data for most GPS sites, the occurrence of moderate earthquakes which causes low amplitude deformation and the simultaneous presence of a visible multi-annual non-tectonic signal. The highlighting of this strong source of deformation and the comparison with areas affected by similar non-tectonic transients, but not influenced by recent earthquakes will be of help in future analysis of

tectonic-related signals in the Apennines area.
Ideally, in order to isolate the tectonic signals, the non-tectonic deformation should be correctly removed from the time-series. As we have highlighted in the previous sections, the exact modelling of the non-tectonic deformation is hard to achieve, given the complexity and plurality of the involved areas and processes. Nevertheless independent data such as rainfall or spring discharge data surely represent a key tool, therefore further efforts have to be done to accurately collect these kinds of data and make them easily available.
Recently an increasing number of refined statistical techniques have been developed with the aim of detecting transient signals in time-series and distinguishing different sources of deformation (e.g. Ji and Herring, 2013; Gualandi et al., 2015; Bekaert et al., 2016; Walwer et al., 2016). These techniques would be surely of help in complex areas as the Apennines, where multiple sources of deformation overlap. Nevertheless their application should always take into consideration complexities as time-shift between time-series, limited number of sites and short datasets. Gualandi et al. (2015), employing the vbICA (variational Bayesian Independent Component Analysis) technique to a sample of GPS time-series (time interval 2007-2013.5) in the L'Aquila area, confirmed the presence of a multi-annual signal in the horizontal components and stated the afterslip as the main source of postseismic deformation, decaying in 150 days (note that, however, a preliminary detrend using pre-seismic data had to be applied to time-series).
The investigation of L'Aquila preseismic signals from surface observations is particularly challenging because of the small involved magnitudes expected for a moderate earthquake. The presence of strong non-tectonic signals make this analysis much harder. As an example, the broad deformation starting 3 years before the mainshock detected by Atzori et al. (2013) from InSAR data occurs suspiciously in a time-interval characterized by a strong variation of the rainfall, and therefore terrestrial water content, amount ($\sim 2007 \div 2009$ i.e. T1 time interval) (Figure 5.3). Borghi et al. (2016) isolated a short preseismic transient signal from GPS time-series of sites near the fault by means

of PCA (Principal Component Analysis). A similar signal has been also detected by Gualandi et al. (2015) by means of the more sophisticated ICA technique. The author however highlights that the evidenced signal mainly rely on only one station contribution.

Further careful analysis are needed to assess the presence of possible pre-seismic signals and of eventual interactions between hydrologically-related deformations and seismicity.

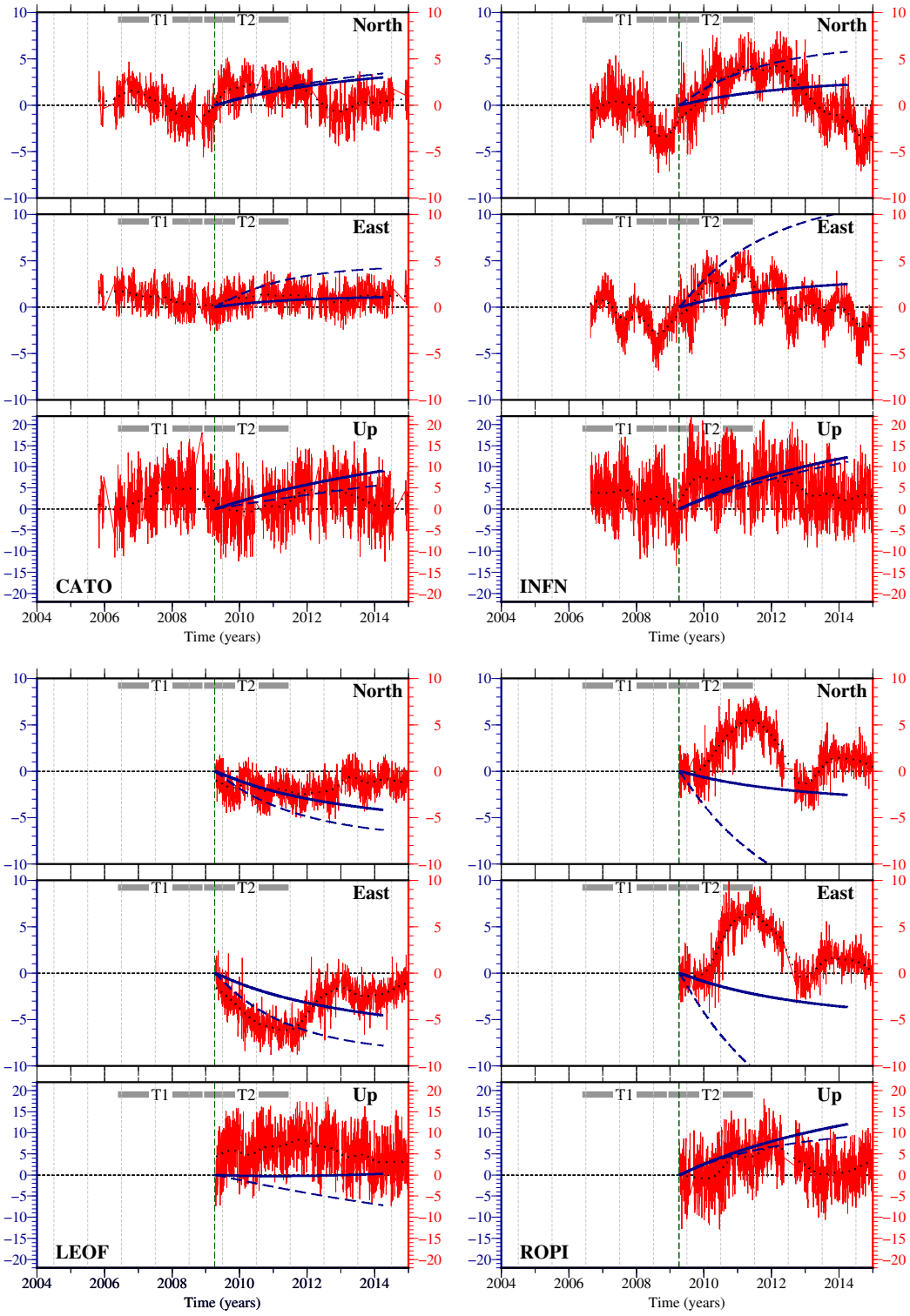

(a) Near filed

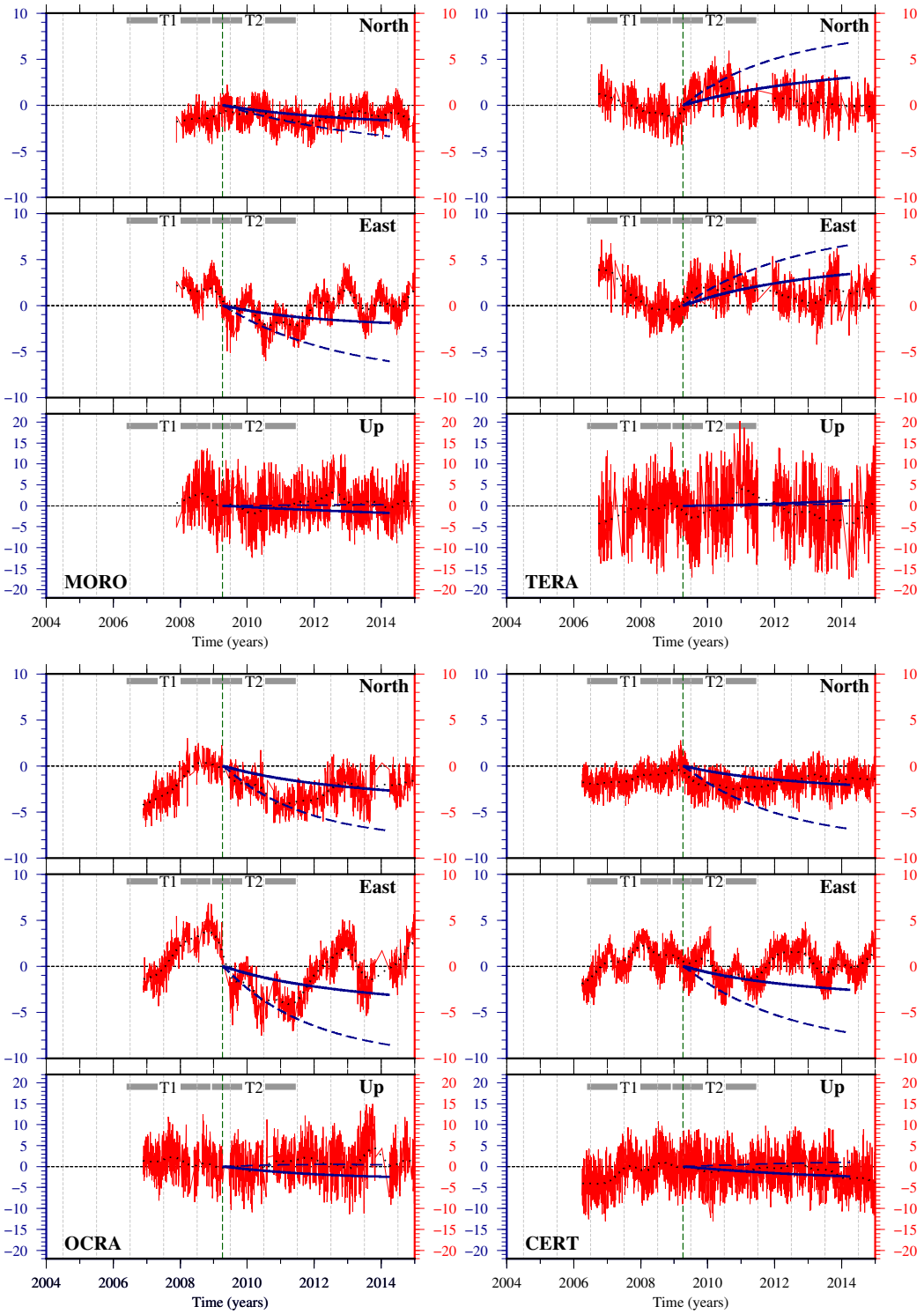

(b) Far field

Figure 6.17: (Continued on the following page.)

Figure 6.17: Comparison between the modelled daily time-series due to postseismic viscoelastic relaxation (blu) and the daily detrended observed time-series (red) for several sites in the near (a) and far (b) field of L'Aquila earthquake. Long term trend and coseismic and instrumental offsets have been removed from the observed time-series, that have been vertically shifted in order to have zero displacement after the mainshock epoch (vertical dashed green line). The dotted black line represents a 2 yr Gaussian filter of the observed time-series. The two models of Figure 6.16 are shown, with $\eta = 10^{18}$ Pas and, respectively $H = 15$ km (dashed blue line) and $H = 30$ km (bold blue line).

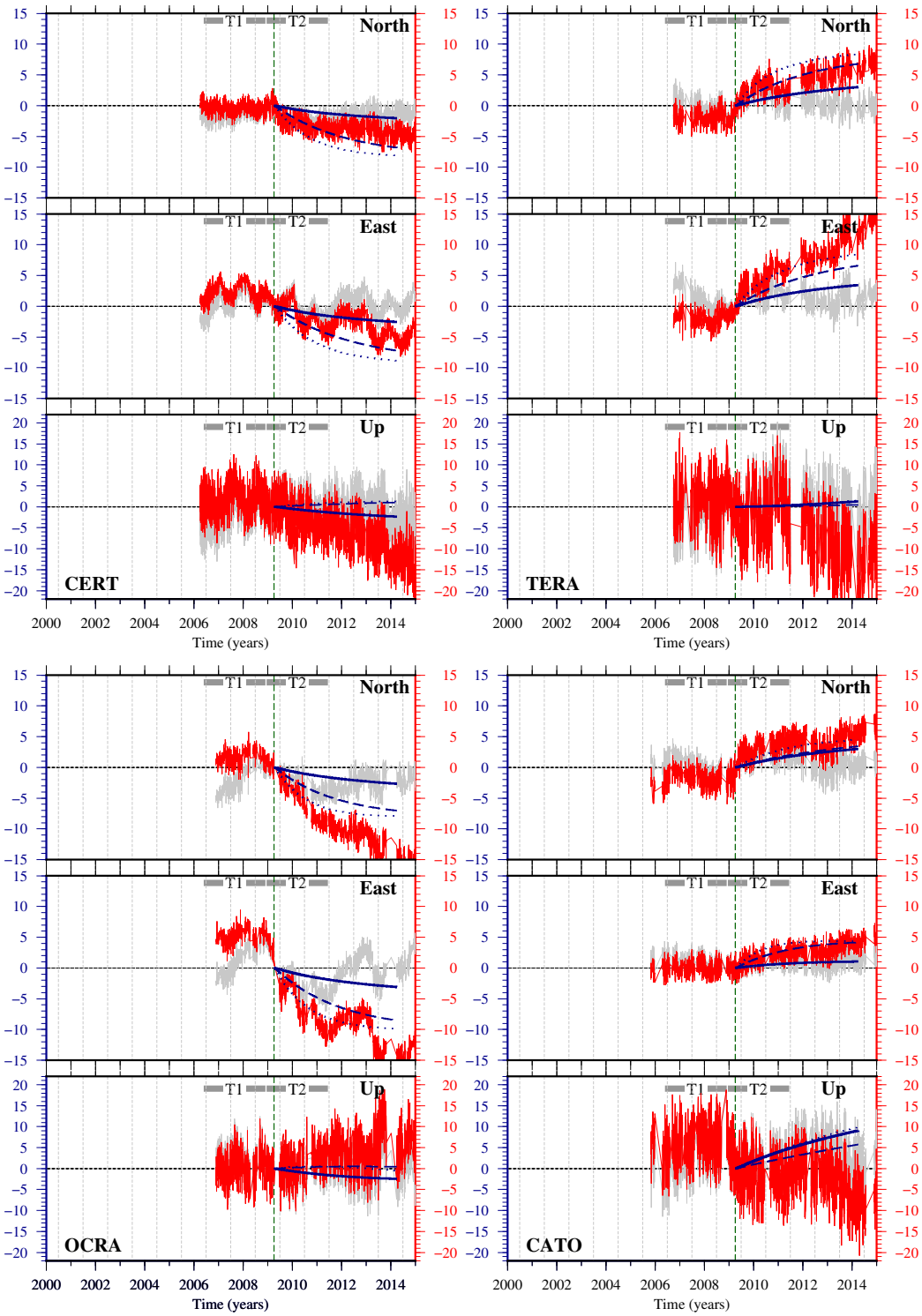

Figure 6.18: (Continued on the following page.)

Figure 6.18: Comparison between the modelled daily time-series due to postseismic viscoelastic relaxation (blu) and the daily observed time-series detrended by using only pre-earthquake data (red) for several sites in Central Italy. Notice that time-series for a model with $H = 15$ km and $\eta = 5\text{x}10^{17}$ Pas (dotted blue line) have been added compared to Figure 6.17. Coseismic and instrumental offsets have been removed from the observed time-series. As a comparison, gray lines show daily observed time-series detrended by using the whole time-series (as in Figure 6.17). All the other elements are the same of Figure 6.17.

Chapter 7

Conclusions

In this thesis we have described a hydrologically-related multi-annual transient signal affecting the GPS time-series of sites located in Central and South-Central Apennines. Unlike most of the hydrologically-related transient signals evidenced from GPS observations (Amos et al., 2014; Chanard et al., 2014, e.g.), which are characterized by high vertical amplitudes and small horizontal deformations, in this case even the horizontal components show noticeably high amplitude (up to 1 cm).

The GPS time-series show that the interseismic ∼3 mm/yr extensional opening in the axial part of the Apennines (D'Agostino, 2014) is modulated by annual and multi-annual signals that modify the stationarity of the tectonic trend. This modulation can be particularly appreciated by projecting the horizontal component perpendicularly to the Apennines ridge and appears to affect mostly the sites located along the Apennines and to progressively vanish towards the coasts. In particular, we have evidenced two successive 2.5 years long time intervals in the GPS time-series in which sites preferentially located close to the carbonate massifs show inward (T1, 2006.4-2008.9) and outward (T2, 2008.95-2011.45) motion.
Despite the lower signal-to-noise ratio, even the vertical component shows both a coherent annual seasonal signal (peak of uplift in summer and of subsidence in winter) and a multi-annual variation characterized by two peaks

of upward motion in 2007-2008 and 2012. However two main differences arise between the horizontal and vertical components: (i) the vertical pattern has the same features everywhere, conversely the horizontal signal show a reversed "sign" from one side of the Apennines to the other, (ii) the amplitude of the vertical transient signal doesn't change significantly over the whole area, whereas the horizontal one decreases drastically in sites located far from the carbonate massifs hosting large karst aquifers.

We have presented three kinds of data that give informations about hydrological phenomena: the rainfall data of four rain-gauges whose location span over the area under examination, the discharge data of some of the main karst springs of Central and South-Central Apennines and the terrestrial water storage (TWS) observations recorded by the GRACE satellite. The latter, being characterized by a 300 km resolution, don't allow to spatially define the source of mass variability at the scale of the study area, but represent an average of the rapidly changing TWS in the Apennines and the more stable mass anomalies in the nearby areas. GRACE data therefore likely provide informations about the TWS temporal variability and the influence of long wavelength changes of the TWS on the observed GPS signal.
All these hydrological data show noticeable inter-seasonal variability and a visible multi-annual trend with significant reduction of rainfall/spring discharge/TWS in drought years 2007-2008 and 2012. The previously defined T1 and T2 time intervals correspond to periods of anomalously low (T1) or high (T2) precipitations/spring discharge/TWS. In particular, all the analysed spring hydrographs are characterized by a smoothed shape with discharge peaks delayed of about 3-4 months compared with rainfall peaks, whereas no significant time-shift arise between the rainfall and the TWS data.

A deepened comparison between GPS data and hydrological observables revealed a significant correlation that leaded us to propose a hydrologically-related cause of our observations. In particular it highlighted a different behaviour and phase for the horizontal and vertical deformations: (i) peaks

in outward horizontal GPS displacements with respect to the Apennines axis occur in late spring-summer and are closely correlated with discharge of the main karst springs; (ii) vertical GPS motion appears to be inversely correlated and approximately in phase with TWS variations recorded by GRACE with peak values (negative GPS, postive TWS) displacements occurring in late fall-winter months. This comparison therefore suggests that vertical deformation reacts almost simultaneously to rainfall loading, whereas horizontal deformation is delayed and better correlated with the spring discharge.

We have then investigated the processes that could have a role in causing the main features of the observed transient deformation, which are common to the whole studied area. We have firstly estimated the deformation due to the elastic response to surface loading, since this model is usually employed to simulate hydrological loads (i.e. ice, snow, continental water storage) (Amos et al., 2014; Chanard et al., 2014, e.g.). The resulting horizontal displacements cannot explain the observed ones, being too small, especially at sites near carbonate aquifers, and showing a reverse versus of motion. Conversely, the significant degree of correlation between vertical GPS and GRACE data and the agreement with modelled vertical displacement suggest that the regional-scale hydrological loads (within a radius of about 1000÷2000 km) can explain most of the observed vertical GPS data. The results of the load models, together with the correlation analysis between the observed displacements and the hydrological data, suggest that two different mechanisms could be involved in the observed deformation. The vertical displacements could be due to the surface loading affecting the whole studied area, whereas the peculiar trend and magnitude of the horizontal deformation could be specifically related to the presence of carbonate aquifers. The carbonate massifs of the Apennines in fact host huge aquifers that are characterized by broad highly fractured phreatic zones with scarcely developed drains (e.g. Fiorillo et al., 2015b). We therefore propose that the horizontal deformation is related to the fluctuations of the water table level and the related hydrostatic pressure variations that cause the opening of

fractures and the consequent deformation of the whole massif.
To try to simulate this complex mechanism and to reproduce the first order features of the observed horizontal deformation we have used two different simple models. The first one mimics the effect of a medium permeated with sub-vertical opening fractures through a big tensile dislocation located approximately in the middle of the fractured aquifer. In this model the deformation induced by hydrostatic pressure variations has been simulated through the "ad hoc" opening of the tensile dislocations. With the second model we have tried a more realistic modelization of the observed phenomenon. In this case the deformation of the medium is directly induced by realistic variations of the hydrostatic pressure and of the elastic constants. We have calculated the displacements due to the variation of the water table height inside a porous aquifer by using a finite difference model based on the effective stress principle. In this case, both planar and non-planar geometries and isotropic and anisotropic material properties have been examined. Despite the applied models are simple and preliminary analysis has been carried out, the results indicate that the proposed mechanism is suitable to explain the observed horizontal deformation.
Further investigations based on the GPS observations should improve the understanding of the deformation and behaviour of the carbonate aquifers of the Apennines, which represent a strongly important resource for the Italian territory.

By focusing on the 2009 L'Aquila earthquake (Central Italy), we finally highlighted the difficulties that arise for the estimation of interseimic trend and small tectonic signals in areas affected by significant non-tectonic deformations. The Apennines area represents a complex region which undergoes active extension and where moderate earthquakes occur. The presence of the highlighted hydrologically-related signal evidence a strong source of non-tectonic deformation which can't be ignored in future studies of tectonic-related processes in the Apennines area. Furthermore it would be really interesting to investigate about eventual interactions between hydrologically-

related deformations and seismicity in this region.

Appendix A

Supplementary figures

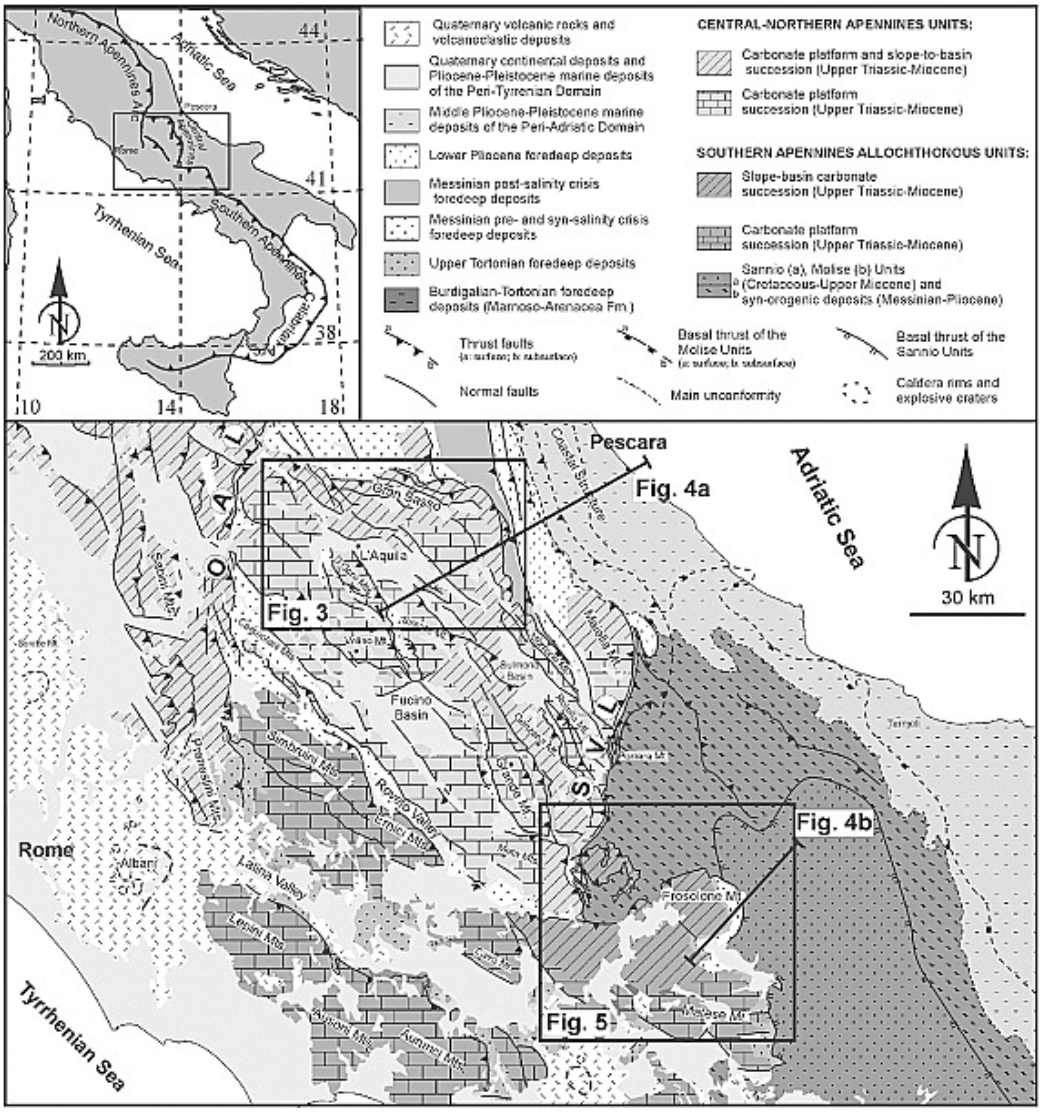

Figure A.1: Tectonic sketch of central Italy. SVL, Sangro-Volturno line; OAL, Olevano-Antrodoco line. Modified from Satolli and Calamita (2008)

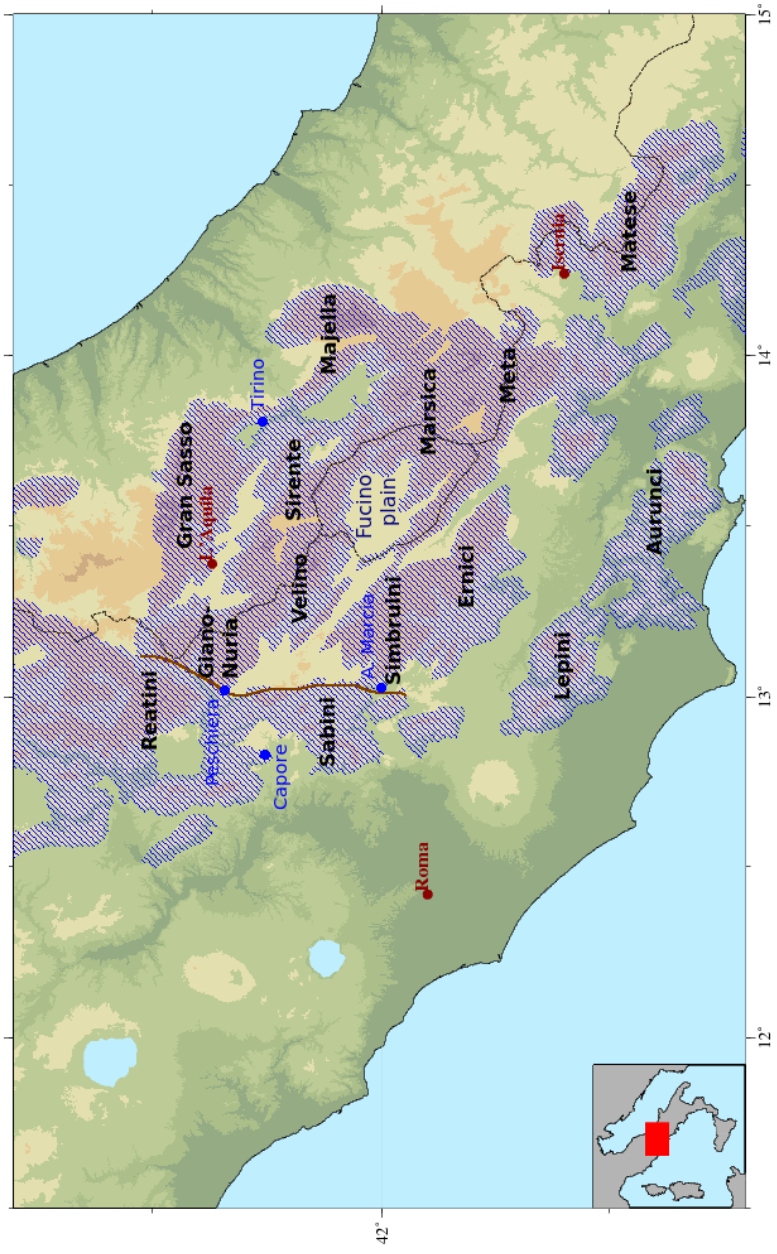
Gran Sasso
Majella
Matese
Ischia
Tirino
Sirente
Marsica
Meta
Fucino
plain
Velino
Giano
Nuria
Simbruini
Ernici
Aurunci
Reatini
Lepini
Sabini
Pescara
Capore
Roma
15°
14°
13°
12°
42°

(a)

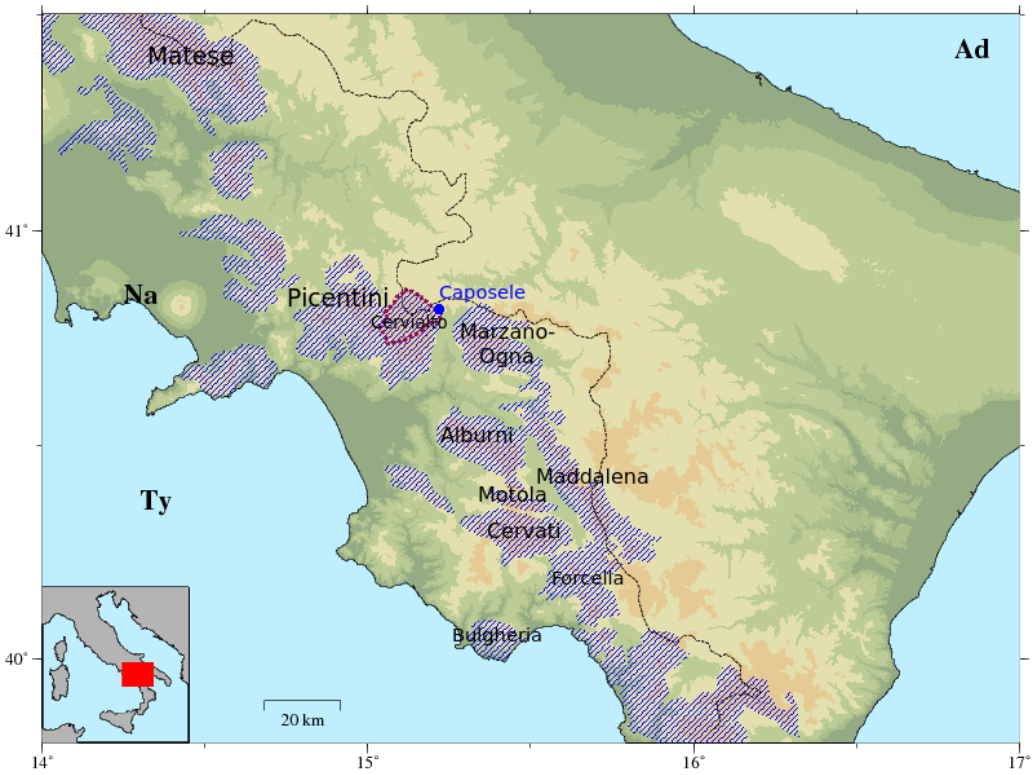

(b)

Figure A.2: Maps of the positions and identification names of the main carbonate massifs of Central (a) and South-Central (b) Italy. The blue circles and names depicts the main carbonate springs. The black dashed line indicates the drainage divide and the blue striped areas outline the main carbonate aquifers. In (a) the brown line depicts the Olevano-Antrodoco thrust that divides the basin and platform domains (Figure 2.4). In (b) the deep pink dotted line surrounds the catchment area of Caposele spring.

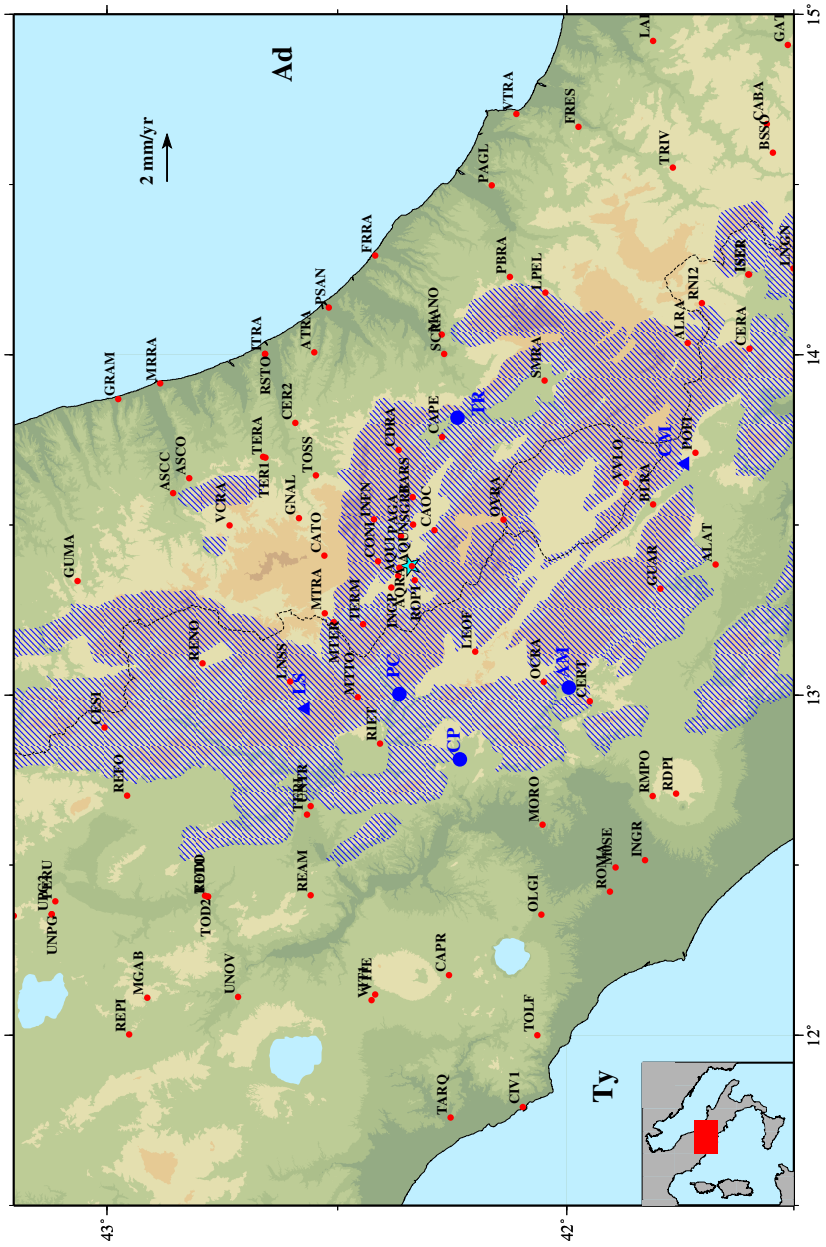
Ad
Ty
2 mm/yr
43°
42°
12°
13°
14°
15°
GRAM
MRRA
RSTO
TRA
ATRA
PSAN
FRRA
PAGL
VTRA
FRES
TRIV
PBRA
LPEL
SCNO
SMRA
CAPE
TR
CDRA
OVRA
ASCC
ASCO
VCRA
TERA
TER1
GNAL
TOSS
CER2
CATO
CONI
INFN
CAOC
GUMA
RENO
MTRA
TERM
MTER
MTTO
LSS
LS
PC
RIFT
LEOF
CP
OCRA
AM
CERT
AYLO
BIRA
CM
POFF
GUAR
ALAT
ALRA
RNI2
CERA
ISER
LNGS
BSSO
CABA
GAT
LAT
RMPO
RDPI
MORO
INGR
ROM
OLGI
REAM
TODI
TOD2
UNPG
UPEL
UNOV
REPI
MGAB
CAPR
TOLF
TARQ
CIV1
REMO
CESI

(a)

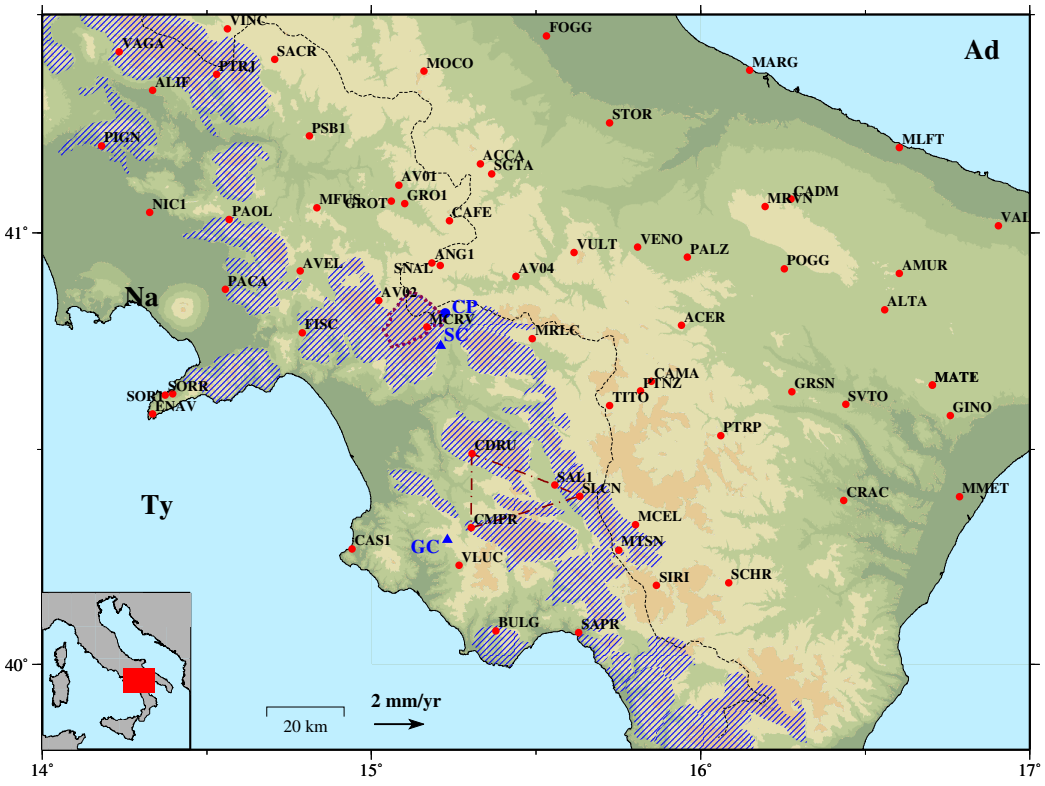

(b)

Figure A.3: Maps of the positions and identification names of the GPS stations used in this work (red circles) for Central (a) and South-Central (b) Italy. The black dashed line indicates the drainage divide and the blue striped areas outline the main carbonate aquifers. The location of the springs (blue circles) and rain-gauges (blue triangles) are also indicated: in (a) Peschiera (PC), Capore (CP), and Acqua Marcia (AM) springs, Leonessa (LS), Campoli Appennino (CM) rain-gauges; in (b) Caposele (CP) spring and Senerchia (SC) and Gioi Cilento (GC) rain-gauges. In (a) the cyan star indicate the 2009 L'Aquila earthquake epicenter location (from `iside.rm.ingv.it`). In (b) the deep pink dotted line surrounds the catchment area of Caposele spring, whereas the brown dot-dashed lines delineate the polygon in which the dilatational strain is calculated.

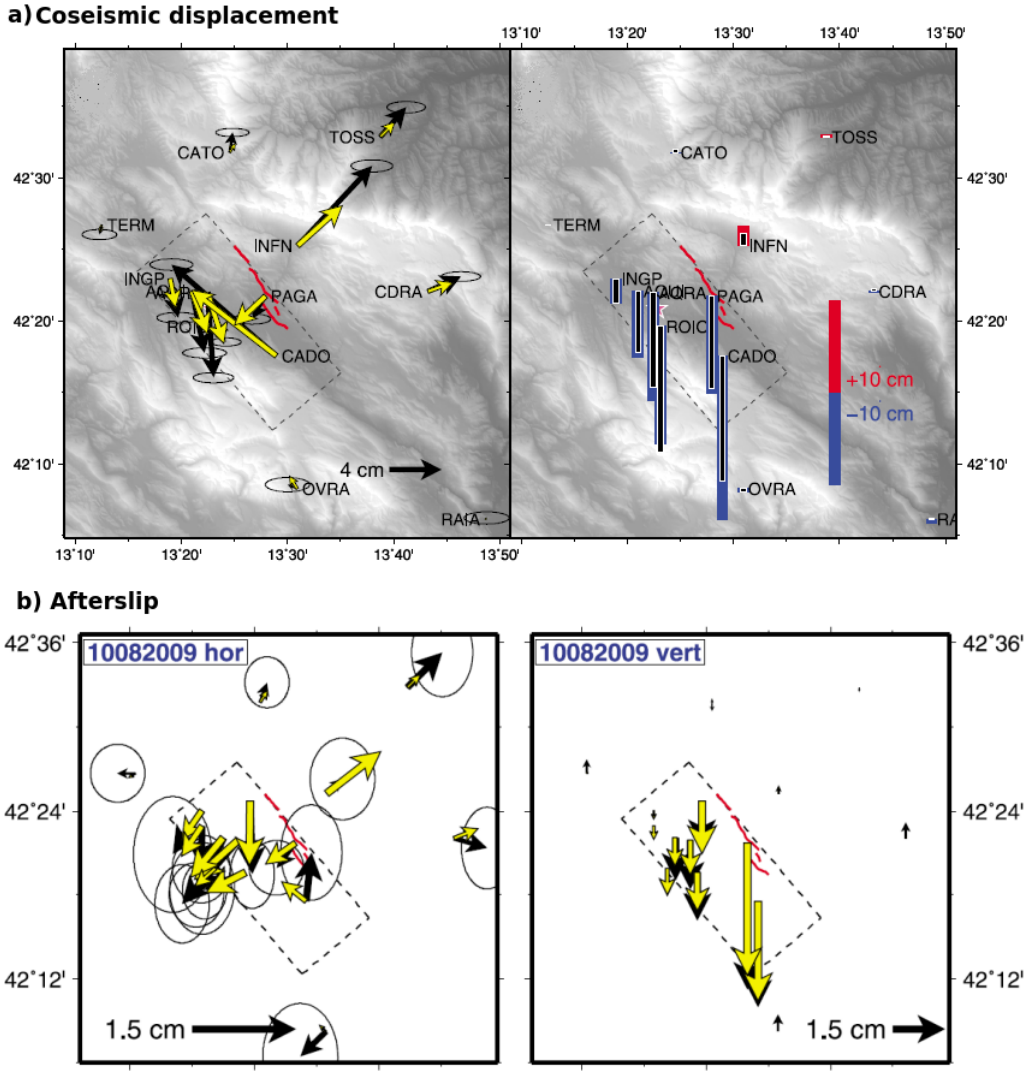

Figure A.4: Costeismic and postseismic observed and modelled (as coseismic slip and afterslip) displacement at GPS sites around L'Aquila earthquake fault. (a) Left: observed (black vectors with 95% CI error ellipses) and calculated (yellow vectors) horizontal displacements; right: vertical observed (red bars, positive; blue bars, negative) and calculated (black bars) displacements. (b) Horizontal (left) and vertical (right) postseismic GPS displacements 4 months after the earthquake (label in the top left corner). Observed displacements are shown as black arrows, whereas yellow vectors represent estimated ones. The black dashed line is the surface projection of the model fault. From D'Agostino et al. (2012).

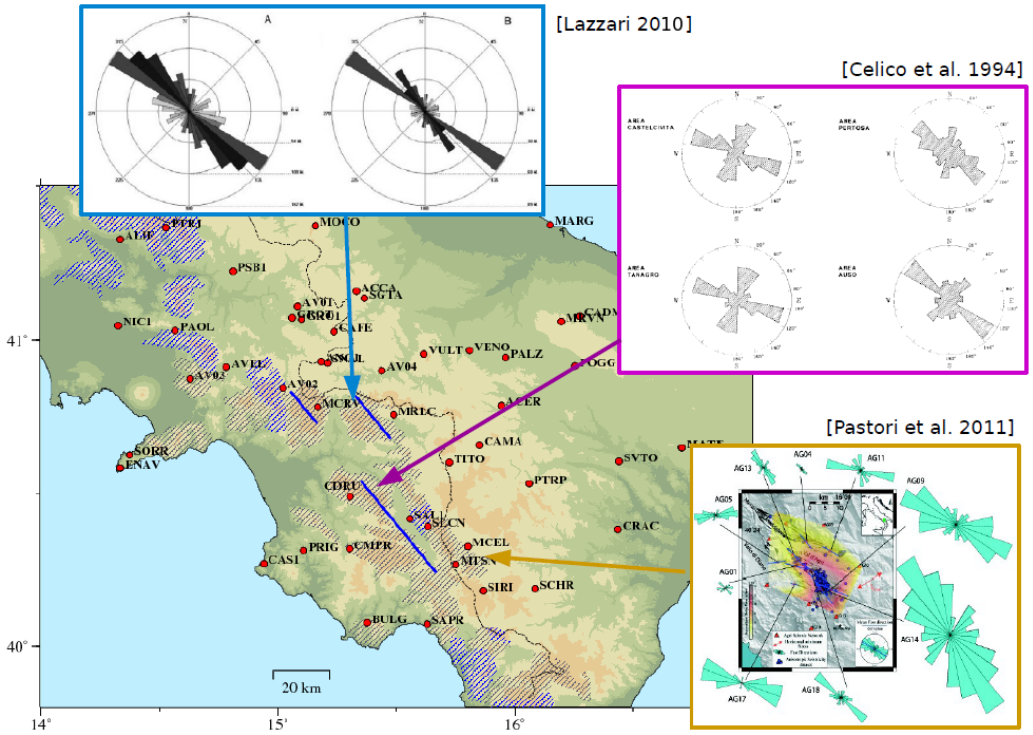

Figure A.5: Some rose diagram representations of the orientation of fractures in South-Central Apennines collected from different works (Celico et al., 1994; Pastori et al., 2009; Lazzari, 2010).

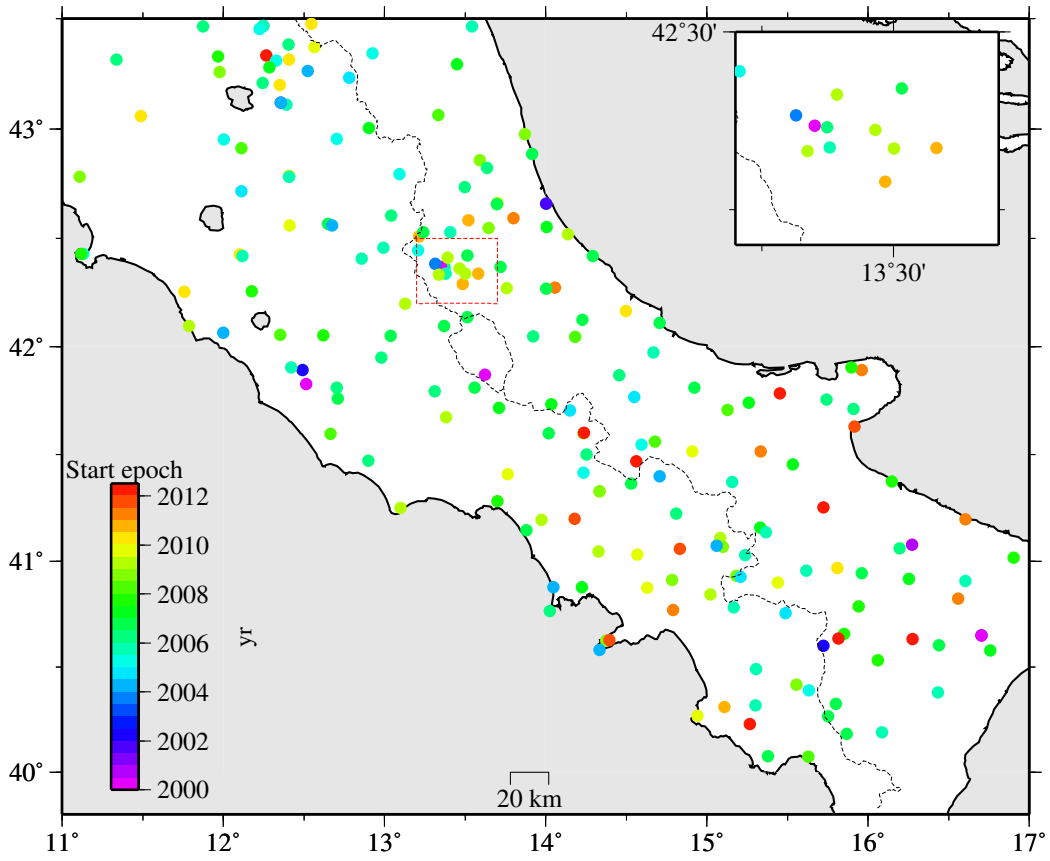

Figure A.6: Map of the time-series start time (color coded) of the Italian GPS network. The inset show a zoom of L'Aquila fault area (red dashed rectangle in the map).

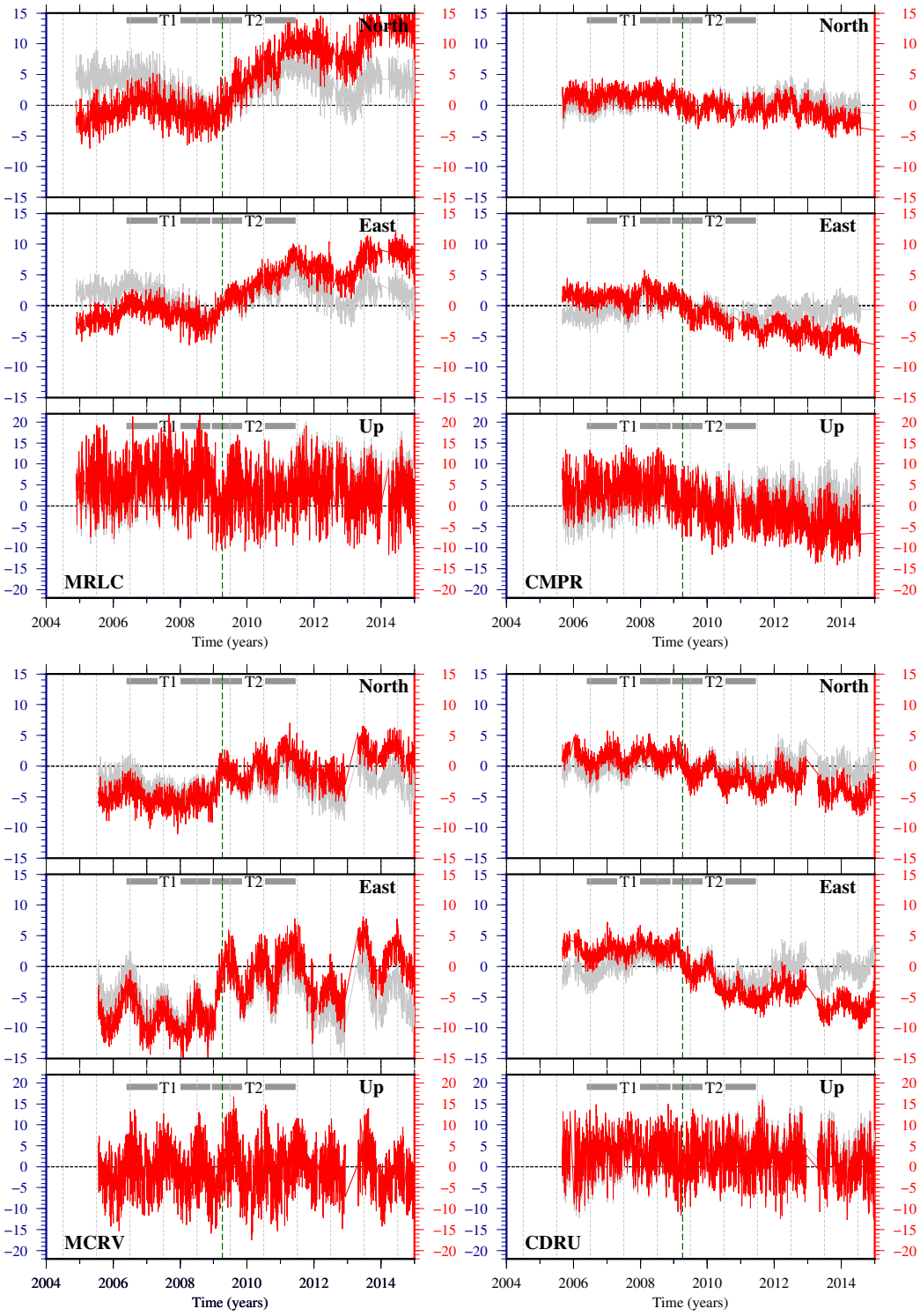

(a) South-Central Italy

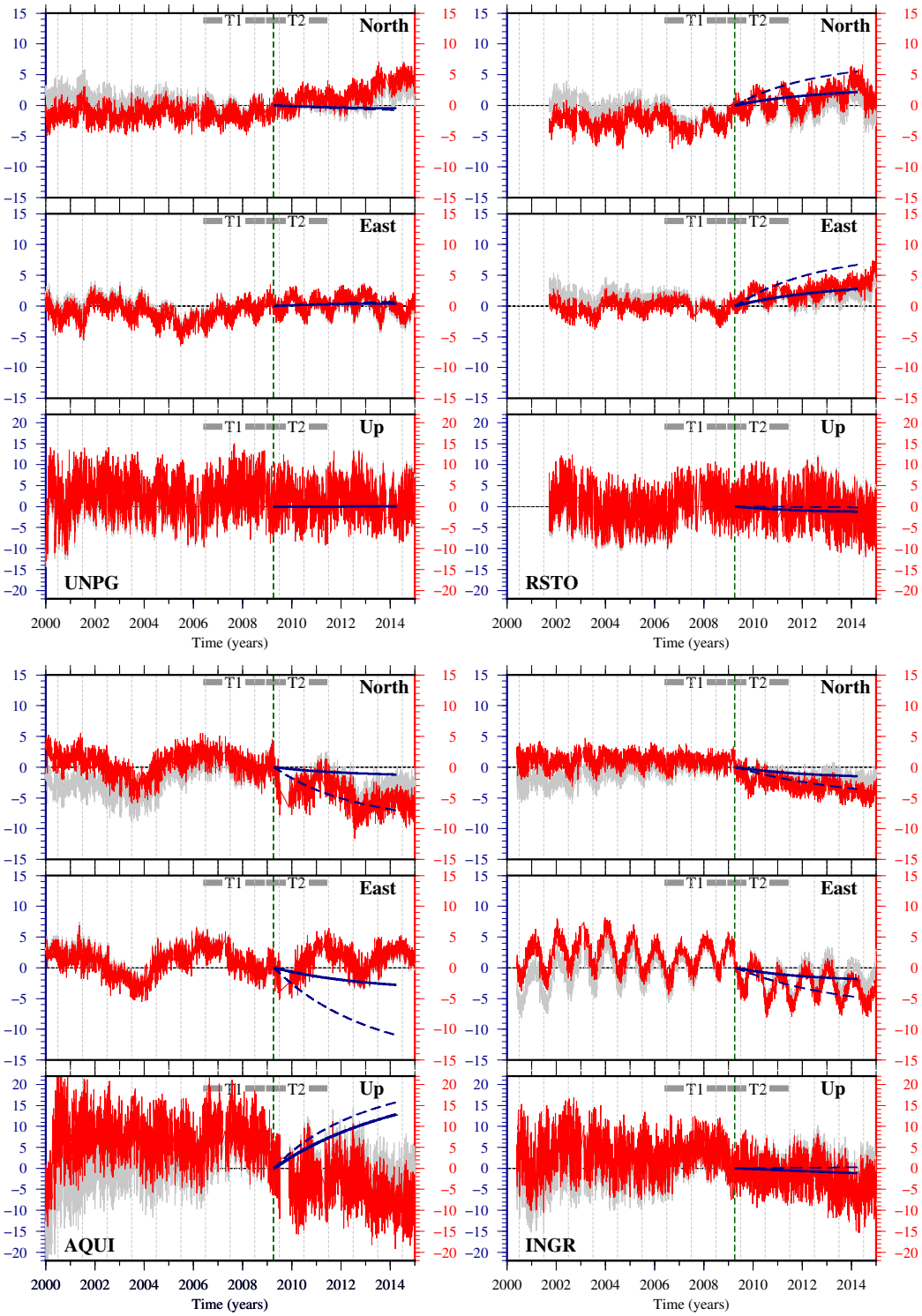

(b) Central Italy

Figure A.7: (Continued on the following page.)

Figure A.7: Daily observed time-series (red) detrended by estimating the long term trend with data prior the L'Aquila earthquake epoch (vertical dashed green line). Coseismic and instrumental offsets have been removed from the observed time-series. As a comparison, gray lines show daily observed time-series detrended by using the whole time-series. In (b) daily time-series due to two models of postseismic viscoelastic relaxation are also represented ($\eta = 10^{18}$ Pas, $H = 15$ km (dashed blue line) and $H = 30$ km (bold blue line)).

Appendix B

Cross-correlation analysis between GPS, GRACE and spring discharge time-series

Cross-correlation analysis provides further insights about the relation between the observed GPS displacements and the temporal variations of the hydrological observables. Firstly a deepened examination is presented about the GPS stations located in the South-Central Apennines, because of the smaller dimensions, the simpler displacement pattern and the lack of recent moderate earthquakes that characterize this area. We will see that, anyway, analogous features can be highlighted also for Central Italy, despite the higher complexity of this region due to the deformation induced by L'Aquila earthquake, the presence of several different carbonate massifs spread on a larger area and noisier spring discharge data.
Cross-correlation has been calculated by using the Matlab function *crosscorr* that provides also approximate confidence boundaries.

Figure B.1 shows cross-correlation plots between the daily horizontal (N45E component) GPS data and the Caposele spring discharge data. The site MCRV, that is the closest to Caposele spring, shows a noticeable high value of maximum correlation (0.89). Correlation is still high at sites that are

tents of kilometres far from Caposele, such as SAL1 (0.77), CDRU (0.72) and is lower but still significant at SLCN (0.63) CMPR (0.52) and MRLC (0.58), whose time-series have a less pronounced seasonal signal. Cross-correlation analysis shows some variability in the time shift associated to the highest value of correlation, that is probably due due to local hydrological effects: MCRV, SLCN and SAL1 are slightly anticipated ($\sim$ 20, 30 and 10 days respectively), whereas CDRU is delayed of about 36 days and CMPR and MRLC show an higher delay ($\sim$ 56 and 72 days respectively).
We have applied the bootstrap statistical method (Moore et al., 2003) in order to associate estimates of uncertainties of correlation and time lag. This technique consists in selecting at random N points from the original sample, where N is the number of observations in original time-series, without regard to whether or not any point has been selected previously. For the new sample of N points (some of which are redundant selections from the original sample, while some points in the original sample are missing), the cross-correlation is recalculated. When this is done many times, a distribution in maximum correlation and time lag is constructed, and from this, one can assign a meaningful statistical uncertainty to the value of the parameters. We performed the re-sampling 500 times and the resultant distributions of maximum correlation values and related time lags are represented in Figure B.2, where also mean values and $1-\sigma$ uncertainties are indicated.

In order to estimate the correlation between GPS horizontal displacement and monthly GRACE data, we have re-sampled GPS time-series at monthly values (Figure B.3). To compare cross-correlation with GRACE and Caposele spring with the same time resolution (1 month), we have re-performed cross-correlation with Caposele spring by re-sampling data at monthly values. The results (Figure B.3) show that the comparison with Caposele spring discharge data provides the highest values of maximum correlation in correspondence to the shortest time-lag values. The opposite occurs for the cross-correlation between the stack vertical GPS displacement and GRACE and Caposele spring discharge: in this case correlation is maximum and time

lag lower for the comparison with GRACE data (see row VSTACK$_S$ in Table B.1).

We have performed an analogous cross-correlation analysis for several sites in Central Apennines, by comparing the horizontal (N65E component) and vertical stacked time-series with Tirino and Acqua Marcia daily spring discharge data and with monthly GRACE equivalent water height data. The results are listed in Table B.1, where we have indicated the maximum values of correlation and related time-lag. Tirino and Acqua Marcia discharge time-series have different shapes, with Tirino showing no significant seasonal variations. This makes GPS time-series with poorly evident seasonal peaks to have higher correlation with Tirino spring and GPS time-series with clear seasonal peaks to have higher correlation with Acqua Marcia spring.
Despite the complexity of this area, for all the analysed GPS horizontal components, the highest correlation values and lowest associated time lags are obtained in the comparison with spring discharge data. In this case correlation has opposite sign between GPS sites on the "Adriatic" and "Tyrrenian" sides of the Apennines.
As regards vertical stacked data, analogously to South-Central Apennines, the comparison with GRACE data provides the highest correlation amount with lowest time shift (see row VSTACK$_C$ in Table B.1).

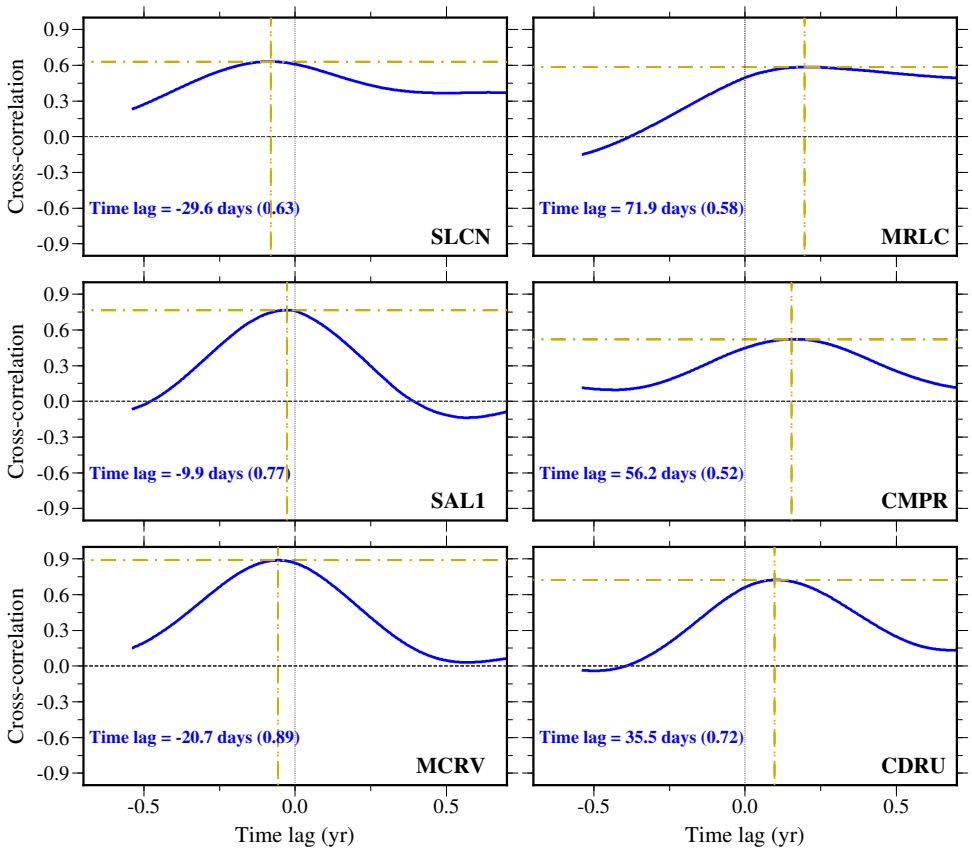

Figure B.1: Plots of cross-correlation calculated for some GPS sites in the South-Central area (pink box in Figure 5.2a) between observed GPS N45E component and Caposele spring discharge daily time-series. The horizontal axis indicates the temporal shift of the observed deformation respect to spring discharge. The vertical axis indicates the value of correlation at different time lags. Horizontal and vertical dashed gold lines pick the maximum value of correlation and the corresponding amount of time lag. Confidence boundary value are $\leq \pm 0.04$.

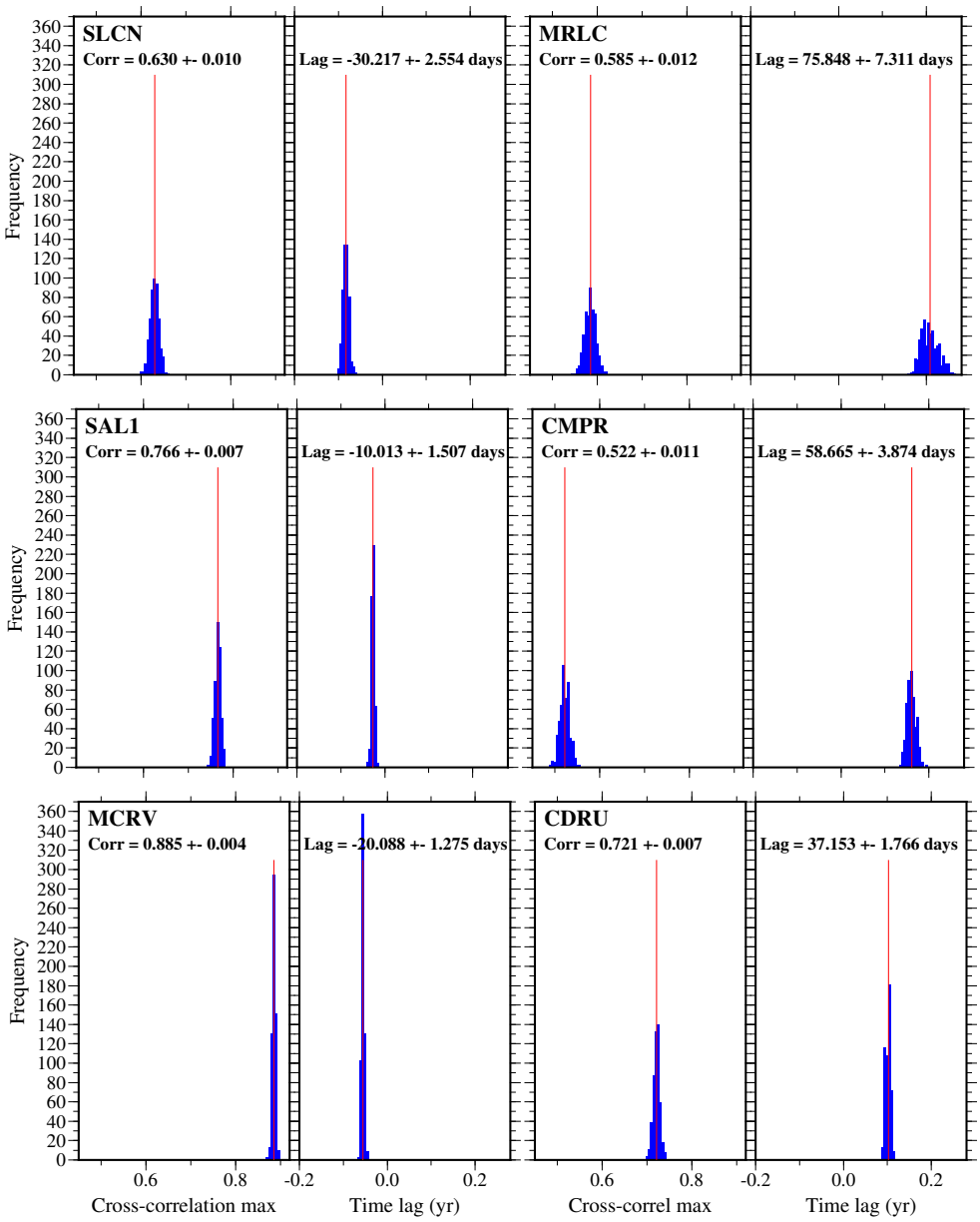

Figure B.2: Cross-correlation peak distribution built by multiple (500) bootstrap realizations. For each GPS station shown in Figure B.1, two histogram plots are shown, one for the maximum correlation value (left) and one for the relative time lag (right). For each plot, the mean and standard deviation values are indicated and the red vertical line picks the mean value.

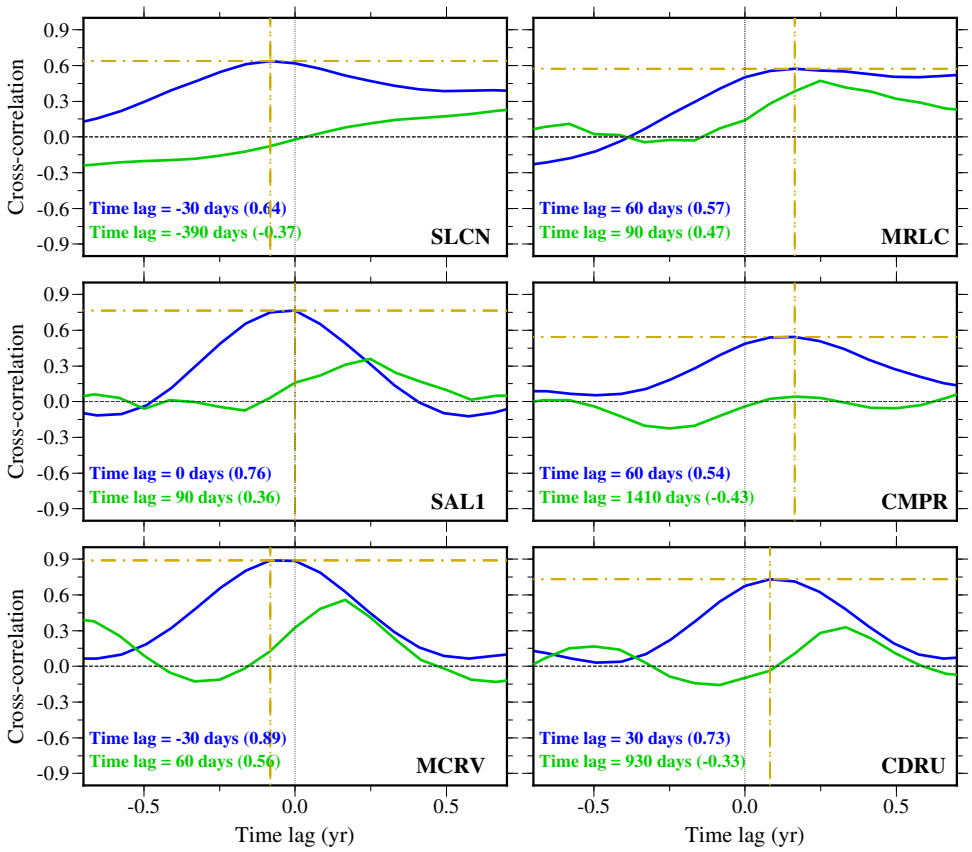

Figure B.3: Plots of cross-correlation calculated for some GPS sites between observed N45E GPS component and monthly spring discharge time-series (blue line) and between observed N45E GPS component and monthly GRACE data (green line). The horizontal axis indicates the temporal shift of the observed deformation respect to spring discharge/EWH. The vertical axis indicates the value of correlation at different time lags. Horizontal and vertical dashed gold lines pick the maximum value of correlation and the corresponding amount of time lag. Confidence boundary value are ≤ 0.2.

Table B.1: Cross-correlation values between N65E horizontal component and spring discharge and GRACE equivalent water height data for several stations in Central Italy. Confidence boundary value are $\leq \pm 0.08$ for daily sampled data and $\leq \pm 0.28$ for monthly sampled data.

GPS site	**Spring discharge**			**GRACE data**	
	Correlation	Time lag (days)	Spring*	Correlation	Time lag (months)
ALRA	0.62	5	Acqua Marcia	0.47	2
CAPE	0.55	-14	Tirino	0.4	21
CATO	0.59	-13	Tirino	0.27	29
CAOC	0.84	90	Acqua Marcia	-0.39	-6
CERA	0.77	-16	Acqua Marcia	0.60	2
CERT	-0.68	47	Acqua Marcia	-0.64	3
CONI	0.68	57	Tirino	-0.24	-1
GUAR	-0.54	12	Acqua Marcia	-0.39	3
INFN	0.74	8	Tirino	0.48	11
LEOF	-0.76	0	Tirino	0.33	-8
LPEL	0.62	-36	Tirino	-0.43	20
MORO	-0.72	-41	Tirino	-0.30	4
OCRA	-0.82	0	Tirino	-0.4	12
OLGI	-0.68	44	Tirino	-0.20	7
PBRA	0.54	-12	Tirino	0.27	4
POFI	-0.68	-41	Tirino	-0.5	4
ROPI	0.73	22	Tirino	-0.44	-10
SCRA	0.73	0	Tirino	-0.22	35
SMRA	0.58	-25	Tirino	-0.24	18
TERI	-0.65	-36	Tirino	-0.4	-6
TOSS	0.87	2	Tirino	0.30	5
UNTR	-0.72	-30	Tirino	-0.34	0
VAGA	-0.76	-21	Acqua Marcia	-0.57	1
VSTACK_C^{**}	-0.38	-73	Acqua Marcia	-0.42	0
VSTACK_S^{**}	-0.61	-116	Caposele	-0.68	-1

* Spring for which the maximum correlation is achieved.

**VSTACK_C and VSTACK_S indicate stacked vertical time-series of GPS stations of, respectively, Central and South-Central Italy.

Bibliography

Abusali, P.A.M., B.E. Schutz, B.D. Tapley, and M. Bevis, 1995, Transformation between SLR/VLBI and WGS-84 reference frames, *Journal of Geodesy*, **69**(2), 61–72.

Adinolfi Falcone R., V. Carucci, A. Falgiani, M. Manetta, B. Parisse, M. Petitta, S. Rusi, M. Spizzico, and M. Tallini, 2012, Changes on groundwater flow and hydrochemistry of the Gran Sasso carbonate aquifer after 2009 L'Aquila earthquake, *Ital. J. Geosci.*, **131**(3), 459-474, doi:10.3301/IJG.2011.34.

Agnew, D., 1996, SPOTL: Some programs for ocean-tide loading. SIO Reference Series 96-8, Scripps Institution of Oceanography.

Agnew, D., 1997, NLOADF: A program for computing ocean-tide loading, *J. Geophys. Res.*, **102**, 5109–5110.

Albano, M., S. Barba, M. Saroli, M. Moro, F. Malvarosa, M. Costantini, C. Bignami, and S. Stramondo, 2015, Gravity-driven postseismic deformation following the Mw 6.3 2009 L'Aquila (Italy) earthquake, *Scientific Reports*, **5**, 16558, doi:10.1038/srep16558.

Allocca V., F. Celico, P. Celico, P. De Vita, S. Fabbrocino, S. Mattia, G. Monacelli, I. Musilli, V. Piscopo, A.R. Scalise, G. Summa, and G. Tranfaglia, 2007, Illustrative Notes of the Hydrogeological Map of Southern Italy, *Ist. Poligrafico e Zecca dello Stato*, Rome, 211 pp.

Allocca V., F. Manna, and P. De Vita, 2014, Estimating annual groundwater recharge coefficient for karst aquifers of the southern Apennines (Italy), *Hydrol. Earth Syst. Sci.*, **18**, 803–817, doi:10.5194/hess-18-803-2014.

'Alvarez-García, F.J., P.M. Lorente-Lorente, and M.J. OrtizBevia, 2012, Quasi-quadrennial variability in European precipitation, *Int. J. Climatol.*, **32**(9), 1295–1309, doi:0.1002/joc.2351.

Amadei, B., 1996, Importance of anisotropy when estimating and measuring in situ stresses in rock, *Int. J. Rock Mech.*, 33, 293–325, doi:10.1016/0148-9062(95)00062-3.

Amoruso, A., L. Crescentini, M. Petitta, S. Rusi, and M. Tallini, 2011, Impact of the 6 April 2009 L'Aquila earthquake on groundwater flow in the Gran Sasso carbonate aquifer, Central Italy, *Hydrol. Process.*, **25**, 1754–1764, doi: 10.1002/hyp.7933.

Amoruso A., L. Crescentini, M. Petitta, and M. Tallini, 2013, Parsimonious recharge/discharge modeling in carbonate fractured aquifers: the groundwater flow in the Gran Sasso aquifer (Central Italy), *Journal of Hydrology, 476*, 136–146, doi:10.1016/j.jhydrol.2012.10.026.

Amoruso, A., L. Crescentini, S. Martino, M. Petitta, and M. Tallini, 2014, Correlation between groundwater flow and deformation in the fractured carbonate Gran Sasso aquifer (INFN underground laboratories, central Italy), *Water Resour. Res.*, **50**, 4858–4876, doi:10.1002/2013WR014491.

Amos, C.B., P. Audet, W.C. Hammond, R. Bürgmann, I.A. Johanson, and G. Blewitt, 2014, Uplift and seismicity driven by groundwater depletion in central California, *Nature, 509*, 483–486, doi:10.1038/nature13275.

Aoudia, A., A. Borghi, R. Riva, R. Barzaghi, B.A.C. Ambrosius, R. Sabadini, L.L.A. Vermeersen, and G.F. Panza, 2003, Postseismic deformation following the 1997 Umbria-Marche (Italy) moderate normal faulting earthquakes, *Geophys. Res. Lett.*, **30**, 1390, doi:10.1029/2002GL016339.

Argus, D.F., Y. Fu, and F.W. Landerer, 2014, Seasonal variation in total water storage in California inferred from GPS observations of vertical land motion, *Geophys. Res. Lett.*, *41*, 1971–1980, doi:10.1002/2014GL059570.

Atzori S., C. Chiarabba, R. Devoti, M. Bonano, and R. Lanari, 2013, Anomalous far-field geodetic signature related to the 2009 L'Aquila (central Italy) earthquake, *Terra Nova*, **25**, 343–351, doi:10.1111/ter.12040.

Avallone, A., G. Selvaggi, E. D'Anastasio, N. D'Agostino, G. Pietrantonio, F. Riguzzi, E. Serpelloni, M. Anzidei, G. Casula, G. Cecere, C. D'Ambrosio, P. De Martino, R. Devoti, L. Falco, M. Mattia, M. Rossi, F. Obrizzo, U. Tammaro, and L. Zarrilli, 2010, The RING network: Improvement of a GPS velocity field in the central Mediterranean, *Ann. Geophys.*, *53*(2), 39–54, doi:10.4401/ag-4549.

Bar-Sever, Y.E., P.M. Kroger, and J.A. Borjesson, 1998, Estimating horizontal gra- dients of tropospheric path delay with a single gps receiver, *J. of Geophys. Res. Solid Earth*, *103(B3)*, 5019–5035.

Bekaert, D.P.S., P. Segall, T.J. Wright, and A.J. Hooper, 2016, A Network Inversion Filter combining GNSS and InSAR for tectonic slip modeling, *J. Geophys. Res. Solid Earth*, **121**, doi:10.1002/2015JB012638.

Beroza, G.C., and S. Ide, 2011, Slow Earthquakes and Nonvolcanic Tremor, *Annu. Rev. Earth Planet. Sci.*, **39**, 271–296, doi:10.1146/annurev-earth-040809-152531.

Bertiger, W., S.D. Desai, B. Haines, N. Harvey, A.W. Moore, S. Owen, and J.P. Weiss, 2010, Single receiver phase ambiguity resolution with GPS data, *Journal of Geodesy*, *84*(5), 327–337, doi:10.1007/s00190-010-0371-9.

Bettinelli P., J.P. Avouac, M. Flouzat, L. Bollinger, G. Ramillien, S. Rajaure, S. Sapkota, 2008, Seasonal variations of seismicity and geodetic strain in the Himalaya induced by surface hydrology, *Earth Planet. Sci. Lett.*, **266**, 332–344. doi:10.1016/j.epsl.2007.11.021.

Beutler, G., M. Rothacher, and S. Schaer, 1999, The International GPS Service (IGS): an interdisci- plinary service in support of earth sciences, *Advances in Space*, **23**(4), 631–653.

Bie, L., I. Ryder, S.E.J. Nippress, and R. Bürgmann, 2014, Coseismic and post-seismic activity associated with the 2008 Mw 6.3 Damxung earthquake, Tibet, constrained by InSAR, *Geophys. J. Int.*, **196**, 788–803, doi: 10.1093/gji/ggt444.

Billi A., A. Valle, M. Brilli, C. Faccenna, and R. Funiciello, 2007, Fracture-controlled fluid circulation and dissolutional weathering in sinkhole-prone carbonate rocks from central Italy, *Journal of structural geology*, **29**, 385–395, doi:10.1016/j.jsg.2006.09.008.

Blewitt, G., D. Lavallée, P. Clarke, and K. Nurutdinov„ 2001, A new global mode of Earth deformation: Seasonal cycle detected, *Science*, **294**, 2342–2345.

Blewitt, G., and D. Lavallée, 2002, Effect of annual signals on geodetic velocity, *J. Geophys. Res.*, **107**(B7), doi:10.1029/2001JB000570.

Blewitt, G., C. Kreemer, W.C. Hammond, and J.M. Goldfarb, 2013, Terrestrial reference frame NA12 for crustal deformation studies in North America, *Journal of Geodynamics*, *72*, doi:10.1016/j.jog.2013.08.004.

Blewitt, G., 2015, GPS and space-based geodetic methods. In G. Schubert (Ed.), *Treatise in Geophysics* (Second Edition), Vol. 3: Geodesy, 307–338, Elsevier, Oxford, doi:10.1016/B978-0-444-53802-4.00060-9.

Bonacci, O., 1993, Karst springs hydrographs as indicators of karst aquifers, *Hydrological Science Journal*, **38**(1), 51-62.

Bonafede, M., and S. Danesi, 1997, Near-field modifications of stress induced by dyke injection at shallow depth. *Geophys. J. Int.*, **130**, 435–448, doi:10.1111/j.1365-246X.1997.tb05659.x.

Boni, C., 1975, The relationship between the geology and hydrology of the Latium-Abruzzi Apennines, In: Parotto, M. and Praturlon, A., *Geological summary of the central Apennines. Quaderni de "La ricerca scientifica"*, **90**, 301–311. *Structural Model of Italy.*

Boni, C., P. Bono, and G. Capelli, 1986, Schema Idrogeologico dell'Italia centrale, – A) Carta idrogeologica (scala 1:500.000); B) Carta idrologica (scala 1:500.000); C) Carta dei bilanci idrogeologici e delle risorse idriche sotterranee (scala 1:1.000.000), *Mem. Soc. Geol.It.*, **35**(2), 991–1012.

Boni, C., 2000, Karst aquifers of the Central Apennines, *Hydrogéologie*, **4**, 49-62.

Boni, C. F., Pianelli, A., Pierdominici, S., and Ruisi, M., 2002, Le grandi sorgenti del fiume Tirino (Abruzzo), *Italian Journal of Geosciences*, *121* (3), 411–431.

Borghi, A., A. Aoudia, F. Javed, and R. Barzaghi, 2016, Precursory slow-slip loaded the 2009 L'Aquila earthquake sequence, *Geophys. J. Int.*, **205**(2), 776–784, doi: 10.1093/gji/ggw046.

Borsa, A.A., D.C. Agnew, and D.R. Cayan, 2014, Ongoing drought-induced uplift in the western United States, *Science*, *345*(6204), 1587–1590, doi:10.1126/science.12602791.

Bouchon, M., H. Karabulut, M. Aktar, S. Özalaybey, J. Schmittbuhl, and M. P. Bouin, 2011, Extended nucleation of the 1999 Mw 7.6 Izmit earthquake, *Science*, **331**(6019), 877–880, doi:10.1126/science.1197341.

Boussinesq, J., 1885, Application des Potentiels à l' Étude de l' Équilibre et du Mouvement des Solides Élastiques, 508 pp., *Gauthier-Villars*, Paris.

Brandimarte, L., G. Di Baldassarre, G. Bruni, P. D'Odorico, A. Montanari, 2011, Relation Between the North-Atlantic Oscillation and Hydroclimatic Conditions in Mediterranean Areas, *Water Resources Management*, **25**(5), 1269–1279, doi:10.1007/s11269-010-9742-5.

Cakir, Z., A.M. Akoglu, S. Belabbes, S. Ergintav, and M. Meghraoui, 2005, Creeping along the Ismetpasa section of the North Anatolian fault (Western Turkey): Rate and extent from InSAR, *Earth and Planetary Science Letters*, **238**(1), 225–234, doi:10.1016/j.epsl.2005.06.044.

Cannavò F., A.G. Camacho, P.J. González, M. Mattia, G. Puglisi, J. Fernández, 2015, Real Time Tracking of Magmatic Intrusions by means of Ground Deformation Modeling during Volcanic Crises, *Scientific Reports*, **5**(10970), doi:10.1038/srep10970.

Cavinato, G.P., D. Cosentino, D. De Rita, R. Funiciello, and P. Parotto, 1993, Tectonic sedimentary evolution of intrapenninic basins and correlation with the volcano-tectonic activity in central Italy, *Mem. Descr. Carta Geol. Ital.*, **49**, 63–75.

Cavinato, G.P., and P. DeCelles, 1999, Extensional basins in the tectonically bimodal central Apennines fold-thrust belt, Italy: Response to corner flow above a subducting slab in retrograde motion, *Geology*, **27**, 955–958.

Celico, P. and M. Civita, 1976, Sulla tettonica del massiccio del Cervialto (Campania) e le implicazioni idrogeologiche ad essa connesse [On the tectonics of the Cervialto Massif (Campania) and related hydrogeological issues], *Boll. Soc. Natur*, Naples, *85*.

Celico, P., L. Pelella, D. Stanzione, and S. Aquino, 1994, Sull'idrogeologia e l'idrogeochimica dei Monti Alburni (SA), *Geologica Romana*, *30*, 687–698.

Celico F., P. Celico, P. De Vita and V. Piscopo, 2000, Groundwater flow and protection in the Southern Apennines (Italy), *Hydrogéologie*, **4**, 39–46.

Celico, F., E. Petrella, and P. Celico, 2006, Hydrogeological behaviour of some fault zones in a carbonate aquifer of Southern Italy: an experimentally based model, *Terra Nova*, **18**, 308–313, doi: 10.1111/j.1365-3121.2006.00694.x.

Celico, F., G. Naclerio, A. Bucci, V. Nerone, P. Capuano, M. Carcione, V. Allocca, and P. Celico, 2010, Influence of pyroclastic soil on epikarst formation: a test study in southern Italy, *Terra Nova*, 22, 110–115, doi:10.1111/j.1365-3121.2009.00923.x.

Chanard, K., J.P. Avouac, G. Ramillien, J. Genrich, 2014, Modeling deformation induced by seasonal variations of continental water in the Himalaya region: Sensitivity to Earth elastic structure, *J. Geophys. Res. Solid Earth*, *119*, 5097–5113, doi:10.1002/2013JB010451.

Cheloni, D., R. Giuliani, E. D'Anastasio, S. Atzori, R.J. Walters, L. Bonci, N. D'Agostino, M. Mattone, S. Calcaterra, P. Gambino, F. Deninno, R. Maseroli, G. Stefanelli, 2014, Coseismic and post-seismic slip of the 2009 L'Aquila (central Italy) MW 6.3 earthquake and implications for seismic potential along the Campotosto fault from joint inversion of high-precision levelling, InSAR and GPS data, **Tectonophysics**, **622**, 168–185, doi:10.1016/j.tecto.2014.03.009.

Chiarabba, C., L. Jovane, and R. Di Stefano, 2005, A new view of Italian seismicity using 20 years of instrumental recordings, *Tectonophysics*, **395**, 251–268, doi:10.1016/j.tecto.2004.09.013.

Cirella, A., A. Piatanesi, E. Tinti, M. Chini, and M. Cocco, 2012, Complexity of the rupture process during the 2009 L'Aquila, Italy, earthquake, *Geophys. J. Int.*, **190**, 607–621. doi: 10.1111/j.1365-246X.2012.05505.x.

Civita, M., 1975. Criteri di valutazione delle risorse idriche sotterranee in regioni carsiche, *Atti 3° Conv. Int. Acque sotterranee*, Palermo, 217-237.

Civita M., and A. Fiorucci, 2010, The recharge-discharge process of the Peschiera spring system (central Italy),*AQUA mundi*, Am02019: 161–178, doi:10.4409/Am-014-10-0019.

Cosentino, D., P. Cipollari, P. Marsili, and D. Scrocca, 2010, Geology of the central Apennines: a regional review, In: (Eds.) Marco Beltrando, Angelo

Peccerillo, Massimo Mattei, Sandro Conticelli, and Carlo Doglioni, *The Geology of Italy, Journal of the Virtual Explorer*, Electronic Edition, ISSN 1441–8142, **36**(12), doi:10.3809/jvirtex.2010.00223.

Cucchi, F, P. Forti, and L. Zini, 2004, The vulnerability of complex karst hydrostructures: Problems and perspectives, *Geofísica Internacional*, **43**(4), 533–540.

Dalla Via, G., G. De Natale, C. Troise, F. Pingue, F. Obrizzo, R. Riva, and R. Sabadini, 2003, First evidence of post-seismic deformation in the central Mediterranean: Crustal viscoelastic relaxation in the area of the 1980 Irpinia earthquake (Southern Italy), *Geophys. J. Int.*, **154**, F9–F14. doi: 10.1046/j.1365-246X.2003.02031.x.

D'Agostino, N., J.A. Jackson, F. Dramis, and R. Funiciello, 2001, Interactions between mantle upwelling, drainage evolution and active normal faulting: an example from the central Apennines (Italy), *Geophys. J. Int.*, *147 (2)*, 475–497, doi:10.1046/j.1365-246X.2001.00539.x.

D'Agostino, N., D. Cheloni, G. Fornaro, R. Giuliani, and D. Reale, 2012, Space-time distribution of afterslip following the 2009 L'Aquila earthquake, *J. Geophys. Res.*, **117**, B02402, doi:10.1029/2011JB008523.

D'Agostino, N. (2014), Complete seismic release of tectonic strain and earthquake recurrence in the Apennines (Italy), *Geophys. Res. Lett.*, *41*(4), 1155–1162, doi:10.1002/2014GL059230.

Davis P.M., 1983, Surface deformation associated with a dipping hydrofracture, *J. Geophys. Res.*, **88**(B7), 5826–5834.

Decriem, J., and T. Árnadóttir, 2012, Transient crustal deformation in the South Iceland Seismic Zone observed by GPS and InSAR during 2000–2008, *Tectonophysics*, **581**, 6–18, doi:10.1016/j.tecto.2011.09.028.

De Vita, P., D. Agrello, and F. Ambrosino, 2006, Landslide susceptibility assessment in ash-fall pyroclastic deposits surrounding Somma-Vesuvius:

application of geophysical surveys for soil thickness mapping, *J. Appl. Geophys.*, **59**(2), 126–139, doi:10.1016/j.jappgeo.2005.09.001.

De Vita P., and S. Fabbrocino, 2007, Influence of the North Atlantic Oscillation on the climatic variability and groundwater resources in carbonate aquifers of Southern Italy, *Italian Journal of Engineering Geology and Environment*, ISSN 1825-6635, **1**, 33–48, doi:10.4408/IJEGE.2007-01.O-03.

De Vita, P., V. Allocca, F. Manna, and S. Fabbrocino, 2012, Coupled decadal variability of the North Atlantic Oscillation, regional rainfall and karst spring discharges in the Campania region (southern Italy), *Hydrology and Earth System Sciences*, **16**, 1389–1399, doi:10.5194/hess-16-1389-2012.

Del Prete, S., M. Manco, and F. Maurano, 2007, Aspetti speleogenetici della Grotta della Prufunnata (Monti Picentini, Campania), *Atti I Convegno Regionale di Speleologia "Campania Speleologica"*, Oliveto Citra (SA).

Desai, C. S., and J.T. Christian, 1977, Numerical methods in geotechnical engineering, *McGraw-Hill Book Company*, 783 pp.

Devoti, R., D. Zuliani, C. Braitenberg, P. Fabris, and B. Grillo, 2015, Hydrologically induced slope deformations detected by GPS and clinometric surveys in the Cansiglio Plateau, southern Alps, *Earth Planet. Sci. Lett.*, *419*, 134–142, doi:10.1016/j.epsl.2015.03.023.

Di Stefano, R., I. Bianchi, M.G. Ciaccio, G. Carrara, and E. Kissling, 2011, Three-dimensional Moho topography in Italy: New constraints from receiver functions and controlled source seismology, *Geochem. Geophys. Geosyst.*, **12**, Q09006, doi:10.1029/2011GC003649.

Dyke, C., 1995, How sensitive is natural permeability at depth to variation in effective stress?, *Proceedings of the International Symposium On Fractured and Joint Rock Masses*, 81–88, Balkema, Rotterdam.

Dziewonski, A., and D.L. Anderson, 1981, Preliminary reference Earth model, *Phys. Earth Planet. Inter.*, **25**, 297–356.

Edge, R.J., T.F. Baker, and G. Jeffries, 1981, Borehole tilt measurements: aperiodic crustal tilt in an aseismic area. *Tectonophys. 71*, 97–109, doi:10.1016/0040-1951(81)90052-4.

Evans, K., and F. Wyatt, 1984, Water table effects on the measurement of earth strain, *Tectonophys.*, *108*, 323–337.

Facciorusso, J., C. Madiai, and G. Vannucchi, 2006, Dispense di Geotecnica, Dipartimento di Ingegneria Civile - Sezione Geotecnica, Università degli Studi di Firenze.

Farrell, W., 1972, Deformation of the Earth by surface loads, *Rev. Geophys.*, **10**, 761–797.

Fiorillo F., 2009, Spring hydrographs as indicators of droughts in a karst environment, *Journal of Hydrology*, **373**, 290-301, doi:10.1016/j.jhydrol.2009.04.034.

Fiorillo, F., 2011, Tank-reservoir drainage as a simulation of the recession limb of karst spring hydrographs, *Hydrogeol. J.*, *19*, 1009–1019, doi:10.1007/s10040-011-0737-y.

Fiorillo, F., 2013, Spring Hydrographs Recession and Analysis of the Caposele spring (Southern Italy) During Dry Periods, *Italian Journal of Engineering Geology and Environment*, **1**, 51–64, doi:10.4408/IJEGE.2013-01.O-04.

Fiorillo, F., and A. Doglioni, 2010, The relation between karst spring discharge and rainfall by cross-correlation analysis (Campania, southern Italy), *Hydrogeology Journal*, *18*(8), 1881–1895, doi:s10040-010-0666-1.

Fiorillo F., and F.M. Guadagno, 2010, Analysis of karst spring discharges during droughts, *Italian Journal of Engineering Geology and Environment*, **2**, 33–49, doi:10.1007/s11269-009-9528-9.

Fiorillo F., and F.M. Guadagno, 2012, Long karst spring discharge time series and droughts occurrence in Southern Italy, *Environmental Earth Sciences*, **65**(8), 2273–2283, doi:10.1007/s12665-011-1495-9.

Fiorillo, F., M. Pagnozzi, and G. Ventafridda, 2015a, A model to simulate recharge processes of karst massifs, *Hydrol. Process.*, *29*, 2301–2314, doi:10.1002/hyp.10353.

Fiorillo, F., M. Petitta , E. Preziosi, S. Rusi, S. Esposito, and M. Tallini, 2015b, Long term trend and fluctuations of karst spring discharge in a Mediterranean area (Central-Southern Italy), *Environmental Earth Sciences*, *74*, 153–172, doi:10.1007/s12665-014-3946-6.

Ford, D., and P. Williams, 2007, Karst Hydrogeology and Geomorphology, Chichester, England, Wiley, 562 p..

Fu, Y., J.T. Freymueller, and T. Jensen, 2012, Seasonal hydrological loading in southern Alaska observed by GPS and GRACE, *Geophys. Res. Lett.*, **39**, L15310, doi:10.1029/2012GL052453.

Fu, Y., D.F. Argus, J.T. Freymueller, and M.B. Heflin, 2013, Horizontal Motion in Elastic Response to Seasonal Loading of Rain Water in the Amazon Basin and Monsoon Water in Southeast Asia Observed by GPS and Inferred from GRACE, *Geophys. Res. Lett.*, **40**, 6048–6053, doi:10.1002/2013GL058093.

Galassi D.M.P., P. Lombardo, B. Fiasca, A. Di Cioccio, T. Di Lorenzo, M. Petitta, and P. Di Carlo, 2014, Earthquake trigger the loss of groundwater biodiversity, *Sci. Rep.* 4:6273, doi:10.1038/srep06273.

González, P.J., and J. Fernández, 2011, Drought-driven transient aquifer compaction imaged using multitemporal satellite radar interferometry, *Geology*, **39**(6), 551–554, doi:10.1130/G31900.1.

Grapenthin, R., F. Sigmundsson, H. Geirsson, T. Árnadóttir, and V. Pinel, 2006, Icelandic rhythmics: Annual modulation of land elevation

and plate spreading by snow load, *Geophys. Res. Lett.*, **33**, L24305, doi:10.1029/2006GL028081.

Gualandi, A., E. Serpelloni and M.E. Belardinelli, 2014, Space-time evolution of postseismic afterslip following the Mw 6.3, 2009 L'Aquila earthquake (central Italy) from principal component analysis inversion of GPS position time-series, *Geophys. J. Int.*, doi:10.1093/gji/ggt522.

Gualandi A., 2015a, Spatial and temporal characterisation of ground deformation recorded by geodetic techniques, [Dissertation thesis], *Alma Mater Studiorum Università di Bologna. Dottorato di ricerca in Geofisica*, 27 Ciclo, doi:10.6092/unibo/amsdottorato/7093.

Gualandi A., E. Serpelloni, M.E. Belardinelli, 2015b, Blind Source Separation problem in GPS time series, *J. of Geodesy*, doi:10.1007/s00190-015-0875-4.

Gudmundsson, A., 2011, Rock Fractures in Geological Processes, *Cambridge University Press*, 1 edition, 591 pages.

Guo, J., Y. Li, Y. Huang, H. Deng, S. Xu, and J. Ning, 2004, Green's function of the deformation of the Earth as a result of atmospheric loading, *Geophys. J. Int.*, **159**(1), 53–68, doi:10.1111/J.1365-246X.2004.02410.x.

Hartmann, A., N. Goldscheider, T. Wagener, J. Lange, and M. Weiler, 2014, Karst water resources in a changing world: Review of hydrological modeling approaches, *Rev. Geophys.*, **52**, 218–242, doi:10.1002/2013RG000443.

Hofmann-Wellenhof B., H. Lichtenegger, and J. Collins, 1993, GPS: theory and practice, Springer, Wien (Austria).

Houze, R. A., 2012, Orographic effects on precipitating clouds, *Rev. Geophys.*, 50, 1–47.

ITASCA, 2011, FLAC, Fast Lagrangian Analysis of Continua, User's Guide, Minneapolis, Minnesota, USA.

Jacob, T., J. Chéry, F. Boudin, and R. Bayer, 2010, Monitoring deformation from hydrologic processes in a karst aquifer using long-baseline tiltmeters, *Water Resources Research*, *46*(9), doi:10.1029/2009WR008082.

Jade, S., and T. Sitharam, 2003, Characterization of Strength and Deformation of Jointed Rock Mass Based on Statistical Analysis, *Int. J. Geomech.*, 43–54, doi:10.1061/(ASCE)1532-3641(2003)3:1(43).

Jean, Y., U. Meyer, and A. Jäggi, 2015, Combination of monthly gravity field solutions from different processing centers, *Geophysical Research Abstracts*, **17**, EGU2015-5879, EGU General Assembly 2015.

Ji, K.H., and T.A. Herring, 2011, Transient signal detection using GPS measurements: Transient inflation at Akutan volcano, Alaska, during early 2008, *Geophys. Res. Lett.*, **38**, L06307, doi:10.1029/2011GL046904.

Ji, K.H., and T.A. Herring, 2013, A method for detecting transient signals in GPS position time-series: Smoothing and principal component analysis, *Geophys. J. Int.*, **193**(1), 171–186, doi: 10.1093/gji/ggt003.

Jolivet, R., C. Lasserre, M.P. Doin, S. Guillaso, G. Peltzer, R. Dailu, J. Sun, Z-.K. Shen, and X. Xu, 2012, Shallow creep on the Haiyuan fault (Gansu, China) revealed by SAR interferometry, *J. Geophys. Res. Solid Earth*, **117**(B6), doi:10.1029/2011JB008732.

Jolly, R. J.H., and D.J. Sanderson, 1997, A Mohr circle construction for the opening of a pre-existing fracture, *Journal of Structural Geology*, **19**(6):887–892, doi:10.1016/S0191-8141(97)00014-X.

Jones, W.K., 2013, Physical Structure of the Epikarst, *ACTA CARSOLOGICA*, **42**(2-3), 311–314.

Kaniuth, K., and S. Vetter, 2006, Estimating atmospheric pressure loading regression coefficients from GPS observations, *GPS Solutions*, **10**(2), 126–134.

King R.W., and Y. Bock, 2005, Documentation for the GAMIT GPS Processing Software Release 10.2, *Mass. Inst. of Technol.*, Cambridge, MA.

Kreemer, C., G. Blewitt, and F. Maerten, 2006, Co- and postseismic deformation of the 28 March 2005 Nias Mw 8.7 earthquake from continuous GPS data, *Geophys. Res. Lett.*, **33**, L07307, doi:10.1029/2005GL025566.

Kreemer, C.W., G. Blewitt, E.C. Klein, 2014, A geodetic plate motion and global strain rate model, *Geochemistry, Geophysics, Geosystems*, **15**1(10), 3849–3889, doi:10.1002/2014GC005407.

Lagler, K., M. Schindelegger, J. Böhm, H. Krásná, and T. Nilsson, 2013, GPT2: Empirical slant delay model for radio space geodetic techniques, *Geophys. Res. Lett.*, *40*, 1069–1073, doi:10.1002/grl.50288.

Lamb, H., 1902, On Boussinesq's problem, *Proc. London Math. Sac.*, **34**, 276.

Lambe, T. W., and R.V. Whitman, 1969, Soil Mechanics, *John Wiley & Sons.*

Landerer, F.W., and S.C. Swenson, 2012, Accuracy of scaled GRACE terrestrial water storage estimates, *Water Resour. Res.*, *48*, W04531, doi:10.1029/2011WR011453.

Langbein, J.O., 2003, Deformation of the Long Valley Caldera, California: Inferences from measurements from 1988 to 2001, *J. Volcanol. Geotherm. Res.*, **127**, 247–267, doi:10.1016/S0377-0273(03)00172-0.

Larson,K., J. Wahr, and P. Kuipers Munneke, 2015, Constraints on Snow Accumulation and Firn Density in Greenland Using GPS Receivers, *Journal of Glaciology*, **61**(225), 101–114, doi:10.3189/2015JoG14J130.

Lazzari, M., 2010, AREA 1. Aspetti geologici e geomorfologici del sic. di Monte Paratiello IT9210190, *RETE NATURA 2000 REGIONE BASILICATA, MISURE DI TUTELA E CONSERVAZIONE.*

LeGrand, H.E. and V.T. Stringfield, 1971, Water levels in carbonate rock terrains, *Groundwater*, **9**, 4–10.

Lekhnitskii, S. G., 1981, Theory of Elasticity of an Anisotropic Body, *Mir Publishers*, Moscow.

Lisowski, M., 2007, Analytical volcano deformation source models, in *Volcano Deformation: Geodetic Monitoring Techniques*, edited by D.P. Bondel, pp. 279–304, Praxis, Chichester, U.K..

Liu, S., Z.-K. Shen, and R. Bürgmann, 2015, Recovery of secular deformation field of Mojave Shear Zone in Southern California from historical terrestrial and GPS measurements, *J. Geophys. Res. Solid Earth*, **120**, 3965–3990. doi:10.1002/2015JB011941.

Longuevergne, L., N. Florsch, F. Boudin, L. Oudin, and C. Camerlynck, 2009, Tilt and strain deformation induced by hydrologically active natural fractures: application to the tiltmeters installed in Sainte-Croix-aux-Mines observatory (France). *Geophys. J. Int.*, *178*, 667–677, doi:10.1111/j.1365-246X.2009.04197.x.

Maccaferri, F., 2010, Numericals and analogue models of fluid-filled fractures propagation in layered media: application to dikes and hydrofractures, [Dissertation thesis], *Alma Mater Studiorum Università di Bologna, Dottorato di ricerca in Geofisica*, 22 Ciclo.

Manga, M., 1996, Hydrology of spring-dominated streams in the Oregon Cascades, *Water Resources Research*, *32*, 2435–2439, doi:10.1029/96WR01238.

Manga, M., 1997, A model for discharge in spring-dominated streams, and implications for the transmissivity and recharge of Quaternary volcanics in the Oregon Cascades, *Water Resources Research*, *33*, 1813–1822, doi:10.1029/97WR01339.

Manga, M., 1999, On the timescales characterizing groundwater discharge at springs, *Journal of Hydrology*, **219**, 56–69

Mangin, A., 1975, Contribution à l'étude hydrodynamique des aquifères karstiques, *Thèse Univ. Dijon. Annales de spéléologie.*

Martarelli L., M. Petitta, A. R. Scalise, and A. Silvi, 2008, Cartografia idrogeologica sperimentale della piana reatina (Lazio), *Mem. Descr. Carta Geologica d'Italia*, LXXXI: 137–156.

Métois, M., N. D'Agostino, A. Avallone, N. Chamot-Rooke, A. Rabaute, L. Duni, N. Kuka, R. Koci, and I. Georgiev, 2015, Insights on continental collisional processes from GPS data: Dynamics of the peri-Adriatic belts, *J. Geophys. Res. Solid Earth*, **120**, 8701–8719, doi:10.1002/2015JB012023.

Miyazaki, S., J.J. McGuire, and P. Segall, 2003, A transient subduction zone slip episode in southwest Japan observed by the nationwide GPS array, *J. Geophys. Res.*, **108**(B2), 2087, doi:10.1029/2001JB000456.

Miklius, A. and P. Cervelli, 2003, Vulcanology: Interaction between Kilauea and Mauna Loa, *Nature*, **421**, 229, doi:10.1038/421229a.

Miller, D.J., and T. Dunne, 1996, Topographic perturbations of regional stresses and consequent bedrock fracturing, *J. Geophys. Res.*, **101**(B11), 25523–25536, doi:10.1029/96JB02531.

Miller, S.A., 2008, Note on rain-triggered earthquakes and their dependence on karst geology. *Geophys. J. Int.*, *173*, 334–338. doi:10.1111/j.1365-246X.2008.03735.x.

Mindlin, R.D., 1936, Force at a point in the interior of a semi-infinite solid, *Physics*, **7**(5), pp. 195–202.

Montgomery-Brown, E.K., D.K. Sinnett, K.M. Larson, M.P. Poland, P. Segall, and A. Miklius, 2011, Spatiotemporal evolution of dike opening and décollement slip at Kīlauea Volcano, Hawai'i, *J. Geophys. Res.*, **116**, B03401, doi:10.1029/2010JB007762.

Mooney, W.D., G. Laske, and T.G. Masters, 1998, CRUST 5.1: A global crustal model at 5°x 5°, *J. Geophys. Res.*, **103**(B1), 727–747, doi:10.1029/97JB02122.

Moore, D.S., G.P. McCabe, W.M. Duckworth, and S.L. Sclove, 2003, The Practice of Business Statistics: Using Data for Decisions, 2nd edn, *WH Freeman*, New York, 859 pp.

Moreau, F., and O. Dauteuil, 2013, Geodetic tools for hydrogeological surveys: 3D-displacements above a fractured aquifer from GPS time series, *Engineering Geology*, **152**, 1–9, doi:10.1016/j.enggeo.2012.10.017.

Obara, K., 2002, Nonvolcanic Deep Tremor Associated with Subduction in Southwest Japan, *Science*, **296**, 1679–1681. doi:10.1126/science.10703.

Okada, Y., 1985, Surface deformation due to shear and tensile faults in a half-space, *Bull. Seism. Soc. Am.*, *75*, 1135–1154.

Okada, Y., 1992, Internal deformation due to shear and tensile faults in a half-space, *Bull. Seism. Soc. Am.*, **82**, 1018–1040.

Owen, S., P. Segall, M. Lisowski, M. Murray, M. Bevis, and J. Foster, 2000, The January 30, 1997, eruptive event on Kilauea volcano, as monitored by continuous GPS, *Geophys. Res. Lett.*, **27**, 2757–2760, doi:10.1029/1999GL008454.

Pastori, M., D. Piccinini, L. Margheriti, L. Improta, L. Valoroso, L. Chiaraluce, and C. Chiarabba, 2009, Stress aligned cracks in the upper crust of the Val d'Agri region as revealed by shear wave splitting, *Geophis. J. Int.*, *179*(1), 601–614, doi:10.1111/j.1365-246X.2009.04302.x.

Pastori, M., L. Margheriti, D. Piccinini, L. Valoroso, A. Wuestefeld, L. Zaccarelli, F. Bianco, M. Kendall, D. Di Bucci, and M. R. Barchi, 2012, Crustal fracturing field and presence of fluid as revealed by seismic anisotropy: case histories from seismogenic areas in the Apennines (Italy), *BGTA*, **53**(4), 417–433, doi:10.4430/bgta00XX.

Parotto M., and A. Praturlon, 1975, Geological summary of the Central Appenines, In: Ogniben L., Parotto M. and Praturlon A. (Eds.), *Structural Model of Italy. Quad. Ric. Scient.*, **90**, 257–311.

Patacca, E., and P. Scandone, 2007, Geology of the Southern Apennines, *Boll.Soc.Geol.It. (Ital.J.Geosci.), Special issue*, **7**, 75–119.

Peltier, W.R., 2004, Global Glacial Isostasy and the Surface of the Ice-Age Earth: The ICE-5G (VM2) Model and GRACE, *Ann. Rev. Earth and Planet. Sci.*, **32**, 111–149, doi:10.1146/annurev.earth.32.082503.144359.

Petitta M., 2009, Hydrogeology of the middle valley of the Velino River and of the S. Vittorino Plain (Rieti, Central Italy), *Italian Journal of Engineering Geology and Environment*, **1**,157–181, doi:10.4408/IJEGE.2009-01.O-09.

Petitta M., M. Caschetto, M.P.D. Galassi, and R. Aravena, 2014, Dual-flow in karst aquifers toward a steady discharge spring (Presciano, central Italy): influences on a subsurface groundwater dependent ecosystem and on changes related to post-earthquake hydrodynamics, *Environ. Earth Sci.*, doi:10.1007/s12665-014-3440-1.

Pollard D.D., and G. Holzhausen, 1979, On the mechanical interaction between a fluid-filled fracture and the earth's surface, *Tectonophysics*, **53**, 27–57, doi:10.1016/0040-1951(79)90353-6.

Rebischung, P., J. Griffiths, J. Ray, R. Schmid, X. Collilieux, and B. Garayt, 2012, Igs08: the igs realization of itrf2008, *GPS solutions*, *16 (4)*, 483–494, doi:10.1007/s10291-011-0248-2.

Riel, B., M. Simons, P. Agram, and Z. Zhan, 2014, Detecting transient signals in geodetic time series using sparse estimation techniques, *J. Geophys. Res. Solid Earth*, **119**1, 5140–5160, doi:10.1002/2014JB011077.

Riva, R., A. Aoudia, L.L.A. Vermeersen, R. Sabadini, and G.F. Panza, 2000, Crustal versus asthenospheric relaxation and post-seismic deformation for

shallow normal faulting earthquakes:the Umbria–Marche (central Italy) case, *Geophys. J. Int.*, **141**, F7–F11. doi:10.1046/j.1365-246x.2000.00146.x

Roe, G.H., 2005, Orographic precipitation, *Annu. Rev. Earth Planet. Sci.*, **33**, 645–671, doi:10.1146/annurev.earth.33.092203.122541.

Roeloffs, E.A., 2001, Creep rate changes at Parkfield, California 1966-1999: Seasonal, precipitation induced, and tectonic, *J. Geophys. Res.*, *106*(B8), 16525–16547, doi:10.1029/2001JB000352.

Rogers, G., and H. Dragert, 2003, Episodic tremor and slip on the Cascadia subduction zone: the chatter of silent slip, *Science*, **300**(5627), doi:10.1126/science.1084783.

Rothacher M., G. Beutler, W. Gurtner, T. Schildknecht, and U. Wild, 1990, BERNESE GPS Software Version 3.2, *Printing Office Univ. of Berne*, Switzerland.

Ruegg, J.C., M. Olcay, and D. Lazo, 2001, Co-, post-and pre (?)-seismic displacements associated with the Mw 8.4 southern Peru earthquake of 23 June 2001 from continuous GPS measurements, *Seismological Research Letters*, **72**(6), 673–678, doi:10.1785/gssrl.72.6.673.

Ruiz, S., M. Metois, A. Fuenzalida, J. Ruiz, F. Leyton, R. Grandin, C. Vigny, R. Madariaga, and J. Campos, 2014, Intense foreshocks and a slow slip event preceded the 2014 Iquique Mw 8.1 earthquake, *Science*, **345**(6201), 1165–1169, doi:10.1126/science.1256074.

Sakumura, C., S. Bettadpur, and S. Bruinsma, 2014, Ensemble prediction and intercomparison analysis of GRACE time-variable gravity field models, *Geophys. Res. Lett.*, **41**, 1389–1397, doi:10.1002/2013GL058632.

Satolli, S., and F. Calamita, 2008, Differences and similarities between the central and the southern Apennines (Italy): Examining the Gran

Sasso versus the Matese-Frosolone salients using paleomagnetic, geological, and structural data, *J. Geophys. Res. Solid Earth*, **113**, 1–16, doi:10.1029/2008JB005699.

Sausse, J., 2002, Hydromechanical properties and alteration of natural fracture surfaces in the Soultz granite (Bas-Rhin, France), *Tectonophysics*, **348**, 169–185, doi:10.1016/S0040-1951(01)00255-4.

Savage, W. Z., H. S. Swolfs, and B. Amadei, 1992, On the stateo f stress in the near-surface of the earth's crust, *Pure Appl. Geophys.*, **138**, 207–228.

Scherneck, H., 1991, A parametrized solid earth tide model and ocean tide loading effects for global geodetic baseline measurements, *Geophysical Journal International*, *106(3)*, 677–694.

Segall, P., 2010, Earthquake and Volcano Deformation, *Princeton University Press*, Princeton, New Jersey, USA.

Sella, G.F., S. Stein, T.H. Dixon, M. Craymer, T.S. James, S. Mazzotti, and R.K. Dokka, 2007, Observation of glacial isostatic adjustment in "stable" North America with GPS, *Geophys. Res. Lett.*, **34**, L02306, doi:10.1029/2006GL027081.

Silverii, F., D. Cheloni, N. D'Agostino, G. Selvaggi, and E. Boschi, 2014, Post-seismic slip of the 2011 Tohoku-Oki earthquake from GPS observations: Implications for depth-dependent properties of subduction megathrusts, *Geophys. J. Int.*, **198**, 580–596, doi:10.1093/gji/ggu149.

Simmons, A., S. Uppala, D. Dee, and S. Kobayashi, 2007, ERA-Interim: New ECMWF reanalysis products from 1989 onwards, *ECMWF newsletter*, 110, 25–35.

Sitharam, T.G., J. Sridevi, and N. Shimizu, 2001, Practical equivalent continuum characterization of jointed rock masses, *International Journal of Rock Mechanics and Mining Sciences*, **38**(3), 437–448.

Stabile T.A., A. Giocoli, V. Lapenna, A. Perrone, S. Piscitelli, and L. Telesca, 2014, Evidences of low-magnitude continued reservoir-induced seismicity associated with the Pertusillo artificial lake (southern Italy), *Bull. Seismol. Soc. Am.*, **104**, 1820–1828, doi:10.1785/0120130333.

Swenson, S.C., 2012, GRACE MONTHLY LAND WATER MASS GRIDS NETCDF RELEASE 5.0. Ver. 5.0. PO.DAAC, CA,USA. Dataset accessed [2015-09-14] at `http://dx.doi.org/10.5067/TELND-NC005`.

Swenson, S.C. and J. Wahr, 2006, Post-processing removal of correlated errors in GRACE data, *Geophys. Res. Lett.*, *33*, L08402, doi:10.1029/2005GL025285.

Tapley, B.D., S. Bettadpur, J.C. Ries, P.F. Thompson, and M. Watkins, 2004, GRACE Measurements of Mass Variability in the Earth System, *Science*, *53*(5683), 503–505, doi:10.1126/science.1099192.

Terzaghi, K., 1936, The shear resistance of saturated soils, Proceedings for the 1st. International Conference on Soil Mechanics and Foundation Engineering (Cambridge, MA), **1**, 54–56.

Tolomei, C., S. Salvi, J.P.M. Boncori, G. Pezzo, 2015, InSAR measurement of crustal deformation transients during the earthquake preparation processes: a review, *Bollettino di Geofisica Teorica ed Applicata*, **56**(2), 151–166, doi:10.4430/bgta0143.

P. Valty, O. Viron, I. Panet, X. Collilieux, 2015, Impact of the North Atlantic Oscillation on Southern Europe water distribution: insights from geodetic data, *Earth Interactions*, **19**(10) doi:10.1175/EI-D-14-0028.1.

Wahr, J., M. Molenaar, and F. Bryan, 1998, Time variability of the Earth's gravity field: Hydrological and oceanic effects and their possible detection using GRACE, *J. Geophys. Res.*, *103*(B12), 30205–30229, doi:10.1029/98JB02844.

Wahr, J., S.A. Khan, T. van Dam, L. Liu, J. H. van Angelen, M. R. van den Broeke, and C. M. Meertens, 2013, The use of GPS horizontals for loading studies, with applications to northern California and southeast Greenland, *J. Geophys. Res. Solid Earth*, *118*, 1795–1806, doi:10.1002/jgrb.50104.

Walwer, D., E. Calais, and M. Ghil, 2016, Data-Adaptive Detection of Transient Deformation in Geodetic Networks, *J. Geophys. Res. Solid Earth*, **121**, doi:10.1002/2015JB012424.

Wan, W., K.M. Larson, E.E. Small, C.C. Chew, and J.J. Braun, 2015, Using geodetic GPS receivers to measure vegetation water content, *GPS Solutions*, **19**(2), 237–248, doi:10.1007/s10291-014-0383-7.

Wang, R., F. Lorenzo-Martín, and F. Roth, 2006, PSGRN/PSCMP–a new code for calculating co- and post-seismic deformation, geoid and gravity changes based on the viscoelastic-gravitational dislocation theory, *Computers & Geosciences*, **32**, 527–541, doi:10.1016/j.cageo.2005.08.006, 2006

Wang, L.-F., R. Wang, F. Roth, B. Enescu, S. Hainzl, and S. Ergintav, 2009, Afterslip and viscoelastic relaxation following the 1999 M 7.4 Izmit earthquake from GPS measurements, *Geophys. J. Int.*, **178**(3), 1220–1237, doi:10.1111/j.1365-246X.2009.04228.x.

Wang, H., L. Xiang, L. Jia, L. Jiang, Z. Wang, B. Hu, and P. Gao, 2012, Load Love numbers and Green's functions for elastic Earth models PREM, iasp91, ak135, and modified models with refined crustal structure from Crust 2.0, *Computers and Geosciences*, **49**:190–199, doi:10.1016/j.cageo.2012.06.022.

Webb F.H., and J.F. Zumberge, 1993, An Introduction to GIPSY-OASIS II, Jet Propulsion Laboratory, JPL , Pasadena, CA, Publication D-11088.

Westerhaus, M., J.B. Altmann, O. Heidbach, 2008, Using topographic signatures to classify internally and externally driven tilt anomalies at

Merapi Volcano, Java, Indonesia, *Geophys. Res. Lett.*, **35**(5), L05310, doi:10.1029/2007gl032262.

Williams, S.D.P., 2008, CATS: GPS coordinate time series analysis software, *GPS Solutions*, **12**(2), 147–153, doi:10.1007/s10291-007-0086-4.

Zandt, G., C.J Ammon, 1995, Poisson's ratio of Earth crust, *Nature*, **374**, 152–155.

Zumberge, J.F., M.B. Heflin, D.C. Jefferson, M.M. Watkins, and F.H. Webb, 1997, Precise point positioning for the efficient and robust analysis of GPS data from large networks, *J. Geophys. Res.*, **102**(B3), 5005–5017, doi:10.1029/96JB03860.

Ringraziamenti

Desidero innanzitutto ringraziare il Dott. Nicola D'Agostino per avermi permesso di svolgere il mio dottorato presso l'Istituto Nazionale di Geofisica e Vulcanologia e per avermi guidato nell'apprendimento di questa affascinante professione, o forse meglio "missione", che è la ricerca scientifica. Un ringraziamento particolare va a Marianne Métois, per la sua amicizia, per la sua instancabile disponibilità e per il suo appoggio. Ringrazio inoltre la Prof.ssa Belardinelli, per i suoi preziosi consigli, e le tante persone che hanno contribuito in qualche modo a questo lavoro, anche con una semplice chiacchierata: Matteo Albano per la simulazione alle differenze finite, il prof Philip England per le interessanti discussioni, Kristel Chanard, Eleonora Rivalta, Daniele Cheloni e molti altri.

Un ringraziamento speciale va ai miei genitori per il loro appoggio incondizionato, per avermi trasmesso l'amore per la natura e per avermi insegnato la curiosità, lo stupore e l'entusiasmo, qualità fondamentali in questa professione, e al mio meraviglioso fratello, che ammiro oltremisura per la sua passione e il suo sorriso. Ringrazio inoltre i miei zii e cugini, la nonna Esmira per il suo affetto smisurato, la nonna Assunta per i suoi racconti e i suoi canti e i nonni che purtroppo ci hanno lasciato e a cui dedico questa tesi.

Non troverò mai le parole adatte per ringraziare Ivano per il suo amore, il suo sostegno e per riuscire sempre a dipanare la matassa dei miei pensieri.

Ringrazio le persone che hanno reso splendidi questi anni: i ragazzi dell'INGV, Marco, Marianne, Daniele, Andreas, Vito, Matteo, Elvira, Francesco, Sergio e Antonio per la loro preziosa compagnia durante le giornate di lavoro, per

i tanti aperitivi e per le gite fuori porta, le mie coinquiline Ilaria, Serena, Margherita, Enrica e Nunzia, gli amici "romani" per i numerosi appuntamenti da Danielone e gli arrosticini pariolini, gli amici biologi, gli Edith and friends, per la buona musica e i tanti arrosti in compagnia e i ragazzi conosciuti ad Oxford.

Un pensiero speciale va agli amici di sempre, che, anche se lontani, rappresenteranno sempre un punto di riferimento e un'ancora di salvezza: Sara, la mia compagna di studi per eccellenza, Serena, Laura, Maria Grazia, Anastasia, Giulia, Paola, Paola, Sabrina, Michele e tanti altri.

Come non ringraziare il mio amato Lillo che riesce sempre a farmi sorridere e che mi ha accompagnato durante questi anni di dottorato da quando, ancora cucciolo, dormiva sulle mie ginocchia mentre studiavo per l'esame di ammissione.

Non posso non ringraziare infine i miei compagni d'avventura del XXVIII ciclo...at the end, we survived!